3 1176 00134 5819
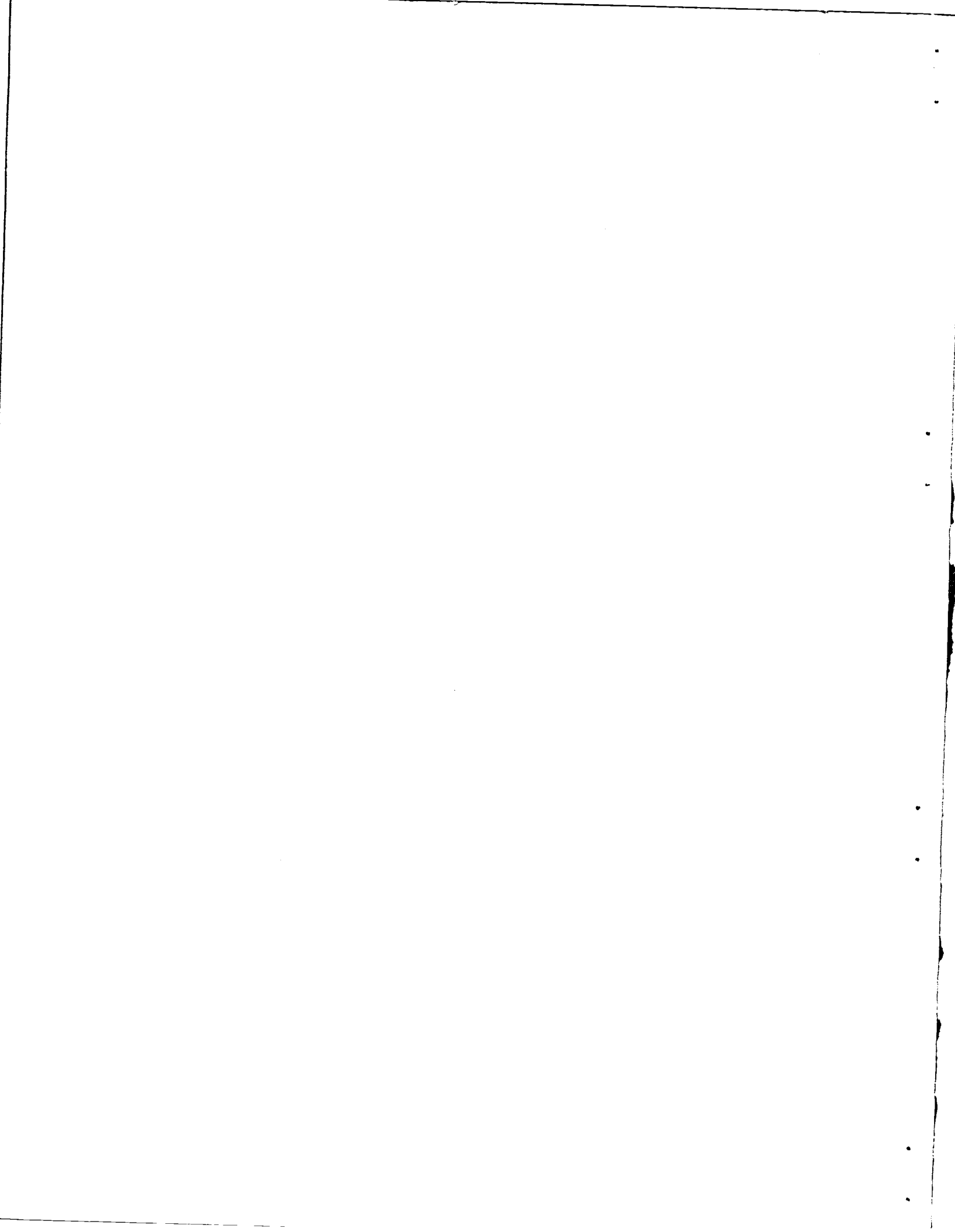
NASA-CR-159532
19790009686
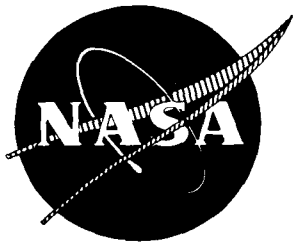
DESIGN, FABRICATION AND SPIN TESTING OF CERAMIC BLADE METAL DISK ATTACHMENT

FINAL REPORT - D1

United Technologies Corporation
Pratt & Whitney Aircraft Group
Government Products Division

46

PRATT & WHITNEY AIRCRAFT GROUP

GOVERNMENT PRODUCTS DIVISION

P. O. Box 2691
West Palm Beach, Florida 33402

In reply please refer to:
HMG:LS:jt:Pgm. Data Mgmt.

9 March 1979

National Aeronautics and Space Administration
Lewis Research Center
21000 Brookpark Road
Cleveland, Ohio 44135

Attention: Mr. James R. Johnston, 105-1
               NASA Project Manager

Subject: Submittal NASA Final Report CR 159532
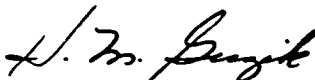
Reference: Contract NAS3-19715
               Design Fabrication and Spin Testing of Ceramic
               Blade Metal Disk Attachment

Gentlemen:

In accordance with the applicable requirements of the subject contract
we herewith submit a master reproducible of Final Technical Report
(P&WA Report No. FR-10179) which is submitted in accordance with Task
IV of the reference contract.

Enclosed is Form DD 250 for acknowledgement and acceptance of the
final report.

UNITED TECHNOLOGIES CORPORATION
Pratt & Whitney Aircraft Group
Government Products Division

H. M. Guzik
Program Data Manager

Enclosures: Master Reproducible and two copies of
             Final Report No. FR-10179

**UNITED
TECHNOLOGIES**

1. Report No. CR-159532	2. Government Accession No.	3. Recipient's Catalog No.
4. Title and Subtitle Design, Fabrication and Spin Testing of Ceramic Blade Metal Disk Attachment		5. Report Date February 1979
		6. Performing Organization Code
7. Author(s) Glenn Calvert		8. Performing Organization Report No. FR-10179
		10. Work Unit No.
9. Performing Organization Name and Address United Technologies Corporation Pratt & Whitney Aircraft Group Government Products Division P.O. Box 2691 West Palm Beach, Florida 33402		11. Contract or Grant No. NAS3-19715
		13. Type of Report and Period Covered Final Report
12. Sponsoring Agency Name and Address National Aeronautics and Space Administration Washington, D. C. 20546		14. Sponsoring Agency Code

15. Supplementary Notes

Project Manager, James R. Johnston, 105-1, NASA-Lewis Research Center
MS 500-313, 21000 Brookpark road, Cleveland, Ohio 44135

16. Abstract

A ceramic turbine blade-metal disk attachment was designed for small, non man-rated turbine engine applications. The selected design consisted of a hot pressed silicon nitride blade having a skewed dovetail attachment with a compliant interlayer between the disk and the blade. Two-dimensional and three-dimensional analyses predicted that life goals (50 hr, 100 cy) could be achieved, considering both NDE limitations and crack growth rates for the ceramic material. Twenty ceramic blades were fabricated to closely-held manufacturing tolerances. New fracture mechanics data (cyclic and steady-state crack growth, and fracture toughness) at elevated temperatures are presented. Although hot spin testing was originally planned to substantiate the design, this portion of the program was canceled and spin test results are not available.

N79-17857 #

17. Key Words (Suggested by Author(s)) High Temperature Ceramics Ceramic Turbine Blade Hot Pressed Silicon Nitride Fracture Mechanics Blade Attachment Compliant Layer		18. Distribution Statement Unclassified-Unlimited		
19. Security Classif. (of this report) UNCLASSIFIED		20. Security Classif. (of this page) UNCLASSIFIED	21. No. of Pages 142	22. Price*

NASA-C-168 (Rev. 10-75)

TABLE OF CONTENTS

LIST OF TABLES

LIST OF ILLUSTRATIONS

LIST OF ILLUSTRATIONS (Continued)

LIST OF ILLUSTRATIONS (Continued)

LIST OF ILLUSTRATIONS (Continued)

LIST OF ILLUSTRATIONS (Continued)

SUMMARY

The objective of this program was to design and substantiate a ceramic turbine blade-metal disk attachment. The blade was to be designed for operation at a gas stream average temperature of 1200°C (2200°F). Design life goal was 50 hr accumulated through 100 cy of nominally 0.5 hr duration. The design was to be appropriate for small, unpiloted applications such as remotely piloted vehicles.

The design approach was to use metal turbine design criteria to arrive at a preliminary blade configuration while generating the crack propagation characteristics for NC 132 hot pressed silicon nitride. The blade was then evaluated with fracture mechanics techniques to predict that the blade design was adequate to meet the life goal. An engine part should be further analyzed using probabilistic techniques, but this was beyond the scope of this program which was limited to spin-test hardware.

The program was planned in three tasks. Task 1, Preliminary Design, consisted of two-dimensional thermal and stress analyses to select a primary attachment design. In addition, fracture mechanics testing, compliant interlayer testing, and nondestructive evaluation (NDE) tests were carried out for subsequent use in detailed design.

Task 2, Detailed Design, included a photoelastic model test to verify the earlier two-dimensional stress analysis. Three-dimensional thermal and stress analyses were then conducted to arrive at a final attachment design.

In the third and final task, 20 ceramic blades were fabricated for hot spin testing. The original plan called for hot spin testing at a Government facility under a separate interagency agreement. However, these spin tests were not carried out due to priority and facility availability problems. This report, therefore, includes only the results of pretest spin pit checkout activities.

The ceramic blade designed in this program was based on an actual turbine design used in the Pratt & Whitney of Canada, Ltd JT15D turbofan engine. This blade had a blade height of approximately 2.5 cm (1 in.). The selected design concept consisted of a monolithic ceramic blade with realistic airfoil shape, full platform, and a skewed dovetail attachment. A compliant layer was used at the blade attachment-disk interface to achieve a uniform load distribution in the attachment region. The blade was designed for NC 132 hot pressed silicon nitride material, and platinum foil was selected for the compliant interlayer.

Results of the photoelastic model testing confirmed the stress levels and stress distributions predicted in the two-dimensional analyses. Results of the three-dimensional analyses showed that stress levels in the airfoil and attachment were acceptable to achieve the life goal, considering both NDE limitations and NC 132 crack growth rates.

Fabrication of 20 ceramic blades was undertaken using existing diamond-grinding techniques. Results showed that close design tolerances could be achieved, and the majority of blades were acceptable for hot spin testing.

Although the planned hot spin testing was not conducted, this program showed that acceptable design characteristics (in terms of predicted stresses and life) could be achieved with existing materials, design techniques, and NDE methods. This program generated NDE data and new fracture mechanics data that could be applied in other programs involving ceramic blade designs. Additional follow-on efforts involving hot spin testing are desirable to substantiate the present blade design and to calibrate the design system.

INTRODUCTION

At the time of initiation of this program, there were two main thrusts within the ceramics community in seeking a viable approach to ceramic blading. These were (1) all-ceramic blades and disk using different density ceramics to form a bonded, one-piece rotor, and (2) hybrid rotors with ceramic blades attached to a metal disk through forging techniques. The intent of this NASA-sponsored program was to explore the technology of attaching ceramic blades to a metal disk using more conventional blade attachment schemes.

The objective of this program was to develop a reliable attachment method for ceramic blades operating at a combustor exit average temperature of 1200°C (2200°F). The application for this design was defined as small, limited life engines used in unpiloted aircraft. Consequently, the Pratt & Whitney Aircraft of Canada, Ltd. (PWAC) JT15D engine was selected as the baseline for which the ceramic blade-metal disk attachment would be designed. The JT15D is a twin-spool turbofan in the 2200lb thrust class that is widely used in the civil aircraft industry, and it has been proposed for use in remotely piloted vehicle (RPV) applications.

The basic philosophy of this program was to design the ceramic blade attachment using only existing technologies; the program was not intended to develop new material compositions or properties, fabrication techniques, inspection methods, or design techniques. Rather it was intended to apply the most advanced technologies existing in the 1975-1976 time frame.

At the outset of the program, a number of decisions were made that set the course of the attachment design. Hot pressed silicon nitride was selected as the blade material; specifically, Norton's NC 132 was selected on the basis of its excellent high temperature strength properties. The disk material selected was Waspaloy, the same material used in the Bill-of-Material JT15D turbine.

It was decided to design the ceramic blade with an actual airfoil rather than a dummy blade. Although a dummy could have been used to provide the correct overall airfoil load to the attachment, it would not have given the proper load distribution into the attachment. This can be of paramount importance in ceramic blades, because the nonuniform load distribution of the airfoil can create locally high stress areas in the attachment that cannot be tolerated in a brittle material. To simplify the airfoil fabrication, the airfoil was designed without twist or taper while maintaining true loads at the root/platform intersection. In addition, the airfoil was designed for spin pit testing rather than engine testing, so that the airfoil was not tilted relative to the attachment. In the vacuum conditions of a spin pit, the untilted blade simulates the engine condition where gas bending loads are counteracted by airfoil tilt.

The basic attachment concept involved the use of a dovetail design rather than a fir tree, with a compliant layer in the blade-disk interface region. A dovetail was used because it provides a determinant loading situation in the attachment. A fir tree, with multiple load paths, results in a nondeterminant loading problem that is aggravated by the high modulus of the ceramic, and a fir tree could result in an overstress condition in the blade attachment. The intent of the compliant layer was to provide a more uniform load distribution along the attachment-disk loading planes.

The design life goal was 50 hr at full-rated temperature, accumulated through 100 cy of nominally 30 min duration. The scope of the program limited the analyses to steady-state conditions only; engine-like transients were not studied. Fracture mechanics were used insofar as practicable for life predictions; the basic design process was based on more conventional criteria (i.e., deterministic as opposed to probabilistic). It is recognized that a rigorous probabilistic design analysis is appropriate for ceramic structures, but this type of analysis was beyond the scope of this program.

Figure 1 presents the overall program approach. The Task I preliminary design was basically a two-dimensional analytical screening of various configurations that were consistent with the basic concept of a dovetail attachment with a compliant layer. In addition, Task 1 generated nondestructive evaluation (NDE) and fracture mechanics data that would be required in the subsequent tasks.

Task 2 was primarily a detailed three-dimensional design of the primary attachment selected at the end of Task 1. Prior to conducting the three-dimensional analysis, a photoelastic model was tested to verify the results of the two-dimensional analysis.

Task 3 consisted of hardware fabrication and engineering direction of hot spin testing. The spin testing was to be conducted at the Naval Air Propulsion Center (NAPC) in Trenton, N.J., under a separate interagency agreement between NSA-LeRC and NAPC. However, due to priority problems the spin test portion of Task 3 was not accomplished, and the program was terminated for the convenience of the Government. This report, therefore, documents the design and fabrication activities and the spin pit shakedown tests conducted prior to program termination.

Task 1

Prelim Design
● 2D Thermal Analysis
● 2D Stress Analysis
● NDE Calibration
● Fracture Mech Testing
● Life Prediction

Task 2

Detailed Design
● Photoelastic Model Testing
● 3D Stress Analysis

Task 3

Fab and Hot Spin Tests
● Blade/Spin Tool Fab
● First Spin Test Series
● Design Mod
● Second Spin Test Series
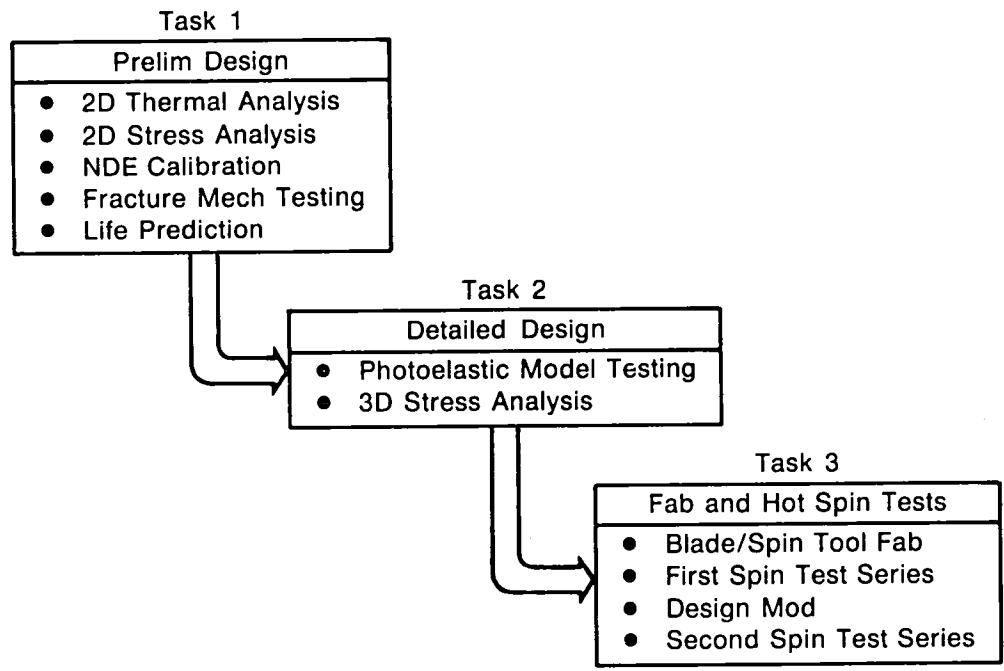
FD 114352

Figure 1. NASA Ceramic Blade Program Approach

TASK I — PRELIMINARY DESIGN

1.0 TWO-DIMENSIONAL ANALYSIS

1.1 Material Selection

The material selected for use in this program was NC 132 hot pressed silicon nitride developed by the Norton Company. This selection was based on the material's mechanical properties, which yielded the highest flexural strength of any commercially available ceramic.

1.2 Approach and Preliminary Design Critieria

The four basic attachments that were studied in this program are shown in Figure 2. These are all variants of a dovetail attachment, and are described as straight, skewed, and curved roots. The fourth configuration consists of the reduction or elimination of the platform, which could be applied to any of the three root configurations. In all cases, a compliant interlayer was used to achieve more uniform load distribution at the blade-disk interface.

The ceramic blade airfoil has a contour that is similar to the Pratt & Whitney of Canada JT15D first turbine blade. This ensures that the load transfer from the airfoil to the attachment will be typical of an engine design. The ceramic airfoil was designed with a constant cross section in the spanwise direction to facilitate fabrication. The spanwise dimension was selected to give the same blade pull as an engine blade made from NC 132 (a blade with twist and taper). The ceramic blade airfoil was radially oriented, so that no bending loads would be induced during spin pit testing. The same situation is achieved in an engine design by tilting the airfoil, so that gas bending loads are offset by centrifugally-induced bending. Overall dimensions of the ceramic blade are shown in Figure 3.

The design approach adopted at the outset of this program was committed to the use of fracture mechanics insofar as practical. However, fracture mechanics data did not exist for NC 132 at the time of design initiation. Consequently, to provide a starting point for the two-dimensional analysis, fracture mechanics data was taken from the work conducted by the National Bureau of Standards (NBS) and published as NBSIR 74-442, "High Temperature Slow Crack Growth in Ceramic Materials," by Dr. A. G. Evans. The applicable data in this program consisted of crack growth in hot pressed silicon nitride (Norton's NC 130) under steady load. Test temperatures for this data ranged from 1200°C (2200°F) to 1400°C (2550°F). The temperatures of interest in the current program are 1200°C, which may be experienced in the airfoil, and a lower temperature level that would be expected in the neck region of the attachment. Therefore, only the 1200°C data had direct relevance to this program.

For preliminary design purposes, the NBS data at 1200°C was used in the form shown in Figure 4. This figure was used to estimate the time to failure for a given initial flaw size and stress level. The NBS data required some extrapolation into the stress intensity range of interest to generate Figure 4.

The criteria adopted for this program required that the blade attachment be designed for the smallest detectable flaw size in the ceramic. For preliminary design purposes, a minimum detectable internal flaw size of 0.08 cm (0.030 in) was assumed. This value is consistent with previously published data for nondestructive evaluation (NDE) of hot pressed silicon nitride. Based on the NBS crack growth data, a 0.08 cm (0.03 in.) internal flaw would permit an allowable stress of about 110 mpa (16 ksi) at 1200°C (2200°F).

4

Basic
Dovetail

Skewed

Curved

Reduced Platform

Root and Platform Variations

Ceramic
Blade

Compliant Interface Material

FD 91750
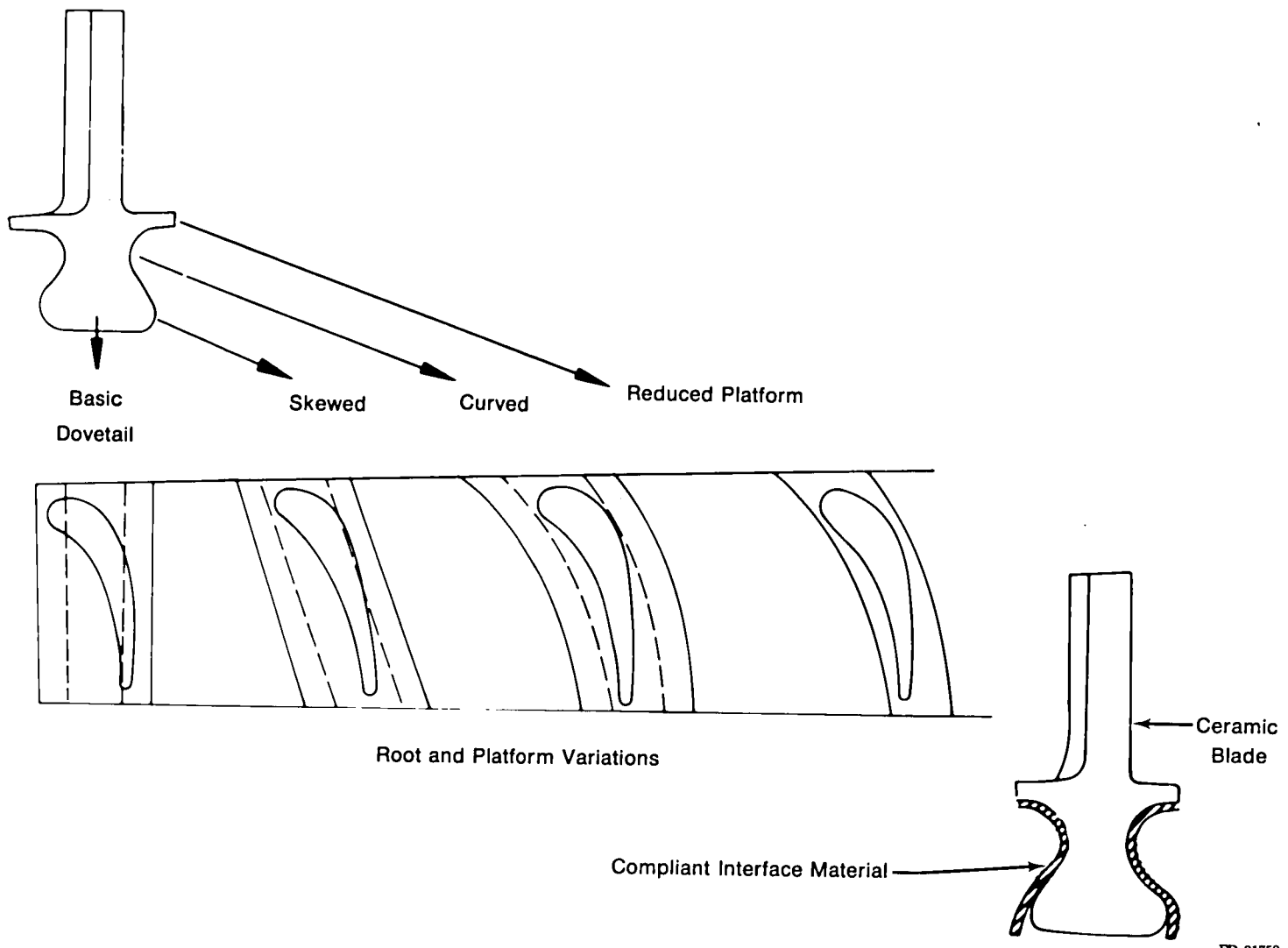
Figure 2. Attachment Concepts

5

24°

(0.480)
1.22

(0.740)
1.88

(0.97)
2.46

Dimensions in (Inches)
and Centimeters

(0.260)
0.66

(0.280)
0.71
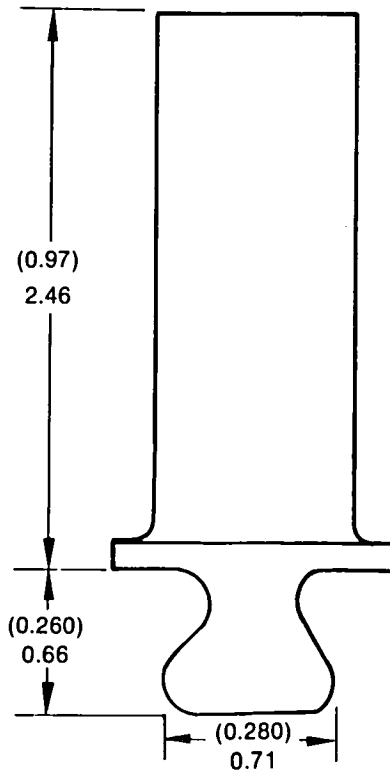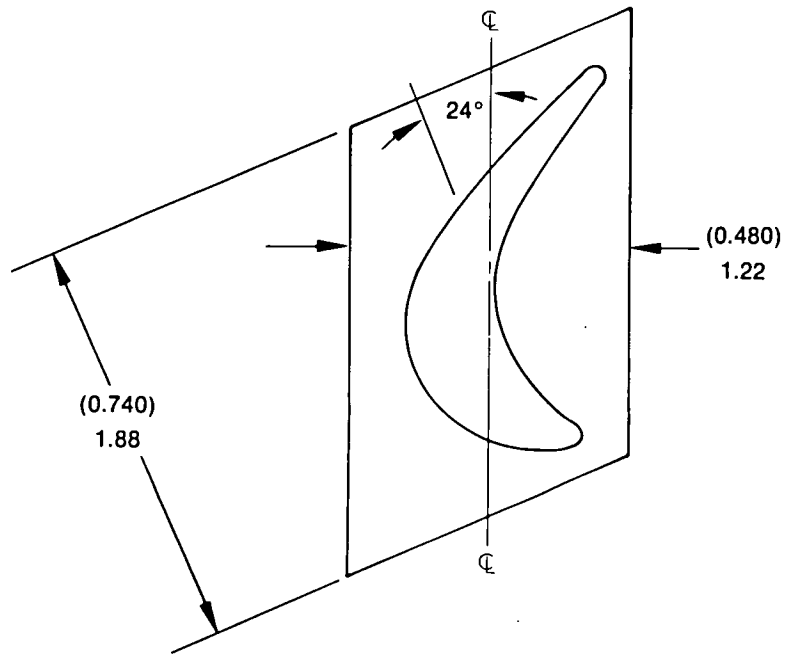
FD 152134

Figure 3. NASA Ceramic Blade Overall Dimensions
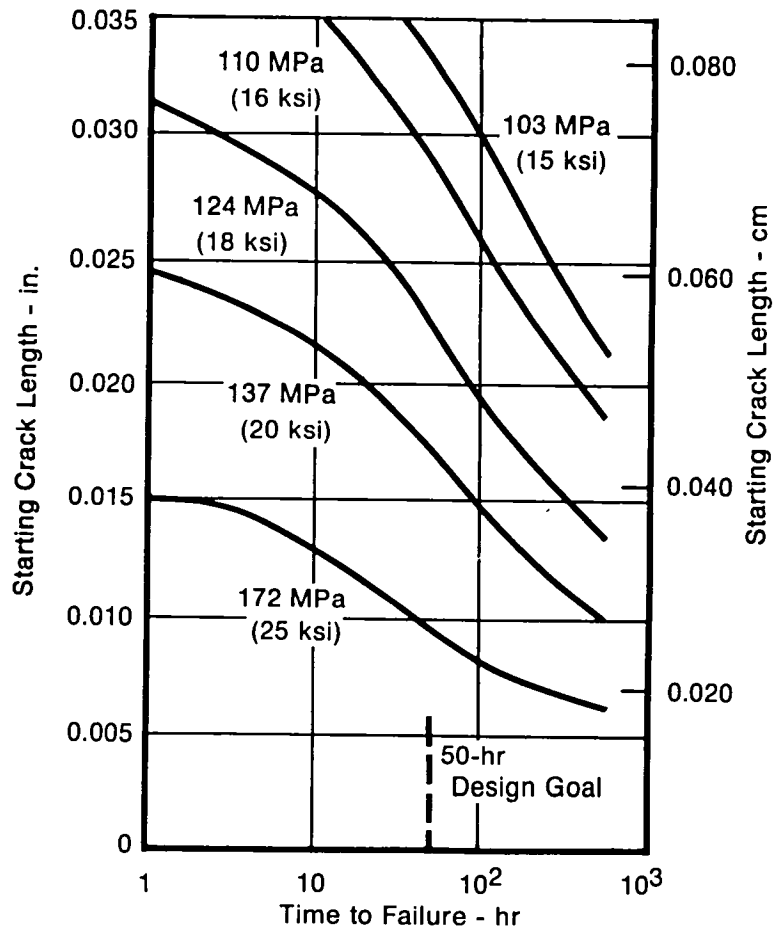
Ref: NBSIR 74-442, "High Temperature Slow Crack Growth
in Ceramic Materials," A. G. Evans, Feb 1974

FD 139313

Figure 4. Preliminary Crack Growth Data (NC 130 at 1200°C)

In addition to the use of fracture mechanics data in the design analysis, the blade attachment was also checked against conventional design criteria. This required the establishment of design allowables for uniaxial tension, creep-rupture in the higher temperature regimes, and flexure strength. Uniaxial tension and creep-rupture would be the dominating criteria where the stress field is essentially uniaxial, such as the airfoil. Flexure would be the dominating criteria where the stress field has steep gradients such as in the platform and dovetail regions. Compression and shear failures are not considered, since ceramic parts usually fail in some other induced mode when loaded in compression or shear.

Using the preliminary design criteria, a nominal blade attachment was sized on the basis of manual calculations to provide the starting point for two-dimensional thermal and stress analysis. The overall dimensions of this dovetail root are presented in Figure 5. The root angle of the 0.52 rad (30 deg) was selected primarily on the basis of the Westinghouse ceramic blade design study as reported in ASME Paper No. 74-GT-96, which indicated that this value was the optimum root angle. Using this initial root geometry, calculations of overall design parameters were completed for a straight, skewed, and curved root. Results are presented in Table I, along with baseline values of the JT15D for comparison. It should be noted that neck stresses shown in Table I are average values and were used primarily for rough sizing purposes.

7

Table I shows that the number of ceramic blades would have to be reduced significantly below the 71 blades in the JT15D. This is a direct result of selecting a dovetail type attachment for the ceramic blades as opposed to the conventional fir tree attachment of the JT15D engine blade. From a load carrying standpoint, fir trees are a more efficient design than dovetails, because the disk lugs (disk material between blades) for a fir tree have their largest area at the base, or inner radius. Dovetails, on the other hand, require a disk lug with a small area at its inner radius, and a large area near its outer radius. The result is that a dovetail lug has limited load carrying capability at its inner radius, and increased dead load from its outer radius. Table I also shows that the number of blades for skewed and curved root blades (54) are lower than the number of straight blades (64). This is a limitation of the disk, which received an additional torque load from skewed and curved attachments.

The broach angle of 0.42 rad (24 deg) selected for the skewed blade is the same as the JT15D blade. As discussed later, 0.42 rad (24 deg) provides the best compromise between leading edge overhang, which is a problem at higher angles, and trailing edge overhang, which is a problem at lower angles. Likewise, the curved root radius of 2.2 cm (0.85 in.) was selected to provide the best overhang compromise.

1.3 Thermal Analysis

A two-dimensional thermal analysis was completed for the attachment geometry as shown in Figure 5. The following assumptions were adopted for the thermal analysis:

- The average rotor inlet gas total temperature was 1200°C (2200°F).

- The spanwise gas temperature distribution was similar to that of the JT15D production engine.

- Spanwise temperature gradients in the ceramic airfoil were the same as the JT15D engine blade.

- The disk live rim temperature was the same as the JT15D engine.

- The compliant interlayer thermal conductivity was equivalent to that of Waspaloy, the disk material.

The thermal analysis model and the resulting temperature predictions are shown in Figure 6. The most significant temperatures are at the airfoil root and at the attachment neck. The predicted temperature at the airfoil root is 1060°C (1945°F), (node 4), and in the attachment neck region (nodes 6 and 7), the ceramic temperatures are predicted at 940°C (1718°F). Nodes 19 and 20 predict an average temperature of 855°C (1570°F) for the interlayer material. These temperature predictions, which were used for the preliminary design analysis, are based on 50% contact between the blade root and the interlayer material. This is a conservative assumption, since the analysis predicted that blade attachment temperatures would be approximately 20°C (70°F) higher with 50% contact as compared to 100% contact (Reference Figure 7). It is expected that the attachment would experience approximately 100% contact due to deformation of the interlayer material.
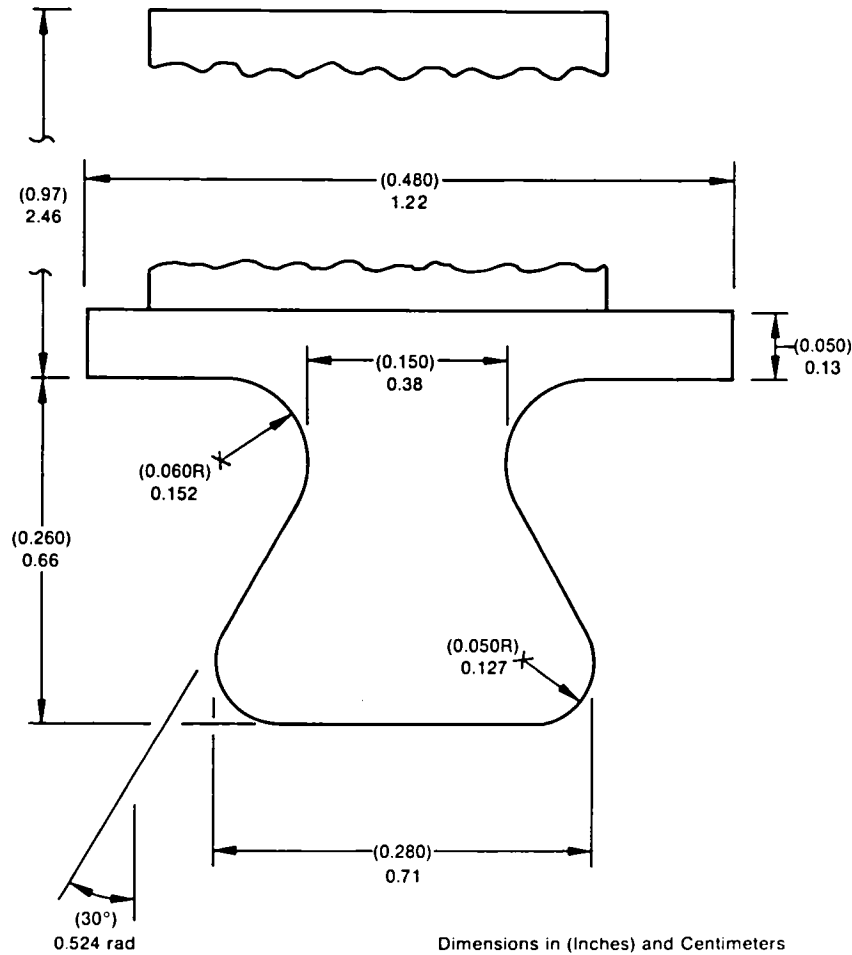
Figure 5. Preliminary Attachment Dimensions

Dimensions in (Inches) and Centimeters

FD 139314

TABLE I.   PRELIMINARY DESIGN PARAMETERS FOR STRAIGHT, SKEWED AND CURVED
ROOTS

Parameter	Straight	Skewed	Curved	JT15D
Broach Angle, rad (deg)	0 (0)	0.419 (24)	0.015 (0.85)*	0.419 (24)
Disk, axial dimension, cm (in.)	1.87 (0.738)	1.87 (0.738)	1.87 (0.738)	1.87 (0.738)
Neck dimension (normal to broach), cm (in.)	0.381 (0.150)	0.381 (0.150)	0.381 (0.150)	N/A
Neck steady-state stress (average), MPa (psi)	102 (14,800)	95.6 (13,870)	99 (14,360)	N/A
Interface bearing stress, MPa (psi)	213.7 (31,000)	275.8 (40,000)	234.4 (34,000)	N/A
Airfoil root stress, MPa (psi)	102 (14,800)	102 (14,800)	102 (14,800)	N/A
Number of blades	60	54	54	71

*Mean radius of curvature, in.; N/A not applicable.
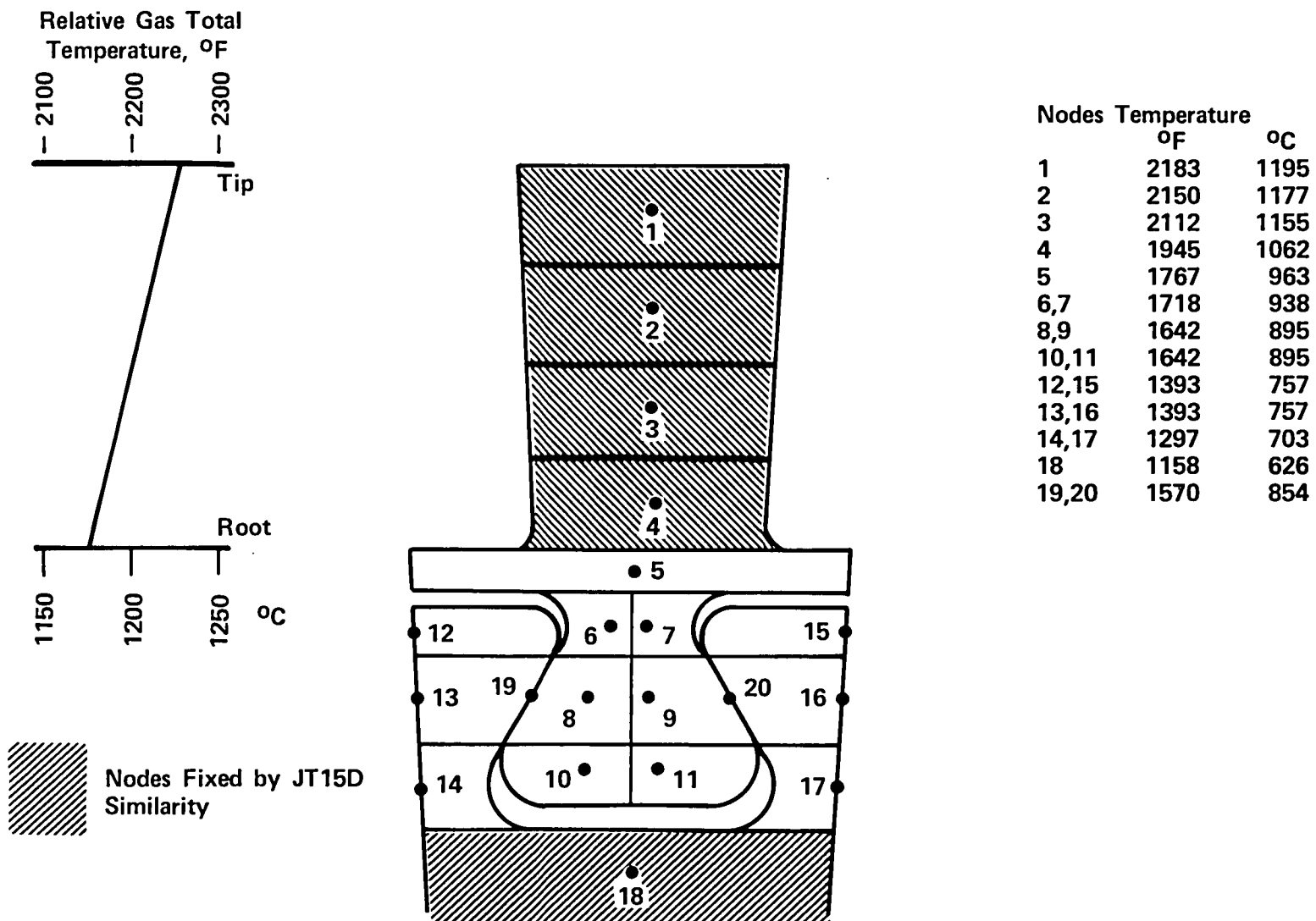
Figure 6. Two-Dimensional Heat Transfer Results

Nodes	Temperature	
	°F	°C
1	2183	1195
2	2150	1177
3	2112	1155
4	1945	1062
5	1767	963
6,7	1718	938
8,9	1642	895
10,11	1642	895
12,15	1393	757
13,16	1393	757
14,17	1297	703
18	1158	626
19,20	1570	854

FD 96132
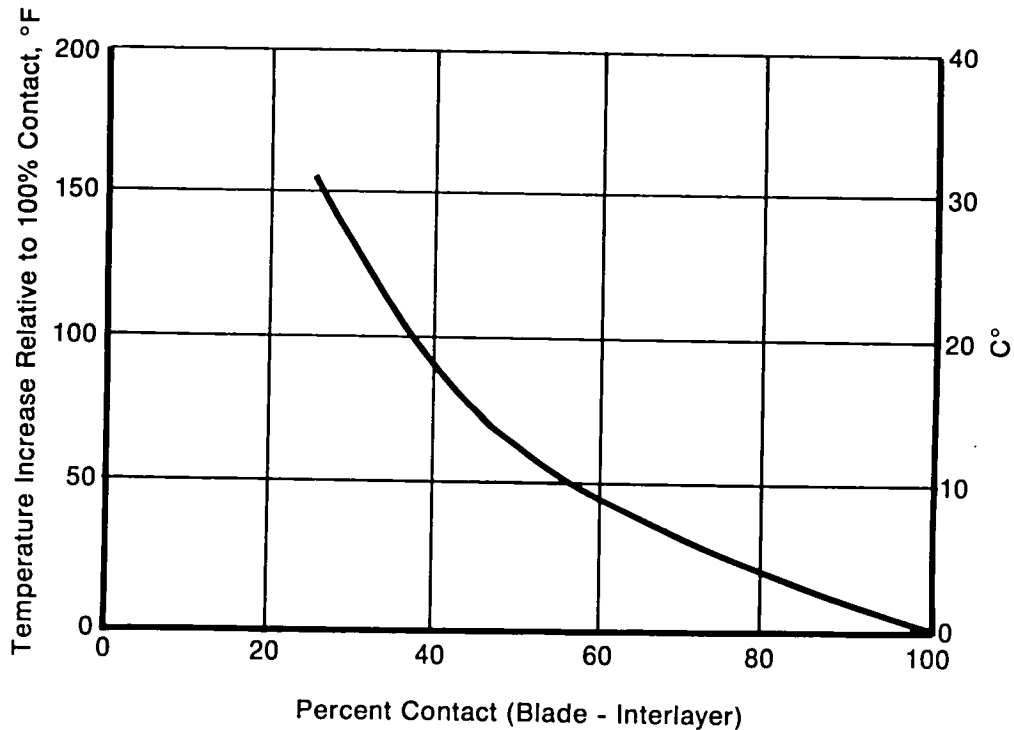
Figure 7. Ceramic Attachment Temperature Variation

1.4 Two-Dimensional Stresses

The initial segment of the stress analysis included a prediction of airfoil stress as a function of span location, based on the JT15D design speed of 30,600 rpm. Results of this analysis, shown in Figure 8, predict a maximum stress of about 103 MPa (15 ksi) at the airfoil root. Since there is essentially a uniform stress condition at the blade root, uniaxial tensile data can be used to judge the acceptability of the design. Figure 9 presents uniaxial tensile and creep-rupture data from Ford, Westinghouse, and PWA, with an approximate two-sigma curve to cover data scatter. At the predicted blade root temperature, 103 MPa (15 ksi) provided an acceptable margin.

The remainder of the two-dimensional stress analysis was directed toward the attachment region of the blade. Figure 10 shows the analytical model, and Figure 11 shows the nodal breakup used in the analysis. It should be noted that no friction was considered in the interlayer region. This was done to simplify the analysis, since the primary objective was to evaluate comparative stresses. Later, in the three-dimensional analysis, friction forces were taken into account. Airfoil loads were broken up into discrete increments, as shown in Figure 12, and applied along the platforms. The analysis was conducted in two steps for each configuration, each step considering one-half of the attachment (Reference Figure 10). Figure 13 defines blade attachment terminology, and it also shows that all configurations were analyzed with the airfoil center of gravity located at the center of the attachment. The contact area between blade and disk was assumed to be 100%.

The results of the stress study are summarized in Figure 14 which compares the maximum principal tensile stresses for the four candidate configurations. The straight dovetail was predicted to experience the maximum tensile stress, followed in order by the curved dovetail, skewed root, and skewed root with reduced platform. The predicted stress level of the interface material was 275.8 MPa (40 ksi) in all cases. On the basis of these results, the skewed root — full platform was selected as the primary approach, with the skewed root — reduced platform being held as a backup configuration.

11
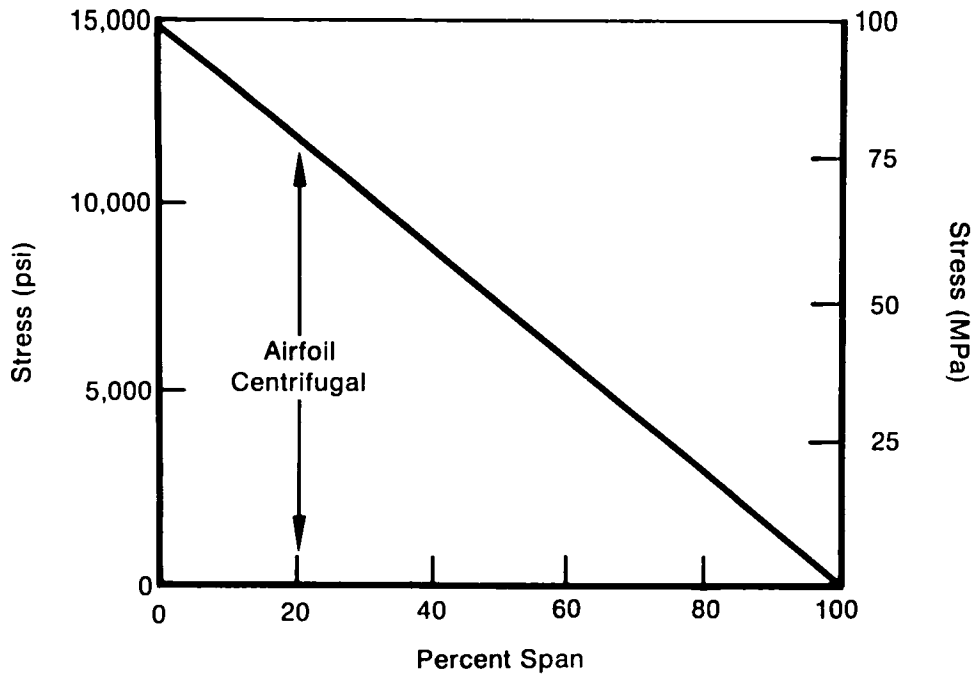
FD 139316

Figure 8. Airfoil Stress Distribution
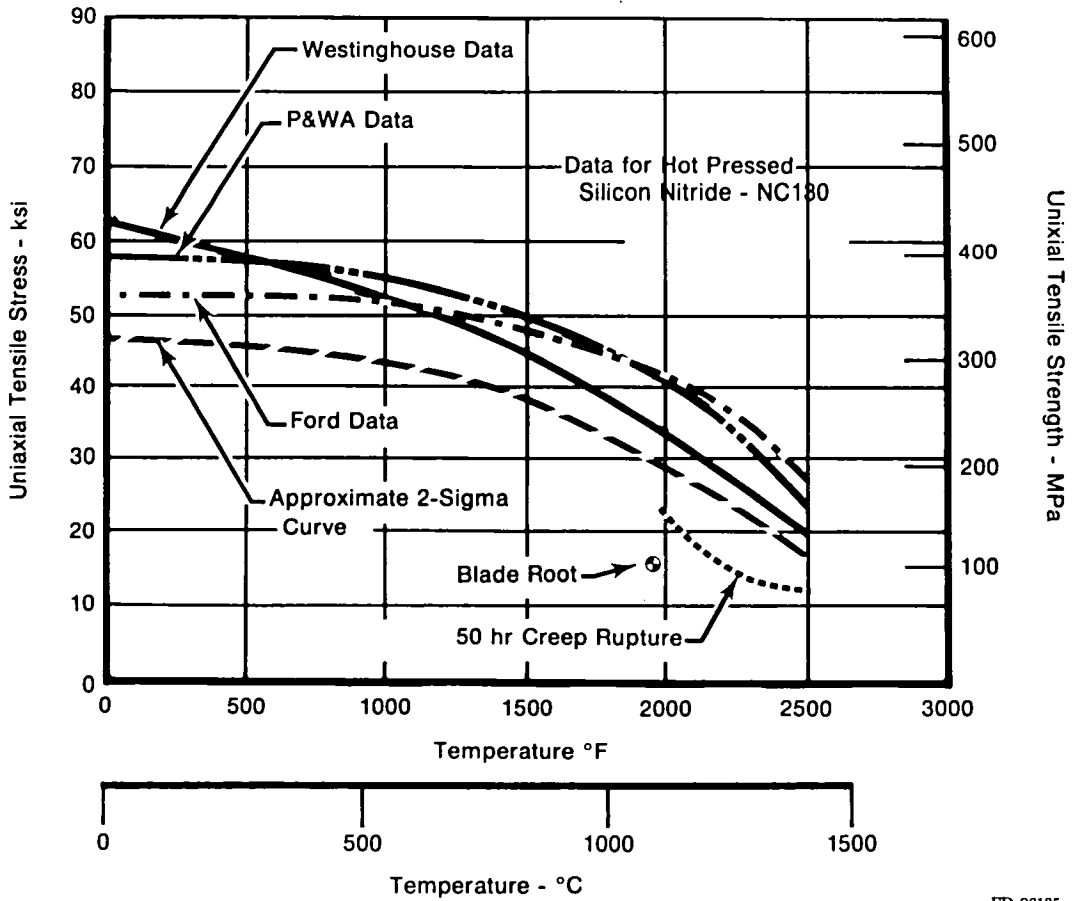
FD 96135

Figure 9. Airfoil Stress Gives Acceptable Margin

12
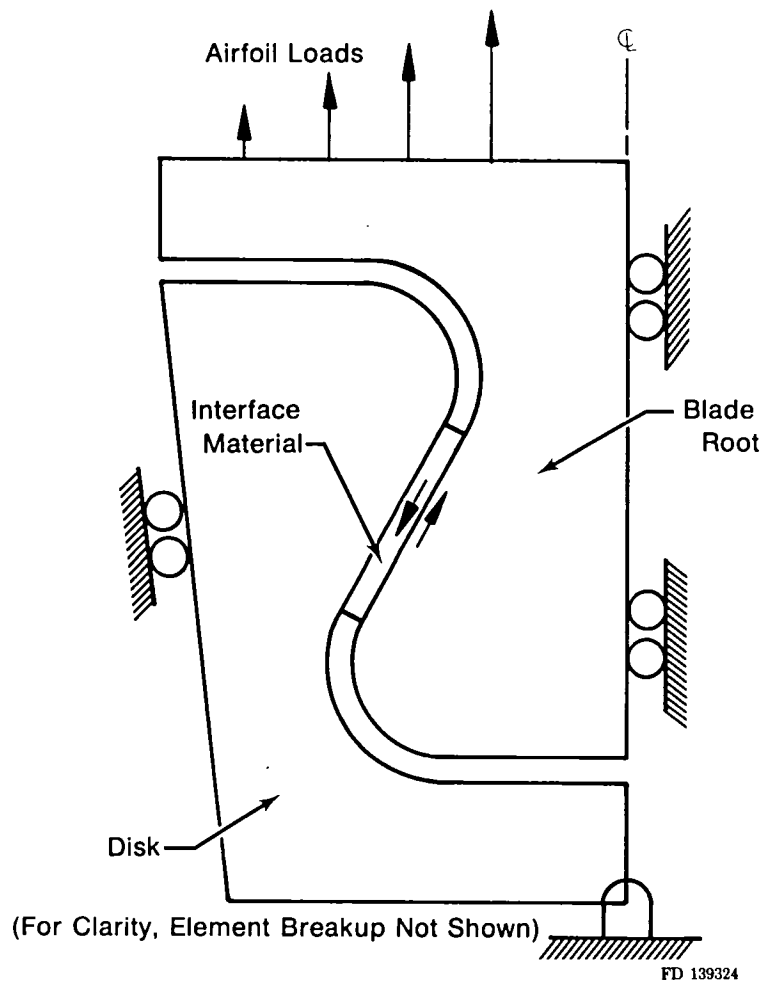
Figure 10. *Two-Dimensional Finite Element Model*

Blade

0.42 rad (24 deg)
Skewed Root,
Full Platform

Interlayer

Disk

0.05 cm
(0.020 in.)
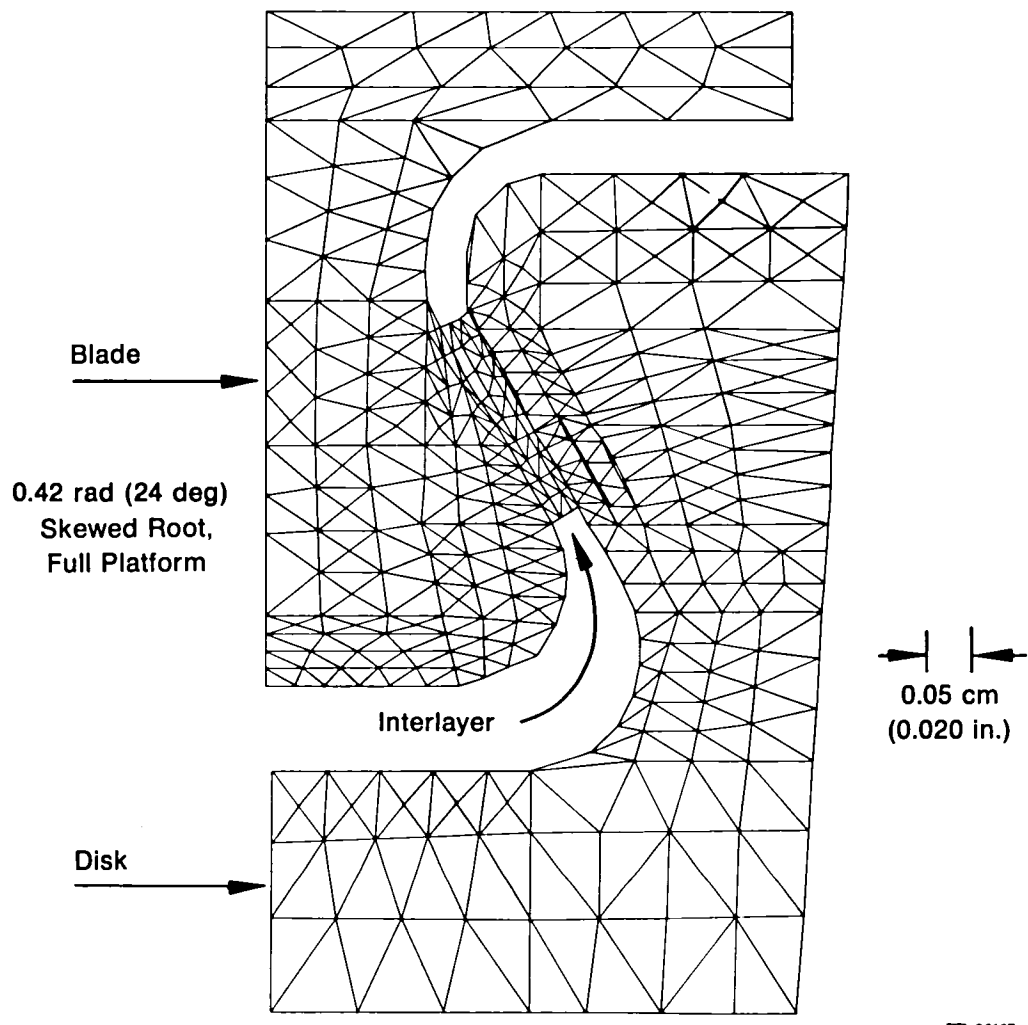
FD 96127

Figure 11. Two-Dimensional Element Breakup

14

Airfoil Load of
This Element
Assumed Evenly
Distributed Along
Platform
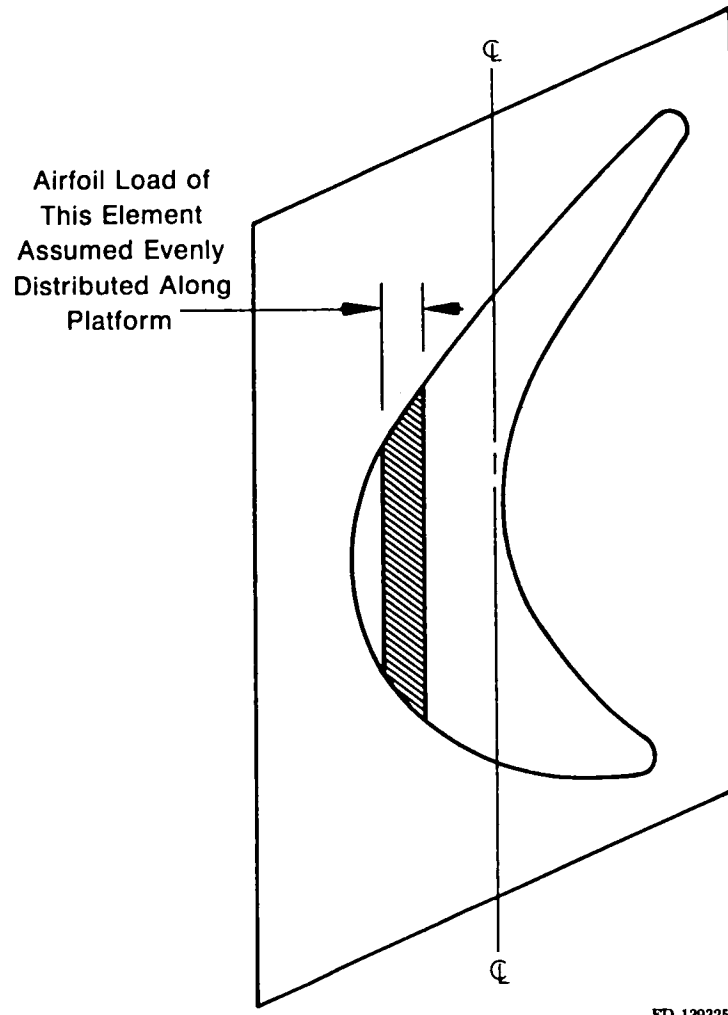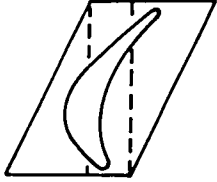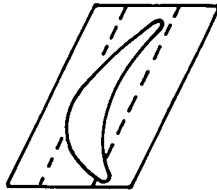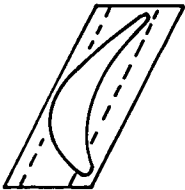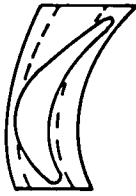
FD 139325

Figure 12. Airfoil Load Element Definition

15

Suction Surface ⟶

Leading Edge

Trailing Edge

End View

Interlayer

100% Contact

56% Contact

Root Angle

Broach Angle

Axial Direction

Airfoil Center of Gravity
Located at Blade Root Center

Bottom View

Note: Reduced Platform Is Tangent
to Airfoil at Trailing Edge
and Suction Surface

Reduced Platform

Full Platform
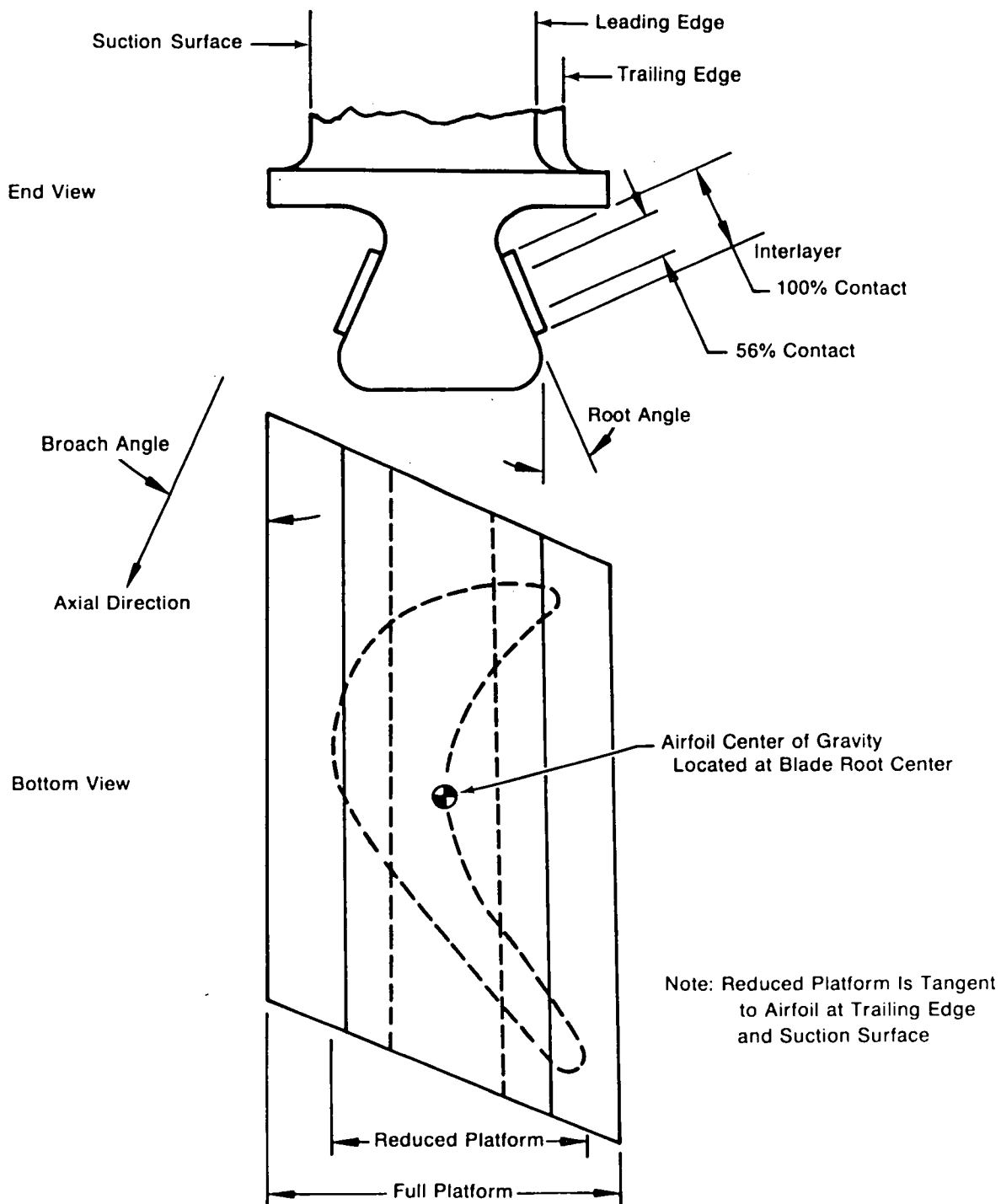
FD 139326

Figure 13. Blade Attachment Terminology

16

Configuration		No. of Blades	Max Principal Tensile Stress MPa (ksi)	
			Suction	Pressure
Straight Dovetail 0 rad (0 deg Broach) Full Platform		60	394 (57.2)	611 (88.7)
Skewed Dovetail 0.419 rad (24 deg Broach) Full Platform		54	238 (34.6)	246 (35.8)
Skewed Dovetail 0.419 rad (24 deg Broach) Reduced Platform		54	198 (28.7)	228 (33.1)
Curved Dovetail (Circular ARC Broach) Reduced Platform		54	276 (40.1)	178 (25.8)

All Configurations Have 0.524 rad (30 deg) Root Angle

FD 96133

Figure 14. Results of Two-Dimensional Stress Study

The higher predicted stress levels for the straight and curved roots were attributed to more severe airfoil overhang for these two configurations, relative to the skewed root. Figure 15 illustrates the relative overhang for the straight, skewed, and curved roots. Although greater overhang was expected for the straight root, it was not anticipated for the curved root. The cause of the curved root overhang is the relatively high camber angle of the airfoil, which would require a smaller-radius circular root for better conformity. However, disk stress limitations preclude the use of a curved root with a smaller radius than that shown. In addition, assembly considerations require that the curved platforms be designed as circular arcs with the same center of curvature as the root; this results in some exposed disk area between blades, which would require some type of thermal protection in an actual engine design.
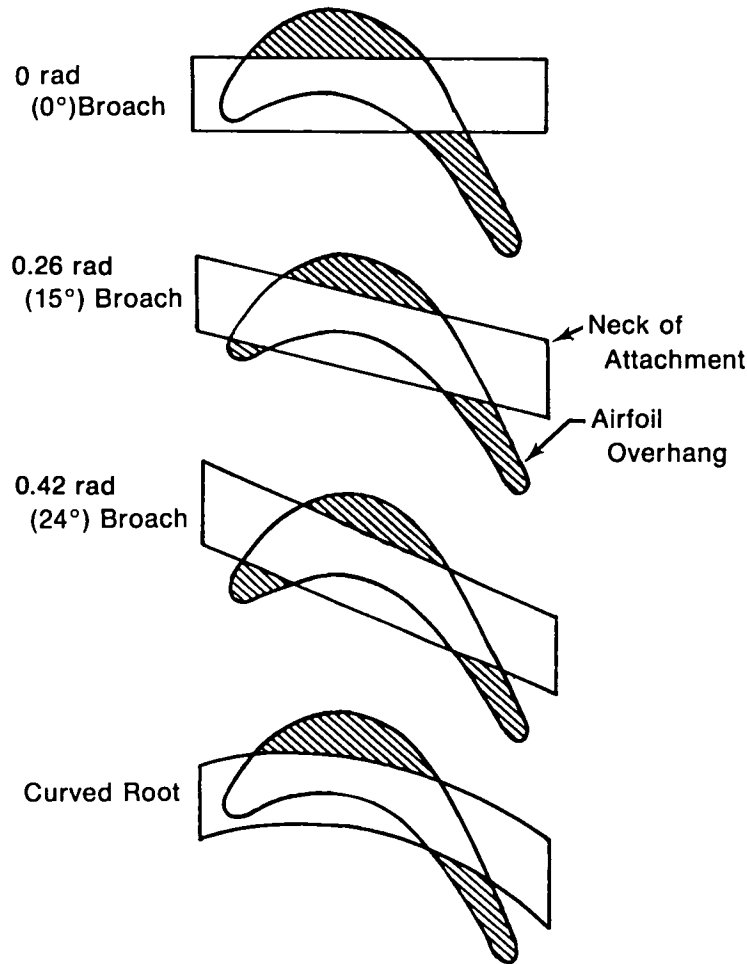
FD 139327

Figure 15. Comparison of Airfoil Overhang

The rationale for selecting the full platform skewed root as the primary configuration (instead of the lower-stress reduced platform version) is that it represents a more desirable design for engine use since the full platforms provide thermal protection for the disk regions between blades.

Two parametric variations of the skewed root were also analyzed in a sensitivity study. The variations were: (1) reduced contact area between the ceramic and the interlayer, and (2) a 0.79 rad (45 deg) root angle instead of the 0.52 rad (30 deg) angle. Results are summarized in

18

Table II. This table shows that the predicted maximum principal stress (tensile) is reduced slightly with 56% contact area. This is the result of moving the area of contact farther from the maximum stress location. In a real situation this would overstress the interlayer material, which would then deform plastically. Plastic deformation would proceed, increasing the contact area and decreasing the stress to a level where deformation would cease. Thus, a ceramic blade should not be overstressed during the period of initial interlayer deformation. The maximum principal stress predicted for a 0.79 rad (45 deg) root angle is shown to be higher than for a comparable 0.52 rad (30 deg) angle, but the magnitude of the increase is small.

TABLE II.   RESULTS OF SENSITIVITY STUDY

Configuration[1]			Number of Blades	Maximum Principal Stress[2]
Platform	Root Angle	Contact Area		
Full	0.52 rad (30 deg)	100%	54	247 MPa (35.8 ksi)
Reduced	0.52 rad (30 deg)	100%	54	228 MPa (33.1 ksi)
Reduced	0.52 rad (30 deg)	56%	54	223 MPa (32.3 ksi)
Reduced	0.79 rad (45 deg)	100%	51	237 MPa (34.3 ksi)

Note: [1]Temperature distribution for 50% contact area used for all cases.
[2]Value shown is max tensile principal stress, which occurs on the pressure side of the root.

Figure 16 presents the stress distribution in the attachment section for the full-platform skewed root. Although the maximum local tensile stress is 240 MPa (34.8 ksi) it is highly localized on the surface at the attachment neck and reduces rapidly to values below 60 MPa (10 ksi) at the centerline. To provide a context for evaluating the acceptability of this stress distribution, four-point flexure data can be used. Figure 17 shows flexure data for NC 130 from Pratt & Whitney Aircraft and Westinghouse, with an approximate two-sigma curve to cover data scatter. At the predicted attachment temperature of 937°C (1718°C), the 228 MPa (33 ksi) predicted stress level provides a satisfactory margin for preliminary design. The steep stress gradients shown in Figure 16 are typical of all configurations studied. At the completion of the two-dimensional stress analysis, it was concluded that the configuration was acceptable for a preliminary design and the effort proceeded into a three-dimensional stress analysis.

2.0   INTERLAYER MATERIAL EVALUATION

Various compliant interlayer material candidates were investigated during this program. The interlayer material characteristics sought for this application are: (1) low resistance to initial deformation, and (2) increasing resistance as deformation progresses. The low initial resistance is desirable to avoid local overloads in the ceramic as the interface material conforms to the anomalies in the mating parts during initial runup. Increasing resistance with deformation is required to avoid extrusion and loss of material from the interface region during subsequent engine operation. In addition, the ideal material would have good resistance to oxidation, and high strain to failure. Preliminary design calculations indicate that the interlayer will be subjected to about 275 MPa (40,000 psi) bearing stress at 855°C (1570°F) and it should have the capability to tolerate induced tensile strains of about 0.06 cm/cm based on a 0.01 cm (0.004 in.) mismatch and a 0.05 cm (0.020 in.) thick interlayer. Mechanically, it is desirable for the interlayer material to extend around the bottom of the dovetail to provide its own radial retention.

19

Figure 16. Two-Dimensional Stress Distribution

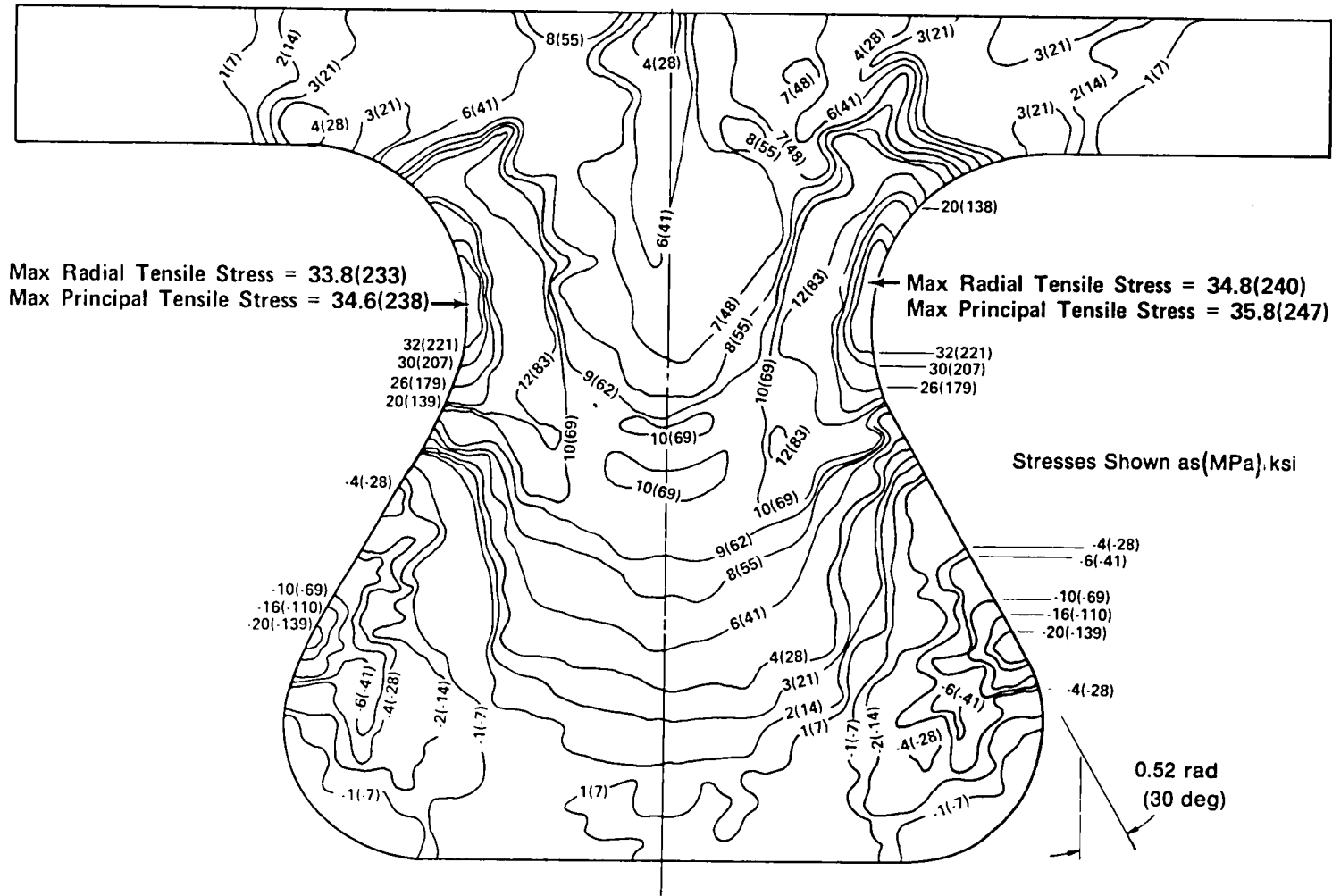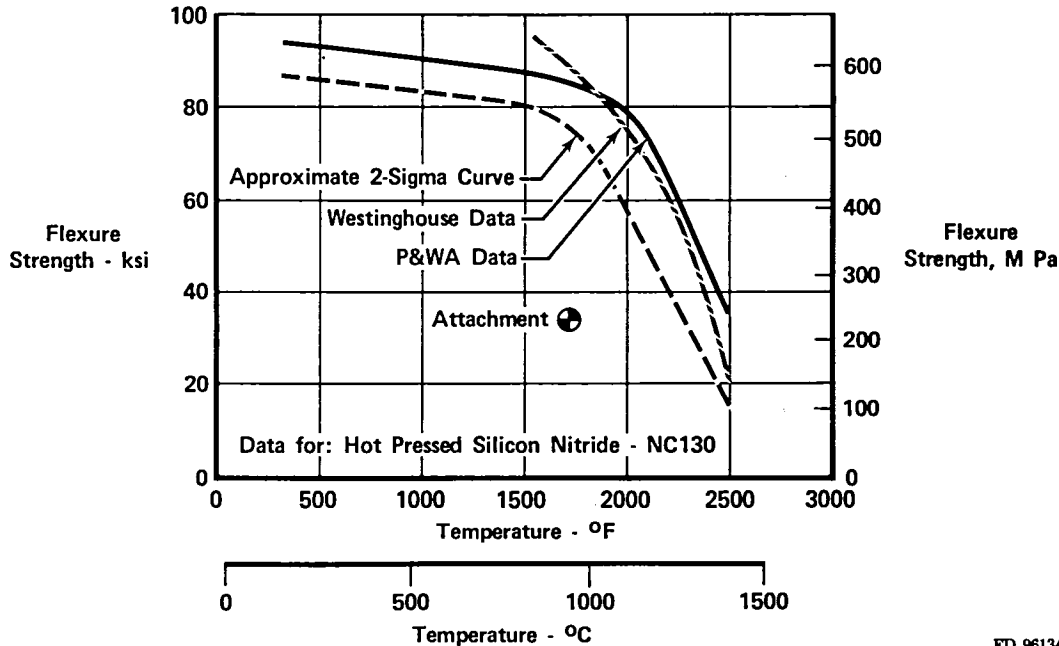Max Radial Tensile Stress = 33.8(233)
Max Principal Tensile Stress = 34.6(238)

Max Radial Tensile Stress = 34.8(240)
Max Principal Tensile Stress = 35.8(247)

Stresses Shown as(MPa) ksi

0.52 rad (30 deg)

FD 96128

20

Figure 17. Preliminary Design Stress vs Flexure Strength

This study considered three general classes of materials: (1) flexible ceramics such as random and woven fiber configurations; (2) solid metal foils; and (3) crushable metal configurations such as wire, perforated sheet, woven fibers, and sintered fibers. At this time, the use of a flexible ceramic as the interface material does not appear feasible. This conclusion is based on the results from a series of tests at P&WA, in which alumina-silica in a random fiber configuration was used as a compliant interface. Spin testing showed that the material spalled out of the assembly and caused failure of the attachment. The estimated 0.06 cm per cm tensile strain requirement for the present application is too high for a ceramic material. With the additional potential problem of embrittlement, it was concluded that ceramic interface materials would not satisfy the requirements of this design, and were therefore eliminated from further consideration.

A rigorous analytical study of the metal interface materials was handicapped by the lack of a verified anaytical model, especially in the case of the crushable materials. In addition, mechanical property data for some commercial configurations were not always available, as they are not normally used for this type of application. The selection of metal interface materials was therefore made on the basis of known properties in oxidation, corrosion, sulfidation, and chemical compatability; manufacturer's recommendations; and engineering judgment. The five selected metal candidates were as follows:

1. Platinum sheet
2. Perforated sheet — Inco 625
3. Woven wire — Inco 600 (Unique Wire)
4. Sintered sheet — Hoskins 875 (Brunswick Corp).

Platinum sheet was selected as a candidate because it has been used with some success in a similar application at P&WA, and it has desirable oxidation properties. Inco 625 was selected for the perforated sheet because it has good oxidation resistance, high elongation at failure, and acceptable mechanical properties. The materials for the woven wire and sintered sheet were selected on the basis of the respective manufacturer's recommendations. It was decided that the

21

0.013 cm (0.005 in.) Peak

Boron Nitride

Lubricated

Ceramic

Interlayer

Waspaloy (Disk Material)
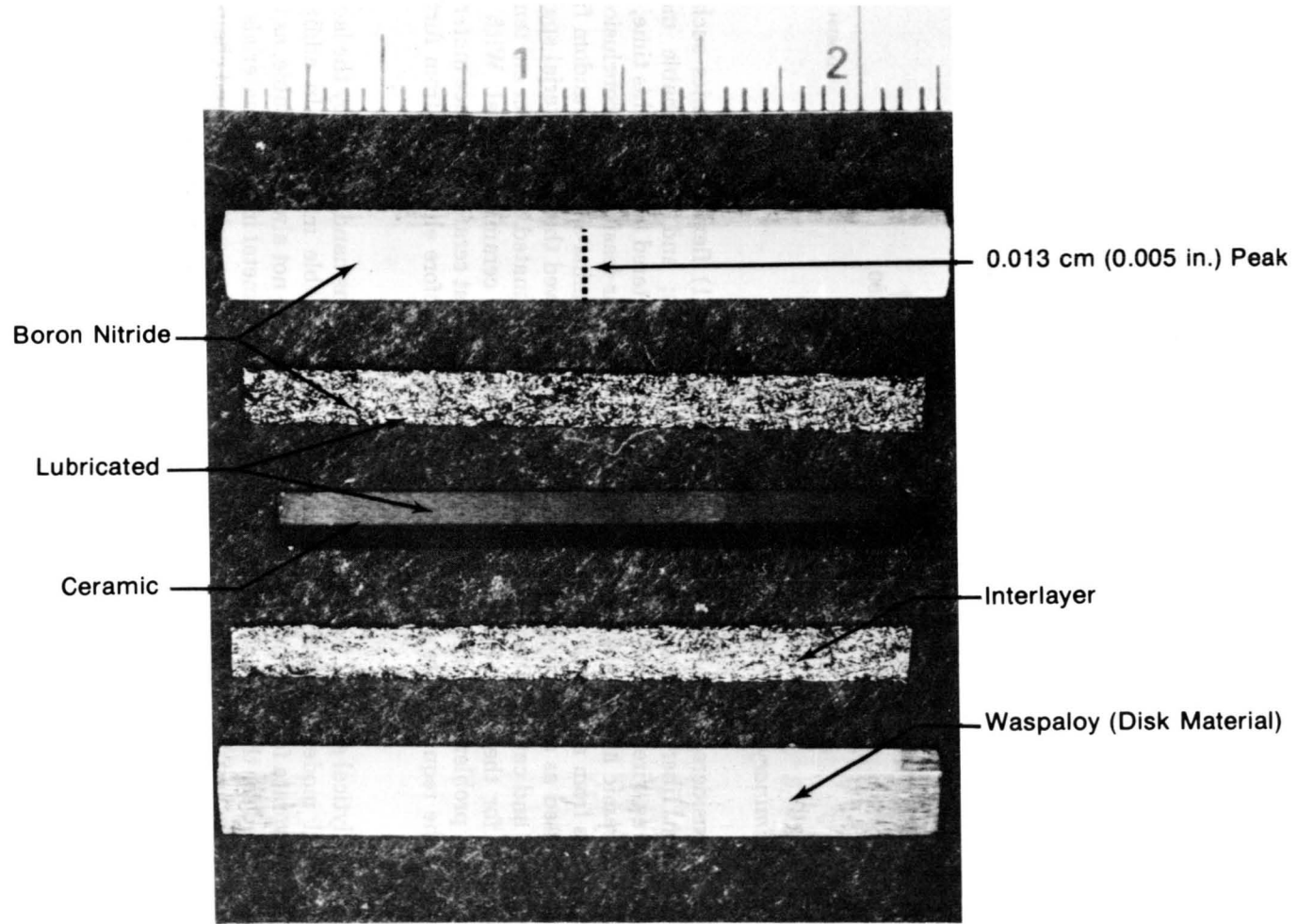
FD 96326

Figure 18. Interlayer Evaluation Specimen

22

fifth and last material would not be selected until the results were available from the evaluation of the previous four materials.

The interlayer test specimens consisted of NC 132 material sandwiched between two layers of interface material, with Waspaloy (disk material) used as the outer pieces. Figure 18 is a photograph of a typical test specimen. The center piece is NC 132, and it is surrounded by the candidate interlayer material, which in turn is sandwiched between the ceramic and Waspaloy end pieces. One of the end pieces was machined with a 0.013 cm (0.005 in.) peak near the mid-point to evaluate the interlayer material's capability to conform to mismatching surfaces.

Results of the first series of tests, consisting of 15 stress cycles from 13.8 to 275.8 MPa (2 to 40 ksi) predicted max stress and 3 temperature cycles from 480 to 870°C (900 to 1600°F) predicted max temperatures, are presented in Figure 19. These tests were conducted in a nonoxidizing atmosphere. Of the four interlayer materials tested, only platinum was compliant enough to permit survival of the ceramic specimen. Platinum was therefore selected for the fifth specimen, which was subjected to 100 stress cycles, 14 to 280 MPa (2 to 40 ksi) at 870° (1600°F). As indicated in Figure 20, the platinum sandwich once again permitted the ceramic centerpiece to remain unbroken.

The two previously tested interlayer assemblies using platinum (Nos. 1 and 5) were then subjected to 927°C (1700°F) temperature for 64 hr in an oxidizing environment. At the end of this time, the sandwiches were disassembled and the ceramic specimens were tested in four-point flexure. The measured moduli of rupture (MOR) in four-point bending for the two specimens were as follows:

- 15-cycle specimen: 814 MPa (118 ksi)
- 100-cycle specimen: 674 MPa (97.8 ksi).

Billet certification data from Norton indicated an average MOR value of 820 MPA (118.9 ksi) based on 20 specimens, with a minimum MOR of 634 MPa (91.9 ksi). Thus, there is no evidence of ceramic strength degradation resulting from intimate contact with the platinum interlayer material. On the basis of these evaluation tests, platinum was selected as the interlayer material.

As a general observation, it was noted that some bonding occurred between Waspaloy, all interface materials, and NC 132, wherever the surfaces were not lubricated with boron nitride. Therefore it was planned to use boron nitride to lubricate all surfaces in the attachment region during the Task III spin pit testing.

3.0 NONDESTRUCTIVE EVALUATION (NDE) METHODS STUDY

The objective of the NDE study was to determine the minimum detectable flaw size in NC 132 as a function of flaw depth. The NDE methods employed were X-radiography and sonic (C-scan) detection for buried defects, and fluorescent penetrant for surface defects. These techniques were applied to a seeded reference master (a billet with known defects) and a billet of HS130 with laser drilled holes in one side. The geometry of the seeded reference master is shown in Figure 21. One-half of the reference master contained imperfections having a density greater than NC 132 (iron), and the other half contained imperfections with a lower density (carbon). Contaminant particle size was 0.1 cm (0.005 in.), 0.08 cm (0.030 in.), and 0.15 cm (0.060 in.). The outside surfaces of the reference master were ground to three thicknesses, which were nominally 1.9 cm (0.75 in.), 1.3 cm (0.50 in.), and 0.8 cm (0.30 in.). These steps were designed to provide defect detection data as a function of material thickness.

Interlayer Material	Result	Remarks
Platinum	Did Not Fail	Selected for Fifth Test Specimen
Perforated INCO 625	Failed 10th Cycle	Basic Concept Appears Feasible - Development Required
Sintered Hoskins 875	Failed 3rd Cycle	Inadequate Strength - Apparent Waspaloy - Ceramic Contact at Peak
Woven INCO 600	Failed 5th or 10th Cycle (Data Indeterminent)	Worst Failure

General Observation:

1) Bonding Between Ceramic-Interlayer-Waspaloy Occurs on Surfaces Without Boron Nitride
2) Perforated Sheet Feasible With Development

FD 139328

Figure 19. Results of Stress/Temperature Cycling Tests

Specimen Definition: Platinum Interlayers, Boron Nitride on All Surfaces

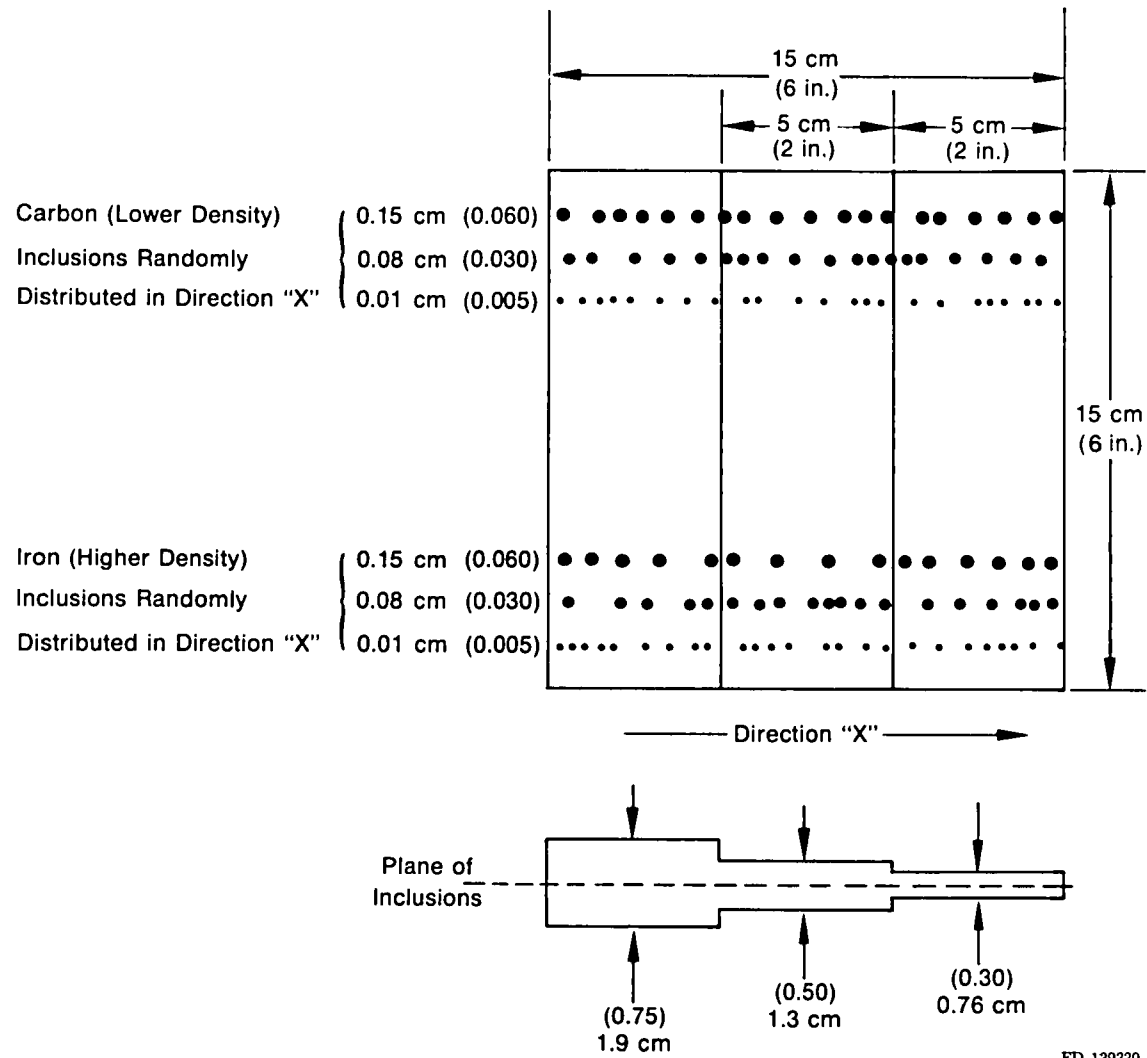|	
Test Program:	100 Cycles 14-275 MPa (2-40 ksi) Stress 870°C (1600°F) Temperature Non-Oxidizing Atmosphere
Result:	● Did Not Fail ● No Bonding
Conclusion:	Platinum Recommended for Interlayer

FD 139329

Figure 20. Results of Fifth Interlayer Test

Figure 21. Seeded Reference Master Geometry

As shown in Figure 22, the appearance of the iron particles in the reference master indicated that some melting or reaction may have taken place during the hot pressing operation, which would reduce the effective size of the particles. In any case, neither iron nor carbon imbedded particles were detected in the 0.01 cm (0.005 in.) size, and the 0.08 cm (0.030 in.) particles were easily detected. Since the reference master did not contain particle sizes between 0.01 and 0.08 cm (0.005 and 0.030 in.), additional work was required to establish the lower limit for X-ray and sonic detection. For X-ray purposes, iron particles and tungsten carbide particles in random sizes from 0.005-0.05 cm (0.002 to 0.020 in.) were attached to one surface of the reference master, and X-rayed through the ceramic. For sonic detection, a previously existing HS 130 billet was laser-drilled with nominal hole sizes at the surface of 0.008-0.040 cm (0.003-0.016 in.). However, these holes appeared to taper down to a smaller dimension as the depth increased. The laser drilled holes did not represent a flat bottom hole (FBH), which is the industry accepted standard for sonic calibration. The C-scan technique detected the 0.040 cm (0.016 in.) holes, but not the 0.008 cm (0.003 in.) holes. However, since the holes were nonstandard, these results remain inconclusive with respect to demonstrated FBH detection sensitivity.

Results of the NDE methods study are summarized in Figure 23. These data were later used in the design analysis of the crack growth data generated for NC 132.

4.0 MATERIAL CHARACTERIZATION

The primary objective of the ceramic characterization was to provide fracture mechanics data for NC 132 hot pressed silicon nitride at the specific temperatures of interest for this design. The types of data desired for this program were as follows:

(1) Steady crack growth
(2) Cyclic crack growth
(3) Critical stress intensity.

4.1 FRACTURE MECHANICS TESTING

The test plan for fracture mechanics testing is shown in Figure 24. The 1200°C (2200°F) data pertains to the airfoil region of the blade, and the 930°C (1700°F) data is required for the attachment region. The 24°C (75°F) data is desirable to evaluate potential problems in the start transient.

All fracture mechanics testing was accomplished with a flat double torsion specimen having the geometry shown in Figure 25. This specimen was identical in size and type with that used by NBS in their earlier work with NC 130, and it was selected for this program to provide a direct comparison of NC 132 and NC 130 crack propagation. Prior to testing, the specimens were notched at one end as shown in Figure 26. The notch configuration, which gradually tapers into the full specimen thickness, has a shape similar to the final crackfront configuration. This enables precracking of the specimen without catastrophic failure while guiding the crack down the centerline of each specimen without the use of a slot running the length of the specimen.

The test apparatus was designed to conduct deadweight loading, constant crosshead displacement and displacement cycling tests (Figures 27 and 28). Load vs time was recorded with a sensitive load cell and strip chart combination, while crosshead displacement was measured with a dial indicator graduated in 0.00025 cm (0.0001 in.) divisions. System stability was checked in monotonic and cyclic modes by testing an unnotched, uncracked specimen below fracture load and noting that for a constant crosshead displacement there was no change in load (zero crack growth causes no change in either load or crosshead displacement).
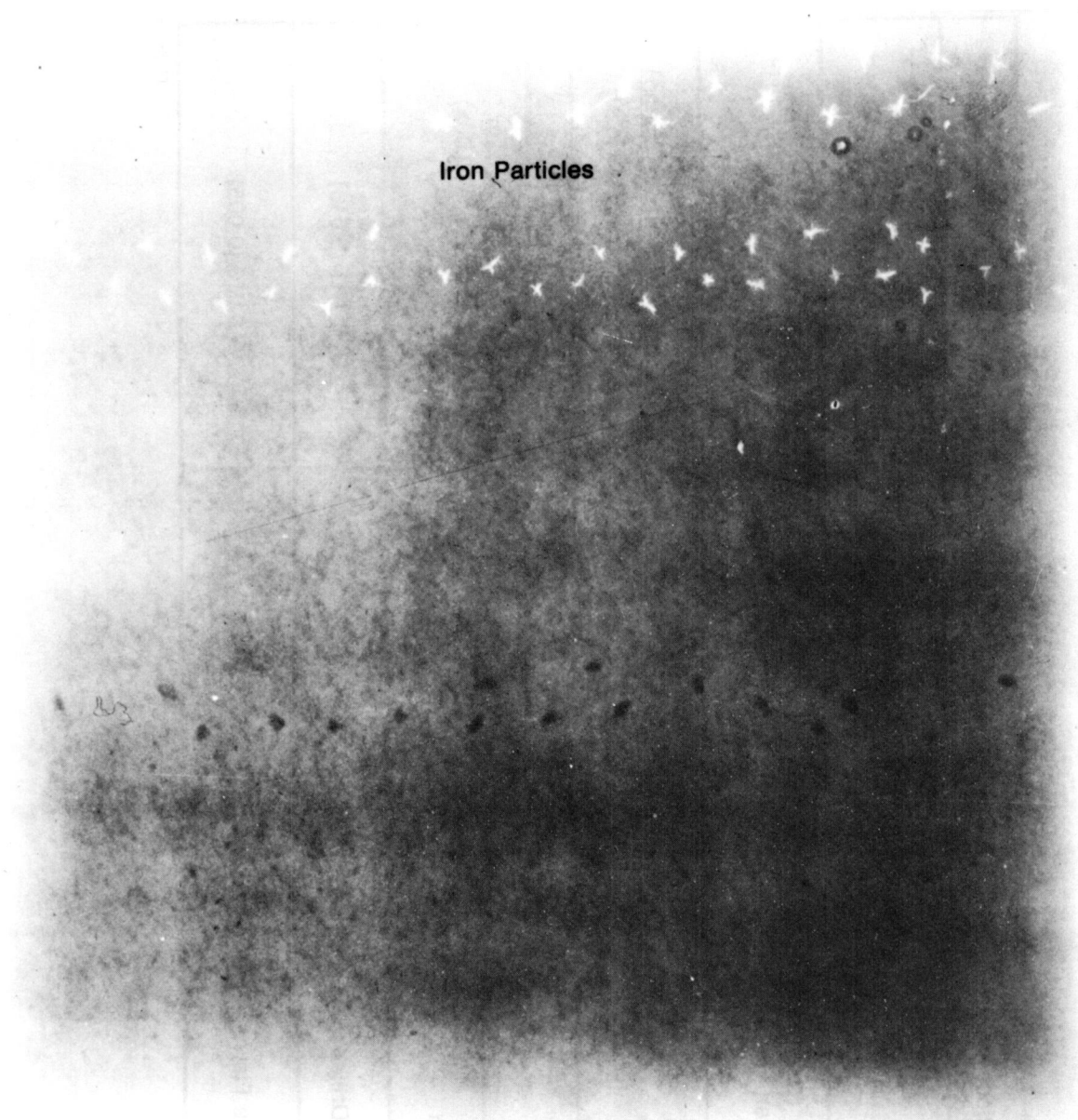
Figure 22. X-ray of Seeded Reference Master

NDE Method	Defect Type	Depth of Defect cm (in.)	Min Detectable - cm (in.)
X-Ray	Iron	1.91 (0.75) 1.27 (0.50) 0.76 (0.30)	0.051 (0.020) 0.025 (0.010) 0.013 (0.005)
	Tungsten Carbide	1.91 (0.75) 1.27 (0.50) 0.76 (0.30)	0.013 (0.005) 0.005 (0.002) 0.005 (0.002)
	Carbon	0.38 to 0.97 (0.15 to 0.38)	Less than 0.076 (0.030) Greater than 0.013 (0.005)
Sonic (C-Scan)	Iron	0.38 to 0.97 (0.15 to 0.38)	Less than 0.076 (0.030) Greater than 0.013 (0.005)
	Carbon	0.38 to 0.97 (0.015 to 0.38)	
	Laser-Drilled Hole	1.91 (0.75)	0.041 (0.016)
Fluorescent Penetrant (ZL30)	Surface Flaw	—	0.013 (0.005)

FD 96136

Figure 23. Results of NDE Study

| Type of Test	Temp, °C (°F)	No. Specimens	Remarks
Monotonic (da/dt)	1200 (2200)	7	Constant Displacement
	1200 (2200)	3	Constant Load
	930 (1700)	5	Constant Displacement
	930 (1700)	1	Constant Load
Cyclic (da/dn)	1200 (2200)	4	Constant Displacement
	930 (1700)	3	Constant Displacement
	24 (75)	4	Constant Displacement
Fracture Toughness	1200 (2200)	3	
	930 (1700)	1	
	24 (75)	4	

FD 96137

Figure 24. Fracture Mechanics Test Matrix
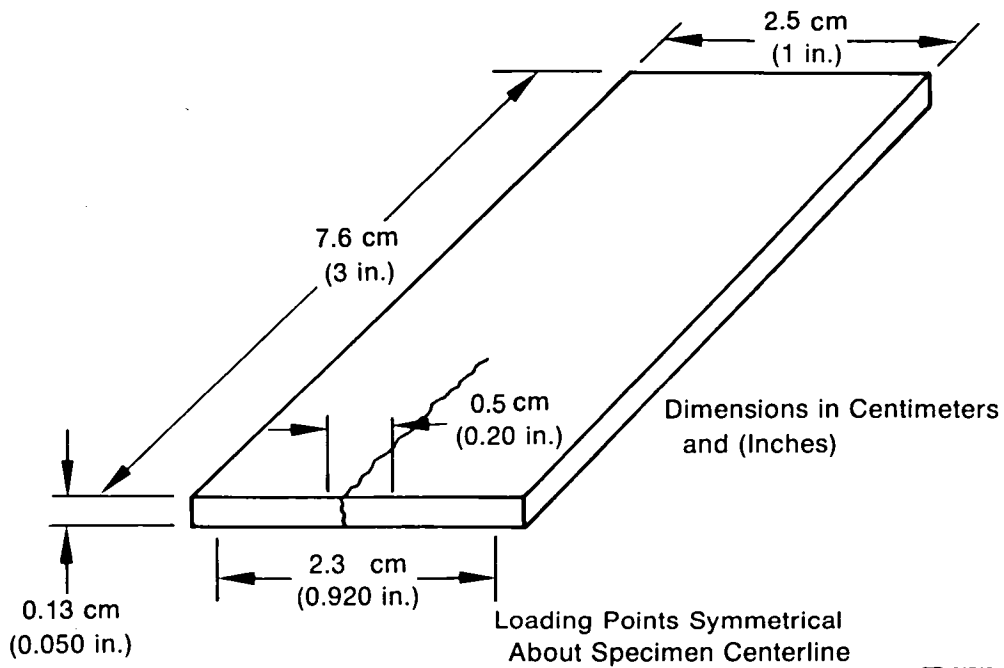
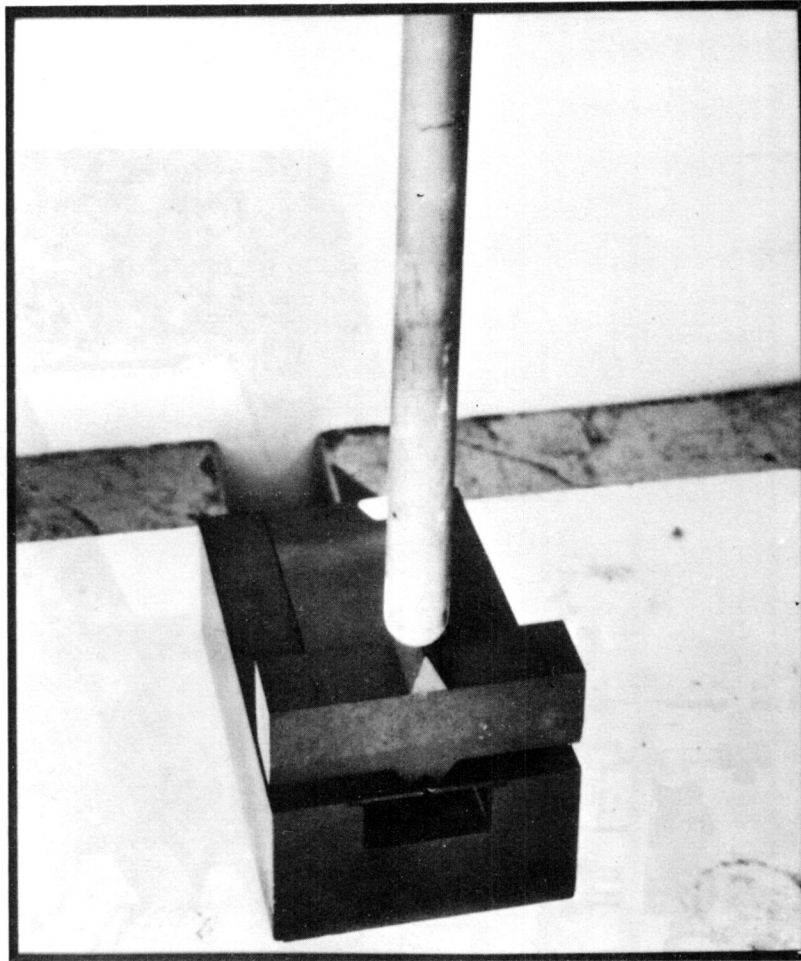*Figure 25. Double Torsion Specimen Geometry*

29
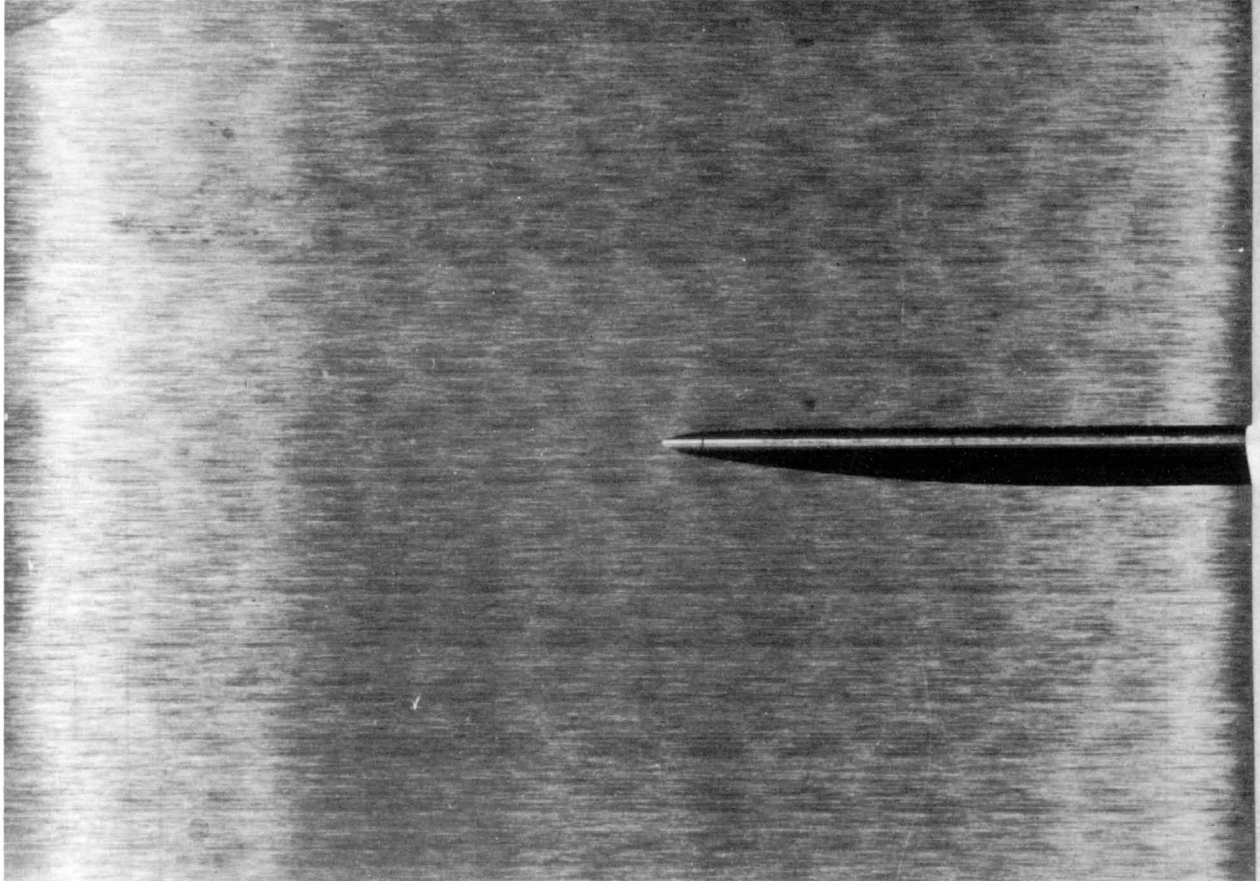
FD 96327

Figure 26. Pre-Crack Notch in Double Tension Specimen

FD 32871A

Figure 27. Fracture Mechanics Test Apparatus

FD 32872A

Figure 28. Fracture Mechanics Loading Fixture

Quantitative crack length determination was accomplished using monochromatic light and an optical flat to accentuate surface distortions adjacent to the crack on a polished specimen surface (Figure 29). This optical method is accurate to plus or minus 0.04 cm (0.015 in.), which is of sufficient accuracy for crack propagation calculations that require only initial or final crack length rather than crack length differences.

Prior to conducting crack growth tests for NC 132, a series of calibration tests were run with glass to verify the test equipment and procedures. Results are shown in Figure 30. The close correlation with literature data (reference 1) verified the test procedures and the effort proceeded to NC 132 testing.

Results of the 1200°C (2200°F) monotonic (constant load) tests are presented in Figure 31. For comparison purposes, NC 130 data taken from the National Bureau of Standards is shown versus the NC 132 data in Figure 32. The crack growth rates of NC 132 are seen to be one to two orders of magnitude greater than that of NC 130, depending on the stress intensity value. Figure 33 presents the measured crack propagation rate of NC 132 at 930°C (1700°F). For the range of stress intensity factors tested, the average crack growth rate at 930°C (1700°F) is lower than that measured for 1200°C (2200°F) as shown by Figure 34. However, the most significant aspect of the 930°C (1700°F) testing was the erratic behavior shown by approximately one-third of the specimens, in which the crack did not propagate continuously, but more or less as a step function. There was also much more data scatter for the 930°C (1700°F) specimens as compared to the 1200°C (2200°F) specimens, which is shown in Figures 31 and 33.

Cyclic crack propagation data is presented in Figures 35, 36 and 37 for test temperatures of 1200°C, 930°C, and 24°C (2200°F, 1700°F and 75°F), respectively. Some variation in the cyclic loading frequency was used in these tests: 28 to 46 cycles per minute at 1200°C (2200°F), 24-44 cycles per minute at 930°C (1700°F); and 38 to 44 cycles per minute at 24°C (75°F). However, no conclusions can be drawn relative to the effect of frequency because the range of frequencies was fairly narrow, and the data scatter (especially at the lower temperatures) was sufficiently large to obliterate any loading frequency effects.

The behavior of the 930°C (1700°F) cyclic specimens showed a trend toward erratic crack growth, similar to that observed in the monotonic tests. In approximately one-third of the tests, the load change per cycle did not decrease continuously, as it should for a constant displacement loading cycle. Instead, all of the load decrease would occur in one cycle.

On the basis of the cyclic data, it can be concluded that the cyclic crack propagation rates at 930 and 24°C (1700 and 75°F) are essentially the same, and are approximately one order of magnitude lower than 1200°C (2200°F), within the range of stress intensities tested. It can also be concluded that at 930°C (1700°F) and below, discontinuous crack growth and wide data scatter can be expected.

Results of the NC 132 fracture toughness tests are presented in Figure 38, with NBS data for NC 130 included for comparison. The NC 132 data shows a slight decrease in fracture toughness from room temperature to 1200°C (2200°F). The NC 130 data showed an opposite trend, with a slight increase in fracture toughness from room temperature to about 1090°C (2000°F) where a significant increase becomes apparent at higher temperatures. However, over the temperature range of interest, 24 to 930°C (75 to 1700°F), there is no appreciable difference in fracture toughness between NC 132 and NC 130.

33

FD 32873A

Figure 29. Crack Length Measurement
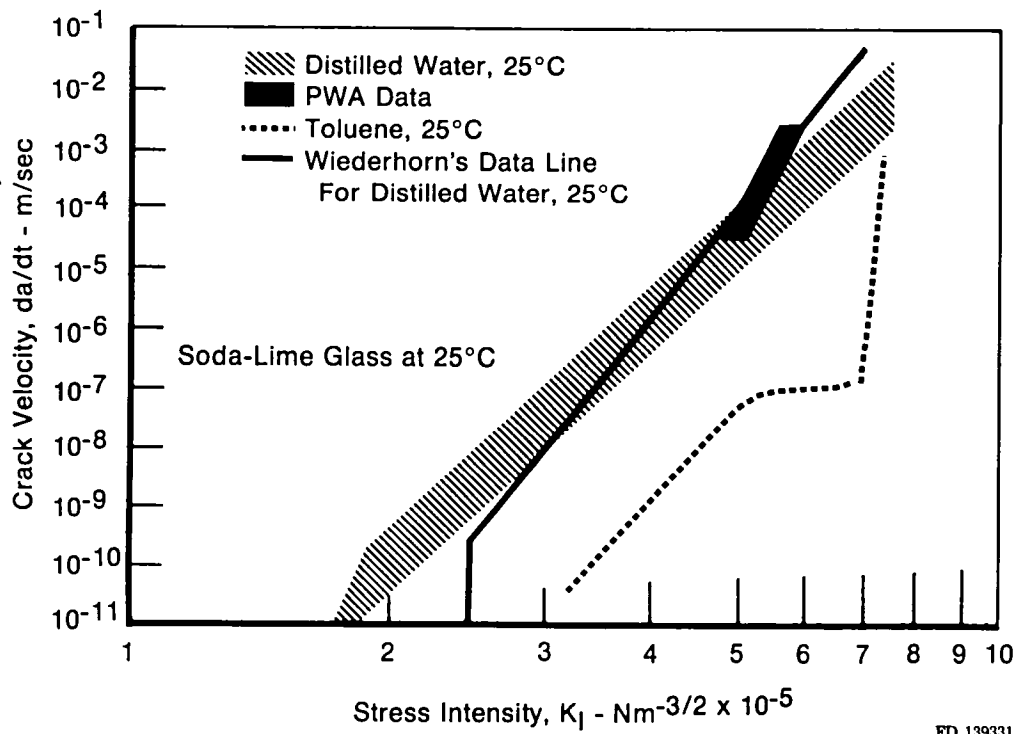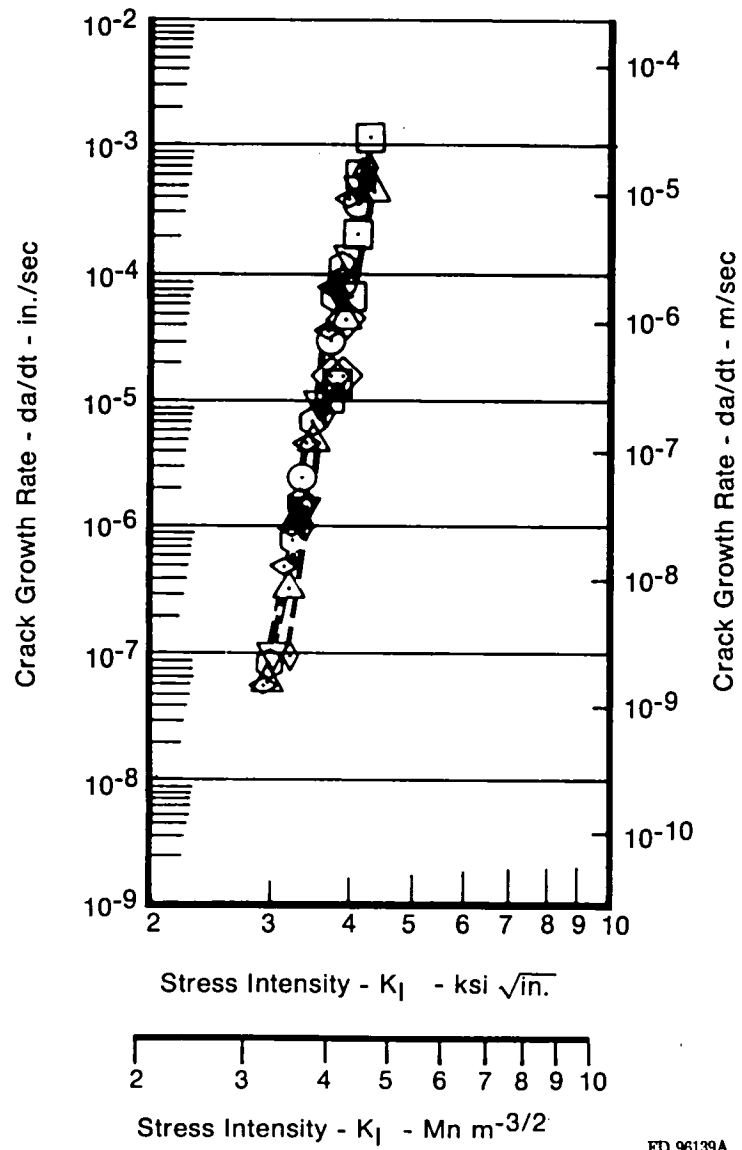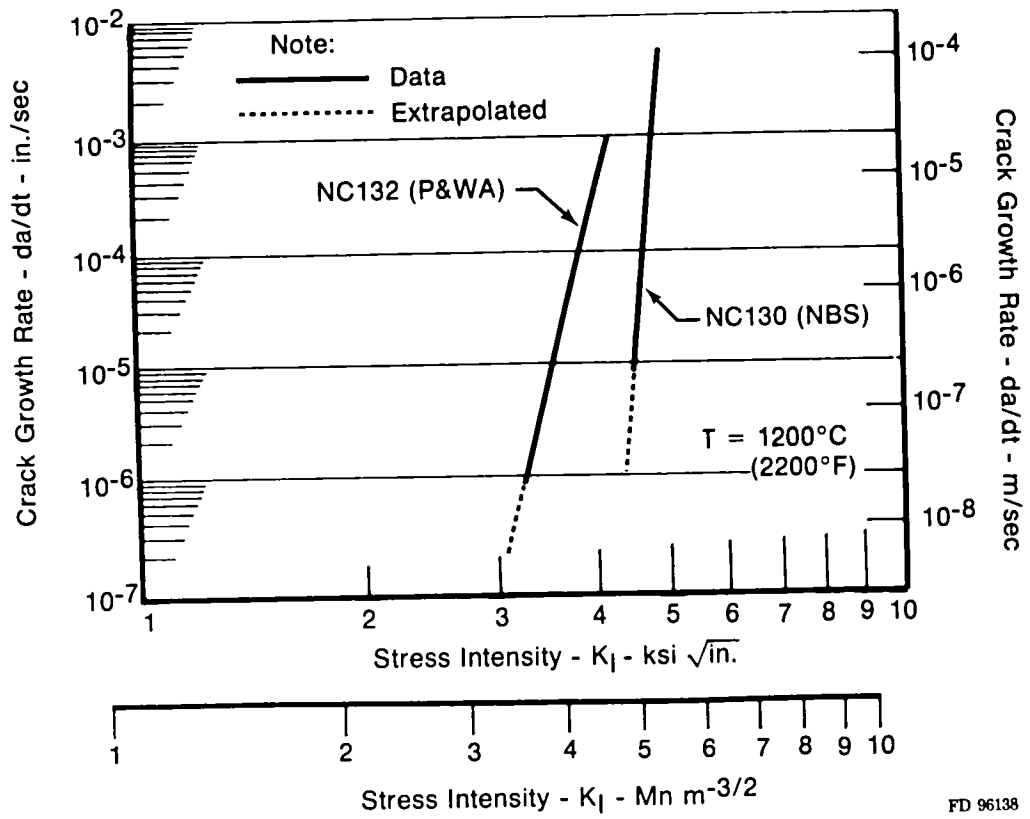
Figure 30. Results of Glass Calibration Tests

FD 139331

35

Figure 31. da/dt at 1200°C (2200°F)

FD 96139A

36

Figure 32. Crack Growth of NC 132 vs NC 130
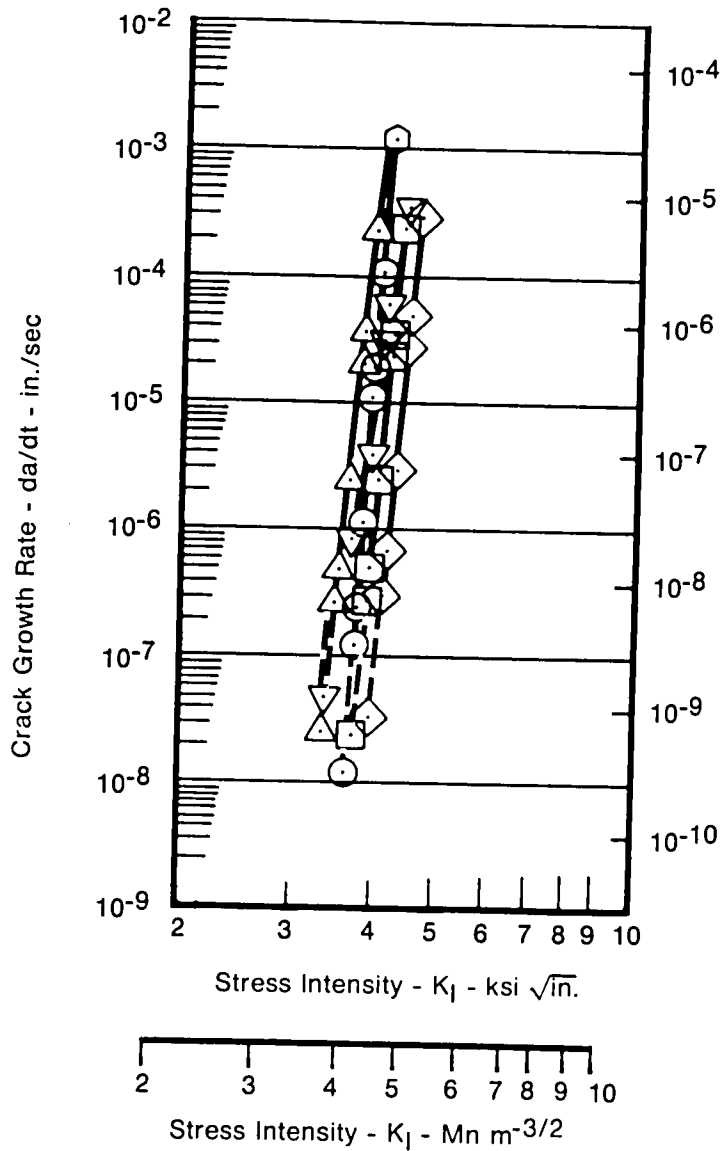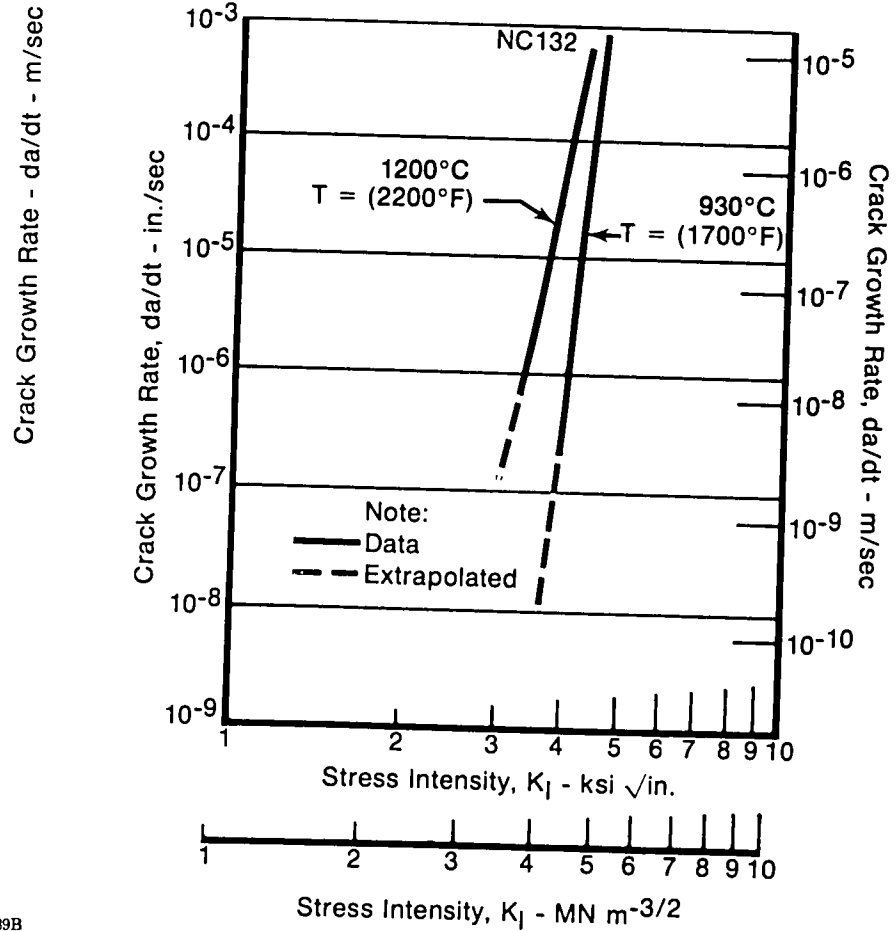
Figure 33. da/dt at 930°C (1700°F)

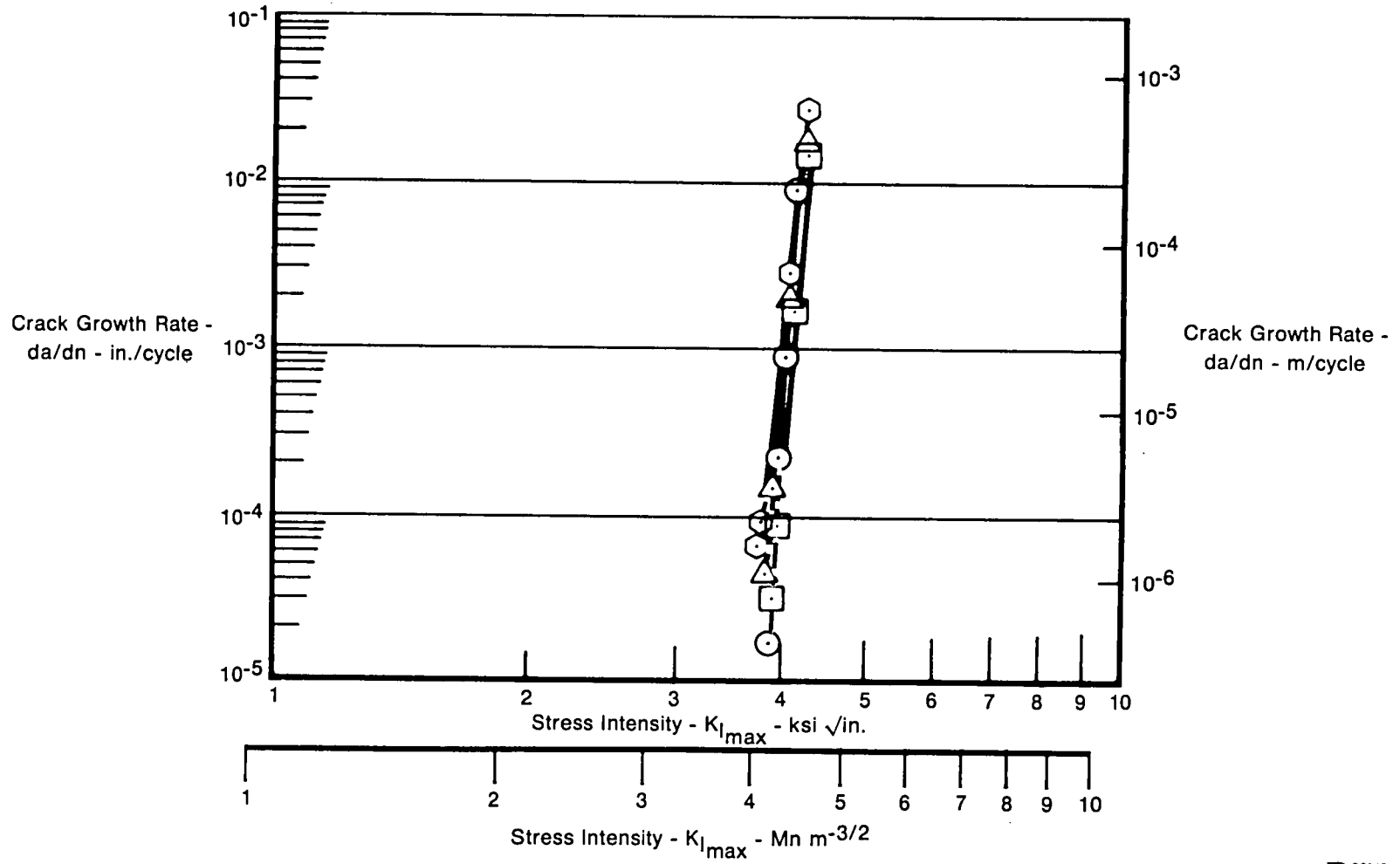Figure 34. Comparison of da/dt at 1200°C (2200°F) and 930°C (1700°F)

38
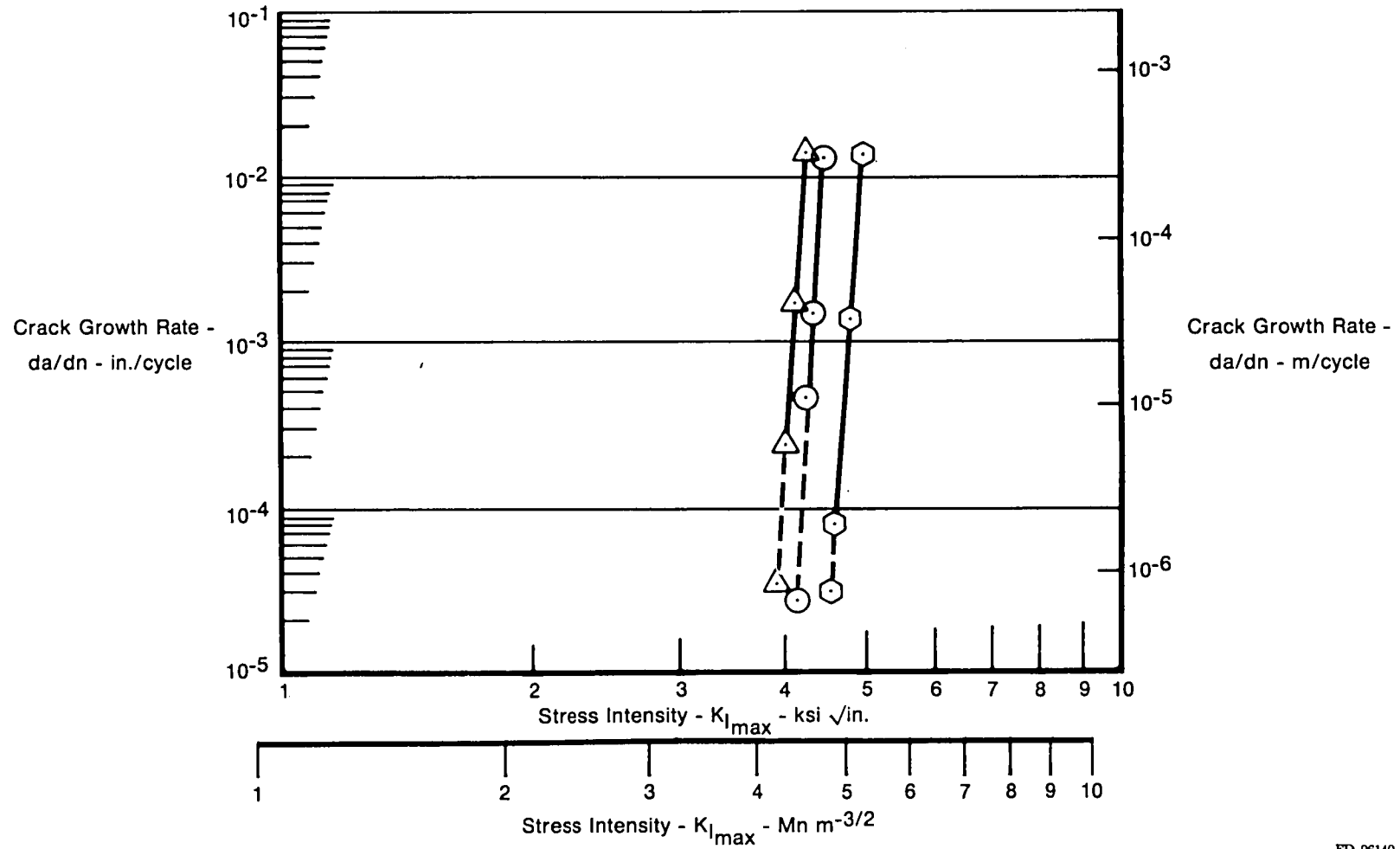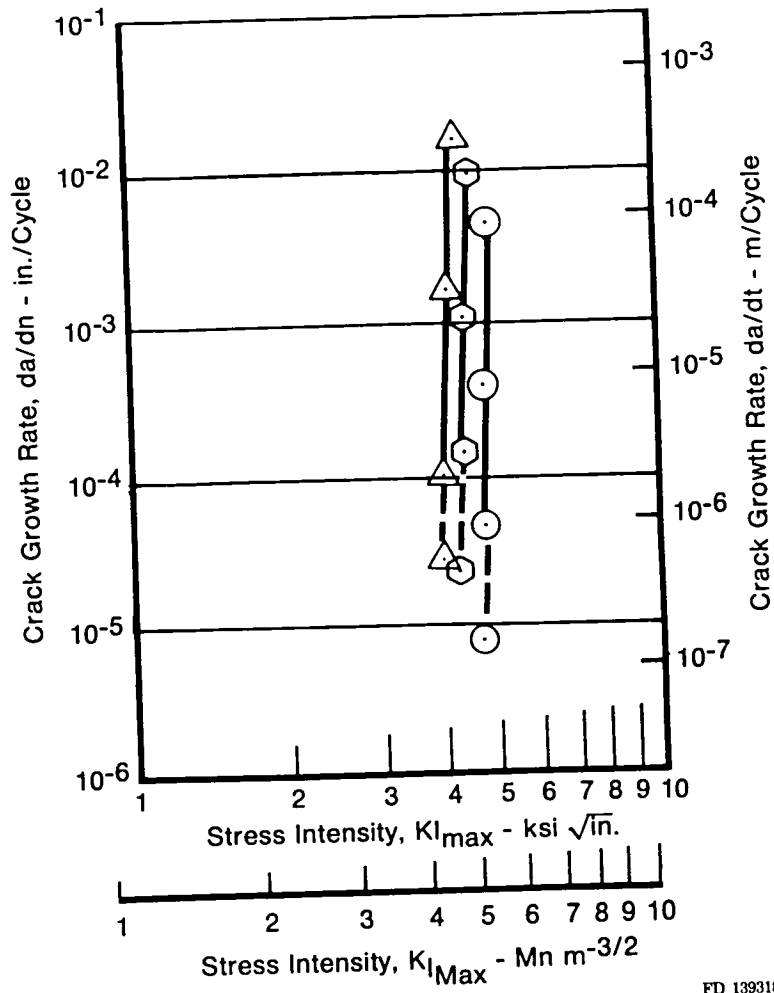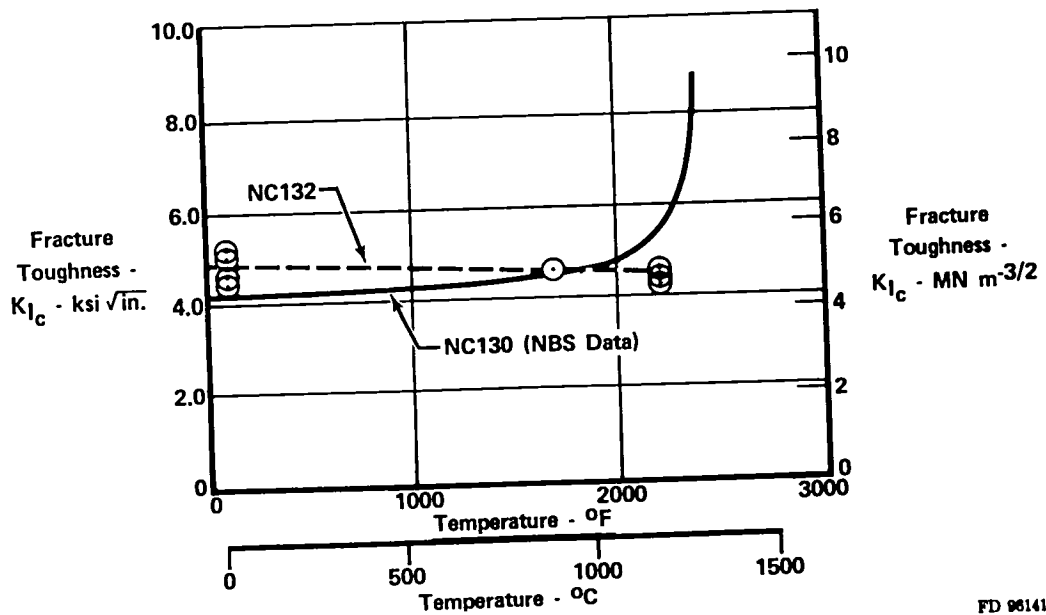
Figure 35. da/dn at 1200°C (2200°F)

FD 96149

Figure 36. da/dn at 930°C (1700°F)

FD 96140

Figure 37. da/dn at 24°C (75°F)

Figure 38. Fracture Toughness of NC 130 and NC 132

4.2 Design Analysis of Crack Growth Data

The final step in the Task I Preliminary Design effort was to conduct a blade life analysis using the results of the two-dimensional stress analysis, nondestructive evaluation, and crack growth testing. The analysis approach was to use the stress distributions at the base of the airfoil and at the attachment neck in conjunction with the crack growth data to calculate the life of the blade for a range of initial flaw sizes. At both locations, two types of flaws were analyzed: a surface flaw, and an internal flaw. In the case of the internal flaw, it was assumed to be located at the center of the section. The surface flaws were assumed to be located at the maximum stress location. The temperatures used for the analysis were taken from the earlier temperature analysis. These were 1060°C (1945°F) in the base of the airfoil, and 940°C (1718°F) for the neck area of the attachment. Accordingly, 1200°C (2200°F) crack growth data was used for the airfoil cases and 930°C (1700°F) data was used for the attachment. Where crack growth data showed scatter the highest rates of crack growth were used, which is a conservative assumption.

Results of the analysis are shown in Figures 39, 40, 41 and 42. To judge the acceptability of the preliminary design, these predictions were used to identify the initial flaw size that yields a 50-hr life, which was the design life goal of the program. These flaw sizes were then compared with the minimum detectable flaw sizes. As long as the minimum detectable flaw was smaller than the 50-hr flaw, the design would be judged to be acceptable. Table III presents the results of this analysis. In all cases, the 50-hr flaw was larger than the smallest detectable flaw, and the preliminary design was judged to be acceptable.

It should be noted that the cyclic crack growth data did not influence the blade life predictions because the monotonic crack growth per operating cycle (30 min) was several orders of magnitude greater than the cyclic crack growth for one cycle. It was concluded that low cycle fatigue should not present any problems in this program, where the design goal was 100 cycles.

TABLE III.   TWO-DIMENSIONAL LIFE PREDICTION SUMMARY

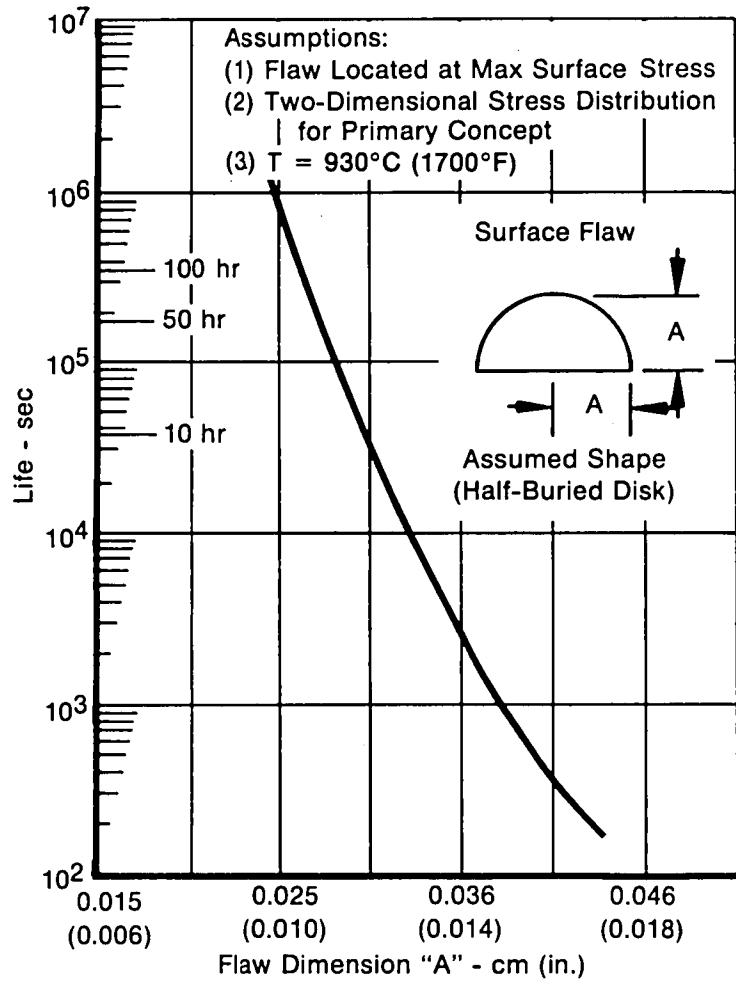| Flaw Type	Location	Temperature	Flaw Size for 50-hr Life	Minimum Detectable Flaw
Surface	Attachment	930°C (1700°F)	0.056 cm (0.22 in.)	0.013 cm (0.005 in.)
Internal	Attachment	930°C (1700°F)	0.424 cm (0.167 in.)	0.041 cm (0.016 in.)
Surface	Airfoil	1200°C (2200°F)	0.031 cm (0.012 in.)	0.013 cm (0.005 in.)
Internal	Airfoil	1200°C (2200°F)	0.132 cm (0.052 in.)	0.041 cm (0.016 in.)

Figure 39. *Life Prediction for Surface Flaw in Attachment*
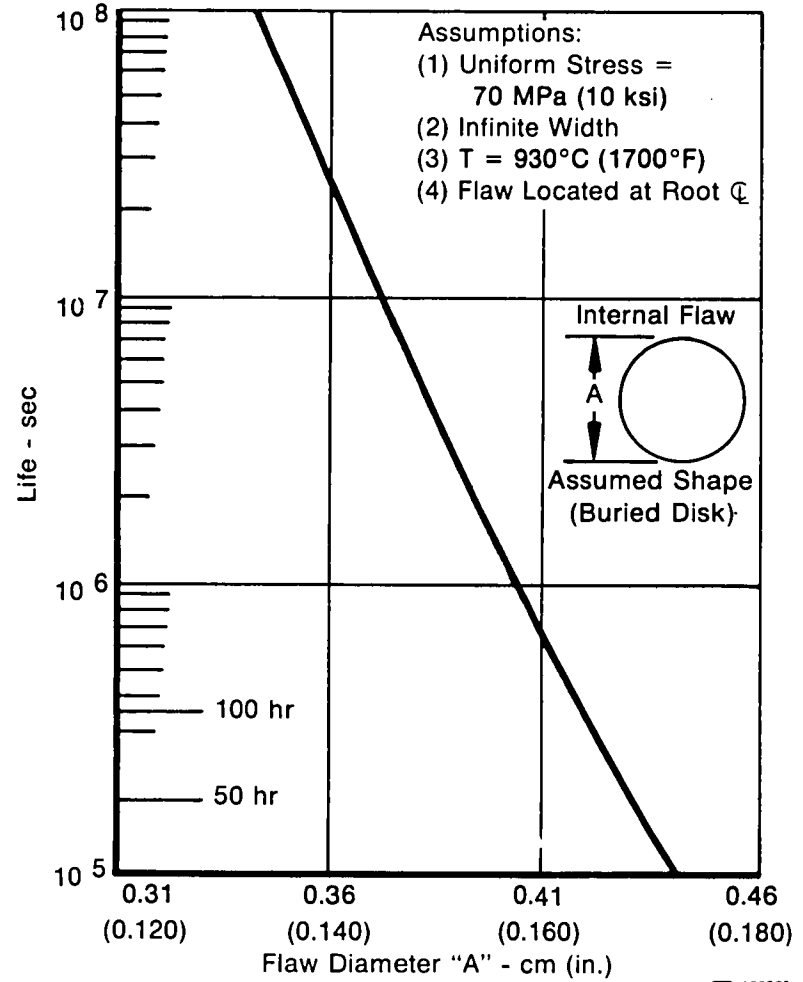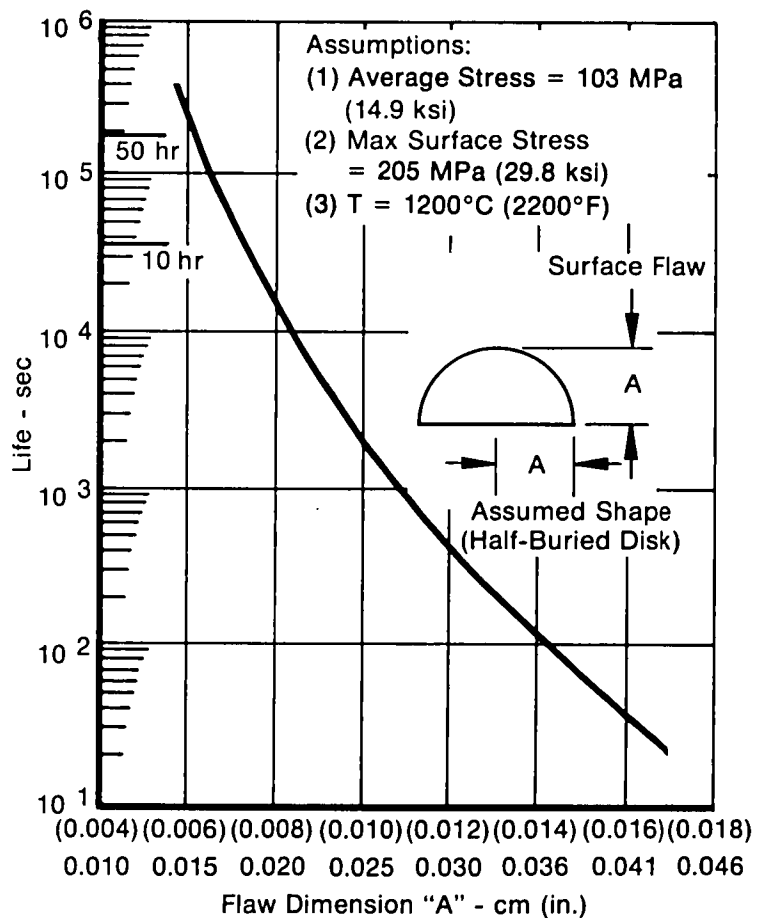

Figure 40. *Life Prediction for Internal Flaw in Attachment*

Figure 41. *Life Prediction for Surface Flaw in Airfoil*

FD 139321

Assumptions:
(1) Average Stress = 103 MPa (14.9 ksi)
(2) Max Surface Stress = 205 MPa (29.8 ksi)
(3) T = 1200°C (2200°F)

Surface Flaw

Assumed Shape (Half-Buried Disk)

Life - sec

Flaw Dimension "A" - cm (in.)
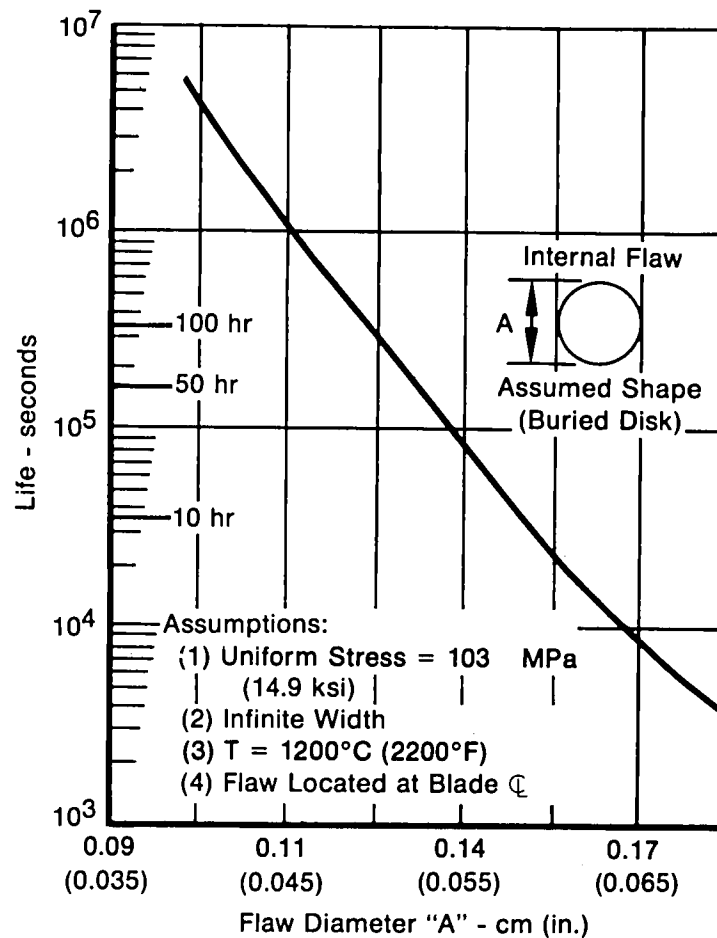
Figure 42. *Life Prediction for Internal Flaw in Airfoil*

FD 139322

Internal Flaw

Assumed Shape (Buried Disk)

Assumptions:
(1) Uniform Stress = 103 MPa (14.9 ksi)
(2) Infinite Width
(3) T = 1200°C (2200°F)
(4) Flaw Located at Blade ℄

Life - seconds

Flaw Diameter "A" - cm (in.)

TASK II — ATTACHMENT DESIGN

1.0 PHOTOELASTIC MODEL TESTING

The objective of the photoelastic model testing was to verify the stress distribution predicted by the two-dimensional finite element analysis of Task I, and to quantify stress concentration factors in the blade root area. This was accomplished by constructing a two-dimensional 10X scale model of the primary attachment concept. A birefringent plastic material was used for the model. As shown in Figure 43, three model blades were constructed, with the center one being designated as the study blade and the two adjacent ones used as slave blades to provide interaction effects. All three blades were loaded in the radial direction. The slave blades were loaded with a single load, equivalent to the model blade pull. The center blade was loaded with five discrete loads, which combined were equal to the model blade pull. The two-dimensional disk model was loaded in the tangential (hoop) direction as well as in the radial direction. The resulting radial stresses in the blade were recorded, converted from model to prototype stresses, and compared to the analytical stress predictions.

The loads selected for the photoelastic model testing were based on the two-dimensional analysis. Figure 44 shows that the ratio of average disk live rim stress to average blade-root neck stress was maintained in the model, although the absolute stress levels in the model were lower. A similar approach was followed in selecting the model blade load distribution. Figure 45 shows the eleven discrete airfoil loads, and their nonuniform distribution, that were used in the two-dimensional analysis. Space limitations in the polariscope precluded the use of more than five discrete loads. Figure 46 shows a five-load distribution that corresponds to the eleven airfoil loads used in the analysis. These were then used to select the model airfoil loads, shown in Figure 47, which matched the two-dimensional load distributions as closely as possible. The overall test setup is shown in Figure 48, and the model blade in the polariscope is shown in Figure 49. The latter figure shows that the compliant interlayer material (platinum in the blade design) was simulated in the model by using sponge rubber between the blades and the disk.

Figure 50 presents a comparison of the calculated and photoelastic radial stress distribution across the plane of maximum stress (i.e., at the neck of the dovetail). For this comparison, the photoelastic model stresses were scaled up to prototype values, and since the model could not simulate thermal effects, the relatively small thermal stress was deleted from the analytical predictions. The correlation between the predicted and measured stresses was quite good.

To verify the location of the maximum root stress, the photoelastic model stresses were measured along the surface of the neck radius. Comparisons of measured and analytically predicted surface stresses are presented in Figures 51 and 52. The photoelastic stresses are shown to be somewhat higher than the analytical values. However, this trend should be expected because the analytical stresses shown occur at the centroids of the finite elements, and are therefore representative of the stress at a point 0.025-0.050 cm (10 to 20 mils) from the surface. Considering the steep stress gradient at the surface (Figure 50), the two-dimensional analytical values should therefore indicate lower stresses. In addition, photoelastic surface stresses tend to be somewhat high due to residual machining stresses in the surfaces. The degree of correlation is seen to be best near the maximum stress point; this is the result of using a finer elemental breakup in the analysis of these regions. The significant aspect of Figures 51 and 52 is the verification of the predicted maximum stress location. For preliminary design use, the photoelastic stress distribution of these figures can be converted to stress concentration factors as shown in Figures 53 and 54. In practice these factors would be applied to the section average stress (total load divided by total area).

45

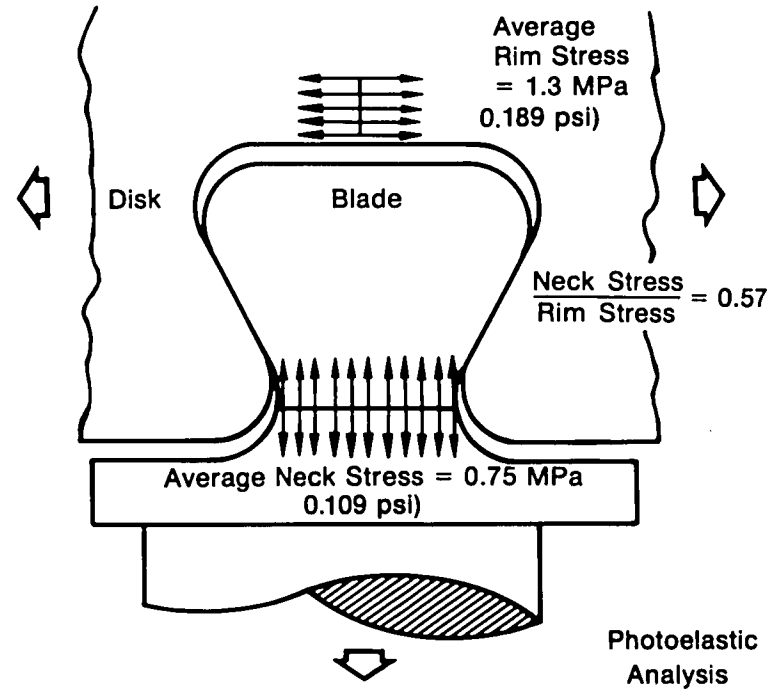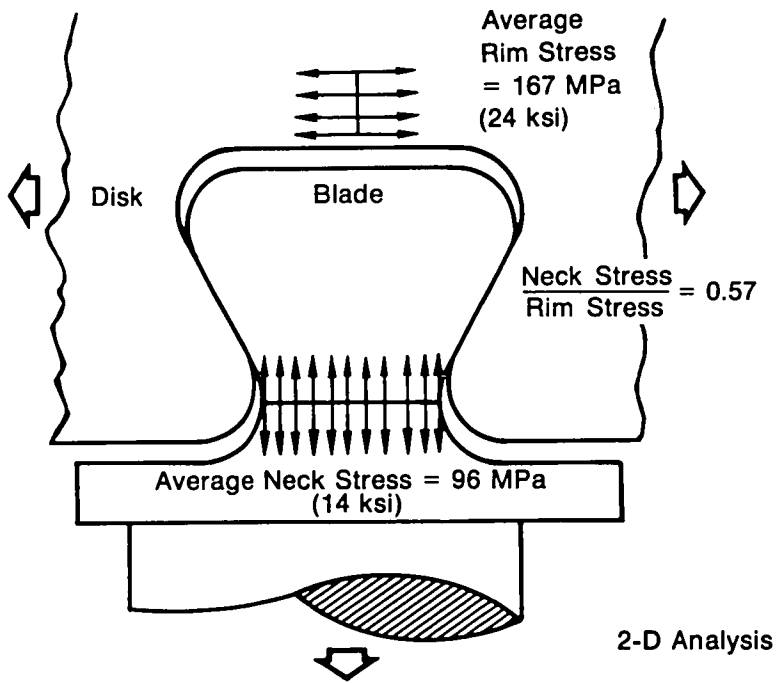Blade Model
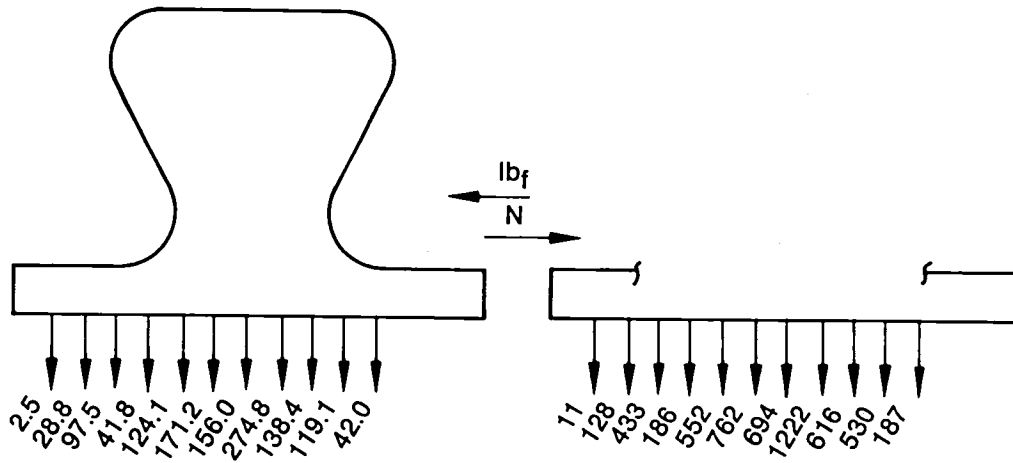
Disk Model
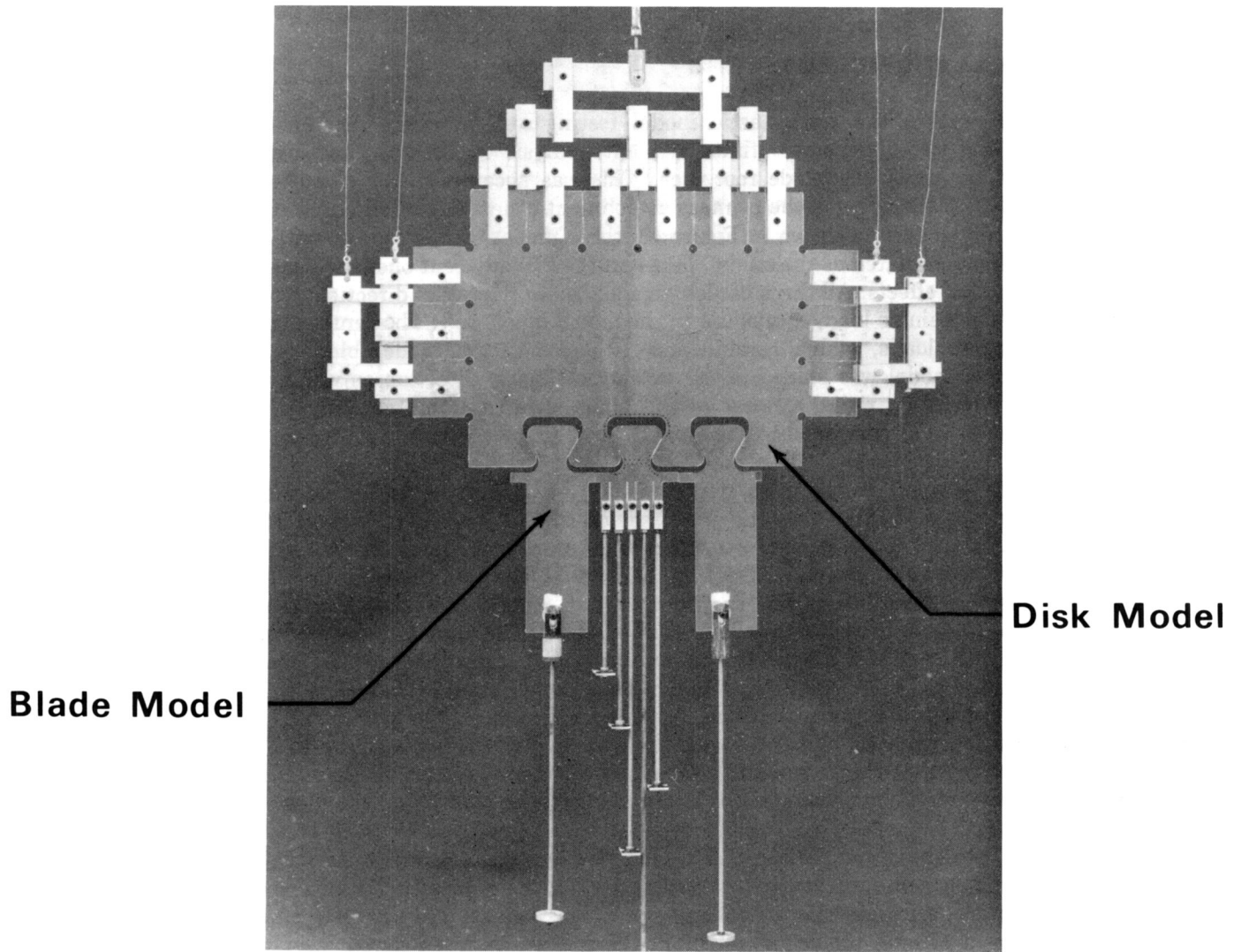
FAE 149111A

Figure 43. Photoelastic Test Models

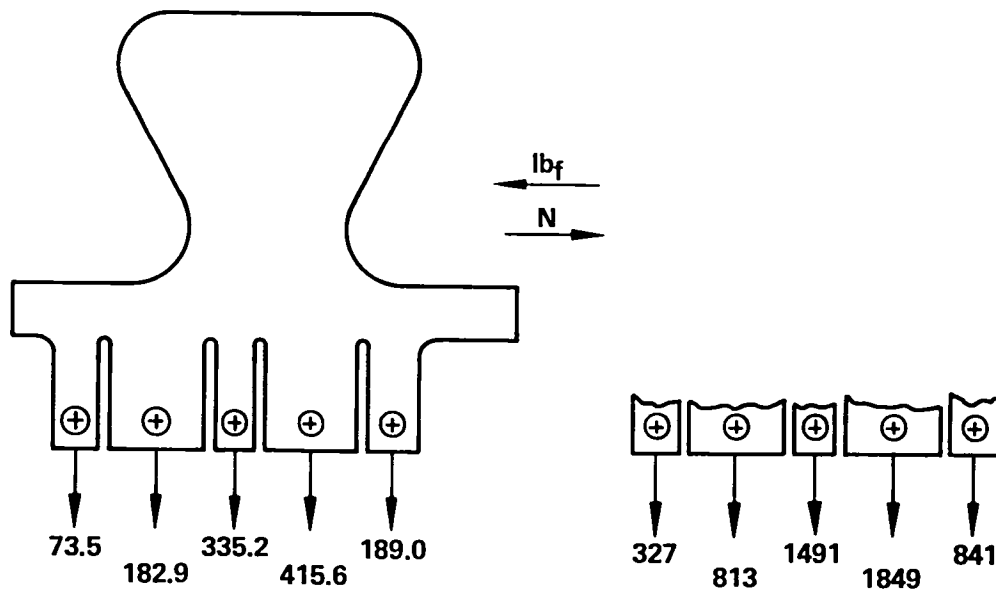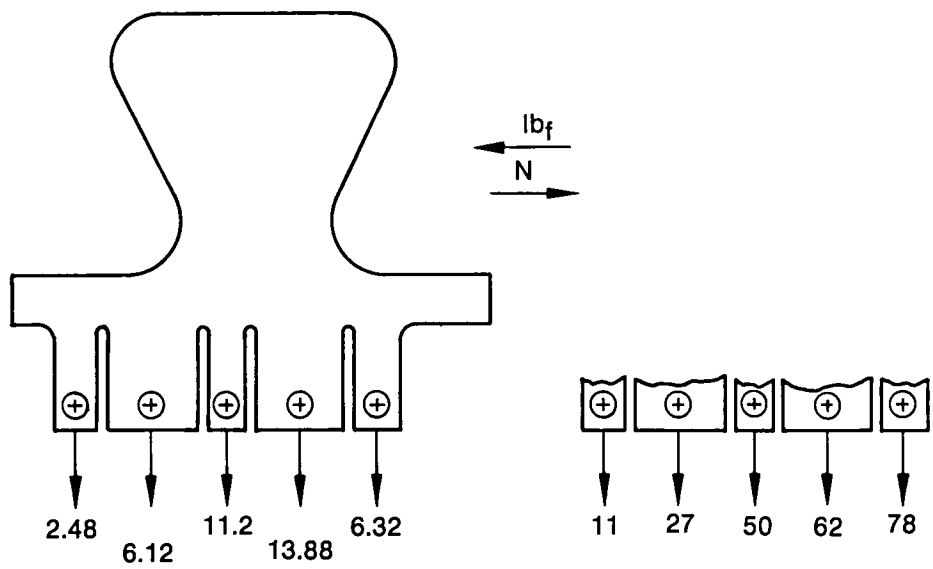*Figure 44. Stress Ratios for Photoelastic Model*

Figure 45. Airfoil Loads from Two-Dimensional Stress Analysis

Figure 46. Two-Dimensional Loads Regrouped for Photoelastic Study

48

Figure 47. Airfoil Loads for Photoelastic Model
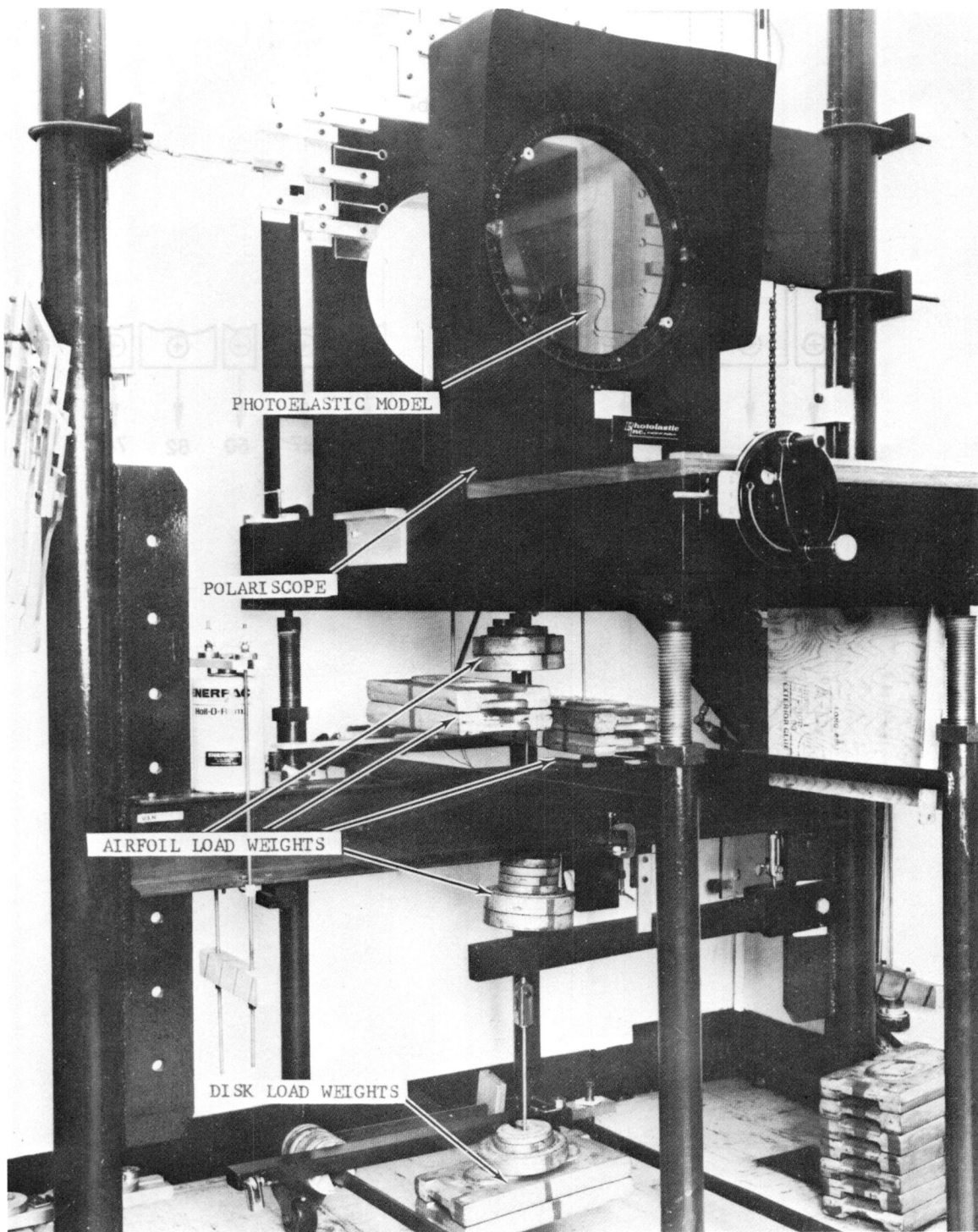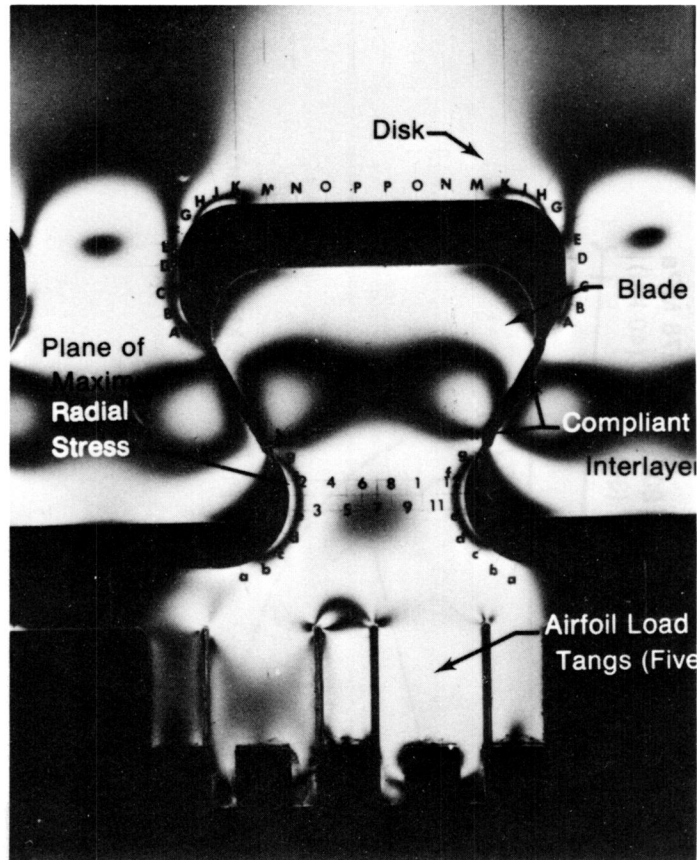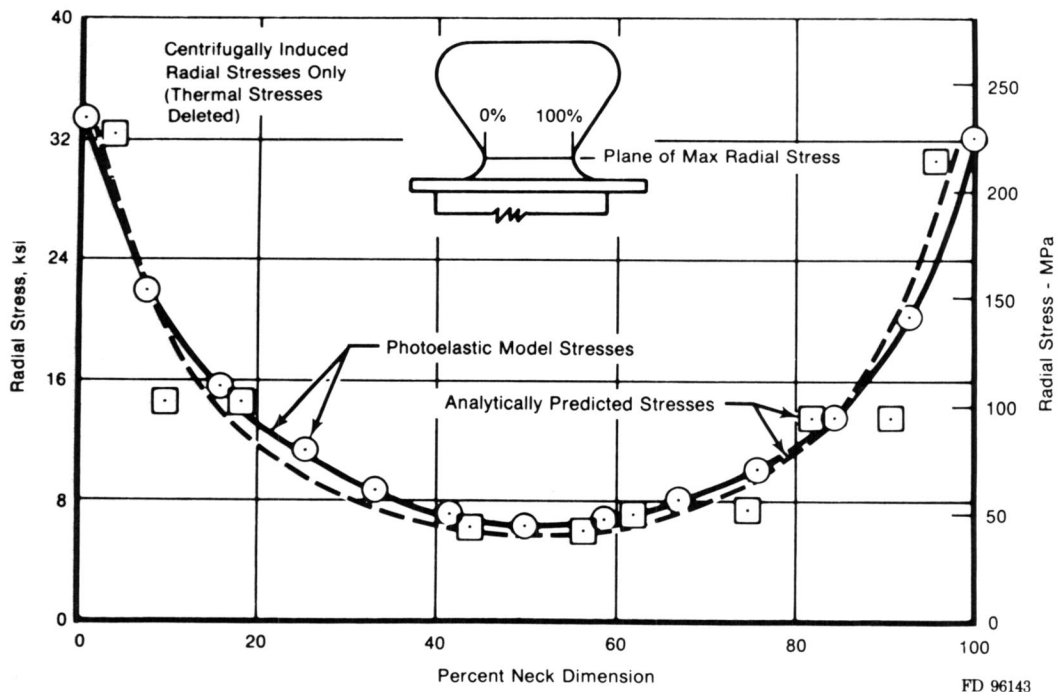
FD 96146

Figure 48. Photoelastic Test Setup

FE 148724A

Figure 49. Photoelastic Model at Test

FD 96143

Figure 50. Analytical vs Photoelastic Stresses

51
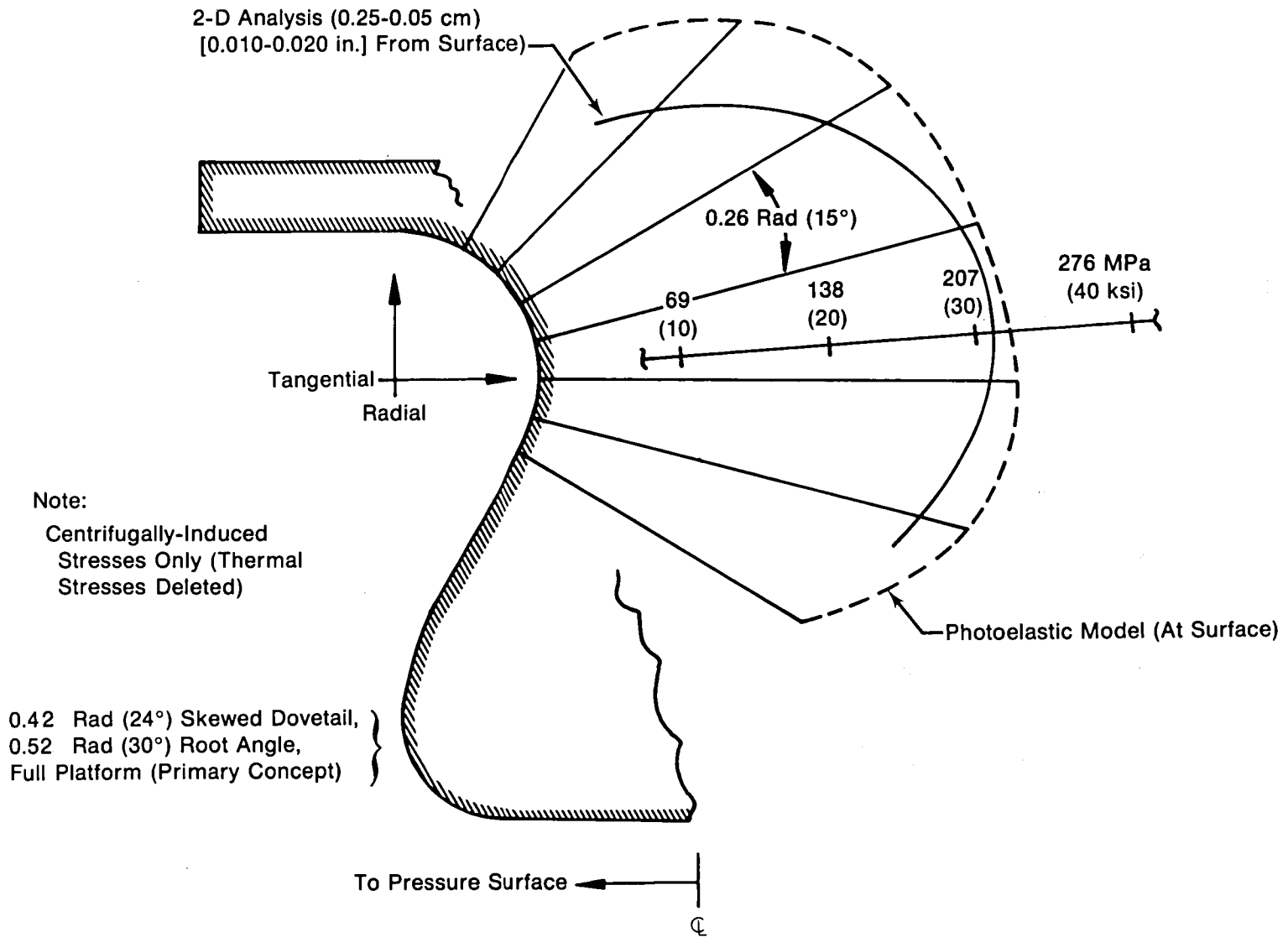
Figure 51. Attachment Surface Stresses (Pressure Side)

FD 139332

Photoelastic Model (at Surface)

0.26 rad (15°)

276 MPa
(40 ksi)

207
(30)

138
(20)

69
(10)

Tangential

Radial

2-D Analysis (0.025-0.05 cm)
[0.010-0.020 in.] From Surface

0.42 (24°) Skewed Dovetail,
0.52 rad (30°) Root Angle
Full Platform (Primary Concept)

Note:
Centrifugally-Induced
Stresses Only (Thermal
Stresses Deleted)

To Suction Surface
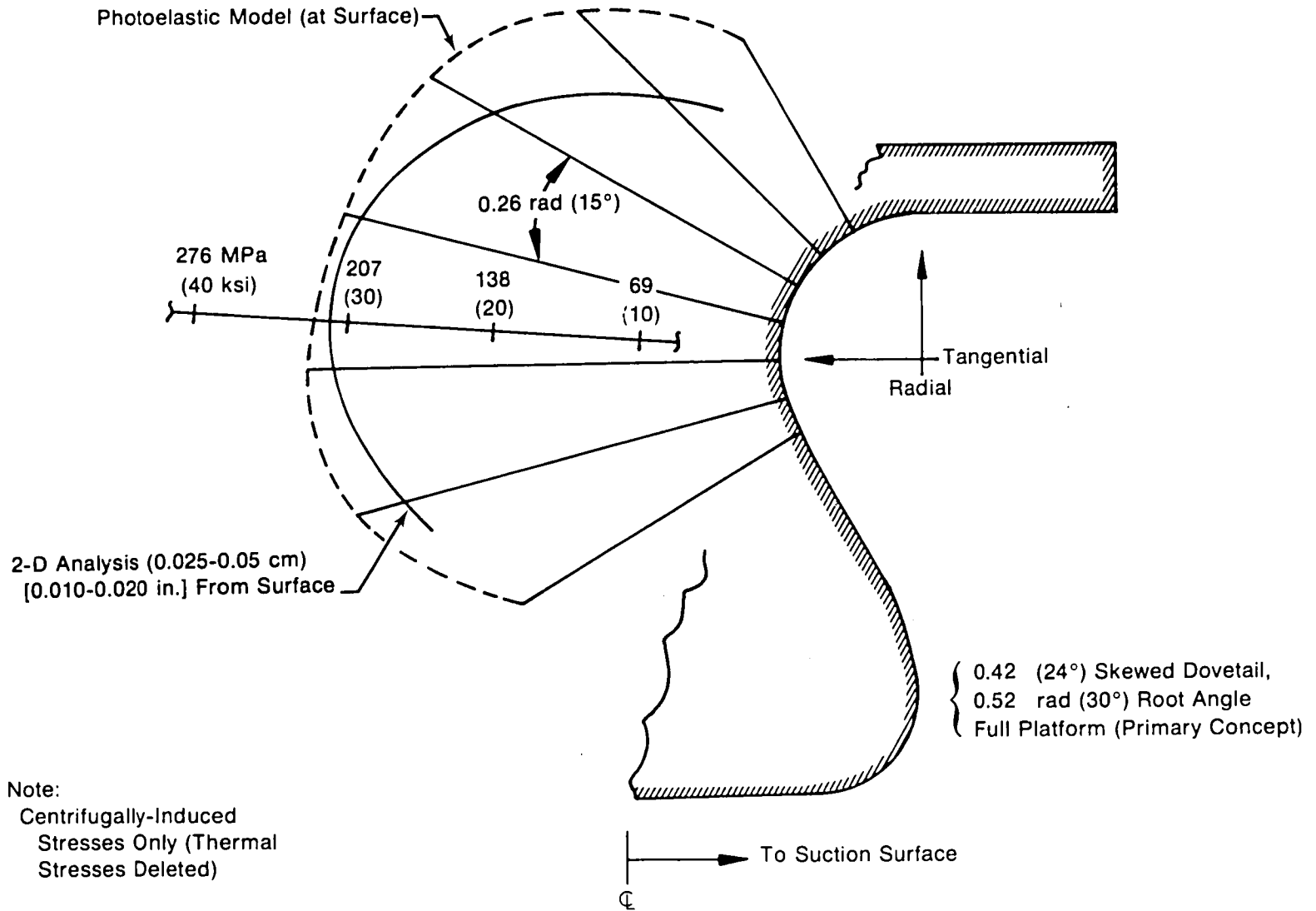
FD 139333

Figure 52. Attachment Surface Stresses (Suction Side)

53

0.26 rad
(15°)

2.2

1.8

1.4

1.0   2.0

1.2   1.6

Stress Concentration
Factor, K_T

Tangential

Radial

Primary Attachment

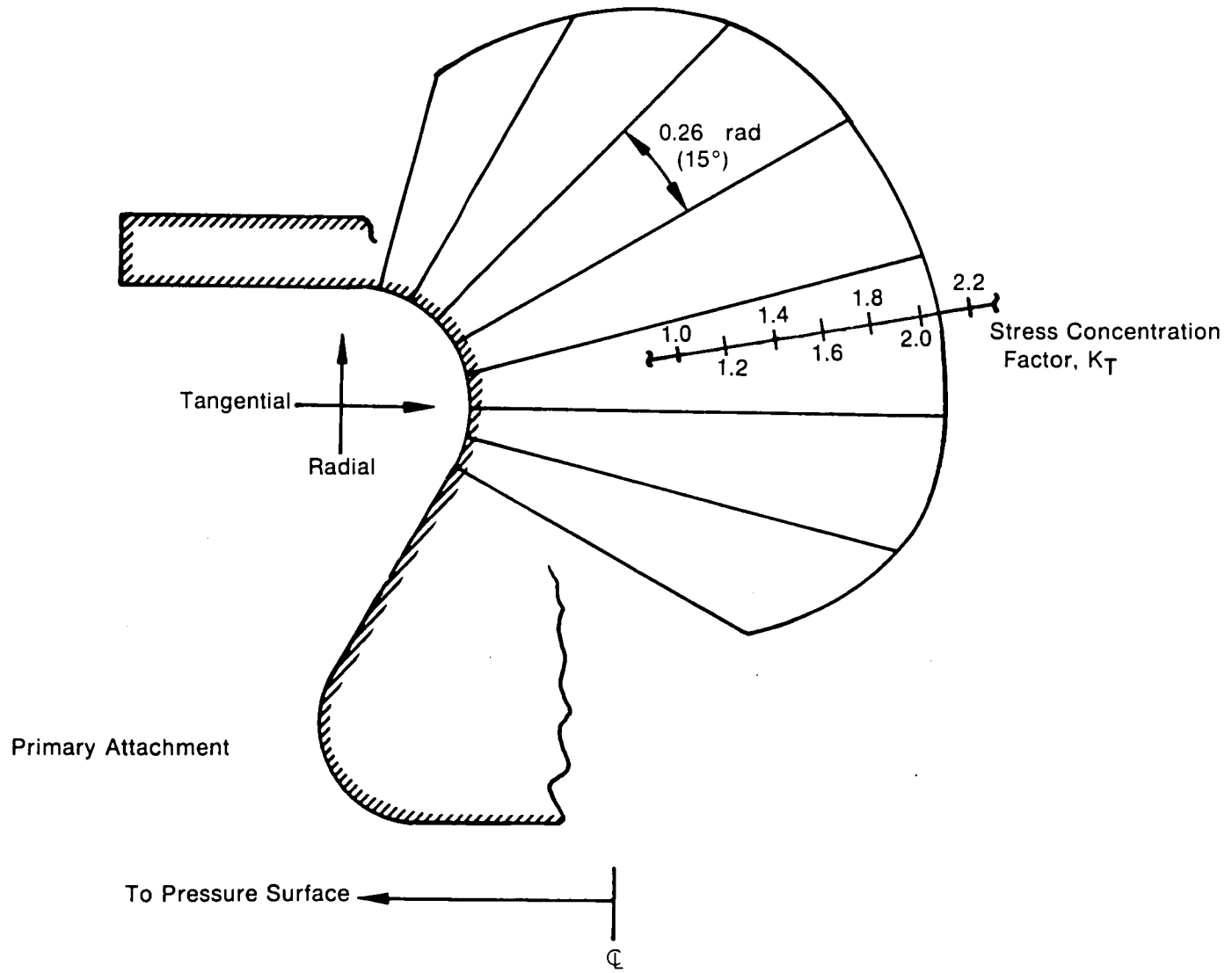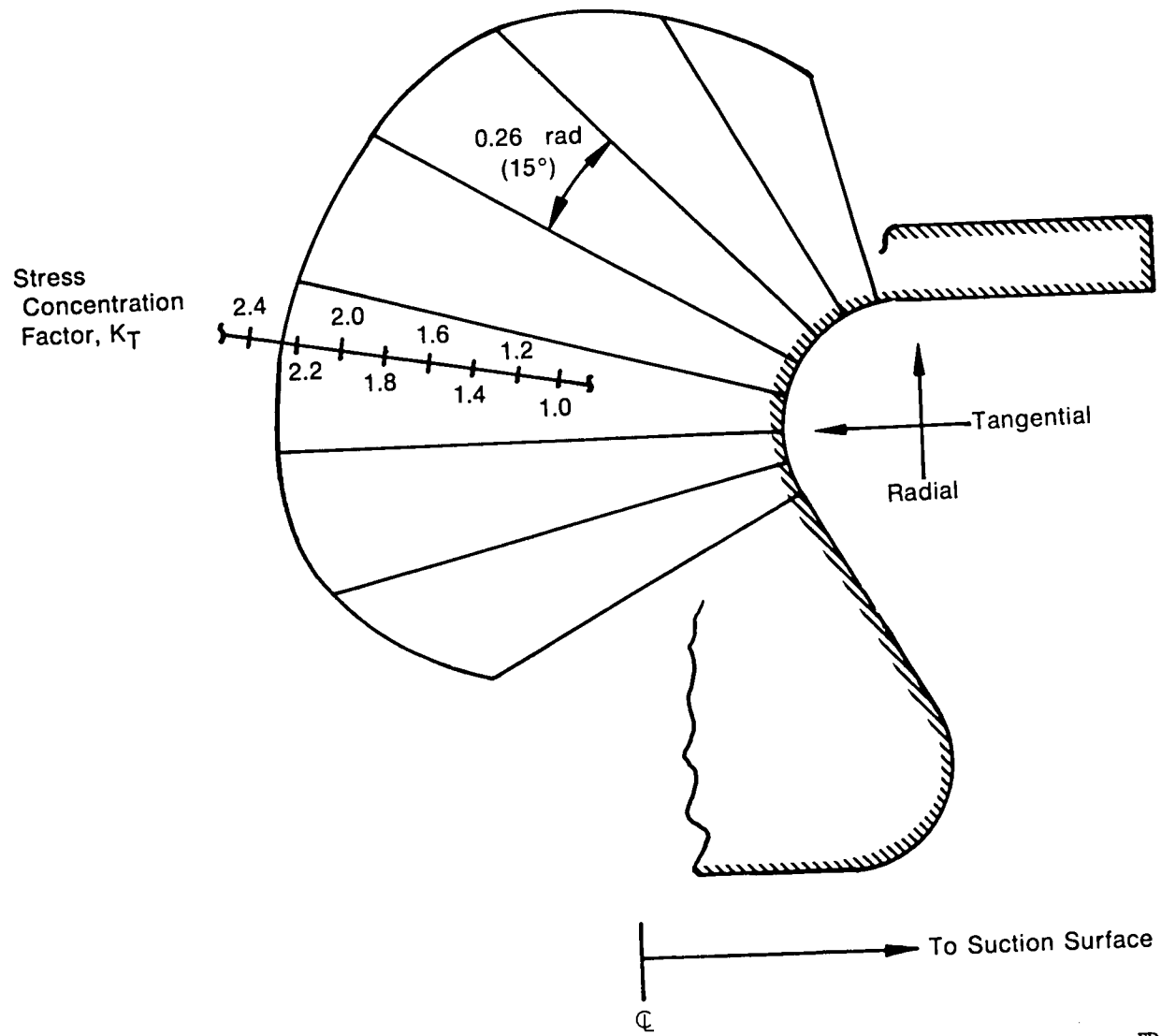To Pressure Surface

℄

FD 139334

Figure 53. Stress Concentration Factors (Pressure Surface)

Figure 54. Stress Concentration Factors (Suction Surface)

FD 139335

2.0 THREE-DIMENSIONAL STRESS ANALYSIS

The three-dimensional thermal and stress analysis of the ceramic blade attachment was performed at the United Technology Research Center (UTRC) using a three-dimensional computer program previously developed at UTRC. This program uses constant strain tetrahedral finite elements. The resultant piecewise linear displacement field is continuous throughout the part analyzed. Cubic strains are calculated by the simultaneous solution of three three-dimensional quadratic regression equations, one each for the x, y, and z displacement fields.

The three-dimensional analysis used boundary conditions taken from the two-dimensional analysis of Task I. In addition, the three-dimensional analysis accounted for shear stresses between the blade attachment and the disk lug along the interface region. Ideally, the shear stresses should be representative of the friction force between NC 132 and the platinum interface material. However, this data was not available from the literature, and the situation was further complicated by the fact that it was planned to lubricate the interface surfaces with boron nitride to promote slipping. Consequently, it was decided to use the shear strength of the platinum at operating temperatures as the interface shear stress in the analysis. This should be a conservative assumption, since it is tantamount to assuming a worst case condition where there is no sliding between the interface surfaces.

The three-dimensional analysis considered the attachment region, platform, and the airfoil root where the airfoil is blended into the platform. Figure 55 shows the overall three-dimensional breakup, and Figure 56 shows the location of the breakup planes. Airfoil loads were input as boundary conditions. The configuration analyzed represents the blade as designed for vacuum spin testing, i.e., it had no airfoil twist, taper, or aerodynamic loads. Typical breakups for the airfoil, platform, and attachment regions are shown in Figures 57, 58 and 59, respectively.

Results from the three-dimensional analysis are summarized in Table IV for speeds of 30,600 rpm (100% design) and 33,600 rpm (110% design), respectively. This figure shows that the maximum predicted tensile stress at 100% speed is 308 MPa (44.7 ksi) which occurs at the Z = 0.225-in. plane. This value is predicted to increase to 354 MPa (51.4 ksi) in the same location at 110% design speed, which is our normal overspeed design point. To provide the proper context for judging the acceptability of these stress levels, Figure 60 presents the predicted temperature levels for the maximum stress plane, and Figures 61 and 62 present the predicted isostress distributions for this plane at 100% and 110% design speeds respectively. The significant feature of these stress distributions is the steep stress gradient, and the highly localized nature of the maximum stress. This is desirable from a failure probability standpoint, and it means that flexure strength is the appropriate data to use for acceptance criteria.

During the time of the attachment design, flexure data for the ceramic material NC 132 was not available but data did exist for NC 130. However, one of the primary differences between NC 132 and NC 130 is improved mechanical properties for NC 132. Consequently, room temperature four-point flexure data for NC 132 was obtained from the Norton Company, and line slope data for NC 130 was used to construct an estimated curve of flexure strength vs temperature for NC 132. Results are shown in Figure 63. The NC 132 curve was constructed by starting with a room temperature four-point flexure strength of 903 MPa (131 ksi) which was the average value of 97 specimens. The slope of the curve to a temperature of about 820°C (1500°F) was assumed to be the same as P&WA data for NC 130, which is also shown in Figure 63. At 1370°C (2500°F), Norton had only three-point flexure data. For consistency, these data were used to estimate a four-point flexure strength. This was estimated on the basis of previously observed data that showed average four-point failure occurred at 87% of the three-point stress at 1370°C (2500°F). Again, the slope of the line from 1370°C (2500°F) to lower temperatures was made parallel to P&WA data for NC 130, thus completing the estimated four-point flexure curve for NC 132.
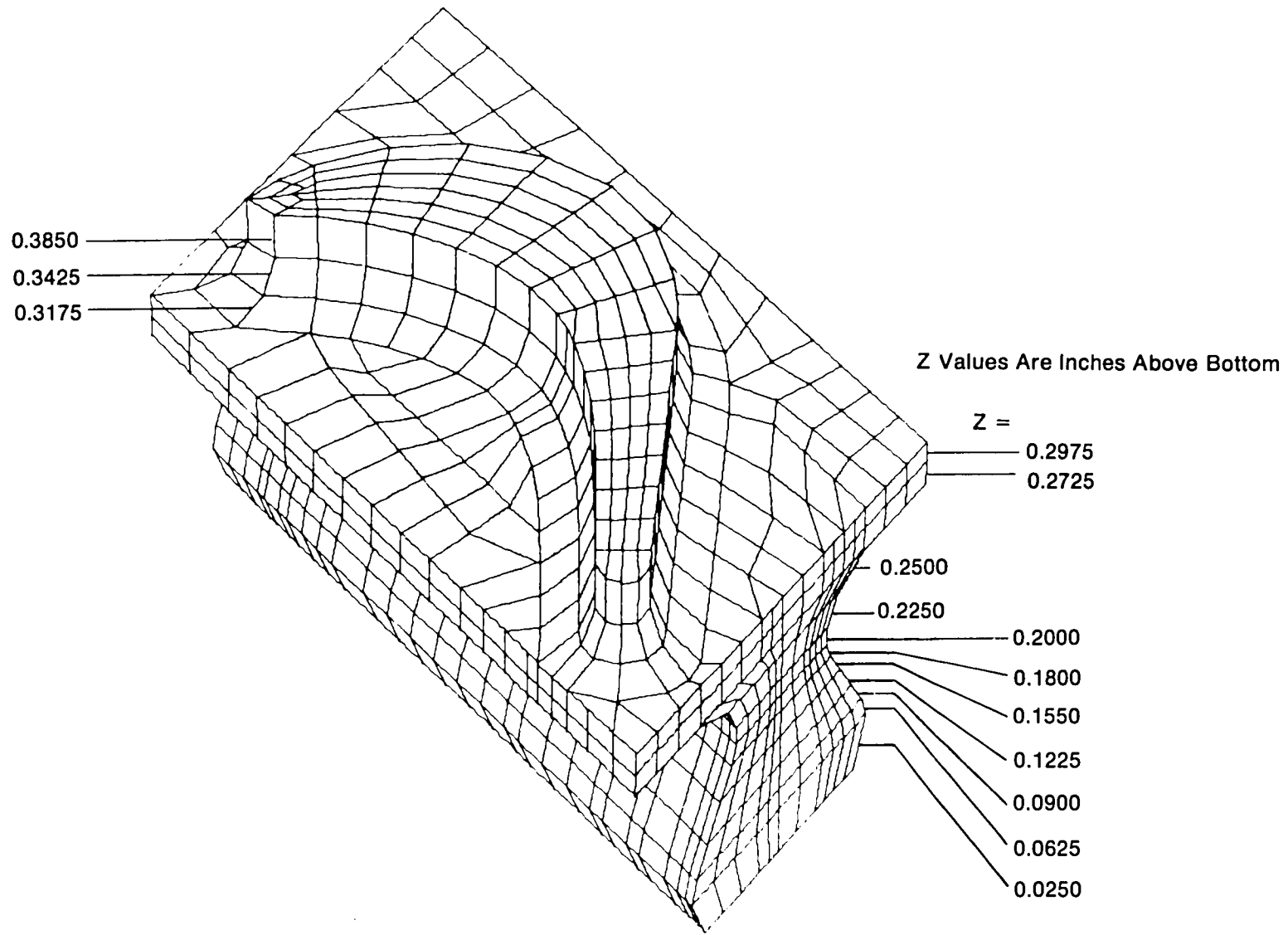
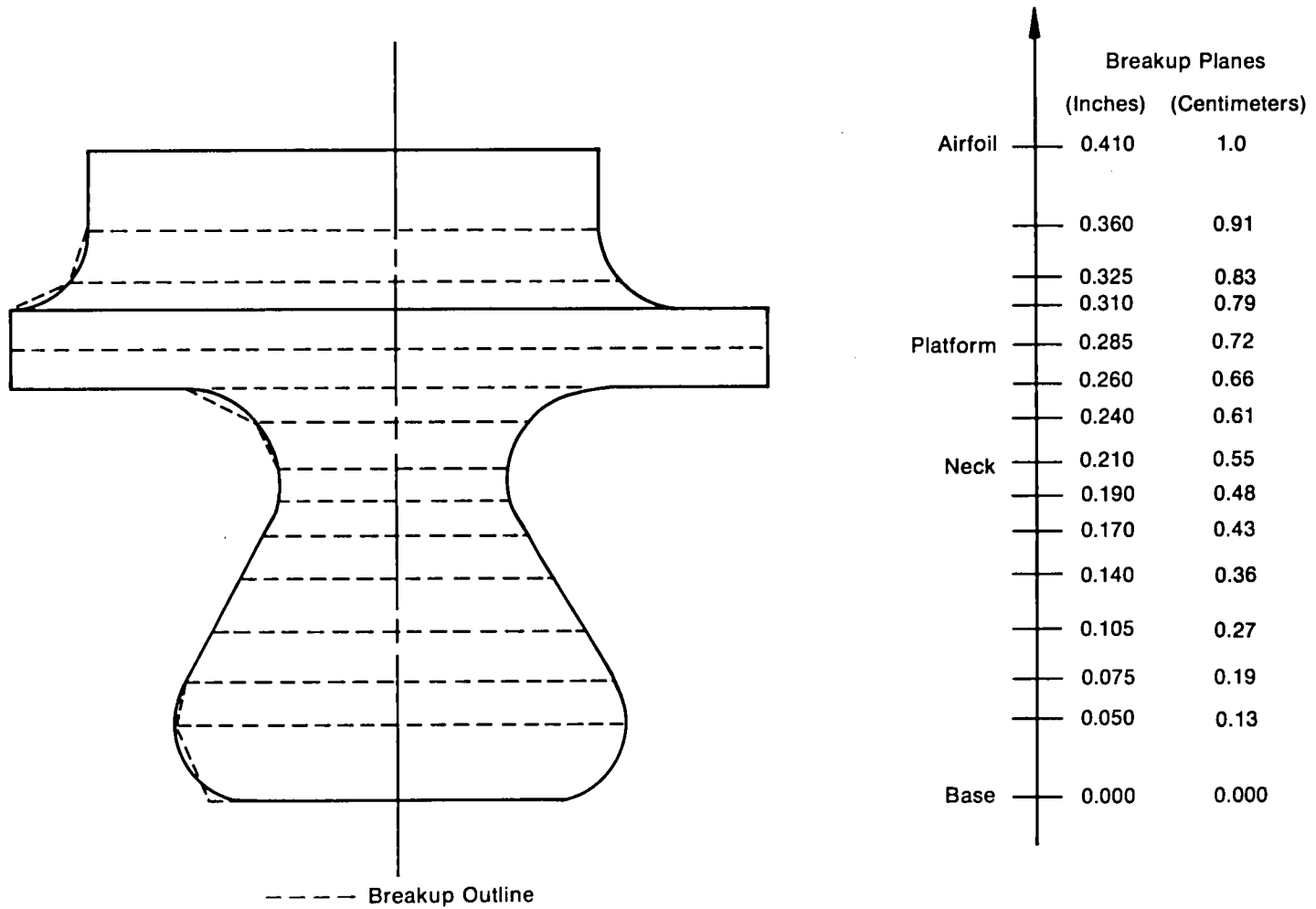Figure 55. *Three-Dimensional Breakup for Pilot Analysis*

FD 96274

	Breakup Planes	
	(Inches)	(Centimeters)
Airfoil	0.410	1.0
	0.360	0.91
	0.325	0.83
	0.310	0.79
Platform	0.285	0.72
	0.260	0.66
	0.240	0.61
Neck	0.210	0.55
	0.190	0.48
	0.170	0.43
	0.140	0.36
	0.105	0.27
	0.075	0.19
	0.050	0.13
Base	0.000	0.000

— — — — Breakup Outline

FD 139323

Figure 56. Location of Three-Dimensional Breakup Planes
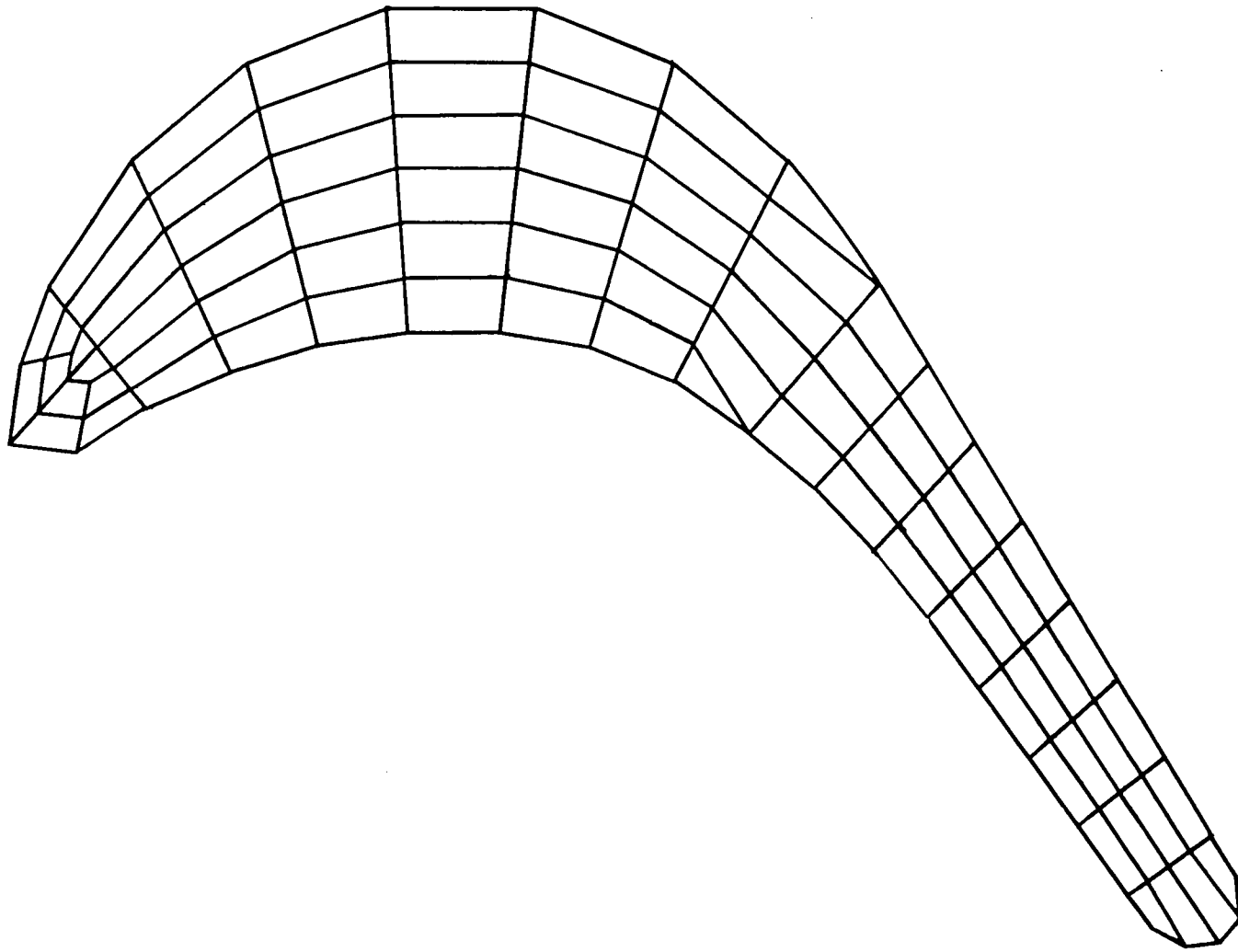
Figure 57. Typical Airfoil Elemental Breakup (Three-Dimensional)
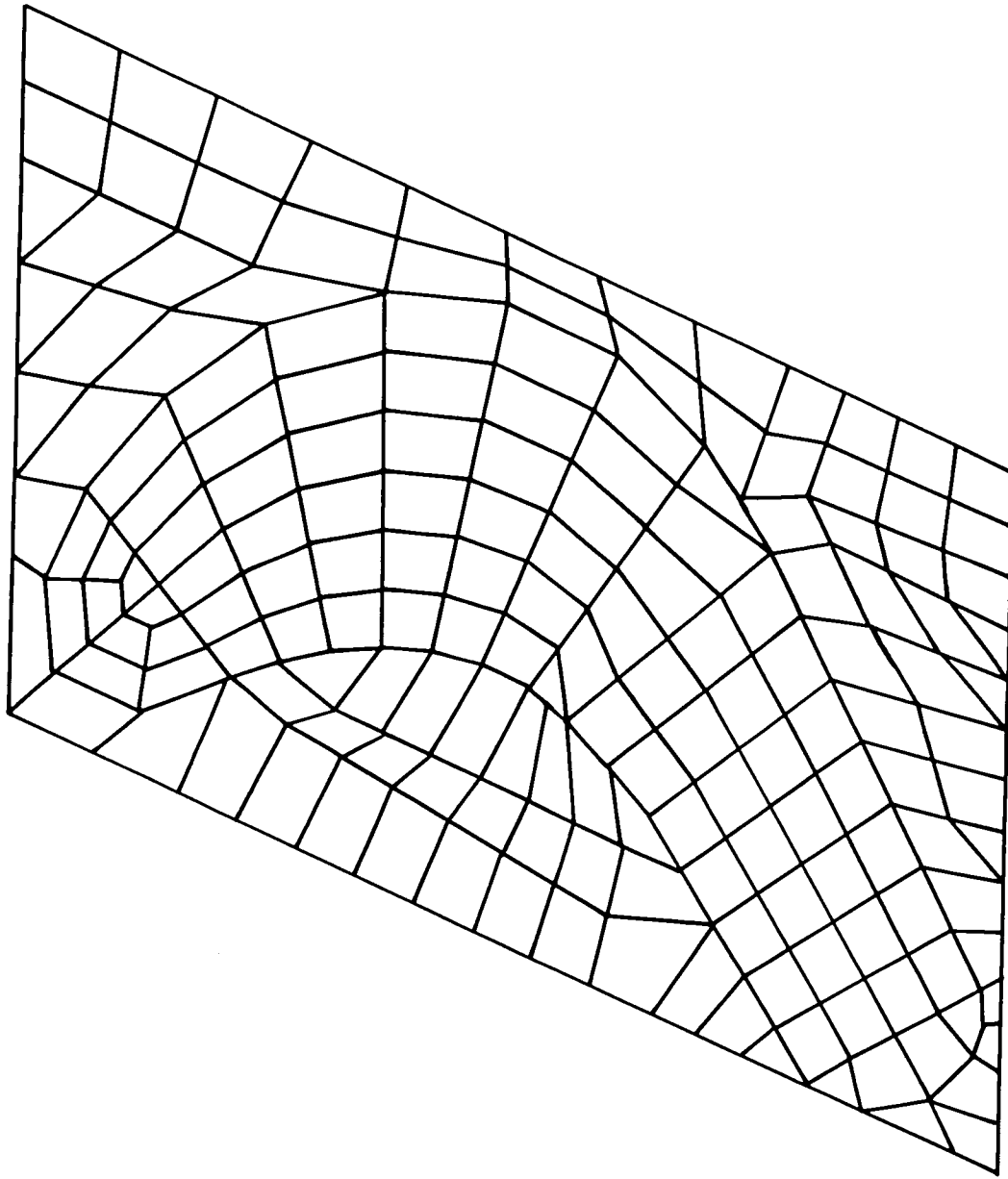
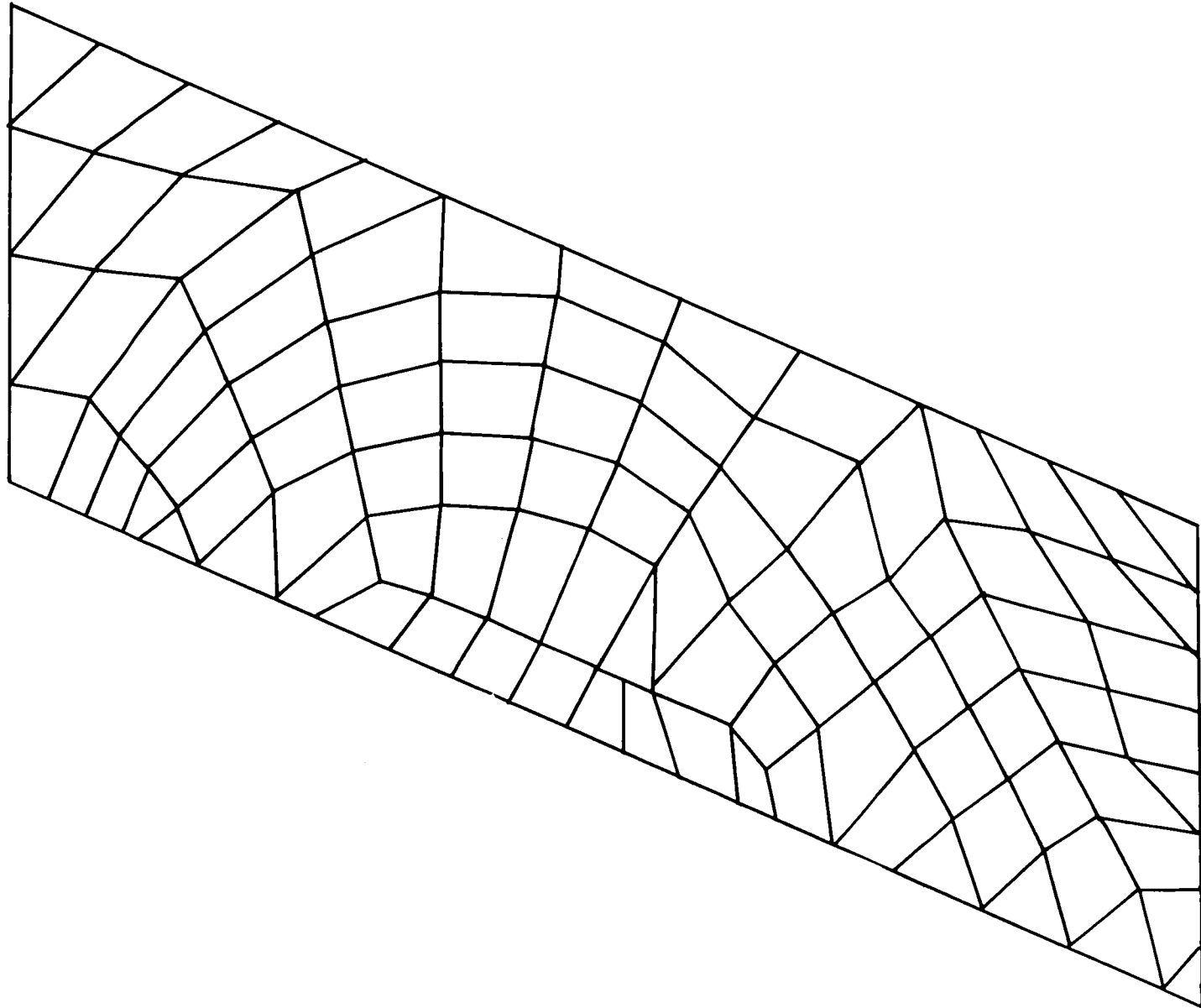*Figure 58. Typical Platform Breakup (Three-Dimensional)*

Figure 59. Typical Attachment Breakup (Three-Dimensional)

FD 152132

TABLE IV. SUMMARY OF THREE-DIMENSIONAL STRESS ANALYSIS

| | Location | | — 100% Design rpm — | | | | — 110% Design rpm — | | | |
| | | | Max Principal Stress (Tensile) | | Average Stress | | Max Principal Stress (Tensile) | | Average Stress | |
Z Plane	X	Y	(ksi)	(MPa)	(ksi)	(MPa)	(ksi)	(MPa)	(ksi)	(MPa)
0.02500	−0.22682	0.37166	12.3	85	− 0.4	− 2.8	10.7	74	− 0.4	− 2.8
0.06250	0.48462	0.53358	19.0	131	− 0.7	− 4.8	15.3	106	− 0.8	− 5.5
0.09000	0.48958	0.52245	29.5	203	− 0.4	− 2.8	23.8		− 0.3	− 2.1
0.12250	0.49713	0.50549	29.5	203	0.8	5.5	22.9	158	1.4	9.7
0.15500	0.12532	0.46348	19.9	137	5.3	36.5	22.6	156	6.7	46.0
0.18000	0.12892	0.45538	24.6	170	9.3	64.1	28.3	195	11.5	79.0
0.20000	0.41420	0.33537	44.1	304	12.5	86.2	51.0	352	15.1	104.0
0.22500	0.41736	0.32827	44.7	308	11.2	77.2	51.4	354	13.5	93.0
0.25000	0.42963	0.30070	27.0	186	7.8	53.8	30.7	212	9.5	66.0
0.27250	0.04625	0.47758	18.2	126	3.5	24.1	21.3	147	4.3	30.0
0.29750	0.11858	0.44867	16.6	115	3.5	24.1	19.6	135	4.2	29.0
0.31750	0.11839	0.45166	17.3	119	7.7	53.1	20.2	139	9.5	66.0
0.34250	0.11812	0.45588	15.8	109	11.4	78.6	18.6	128	13.9	96.0
0.38500	0.37895	0.32188	14.7	101	13.0	89.6	17.6	121	15.8	109.0
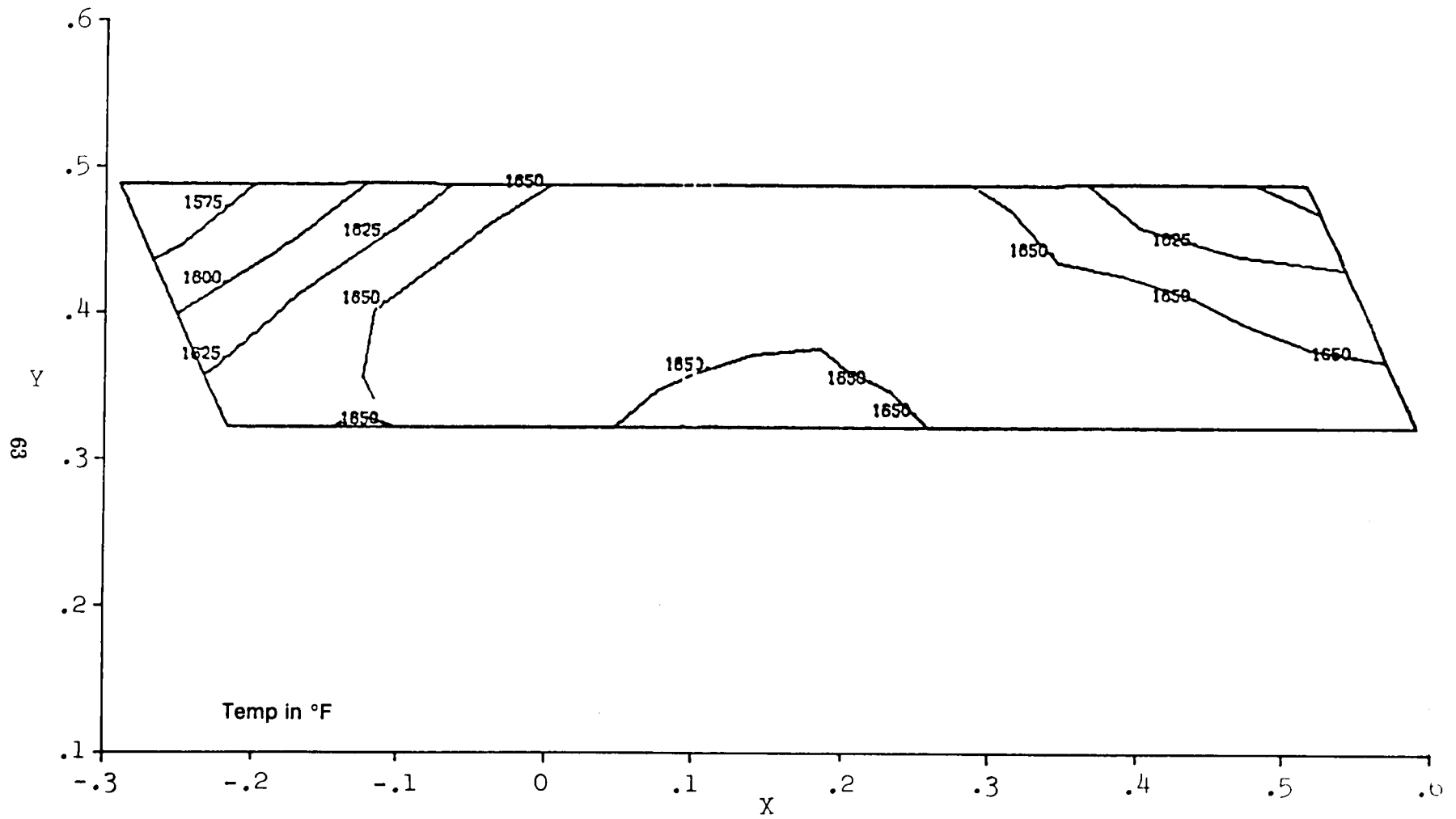
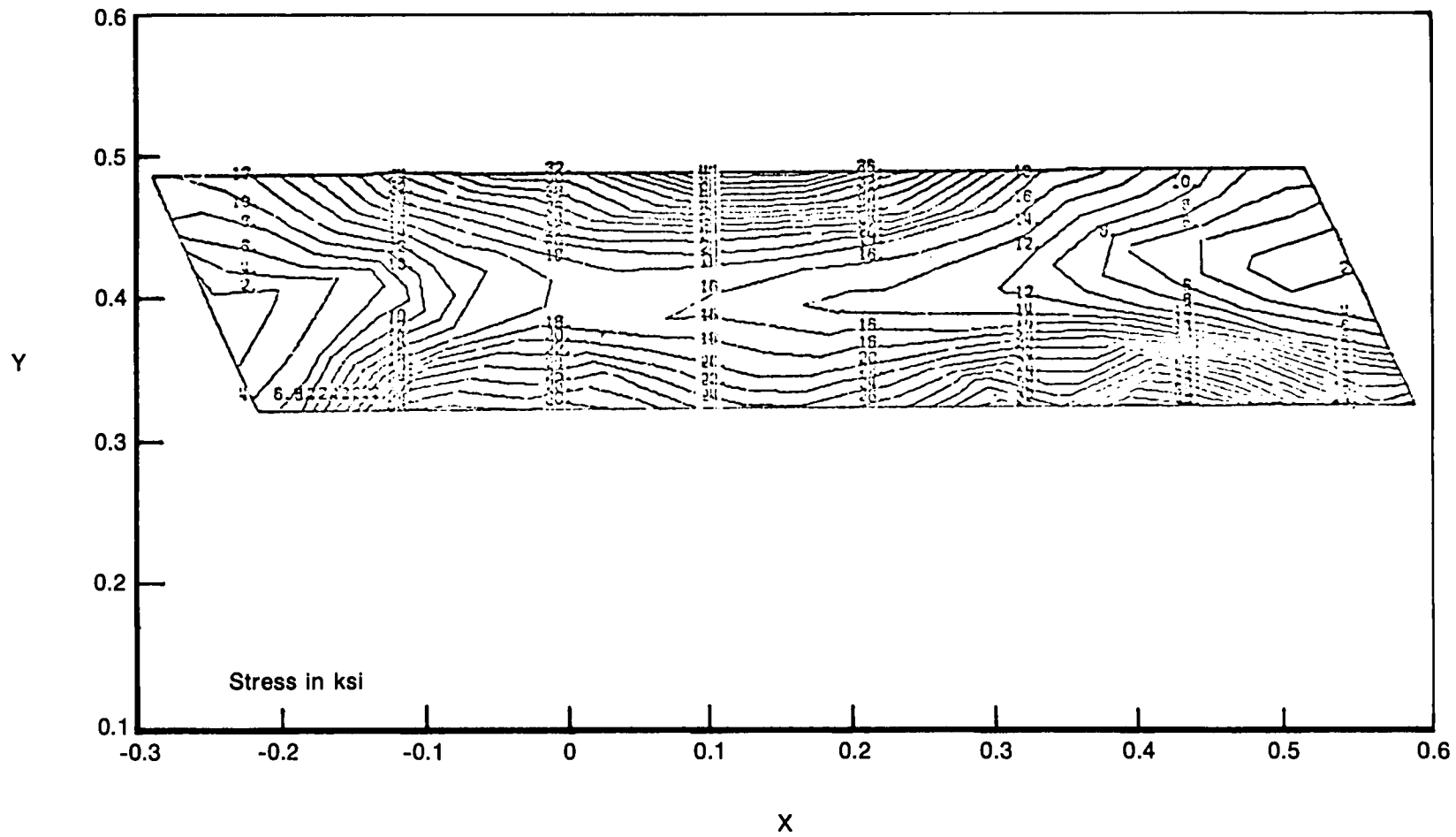Figure 60. Three-Dimensional Temperatures for Maximum Stress Plane (Attachments)

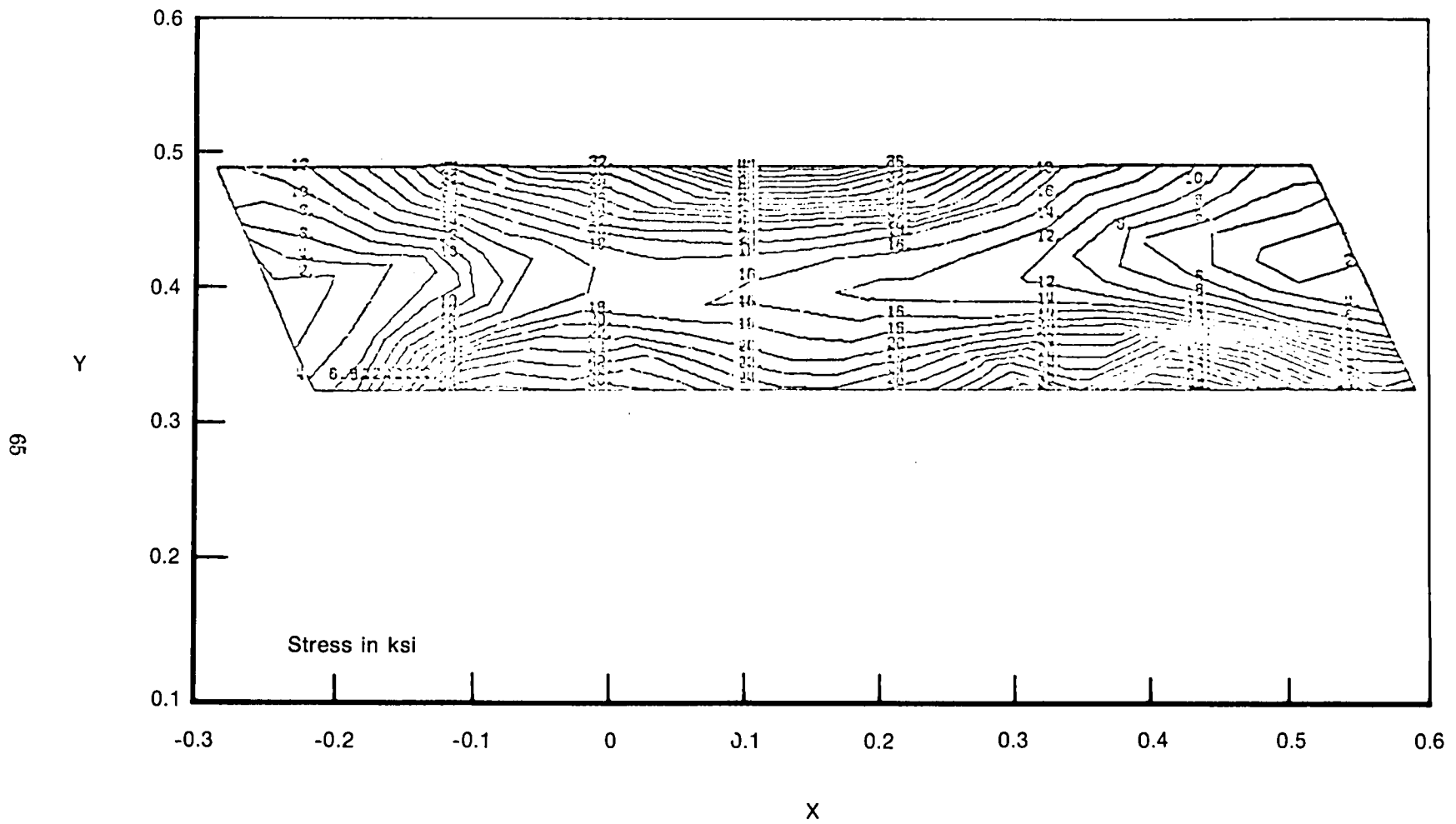Figure 61. Attachment Isostress Plot (100% rpm)

FD 142531

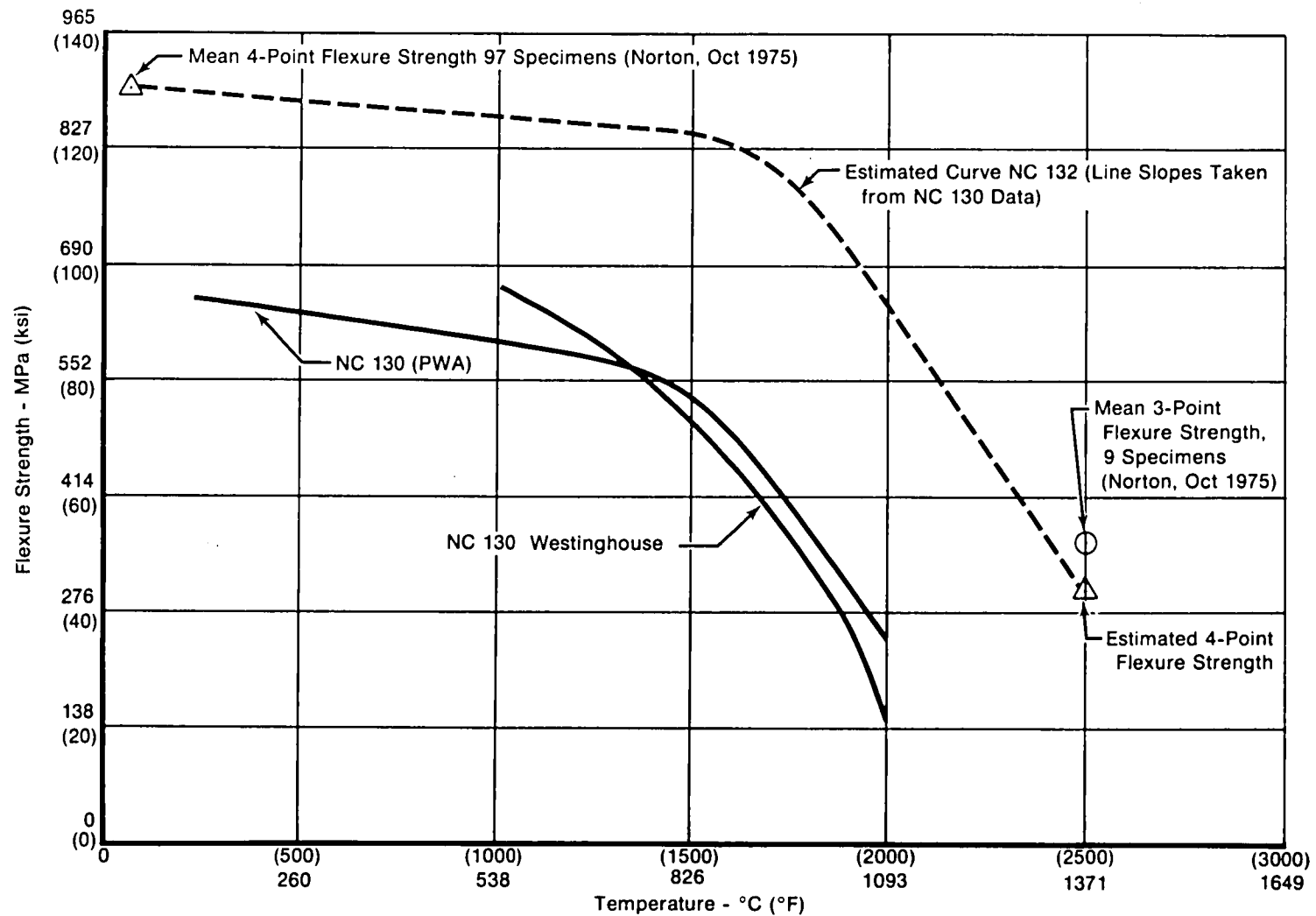*Figure 62. Attachment Isostress Plot (110% rpm)*

FD 139342

*Figure 63. Estimated 4 Point Flexure Curve for NC 132*

FD 139336

Prior to conducting a fracture mechanics evaluation of the blade design, the calculated stresses were compared to conventional metal failure design criteria. Figure 64 shows the 100% and 110% rpm maximum predicted stresses in the attachment compared to the mean curve for NC 132. Also shown is the lower bound for two standard deviations (2 sigma), which was obtained from the Norton Company (97.5% of all specimens will have strengths higher than the 2-sigma lower bound). Our usual metal design criteria for blade attachments allows a maximum tensile stress in the neck equal to 81% of the yield strength at the maximum transient speed, which is nominally 110% of design. Since ceramics do not exhibit a yield point, it is more appropriate to express this criteria in terms of ultimate tensile strength. For a current high-temperature blade metal alloy, PWA 1422 (DS Mar M 200 with Hf), the yield strength at its maximum use temperature is 869 MPa (126 ksi), or 90% of its ultimate strength of 958 MPa (139 ksi). Thus, 81% of its yield strength would be equivalent to 73% of its ultimate strength. In the case of the ceramic blade predicted stress of 354 MPa (51.4 ksi) at 110% speed and 900°C (1650°F), this stress is 57% of the 2-sigma value which places it well below the 73% metal criteria normally used. The blade attachment stress predictions at 110% speed were thus considered acceptable using conventional criteria, though final acceptance would be based on the results of the fracture mechanics evaluation described later.

The second critical region of the blade is the base of the airfoil. As shown in Figure 65, the three-dimensional analysis predicted temperatures in the 1010-1050°C (1850-1925°F) range for this region, slightly less than the 1060°C (1945°F) predicted by the two-dimensional analysis. Table IV showed a maximum predicted stress at 100% speed of 119 MPa (17.3 ksi) at Z = 0.3175. The stress distribution for this plane is shown in Figure 66, which shows that the maximum stress occurs in the airfoil rather than on the surface. The stress at 100% rpm was later used for the fracture mechanics life prediction for the design.

The predicted airfoil stress at 110% speed was used to judge design acceptability for uniaxial tensile failure. Table IV shows a maximum stress at 110% speed of 139 MPa (20.2 ksi) at Z = 0.3175 in. The predicted stress distribution for this plane at 110% rpm is presented in Figure 67. Our usual criteria for metals is that the maximum tensile stress in the airfoil at 110% speed should not exceed 51% of the yield strength, which is approximately 46% of the ultimate tensile strength using the previous example of PWA 1422.

Uniaxial tensile data was used to assess the airfoil stresses, since it is essentially uniformly stressed. However, Norton did not at that time have any uniaxial tensile data for NC 132. An approximate 2-sigma curve was estimated using the ratio of four-point flexure data for NC 132 vs NC 130 and applying this ratio to the previously established 2-sigma curve for NC 130 uniaxial tensile properties. This has been done in Figure 68 and the 138 MPa (20 ksi) maximum predicted airfoil stress has been plotted in the same figure. The predicted 2-sigma value for NC 132 is 290 MPa at 1050°C (42 ksi at 1925°F), which yields a predicted maximum stress equal to 47% of the 2-sigma lower bound. Forty-seven percent was only slightly higher than the normal 46% criteria, and was judged to be acceptable for this program.

A complete set of three dimensional results are presented in the appendix for temperatures, stress at 100% speed, and stress at 110% speed.
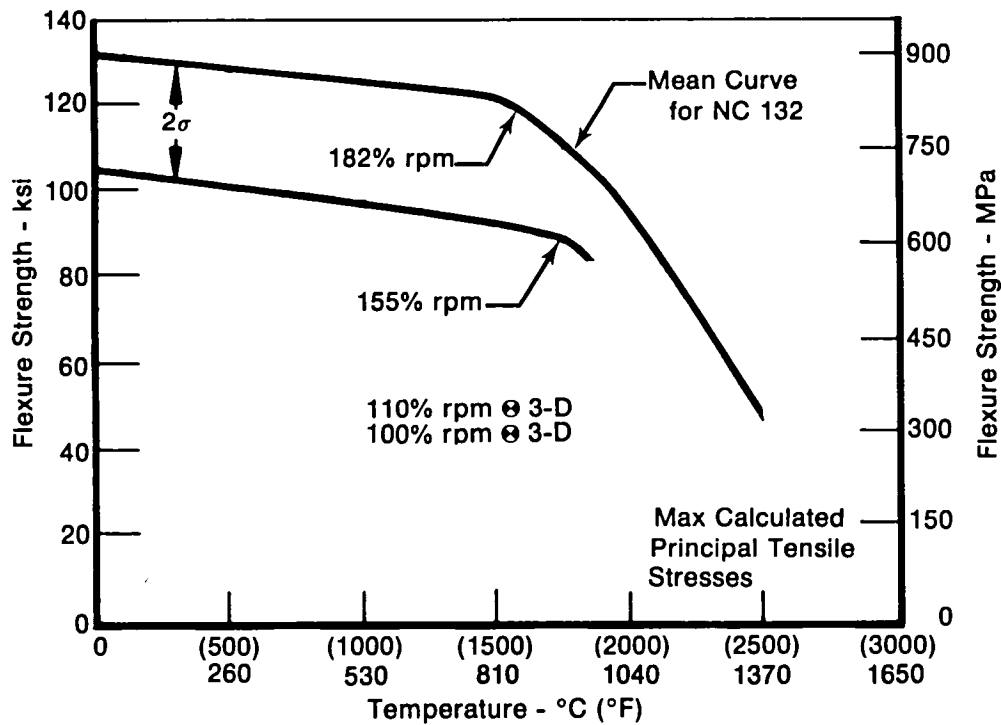
Figure 64. Three-Dimensional Attachment Stress vs NC 132 Flexure Strength

Disk stresses were also calculated during the two-dimensional analysis. For the blade configuration selected, the disk rim stress was 407 MPa (59 ksi) compared to an allowable stress of 834 MPa (121 ksi) and the lug neck stress was 303 MPa (44 ksi) compared to an allowable value of 393 MPa (57 ksi). These calculated stresses were based on 54 blades. It was anticipated that the number of blades tested in this program will be in the range of two to four, and they would be located at much larger gaps than required for a full set of 54. Therefore the actual disk stresses will be much lower than the two-dimensional predictions. (As discussed in Task III, some local stress problems were encountered as a result of retaining pin holes through the disk; these problems were solved by changing the details of blade retention.)
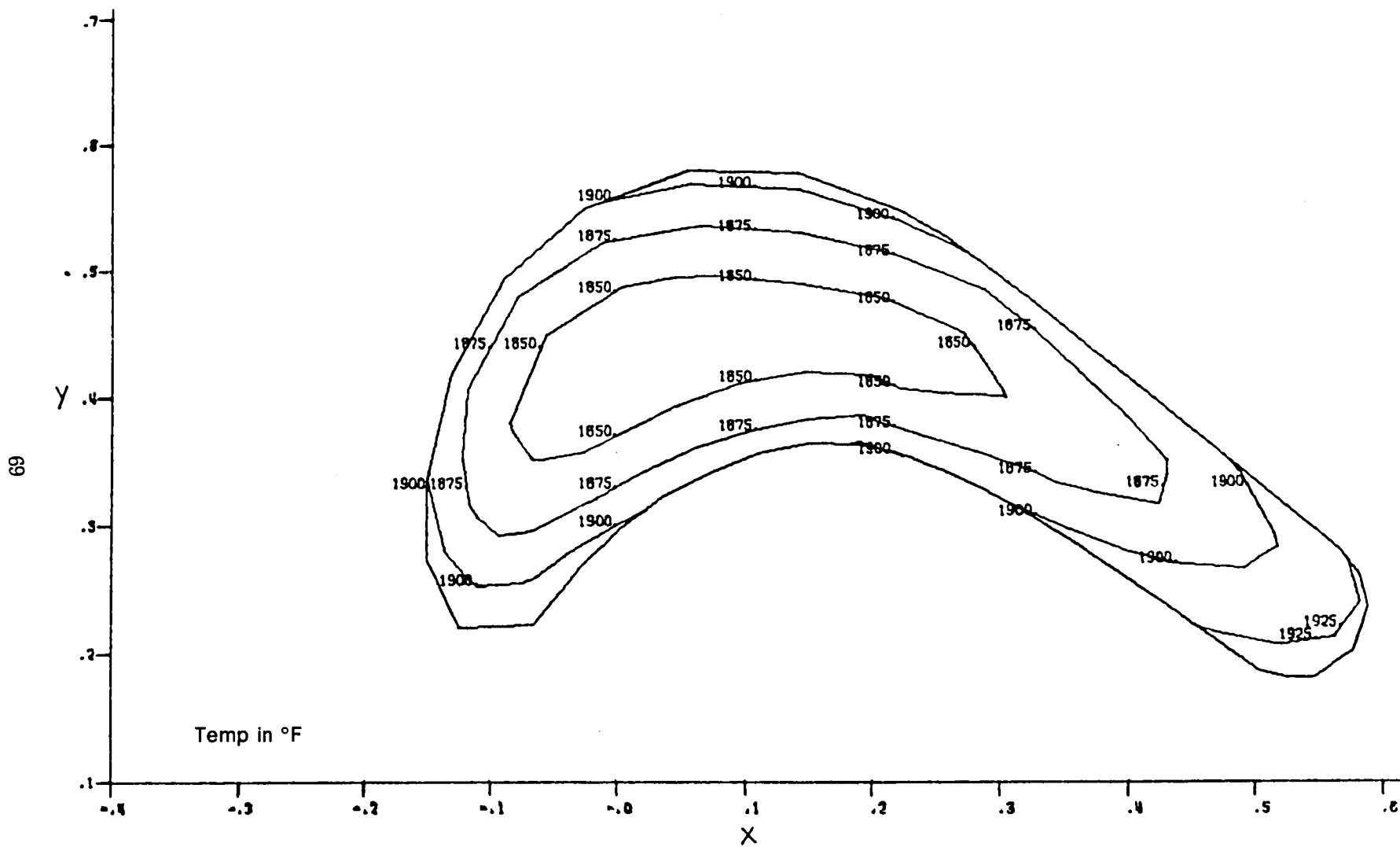
Figure 65. Three-Dimensional Temperatures for Maximum Stress Plane (Airfoil)
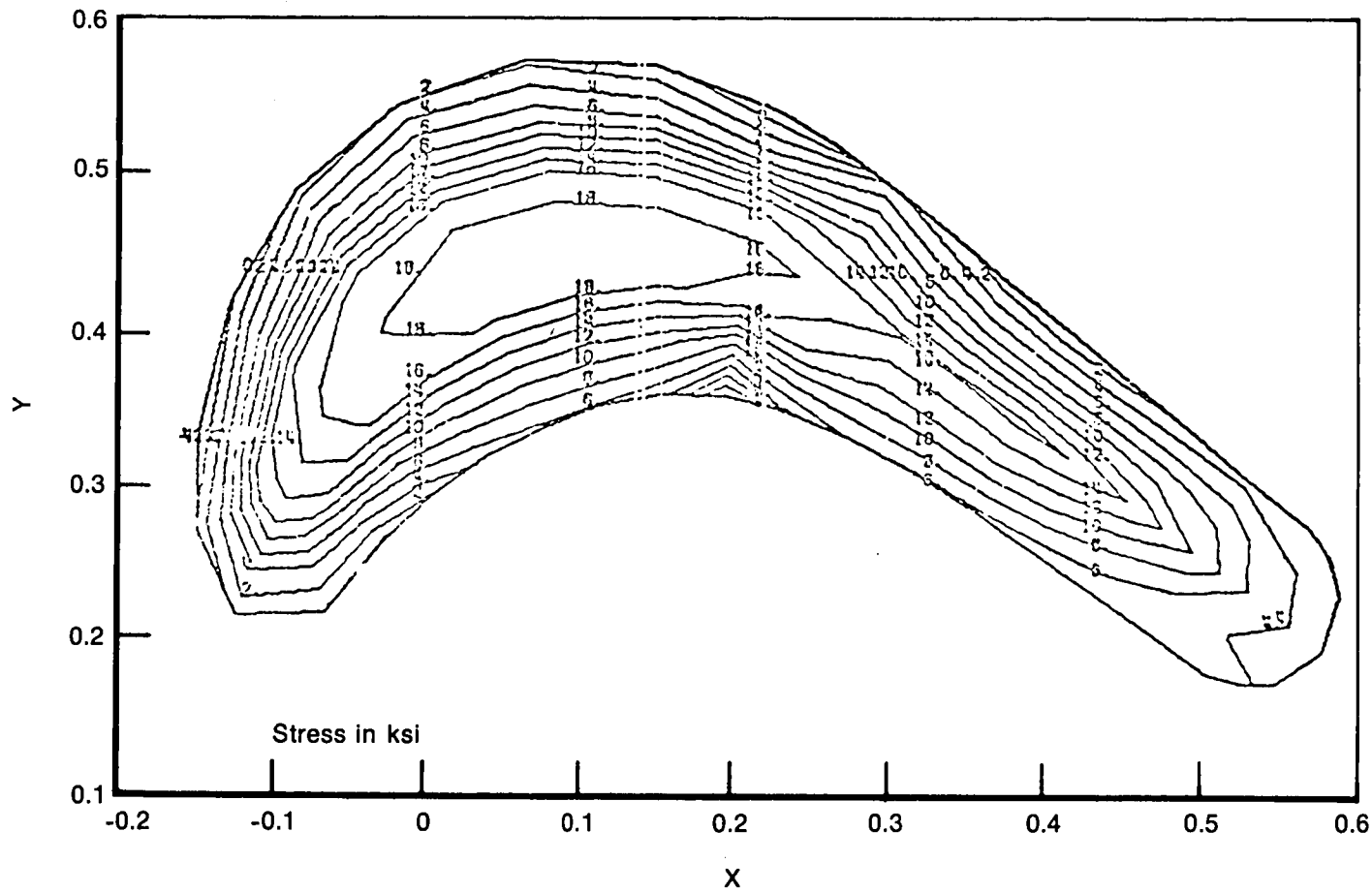
Stress in ksi

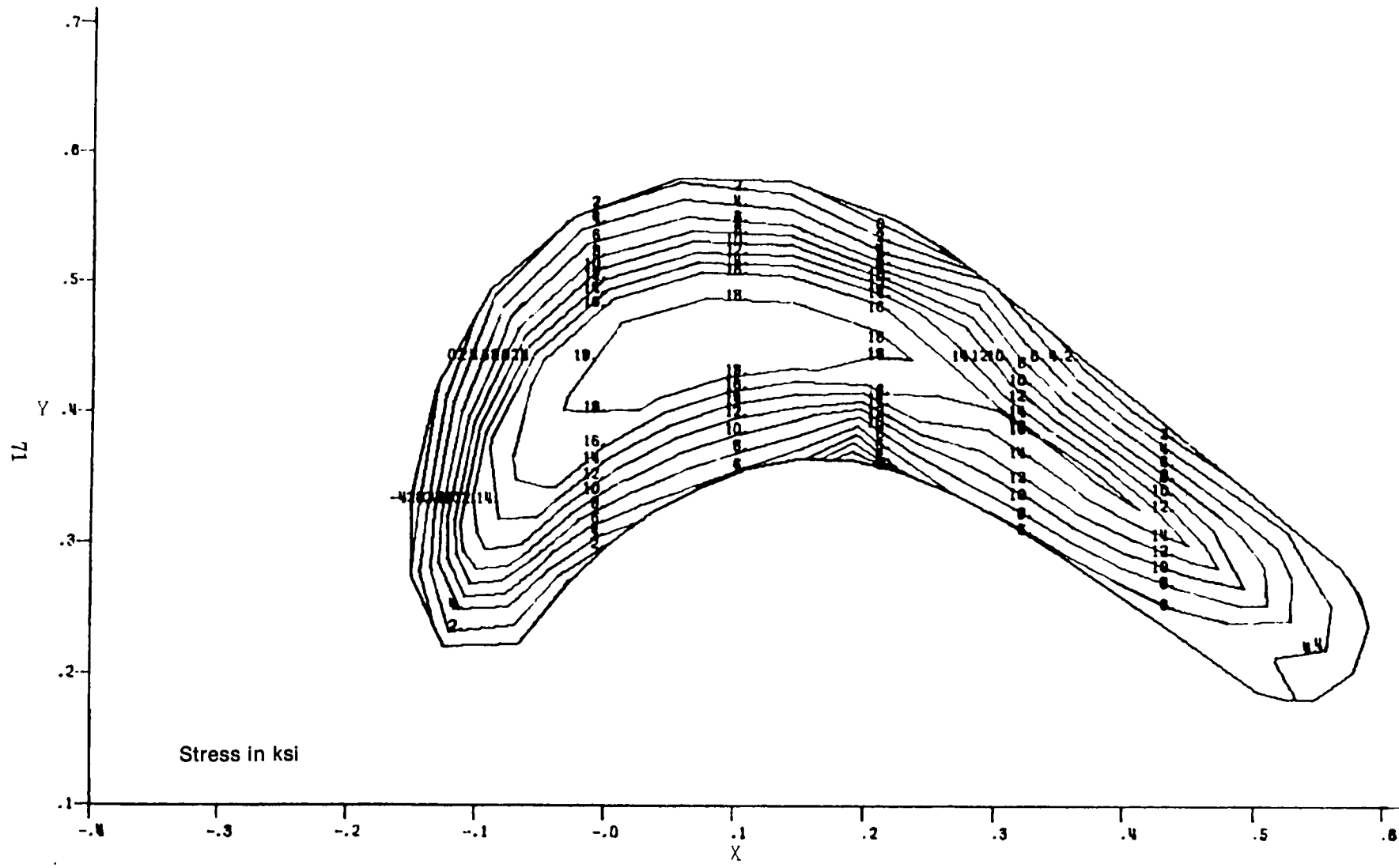Figure 66. Airfoil Isostress Plot (100% rpm)
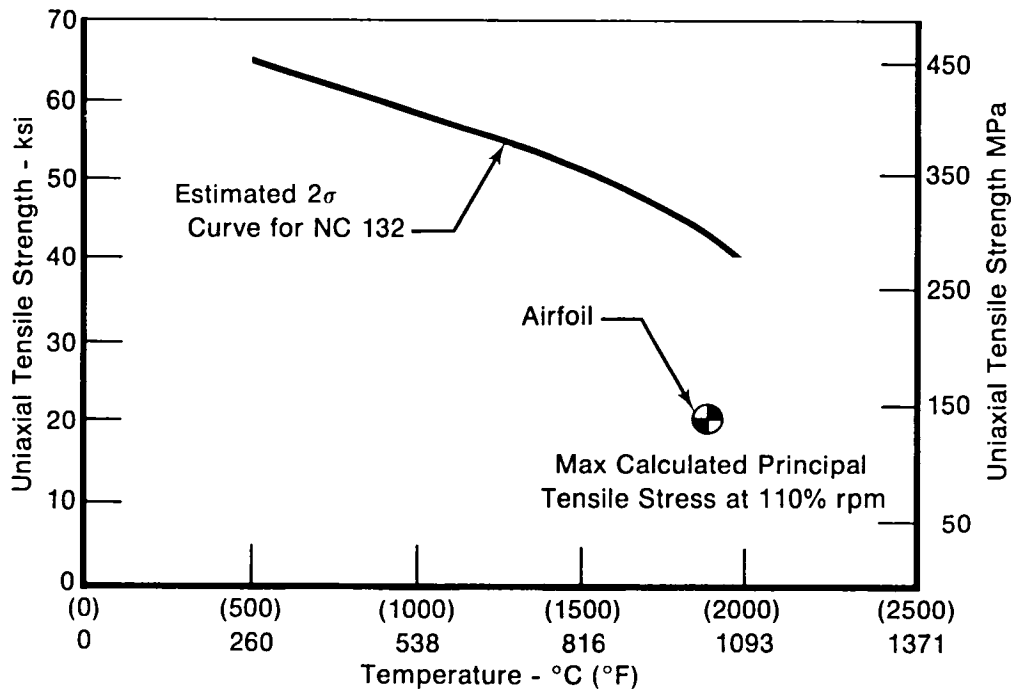
Figure 67. Airfoil Isostress Plot (110% rpm)

Figure 68. Airfoil Stress vs Estimated NC 132 Uniaxial Tensile Strength

3.0 FRACTURE MECHANICS EVALUATION OF THREE-DIMENSIONAL ANALYSIS

The predicted stresses at 100% rpm were used as the appropriate parameter for assessing blade life using fracture mechanics criteria. The earlier two-dimensional life analysis was updated using three-dimensional stresses, and the results are shown in Table V. Again, the 50-hour flaw sizes based on three-dimensional stresses were smaller than the minimum detectable flaw size, and the design was judged to be acceptable for fracture mechanics design criteria.

It should be noted that the airfoil 50-hour surface flaw size for three-dimensional stresses was slightly larger than that estimated in the two-dimensional analysis. This was the result of assuming a stress concentration factor in the two-dimensional stress analysis that was slightly higher than that predicted by the detailed three-dimensional stress analysis.

The scope of this program did not include a rigorous probabilistic design analysis, in which the probability of failure of the part would be calculated by integrating the probability of failure for each element over the entire volume. However, it is recognized that this type of analysis will ultimately be required for ceramic blades in gas turbine service.

At the conclusion of Task II, all aspects of the ceramic blade design were considered acceptable, and the fabrication of test hardware was initiated.

TABLE V. FINAL FRACTURE MECHANICS EVAL-
UATION

Flaw Type	Location	Temp (°F)	Temp (°C)	Flaw Size For 50-hr Life (2-D) (in.)	Flaw Size For 50-hr Life (2-D) (cm)	Flaw Size For 50-hr Life (3-D) (in.)	Flaw Size For 50-hr Life (3-D) (cm)	Min Detectable Flaw (in.)	Min Detectable Flaw (cm)
Surface	Attachment	1700	930	0.022	0.06	0.008	0.02	0.005	0.01
Internal	Attachment	1700	930	0.167	0.42	0.159	0.40	0.016	0.04
Surface	Airfoil	2200	1200	0.012	0.03	0.015	0.04	0.005	0.01
Internal	Airfoil	2200	1200	0.052	0.13	0.039	0.10	0.016	0.04

TASK III — BLADE FABRICATION AND TEST

The scope of this program initially consisted of the design.activity previously described under Task I and II, and blade fabrication and engineering test direction under Task III. However, the test portion of the program was subsequently cancelled for the convenience of the Government. Due to the cancellation of the program, the scope of this report for Task III will cover only the test program planning, blade fabrication, spin test tooling, and spin pit checkout runs. The spin pit checkout runs are included because they may be of value to other programs following a similar test approach.

1.0 TEST PROGRAM PLAN

The objective of the spin test programs was to demonstrate the capability of the ceramic blade to withstand a total run time of 50 hr, consisting of 100 nominal 30-min cycles. A test program was selected as follows:

Hours 0 to 10	*Test Conditions*
0-1	2 cy*, 0 to 15,000 rpm
0-2	2 cy, 0 to 20,000 rpm
2-3	2 cy, 0 to 25,000 rpm
3-10	14 cy, 0 to 30,600 rpm

Hours 11-50

Inspect assembly, thereafter run 10-hr, 20-cy test series from 0 to 30,600 rpm with inspections after every 10-hr increment. Total run time, 50 hr and 100 cy.

*Test Procedure:

(1) Bring up blade and disk temperature at low rpm
(2) Accelerate to test rpm in approximately 2.5 min
(3) Maintain test rpm for approximately 25 min
(4) Decelerate to low rpm in approximately 2.5 min
(5) For subsequent cycles, repeat (2), (3), and (4)
(6) For inspection, cool to room temperature at zero rpm.

The first 10-hr interval was designed to be a conservative approach to running at full speed, since rpm was gradually increased to design speed over the initial three hours of testing. Accelerations to speed were much slower than actual engine testing because the scope of design analysis covered only steady-state conditions, not engine transients. Characteristic engine temperature transients were therefore not planned during the spin test. Spin test steady-state temperatures were defined as predicted engine temperatures at the disk live rim and the base of the airfoil (reference Task I), which would result in engine-like thermal gradients and temperature levels in the ceramic blade attachment.

The basic instrumentation for the test assembly was planned to consist of thermocouples to monitor disk temperatures, and pyrometers to measure blade temperatures. No external instrumentation was planned to be attached to the blades, because of the undesirability of modifying the blade surface geometry with slots or roughened surfaces.

2.0 TEST HARDWARE FABRICATION

The manufacturing design for the ceramic blade is presented in Figure 69. The ceramic blades were machined in three major steps after machining rough blocks from a 15.4 × 15.4 × 1.9 cm (6 x 6 x 0.75 in.) billet of NC 132. First; the root forms were machined as shown in Figure 70. The airfoil was then rough-machined (shown in Figure 71), followed by finish machining of the airfoil. Figure 72 shows one of the finish-machined blades. Since these blades were ground in a circumferential direction, which is normal to the primary stress direction, they were given a heat treatment prior to spin testing. This consisted of a 982°C (1800°F) oxidation heat treat for 50 hr, which has been shown by Garrett in their DARPA-sponsored program to be beneficial for transverse-ground flexural specimens. Inspections of the finish-machined blades showed that the fabrication vendors were able to hold dimensions and surface finishes to the design tolerances, as shown in Figure 73.

The manufacturing design for the platinum interlayer is presented in Figure 74. As designed, this part performed two functions: (1) it provided a uniform load-distribution between the blade and the disk, and (2) it was designed to provide blade retention within the disk. Blade retention was to be achieved by bending the tabs, two over the blade and two over the disk. The platinum interlayers were hydroformed using the fixture shown in Figure 75, which also shows a completed part.

Figure 76 shows the disk attachment manufacturing design. As shown, there was a hole machined near the bottom of the disk slot. This hole was used for a bolt/washer assembly that provided positive blade retention in the event of failure of one of the platinum tabs. The basic disk itself was a JT15D engine Bill-of-Material part without final machined attachments. Figure 77 shows a blade and interlayer piece assembled into the spin disk. In this photograph, the platinum retention tabs have not been bent down into place. In actuality, it was later decided to delete the tabs for the initial tests since the bolt/washer assembly would provide blade retention.
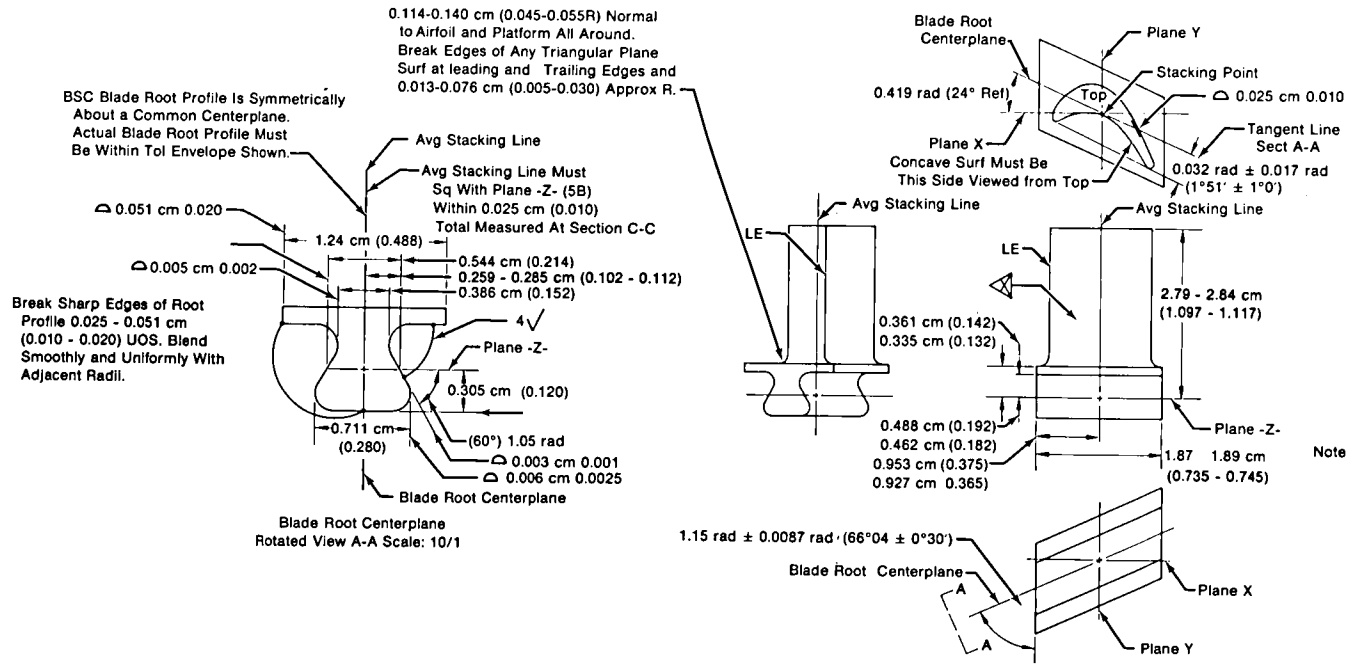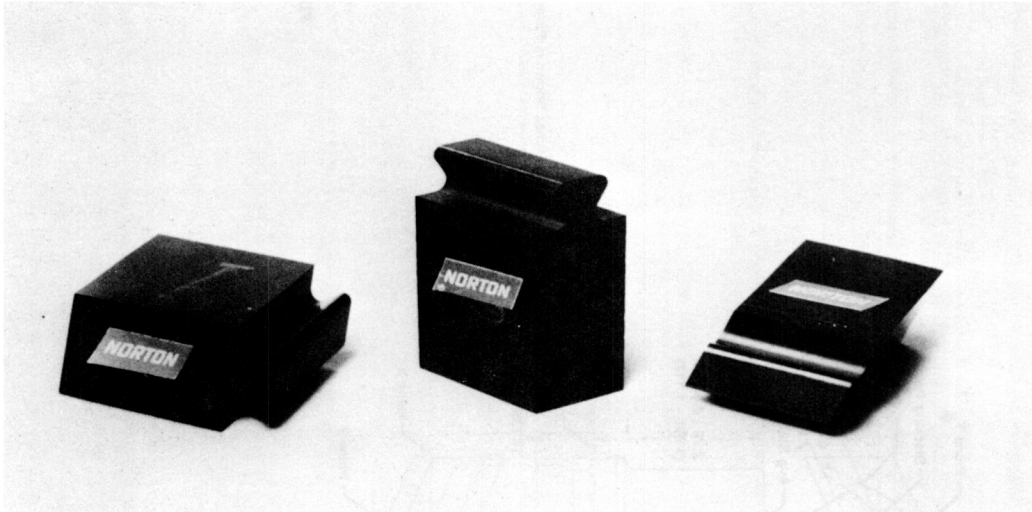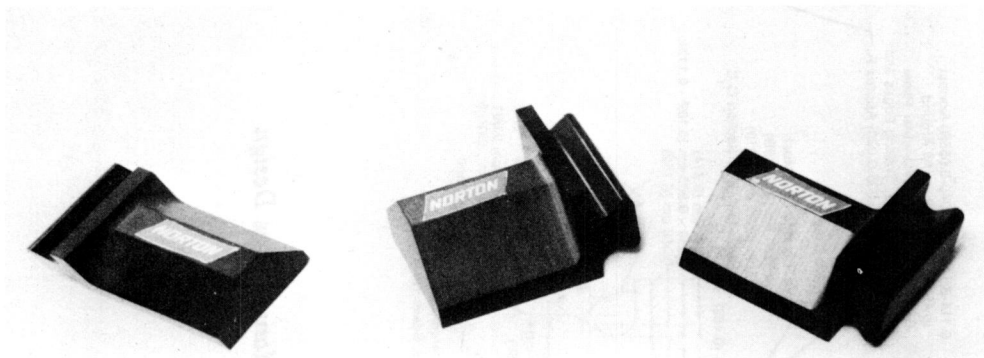
0.114-0.140 cm (0.045-0.055R) Normal to Airfoil and Platform All Around. Break Edges of Any Triangular Plane Surf at leading and Trailing Edges and 0.013-0.076 cm (0.005-0.030) Approx R.

BSC Blade Root Profile Is Symmetrically About a Common Centerplane. Actual Blade Root Profile Must Be Within Tol Envelope Shown.

Avg Stacking Line

Avg Stacking Line Must Sq With Plane -Z- (5B) Within 0.025 cm (0.010) Total Measured At Section C-C

⌒ 0.051 cm 0.020

⌒ 0.005 cm 0.002

Break Sharp Edges of Root Profile 0.025 - 0.051 cm (0.010 - 0.020) UOS. Blend Smoothly and Uniformly With Adjacent Radii.

1.24 cm (0.488)

0.544 cm (0.214)
0.259 - 0.285 cm (0.102 - 0.112)
0.386 cm (0.152)

4√

Plane -Z-

0.305 cm (0.120)

0.711 cm (0.280)

(60°) 1.05 rad

⌒ 0.003 cm 0.001
⌒ 0.006 cm 0.0025

Blade Root Centerplane

Blade Root Centerplane
Rotated View A-A Scale: 10/1

Blade Root Centerplane

Plane Y

Stacking Point

0.419 rad (24° Ref)

Top

⌒ 0.025 cm 0.010

Plane X
Concave Surf Must Be This Side Viewed from Top

Tangent Line Sect A-A

0.032 rad ± 0.017 rad (1°51' ± 1°0')

Avg Stacking Line

Avg Stacking Line

LE

LE

2.79 - 2.84 cm (1.097 - 1.117)

0.361 cm (0.142)
0.335 cm (0.132)

0.488 cm (0.192)
0.462 cm (0.182)
0.953 cm (0.375)
0.927 cm 0.365)

Plane -Z-

1.87   1.89 cm
(0.735 - 0.745)

Note: Dimensions in Inches Shown in Parentheses

1.15 rad ± 0.0087 rad (66°04 ± 0°30')

Blade Root Centerplane

A

A

Plane X

Plane Y

Figure 69. Ceramic Blade Manufacture Design

FD 114296

75

Figure 70. Ceramic Blade Root Forms

Figure 71. Ceramic Blade With Rough Cut Airfoils

FE 153482

Figure 72. Finished Machined Ceramic Blade
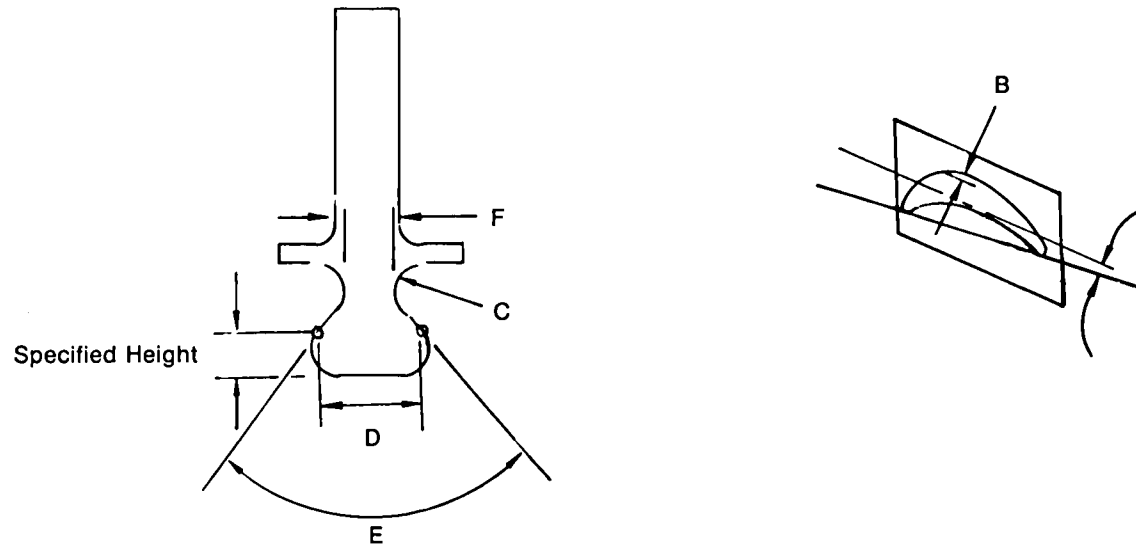
Location	Type of Dimension	Design Spec	Min	Max	Average	No. Deviations*
A	Airfoil-to-Root Angle	$4.9' \times 10^{-2}$rad $\pm$ 1.7453×10^{-2}	4.6×10^{-2}rad	4.8×10^{-2}rad	4.7×10^{-2}rad	
		(2°51' $\pm$ 1°0'	(2° 40')	(2° 48')	0 of 18	
B	Contour Band	0.000 - 0.025 cm	-0.003 cm	-0.02 cm	-0.01 cm	
		(+0.000 - 0.010 in.)	(-0.001 in.)	(-0.008 in.)	(-0.005 in.)	0 of 18
C	Surface Finish	3.8×10^{-5}cm	1.27×10^{-5}cm	5.8×10^{-5}cm	3.53×10^{-5}cm	
		(15×10^{-6} in.) (Arith Ave)	(5×10^{-6} in.)	(23×10^{-6} in.)	(13.9×10^{-6}cm)	2 of 18
D	Width of Gage Point at Specified Height	0.54 cm $\pm$ 0.005 cm	0.54 cm	0.55 cm	0.55 cm	
		(0.214 $\pm$ 0.002)	(0.2130)	(0.2151)	(0.2144)	0 of 22
E	Root Angle	1.05 rad	1.04 rad	1.05 rad	1.045 rad	
		(60°)	59°47'	(60°0'	59°55'	0 of 22
F	Neck Width	0.39 cm $\pm$ 0.005 cm	0.38 cm	0.38 cm	0.38 cm	
		(0.152 $\pm$ 0.002)	(0.1502)	(0.1520	(0.1505)	0 of 22

* A Total of 22 Attachments Were Machined. During Subsequent Grinding, Two Were Deviated Because of Platform Fracture or Chipping, and Two Were Deviated Because of Trailing Edge Chipping. These Four Airfoils Are Not Included in Data for Locations A, B, and C.

FD 114351

Figure 73. Fabrication Experience Summary
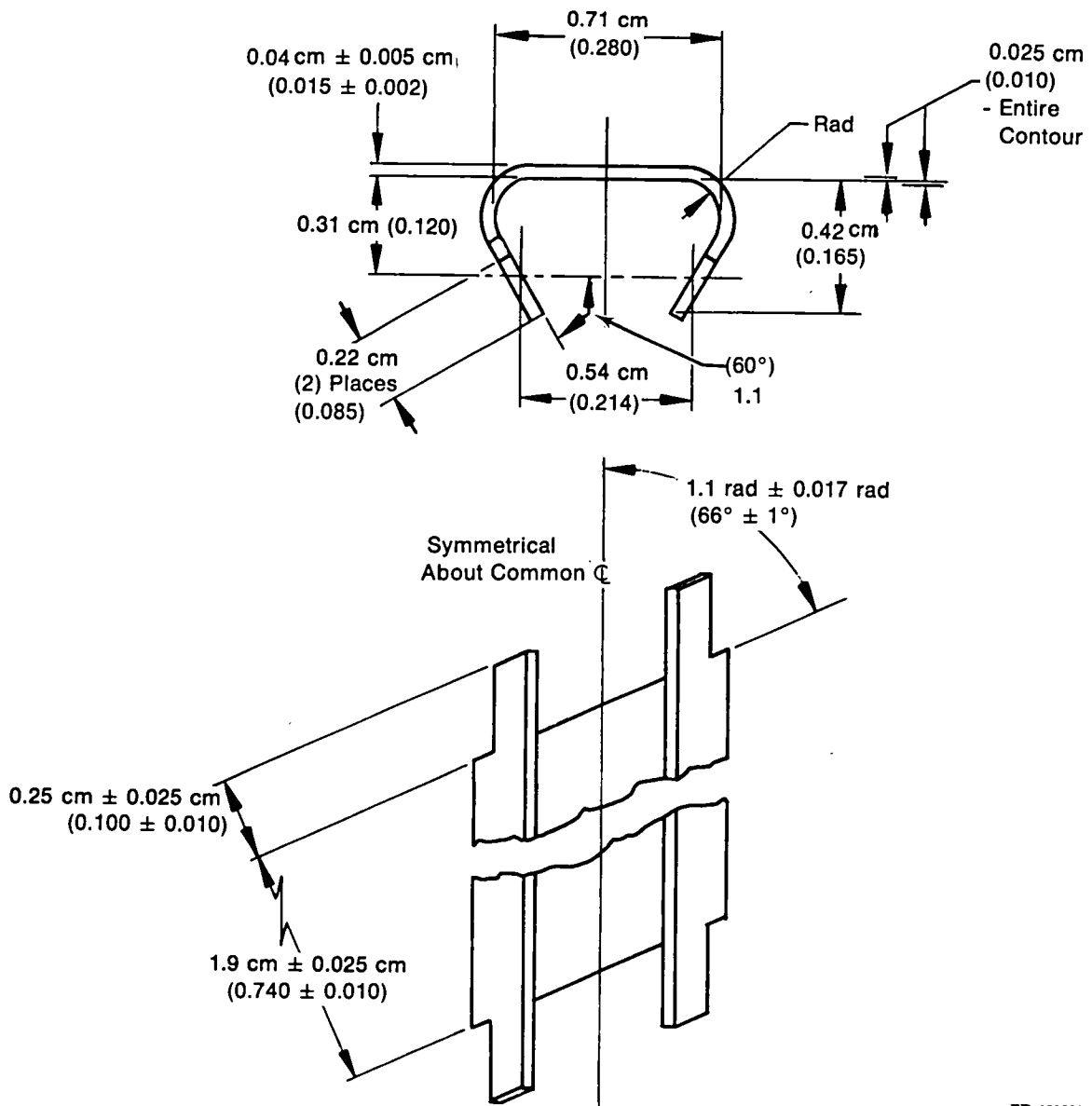
Figure 74. Platinum Interlayer Manufacturing Design (STF 29044)

FD 139339
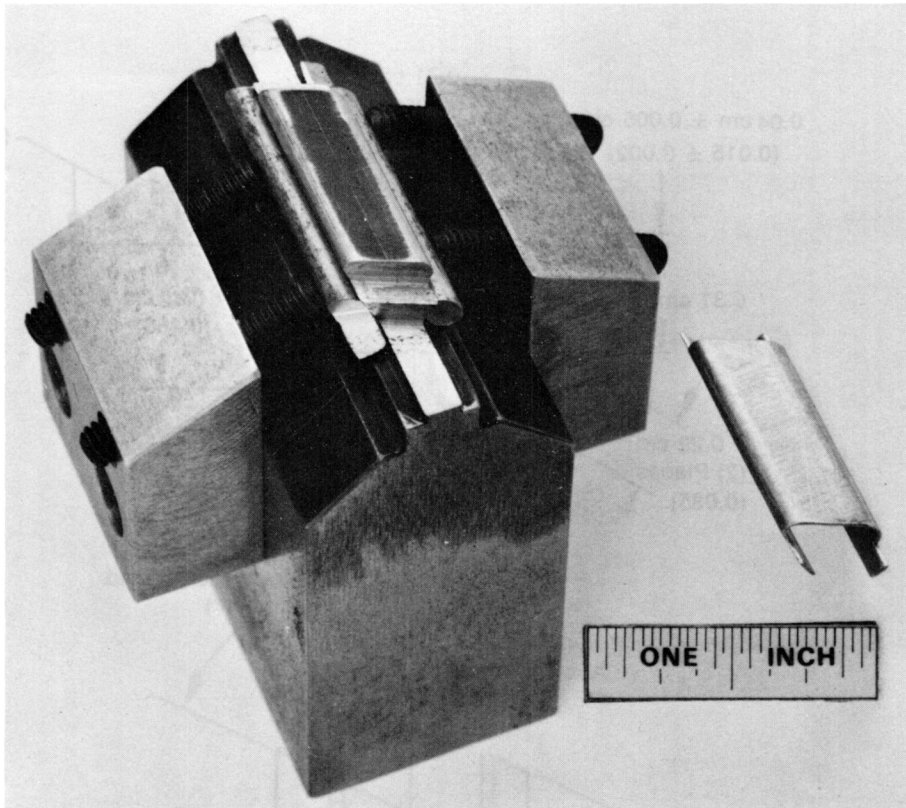
Figure 75. Platinum Interlayer Manufacturing Fixture

0.419 rad ± 0.0015 rad
(24°′ ± 0°5′)

Slot Centerplane

Permissible Tol
Envelope Measured Normal
to Surf Is ±(0.002)UOS.
All Envelope Radii Must
Be True Radii. Blend
Between Tol Surf Must Be
Continuous and Smooth.
Tol on Radii as Shown.

0.462 cm
(0.182)

0.3162 cm (0.1245)

2 Slots Loc as Shown
3.14 rad (180°) Apart

| ⊕ | B | A Ⓜ | 0.010 cm (0.004) Total Ⓜ |

Angular Relation to Features
Other than /D̄/Not Important

Slot Centerplanes
Must Be Parallel With Their
Respective Radial Centerlines
Within 0.0029 rad (0°10′)

0.368 - 0.394 cm
(0.145 - 0.155) dia
2 Holes 3.14 rad
(180°) Apart
B A M 0.025 cm

dia   0.114 - 0.140 cm
(0.0455 - 0.055) R

| ⊕ | B | A Ⓜ | 0.025 cm (0.010) dia Ⓜ |

Slot Profile Must Be
Symmetrical About Slot
Centerplane and Within
Tol Envelope Specified

R

81

Plane -Z-

0.381 cm (0.150)

1.05 rad ± 0.0058 rad
(60°0′ ± 0°20′)

10.523 cm (4.143)
To ₵ of dia -A-

5.7 cm (2.3)
Ref dia A

0.851 cm
(0.335)

11.32 cm (4.458)
11.31 cm (4.454)
To ₵ of dia -A-

Note: Dimensions Shown In
Parentheses Are Inches

View of Slot Profile
(Rotated) Normal to
Slot Centerplane
Scale: 10/1

Disk Radial Plane

Figure 76. Disk Attachment Manufacturing Design
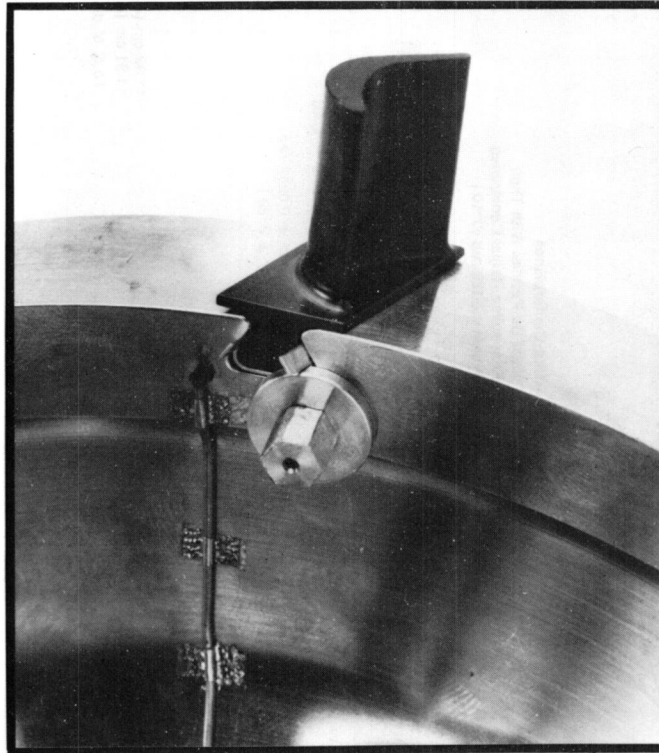
Figure 77. Blade/Interlayer/Disk Assembly

3.0 SPIN TEST SHAKEDOWN

Figure 78 shows a cross section of the spin test hardware in the test configuration. This assembly was designed with upper and lower catcher bearings to prevent loss of the disk and spin arbor in the event of drive spindle failure. The bumper gaps were selected so that the spin arbor will not contact the bumper bearing as a result of blade failure. The mass distribution of this assembly was such that, if a blade was failed, it could be replaced and the assembly retested without requiring a rebalance of the rotor. At the top of the assembly, two proximity probes were mounted at 1.6 rad (90 deg) to each other, and their signals were read out on an oscilloscope during spin test. The resulting scope presentation shows the location of the shaft centerline relative to the nominal center, and it indicates the type of shaft movement about its mass center. This concept has been successfully used to detect shaft instabilities and shaft displacements outside of predetermined limits. Internal holes machined into the shaft provided instrumentation wire routing for disk thermocouples.

In the detail design of the rotating parts, it was found that the Bill-of-Material JT15D disk would grow more than the arbor through the range of test speeds. This would result in either loosening of the snap fits at speed or excessive initial interference, with an overstress condition at the interface. The solution was to modify the arbor geometry to achieve a lower spring rate, which would result in a reasonable interference fit at assembly that remained tight throughout the speed range. The final configuration is shown in Figure 79. The arbor was slotted circumferentially and axially, so that the pilot diameter on the arbor was essentially a series of fingers cantilevered in the radial direction. Figure 79 also shows that instrumentation access holes were added to the lower snap fit (left hand side in the figure) so that metal temperatures could be monitored in that region. Thermocouple locations for the spin test disk are shown in Figure 80.
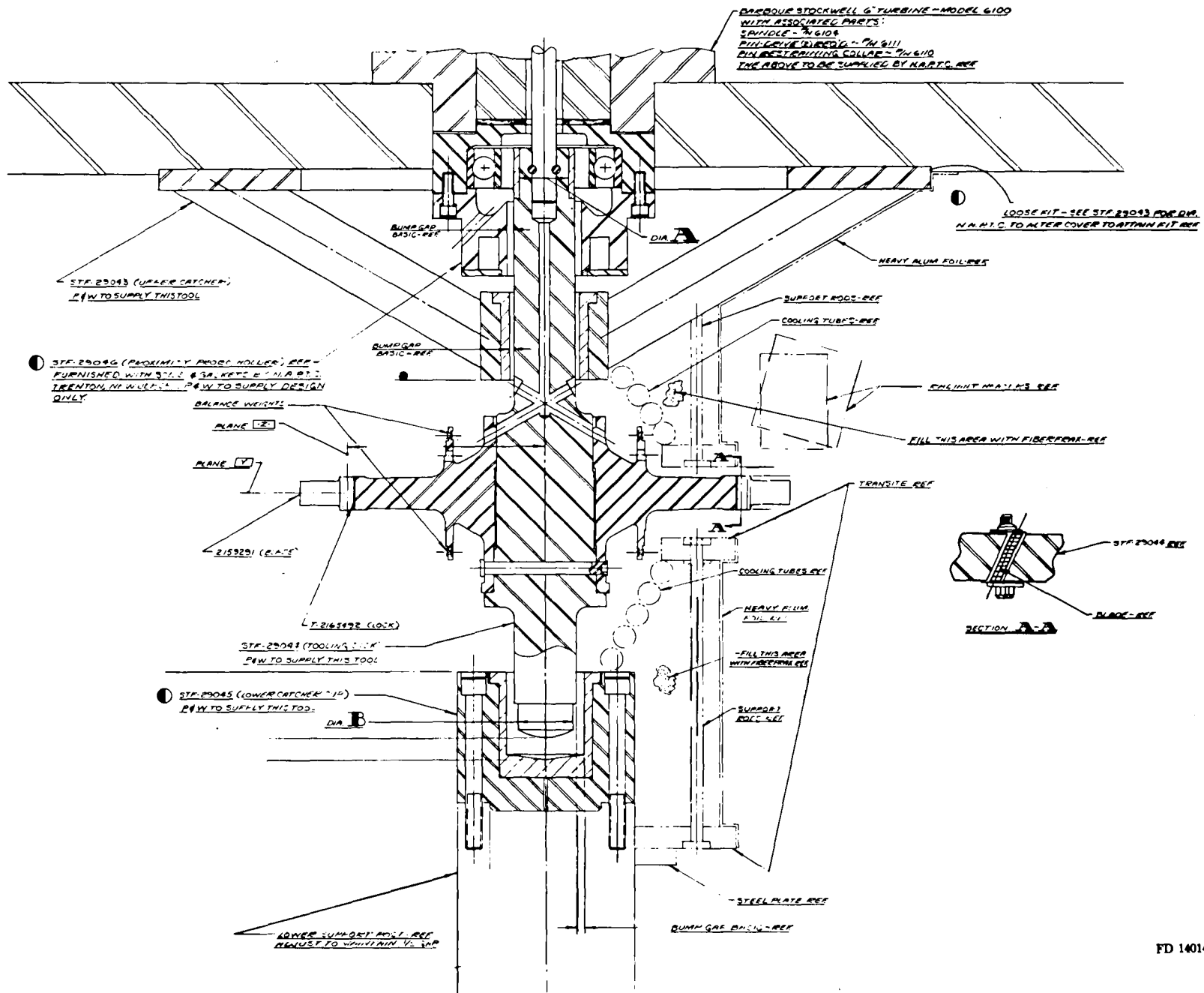
Figure 78. Spin Test Hardware

83

FD 140148
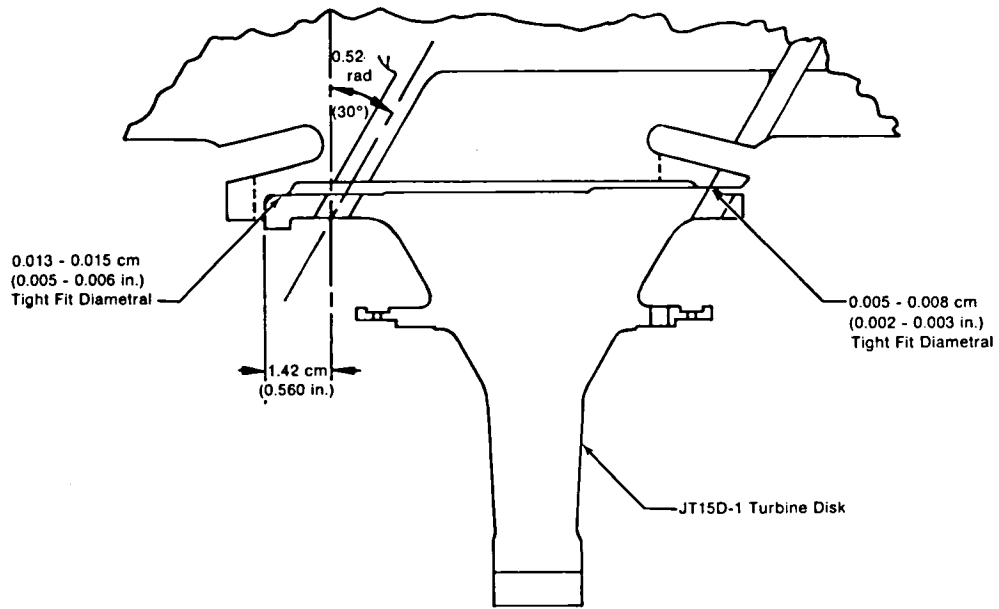
Figure 79. Spin Test Disk Configuration
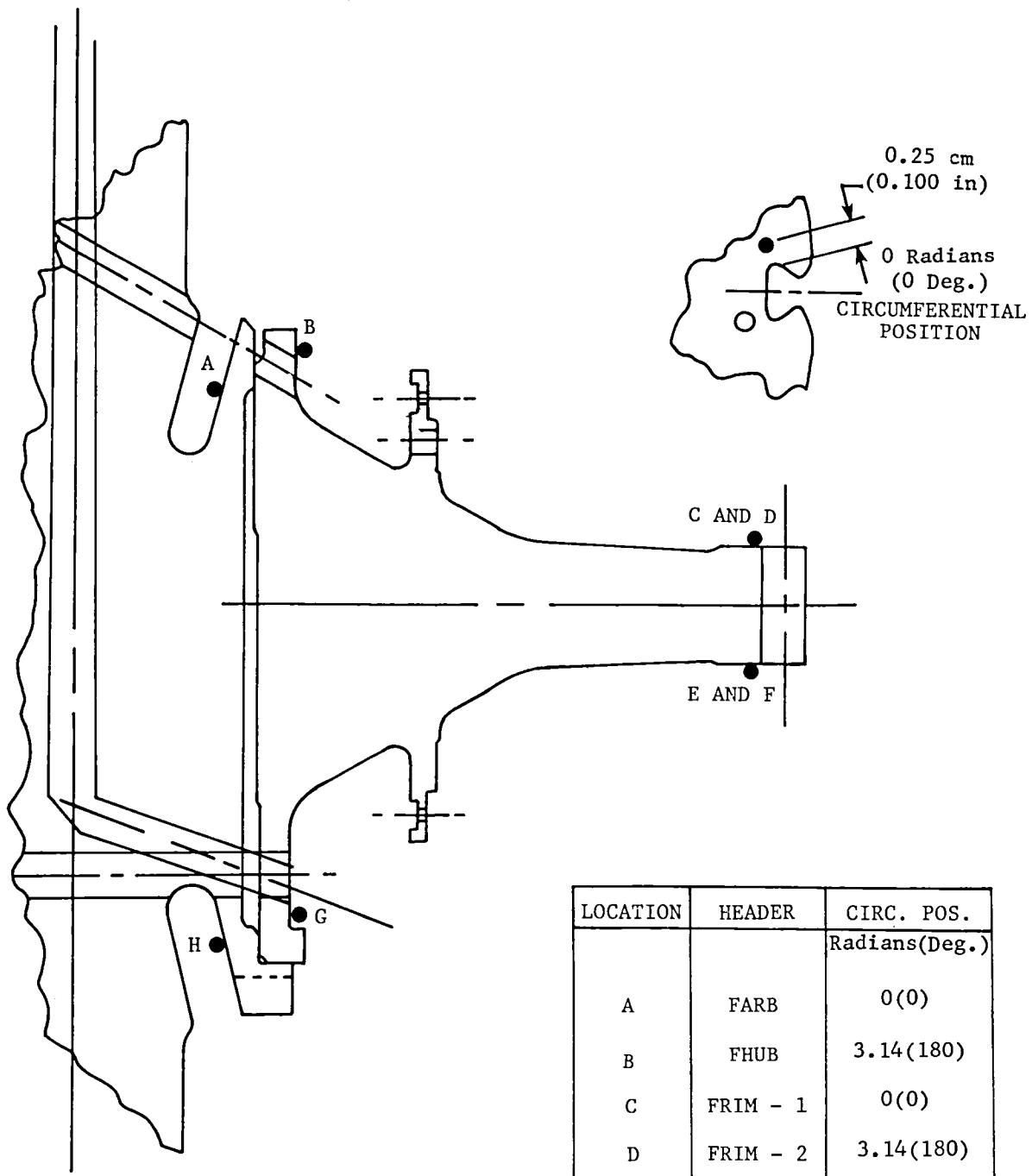
LOCATION	HEADER	CIRC. POS.
		Radians(Deg.)
A	FARB	0(0)
B	FHUB	3.14(180)
C	FRIM - 1	0(0)
D	FRIM - 2	3.14(180)
E	RRIM - 1	0(0)
F	RRIM - 2	3.14(180)
G	RARB	0(0)
H	RHUB	3.14(180)

Figure 80. Spin Test Disk Thermocouple Locations

These locations were chosen to monitor the relative thermal growth at the two snap fits to ensure that the control diameters remained tight. The live rim temperature was the primary test parameter to be set during spin test. A photograph of the rotating assembly (minus blades) is shown in Figure 81.
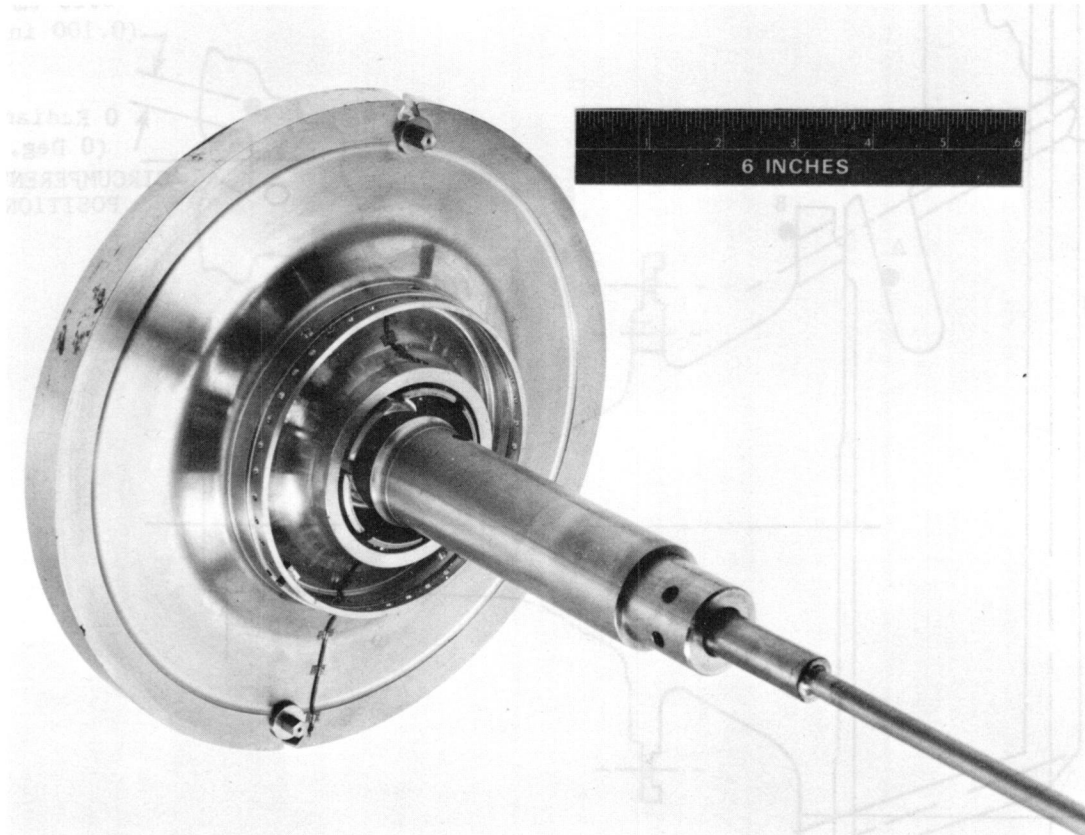
Figure 81. Spin Test Hardware

FE 153444

Three types of rig problems were encountered during shakedown testing. These were (1) lamp placement, (2) blade temperature measurement, and (3) disk cracking. Rig shakedown problems and solutions are described in detail in the following paragraphs.

The main purpose of the quartz radiation lamps was to heat the blade while a water cooled radiation heat sink maintained disk temperatures. The first lamp placement arrangement used at NAPC consisted of four lamps equally spaced around the disk periphery and aimed toward the disk center. However, this arrangement provided too much heat to the disk, and was abandoned in favor of a six-lamp arrangement. In this arrangement, the lamps were positioned so that the primary direction of radiation was in the axial direction relative to the blade, as shown in Figure 82. Three lamps were placed on each side of the ceramic blades, and the top lamps were located between the lower lamps, as shown in Figure 83. This arrangement resulted in maximum blade heating with the least disk heating. The alternate spacing between the upper and lower banks provided a relatively even heat source for the rotating blades.
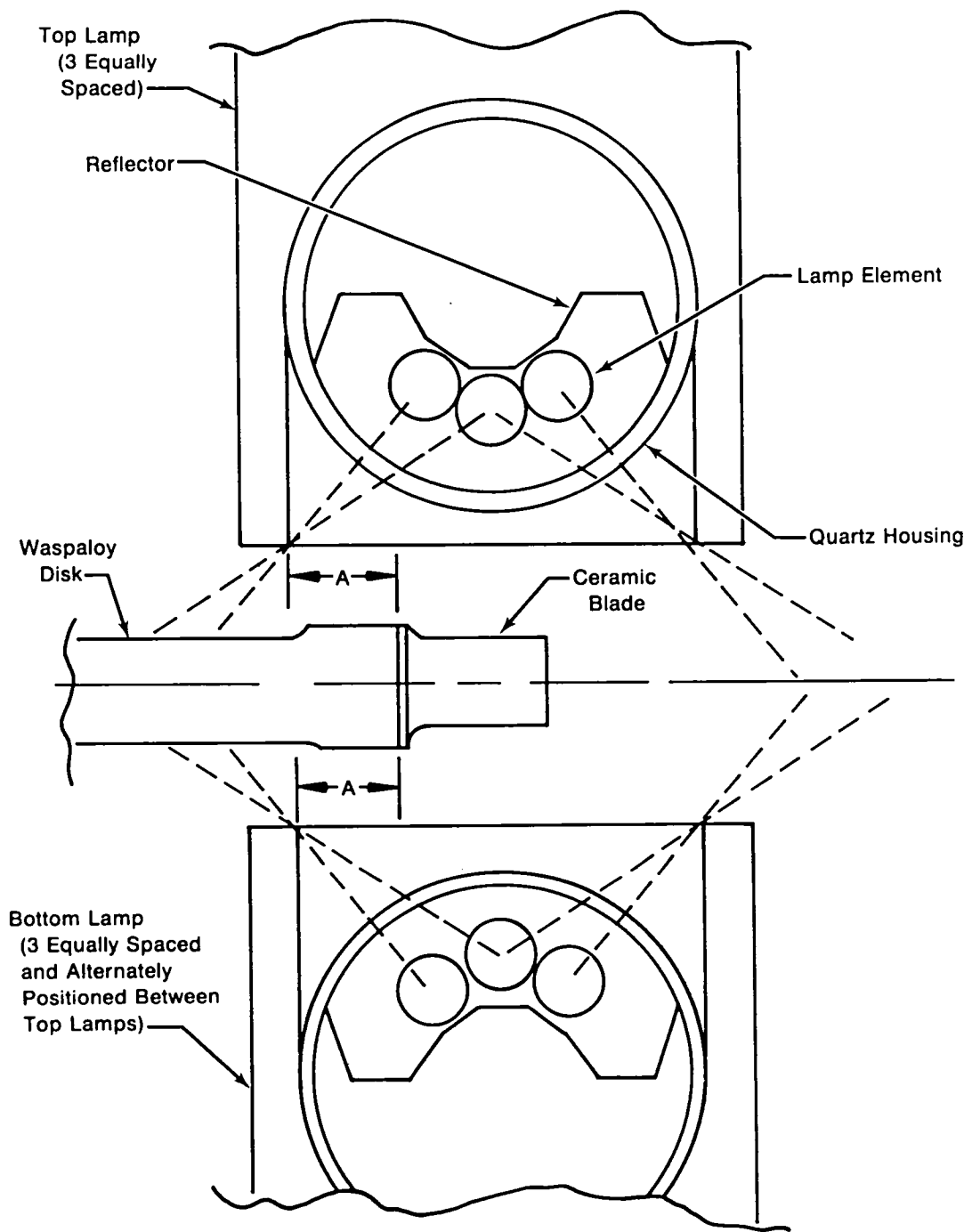
Figure 82. Six Lamp Heater Arrangement

FD 139349

Typical Lower
Heater Assembly

Test Blade

Lamp Aperture

Upper Heater
Assembly

Rotation

Disk Rim
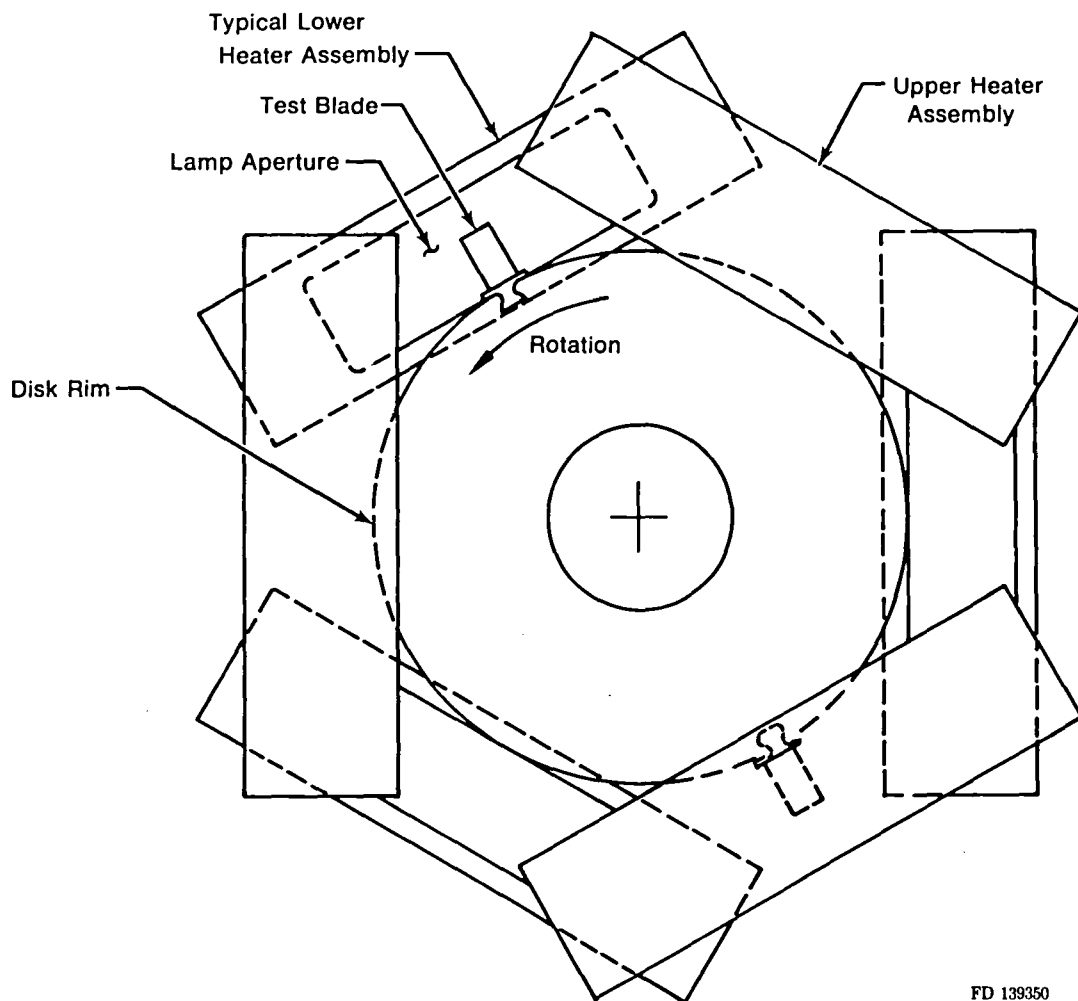
FD 139350

Figure 83. Six Lamp Heater Spacing

Optical pyrometers were originally planned to be used for blade temperature measurement. To use the pyrometer for measuring ceramic blade temperatures, the emissivity of the ceramic material must be known. Because emissivity data was not readily available for Norton NC 132 material it was necessary to measure emissivity experimentally. The emissivity was determined using an optical pyrometer that compared the emissivity of the ceramic blade with the emissivity of a standard graphite block. The ceramic blade and the graphite block were placed in a furnace with a quartz viewing window. The pyrometer, positioned outside the furnace, was then alternately focused on the blade and graphite block. The calibration was conducted over a range of temperatures from 870 to 1180°C (1600 to 2150°F). Figure 84 presents the ceramic blade emissivity versus temperature data.

Initial attempts to measure blade temperature by optical pyrometry were unsuccessful. The data clearly showed that the pyrometer was subjected to large amounts of radiation in addition to the blade radiation. The additional energy came from some light emitted by the lamps directly into the pyrometer, plus significant reflected energy from the blades and disk rim. Attempts to shut off the lamps at the time of temperature measurement proved unsuccessful because the power decay lasted for approximately 5 seconds, allowing the blade to cool down considerably. A static test was then conducted on a static blade with the pyrometer focused at the airfoil root as shown in Figure 85. The lamp power was brought up until the pyrometer indicated a temperature of 730°C (1340°F). A thermocouple temporarily attached to the back side of the airfoil indicated a blade temperature of less than 150°C (300°F). This result showed conclusively that optical pyrometers could not be used for this program.

88
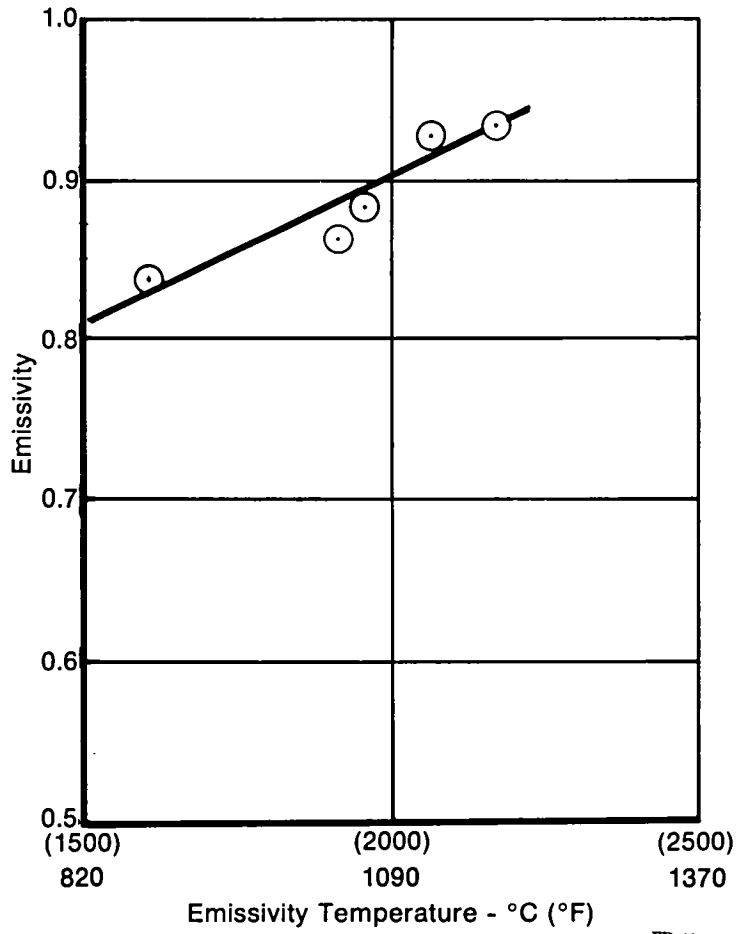
Figure 84. NC 132 Emissivity
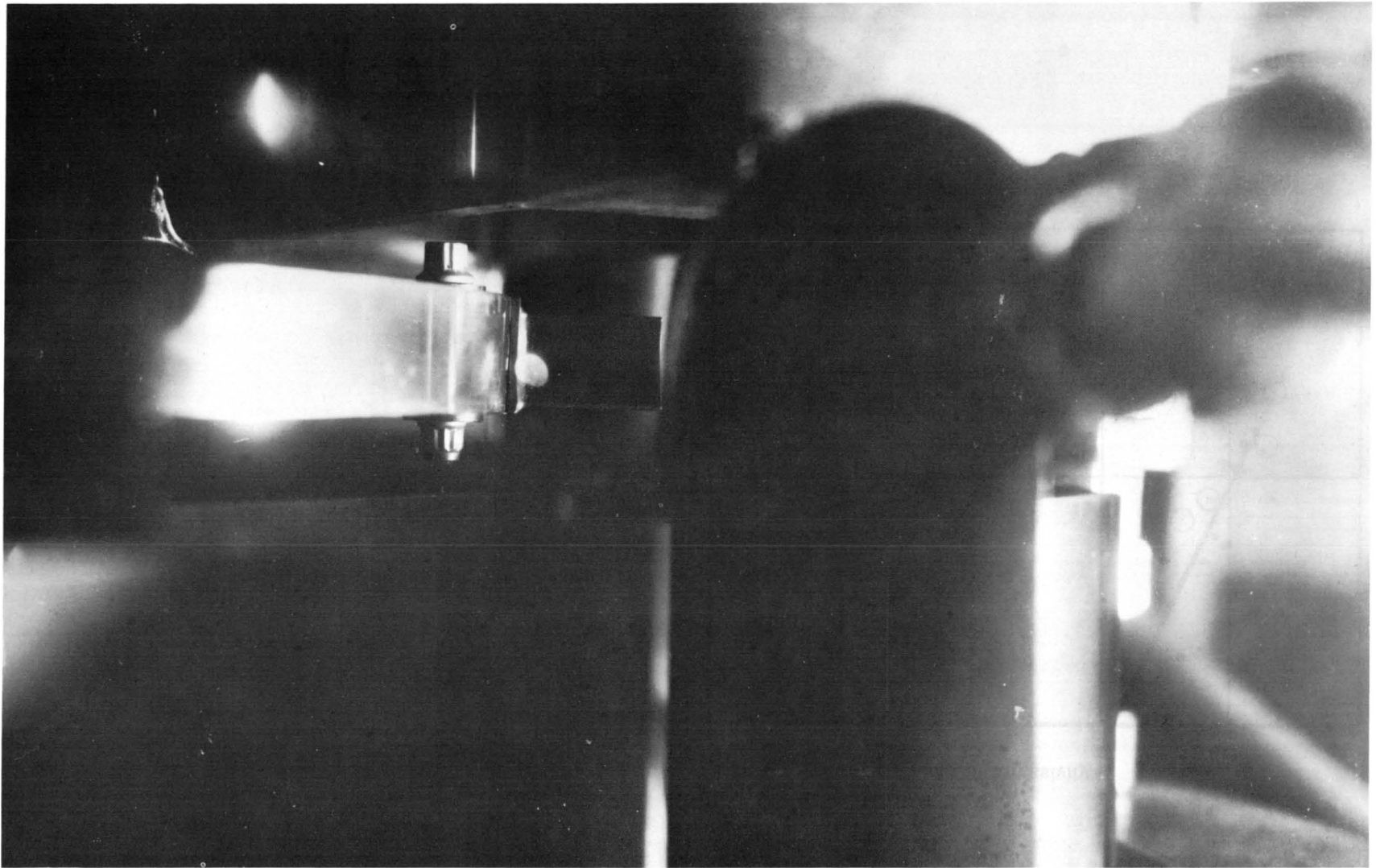
Figure 85. Pyrometer Focused on Airfoil Root

In lieu of pyrometers, thermocouples were attached to a pair of workhorse blades and blade temperatures were calibrated as a function of lamp power setting. The workhorse blades were slotted and instrumented with thermocouples as shown in Figure 86. The results from this type of testing are presented in Figure 87. The significance of the temperatures shown in this figure is that the disk live rim target temperature was reached before the design blade root temperature was obtained. One approach to solving this problem would be to use more elaborate shielding over the disk, and possibly resort to some type of disk cooling augmentation. In this program, it was concluded that additional fixes were too extensive for the scope of the program, and that meaningful spin testing could be accomplished at the reduced temperature gradient in the attachment. The net effect would have been a reduction in the ratio of test stress to mean flexure strength from 0.57 (design) to 0.55 (reduced airfoil temperature).
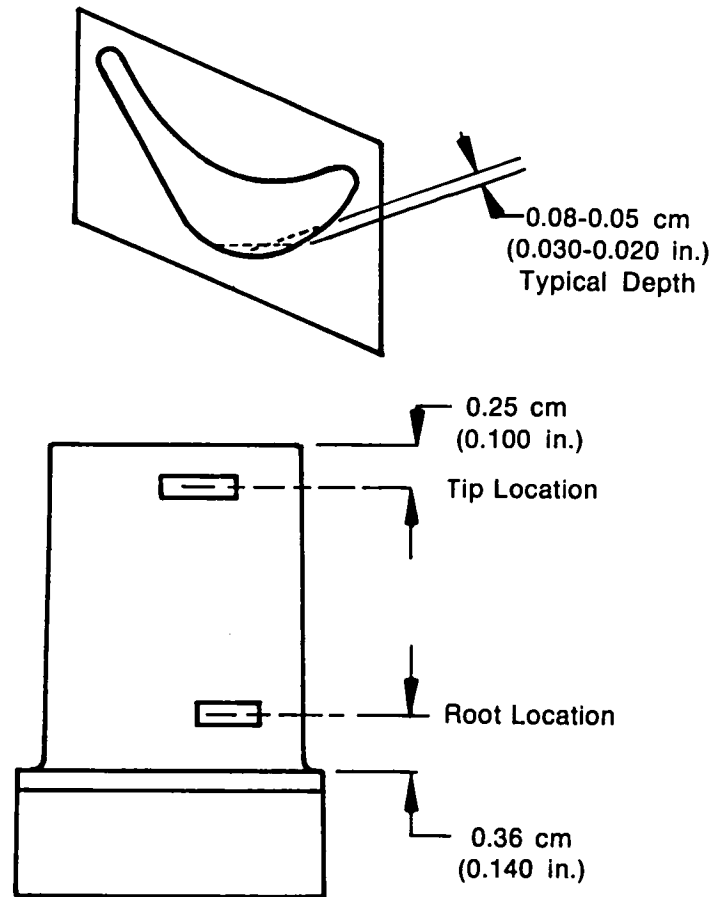
FD 152133

Figure 86. Thermocouple Location for Calibration Blades

91
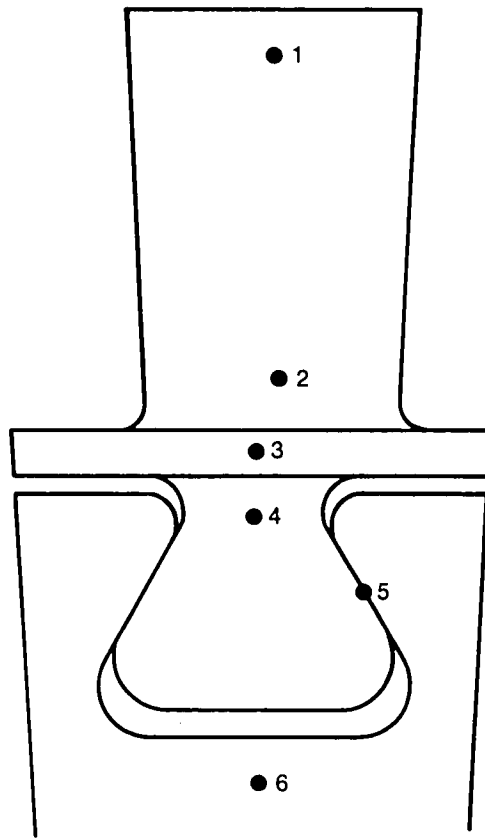
Location	Design Temperature		Test Temperature	
	°F	°C	°F	°C
1	2183	1200	1325	720
2	1925	1050	1306	710
3	1767	960	(1280)*	690
4	1650	900	(1260)	680
5	1570	850	(1240)	670
6	1150	620	1150	620

*( )Indicates Value Interpolated from Measured Data

FD 140146

Figure 87. Test Temperature

The third problem encountered in the shakedown tests concerned the bolted blade disk retention. Early checkout runs showed distress in the bolt shank, and the bolt material was changed from A286 to Waspaloy and the bolt size increased from 0.35 cm (0.138 in.) to 0.48 cm (0.190 in.). However, this required a corresponding enlargement of the hole through the disk, with the result that the next check run showed disk distress at the bolt hole. The solution to this problem was to redesign the blade retention to eliminate the bolt. The resulting redesign consisted of a 0.025 cm (0.010 in.) thick Inconel 625 locking tab inserted under the compliant layer and bent radially outward. This tab is shown in Figure 88, and the hardware is shown in Figure 89. One end of the tab is preformed, and the second tab is bent at assembly. In the running configuration, the bent tabs cover both the blade and a portion of the disk lug. Retention design modification included a photoelastic analysis to determine the additional stress imposed at the neck of the blade attachment from the centrifugal load of the compliant layer and tab lock against the base of the blade dovetail. The existing model was reused and the original design load setup was duplicated. The additional force, calculated to be 25% of combined blade, platform and neck pull, was applied to the base of the blade dovetail. Results showed a 4% increase in tensile stress at the edges of the attachment neck, which was judged to be acceptable.
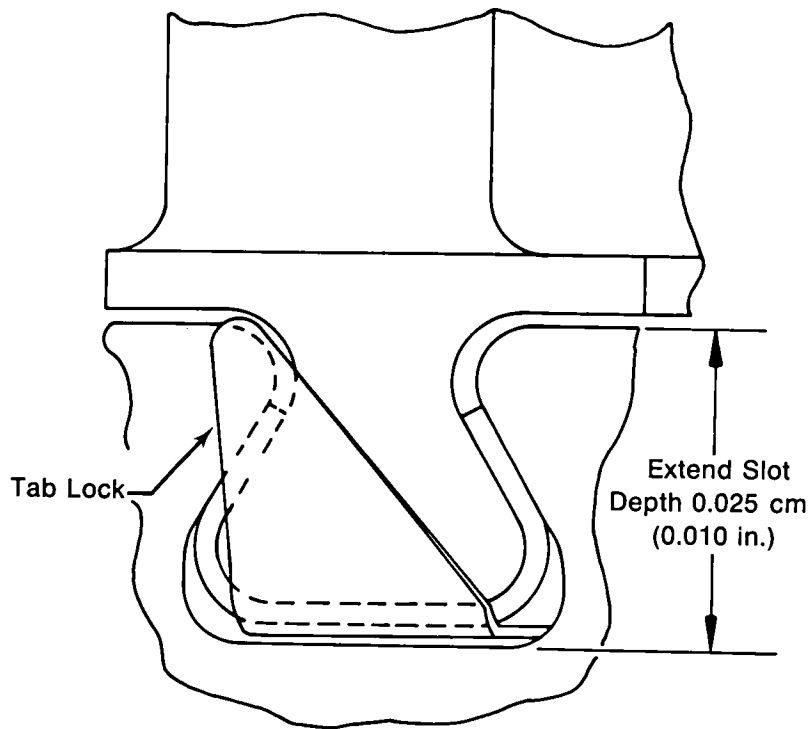
FD 140147

Figure 88. Revised Blade Retention Design

93
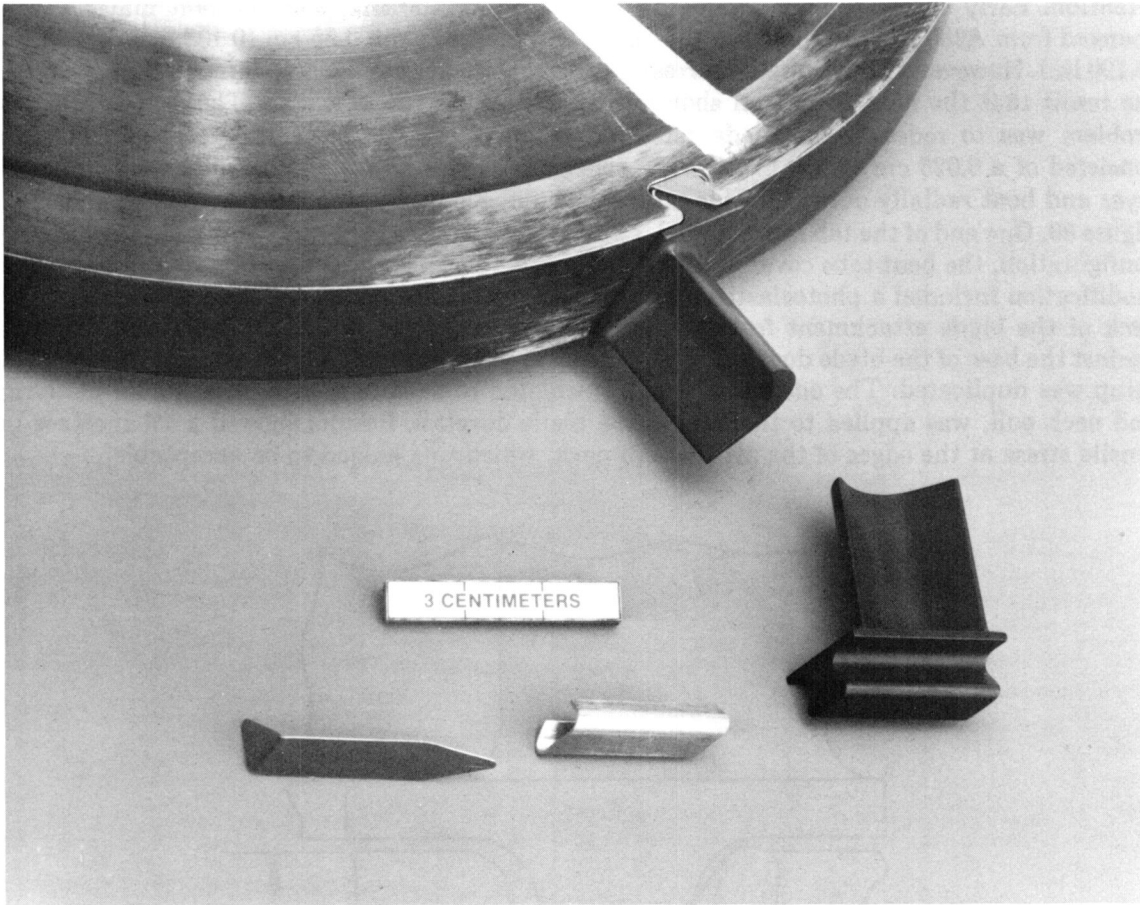
Figure 89. Revised Blade Retention Hardware

CONCLUSIONS AND RECOMMENDATIONS

1. It appears feasible to design ceramic blade-metal disk attachments that have acceptable design characteristics in terms of predicted stresses and life, using existing material properties, design techniques, and NDE methods.

2. For the airfoil contour studied, a skewed dovetail attachment gave lower peak stresses than either a straight axial dovetail or curved dovetail.

3. Conventional deterministic design criteria was used to arrive at an acceptable general attachment configuration. Detailed life predictions, however, should be based on fracture mechanics data (primarily steady crack growth and critical stress intensity) and NDE capability. Moreover, ceramic parts for gas turbine service should also be analyzed by probabilistic techniques, in which the probability of failure of the part would be calculated by integrating the probability of failure for each element over the entire volume.

4. This program generated fracture mechanics and NDE data that can be usefully applied in other programs involving the use of NC 132 hot pressed silicon nitride.

5. The ceramic blade fabrication experience showed that close tolerance designs can be manufactured with existing diamond-grinding techniques.

6. Platinum sheet was the best interlayer material evaluated. Results show, however, that less expensive materials have the potential to provide acceptable cushioning characteristics through geometry features, such as perforations in a sheet material.

The following additional efforts are recommended:

A. The planned hot spin tests should be conducted to prove the capability of the design to achieve the 50-hr, 100-cycle goal.

B. Destructive spin tests shold be conducted to calibrate the design system. This would require the design and fabrication of spin test tooling capable of higher rotational speeds than the engine disk used in this program.

C. A compliant interlayer development program should be undertaken to exploit the full potential of perforated sheet metal in alloys less expensive than platinum.

APPENDIX A

FRACTURE MECHANICS DATA ANALYSIS

DATA ANALYSIS PROCEDURES

The data from each constant displacement test is of a load vs time decaying exponential form, which is plotted on a log-log graph and a best-fit linear relationship taken to determine crack propagation rate vs stress intensity factor. Using the above data along with that obtained from constant load tests, an average crack growth rate vs stress intensity factor curve is determined. Two equations form the basis for da/dt data analysis (Reference 2):

$$K_I = PW_m \left[\frac{3(1+V)}{Wtn^4} \right]^{\prime\prime}$$ (1)

where

K_I = stress intensity factor

P = total applied load

W_m = specimen moment arm

V = Poisson's ratio (taken as 0.273 for NC 132, based on sound velocity measurements, and $E = 46.0 \times 10^6$ psi).

W = specimen width

tn = specimen thickness

and,

$$(da/dt)_y = \frac{P_i a_i}{P^2}(dP/dt)_y$$ (2)

where

da/dt = crack propagation rate
P_i = initial test load
a_i = initial crack length
P = load at time, t.

Subscript "y" designates that equation (2) is valid only at a constant crosshead displacement.

The approach taken for analysis of constant crosshead displacement da/dt testing is summarized as follows:

1. Load and time data are taken from the strip chart and plotted on a log-log graph, with load along the Y-axis and time, t + 1, along the X-axis.

96

2. A best-fit line is drawn along the graph and the Y-intercept and slope are taken for use in the linear equation,

$$\text{Log } P = a + b \text{ Log } (t + 1), \tag{3}$$

where

a = Y-intercept
b = slope.

Equation (3) may be differentiated to give,

$$dP/dt = Pb/(t + 1) \tag{4}$$

and taking the antilog of Equation (3),

$$P = 10^{a+b \text{ Log } (t + 1)}. \tag{5}$$

Substituting Equations (4) and (5) into Equation (2) produces an equation relating crack growth rate to time,

$$da/dt = P_i a_i b/(t + 1)10^{a + b \text{ Log } (t + 1)}. \tag{6}$$

Using Equations (1) and (6) to determine K_I and da/dt, respectively, several points may be taken from the load, time plot and K_I and da/dt calculated for each time, t.

3. Data is then presented on the standard, log-log da/dt vs K_I plot and a best-fit linear relationship established.

APPENDIX B

**Results of Three-Dimensional Analysis;
Temperature Distributions at Design Conditions**

**Temperatures shown in °F only
See Figure 55 for Z plane locations**
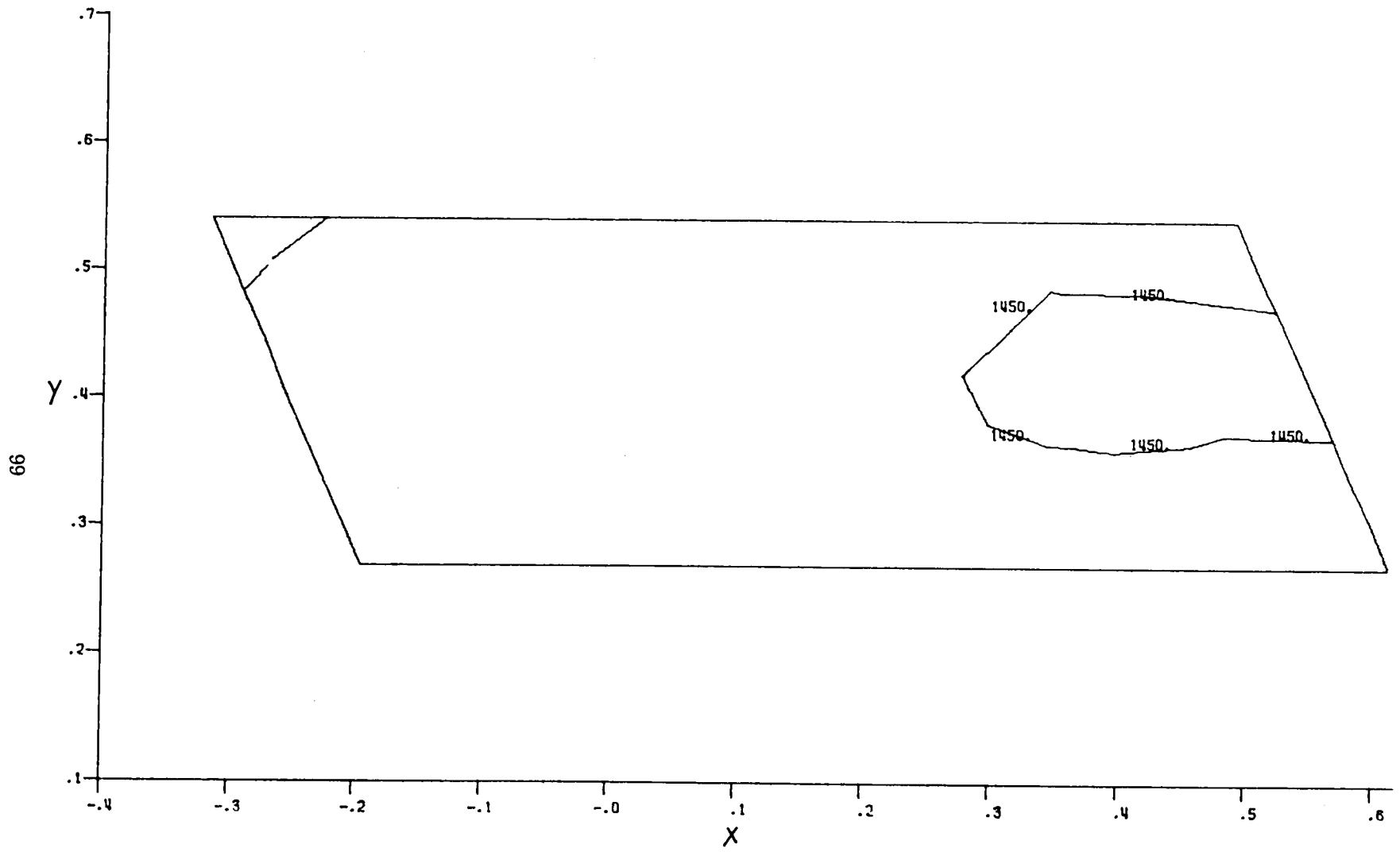
Figure B-1. Three-Dimensional Temperatures, Z = 0.0250 Plane
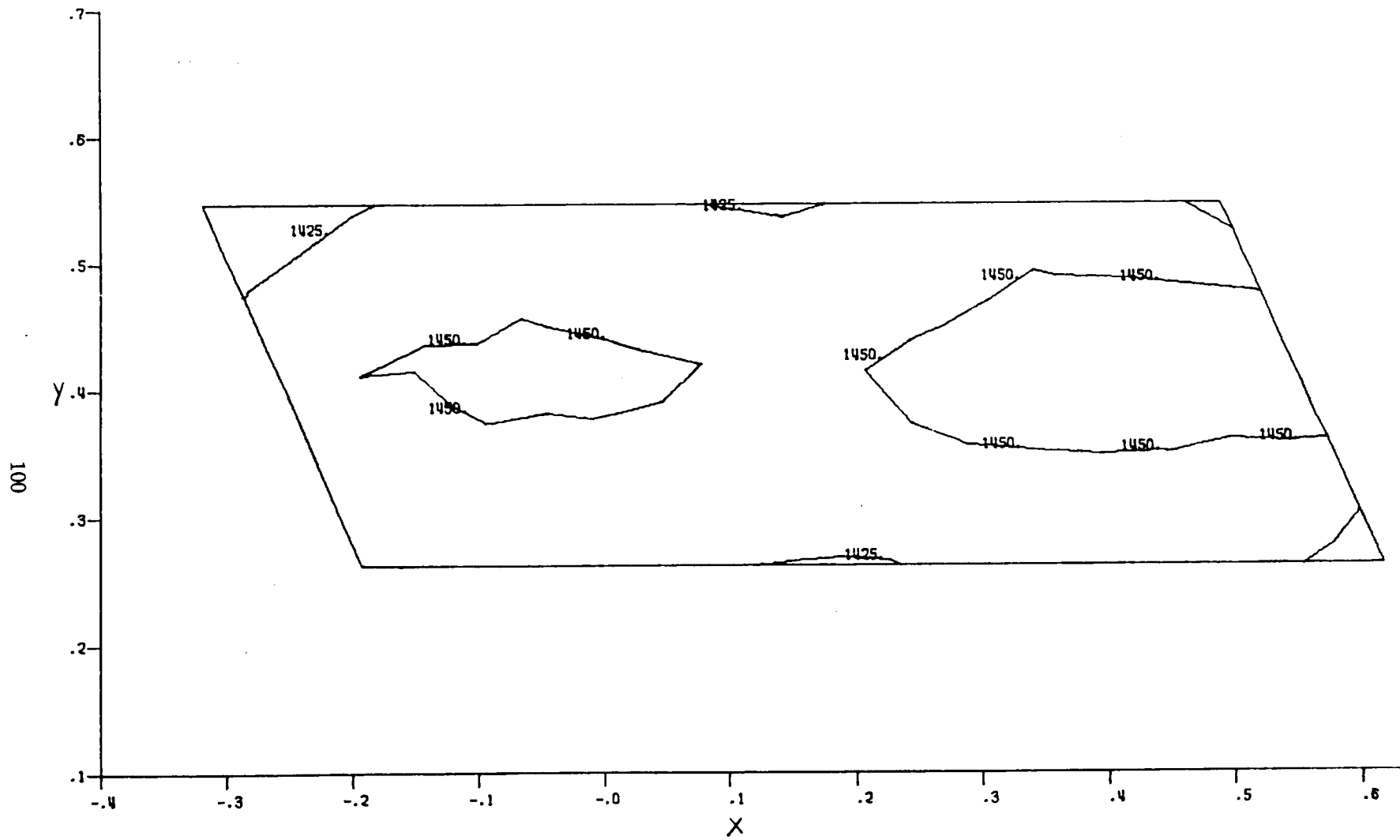
Figure B-2. Three-Dimensional Temperatures, Z = 0.0625 Plane
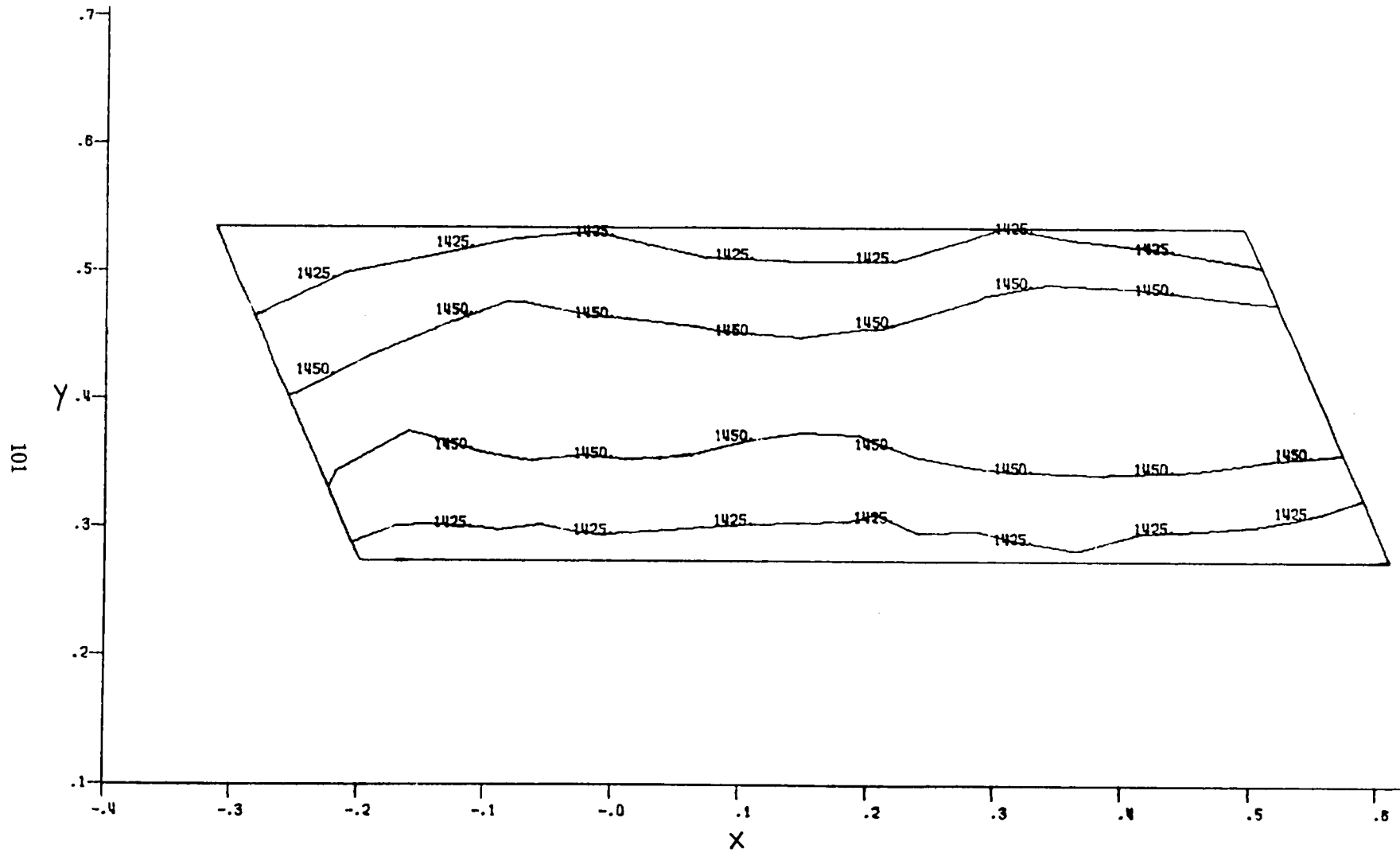
Figure B-3. Three-Dimensional Temperatures, Z = 0.0900 Plane
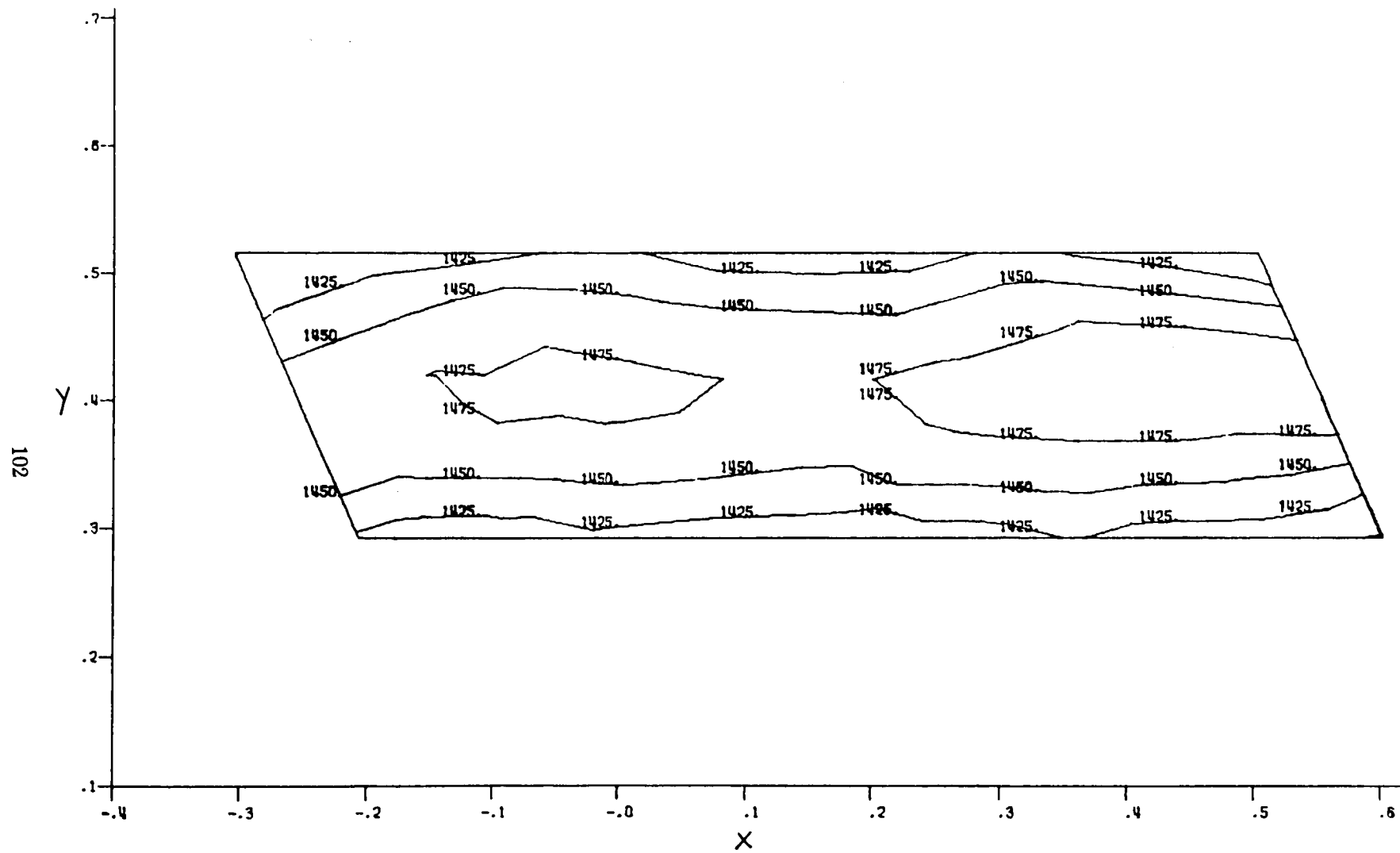
Figure B-4. Three-Dimensional Temperatures, Z = 0.1225 Plane
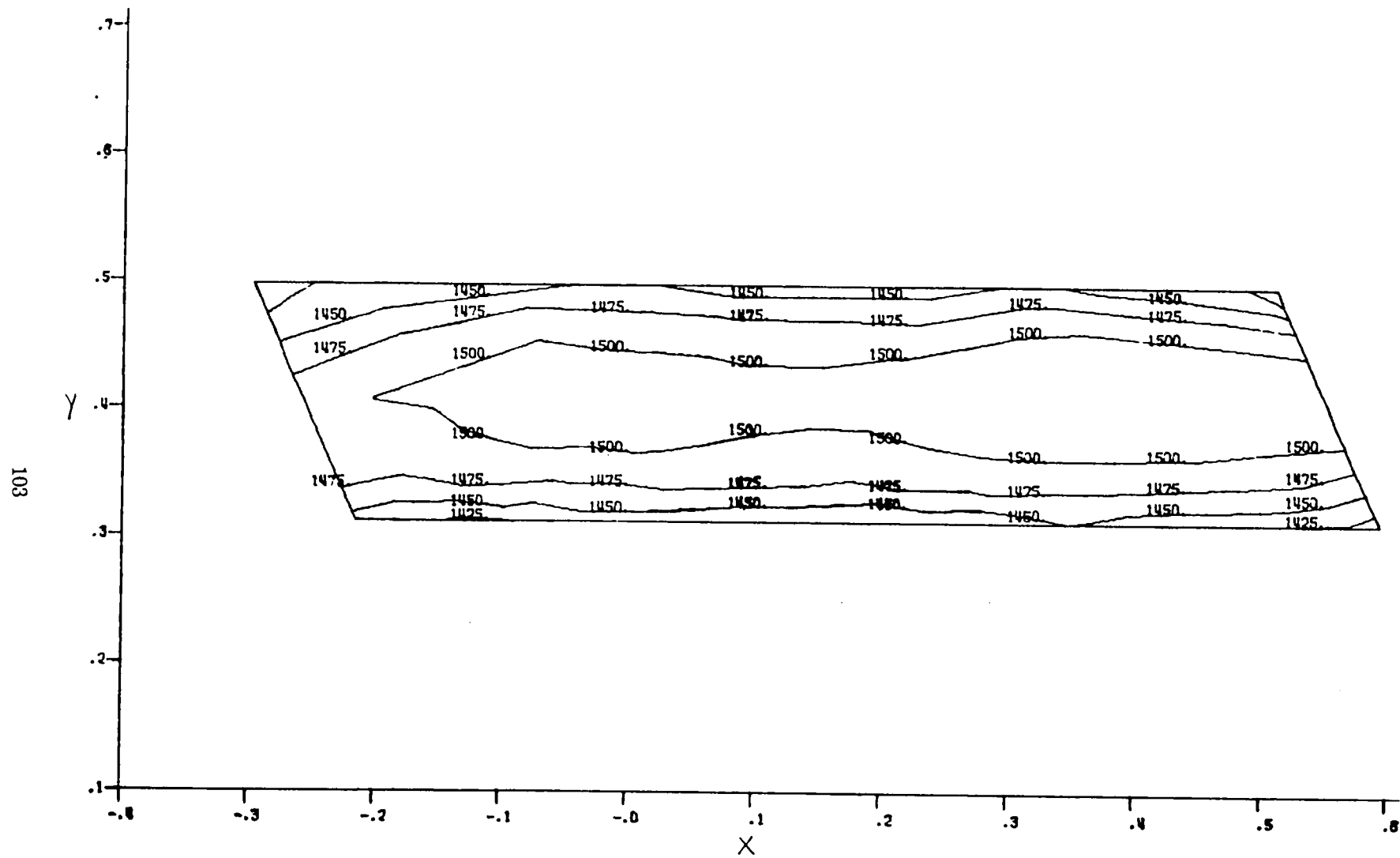
Figure B-5. Three-Dimensional Temperatures, Z = 0.1550 Plane

103
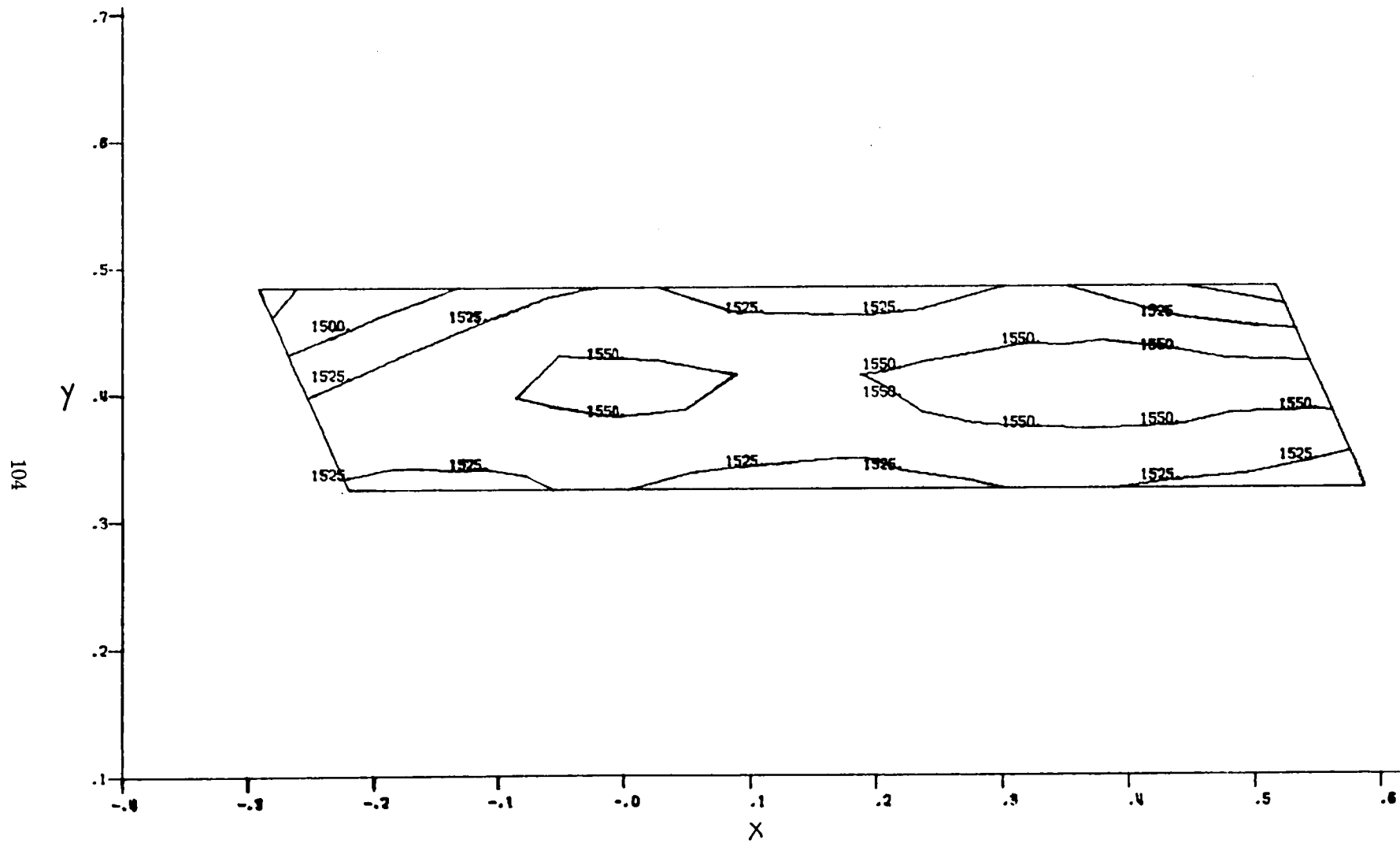
Figure B-6. Three-Dimensional Temperatures, Z = 0.1800 Plane
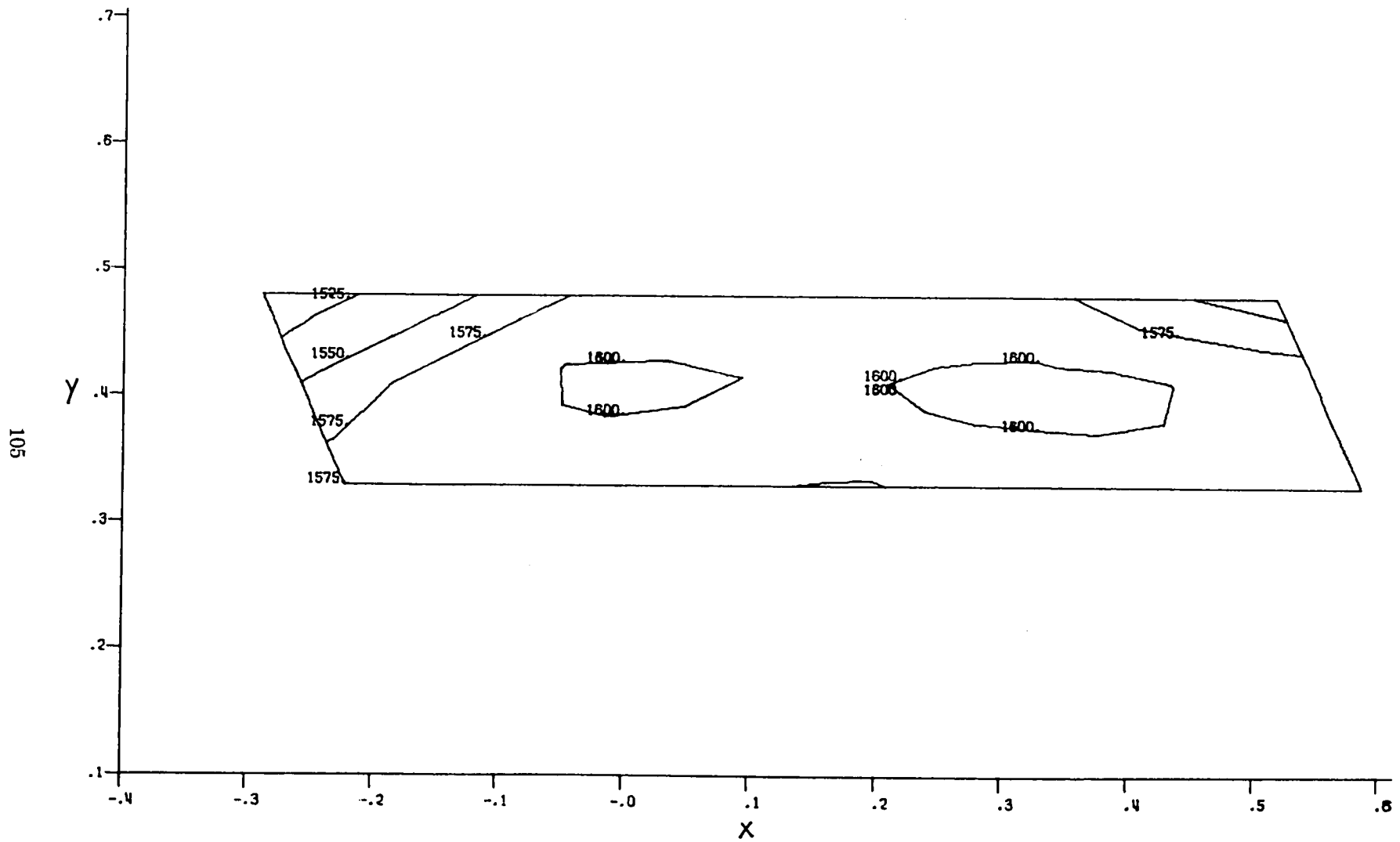
Figure B-7. Three-Dimensional Temperatures, Z = 0.2000 Plane
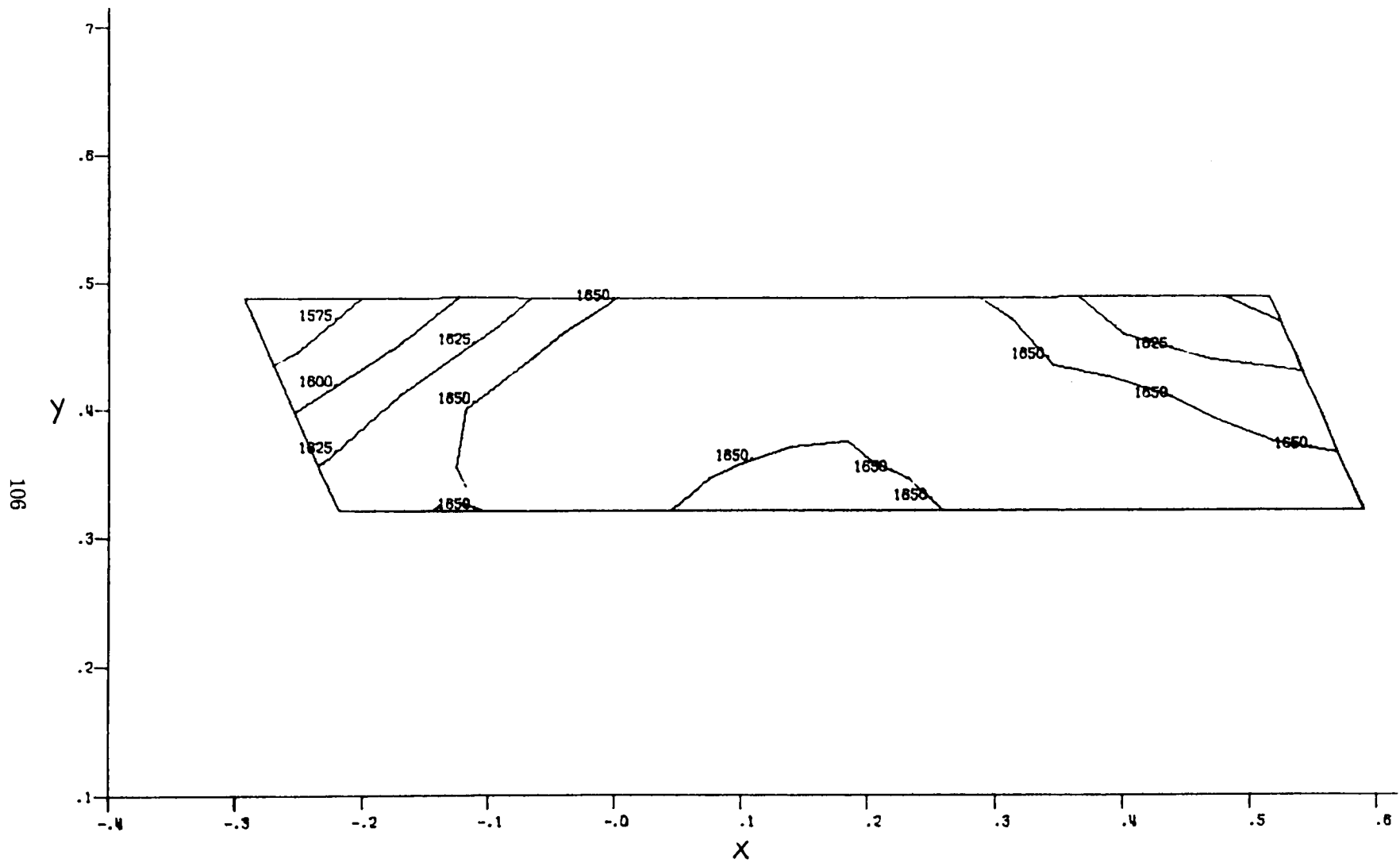
Figure B-8. Three-Dimensional Temperatures, $Z = 0.2250$ Plane
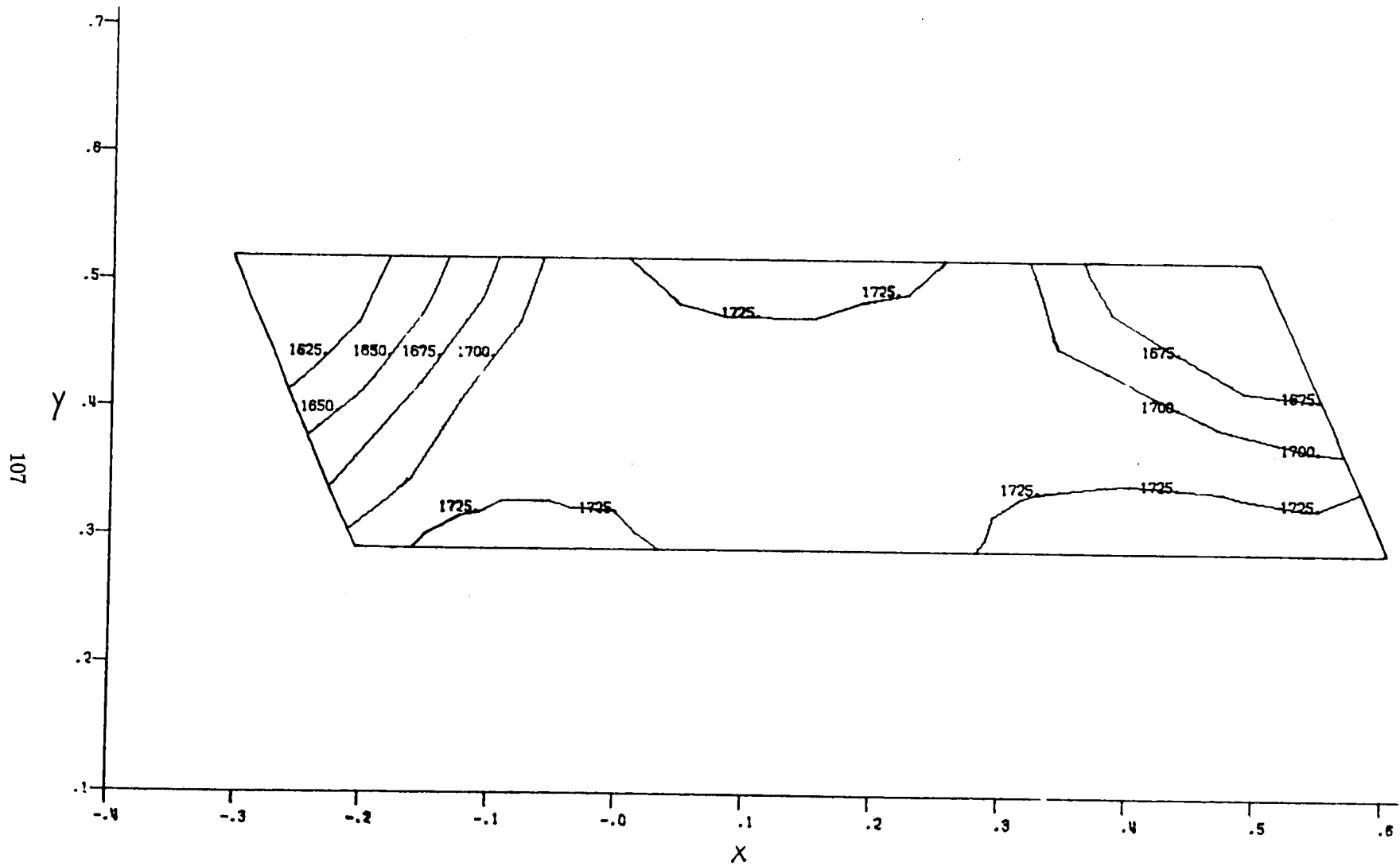
Figure B-9. Three-Dimensional Temperatures, Z = 0.2500 Plane
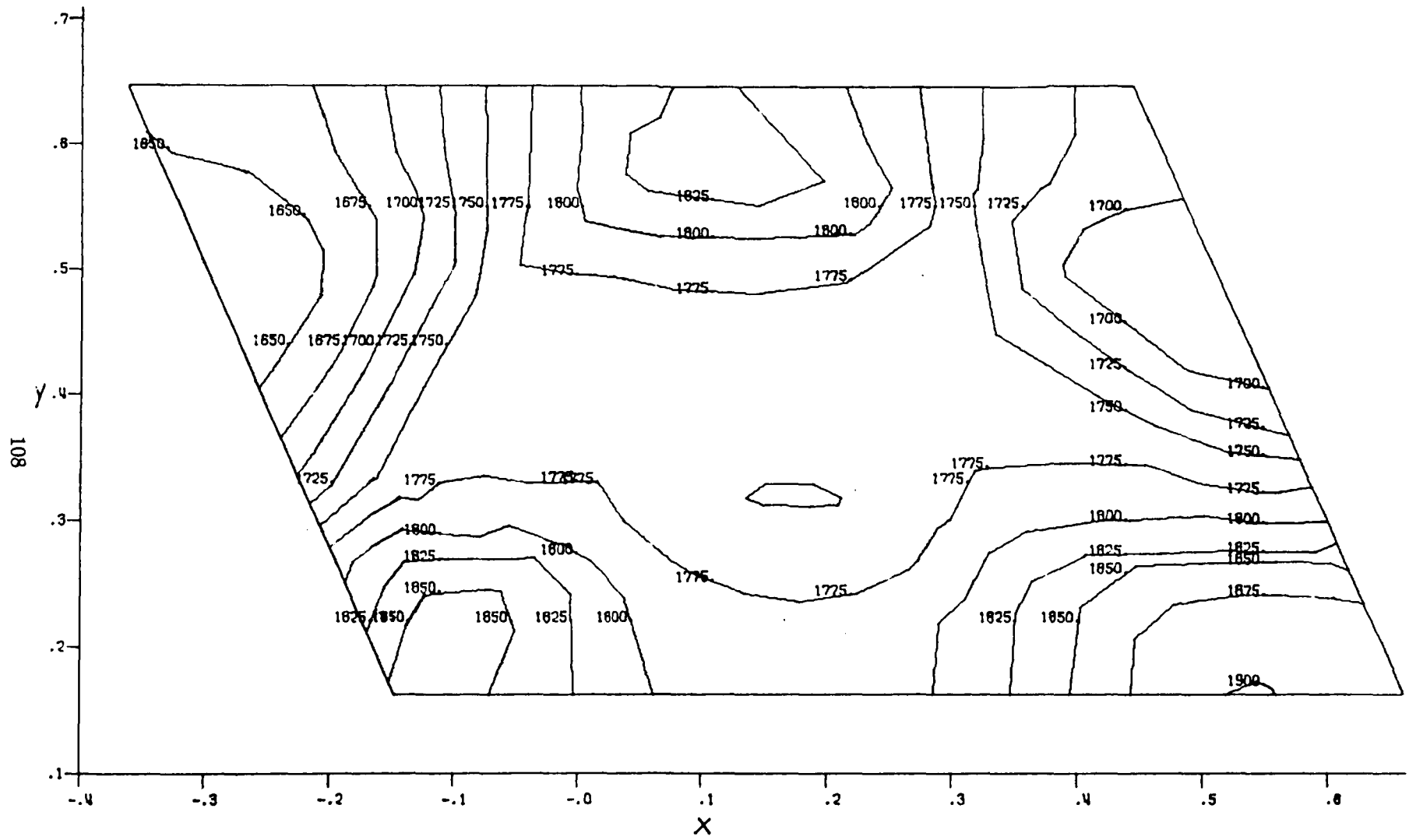
Figure B-10. Three-Dimensional Temperatures, Z = 0.2725 Plane
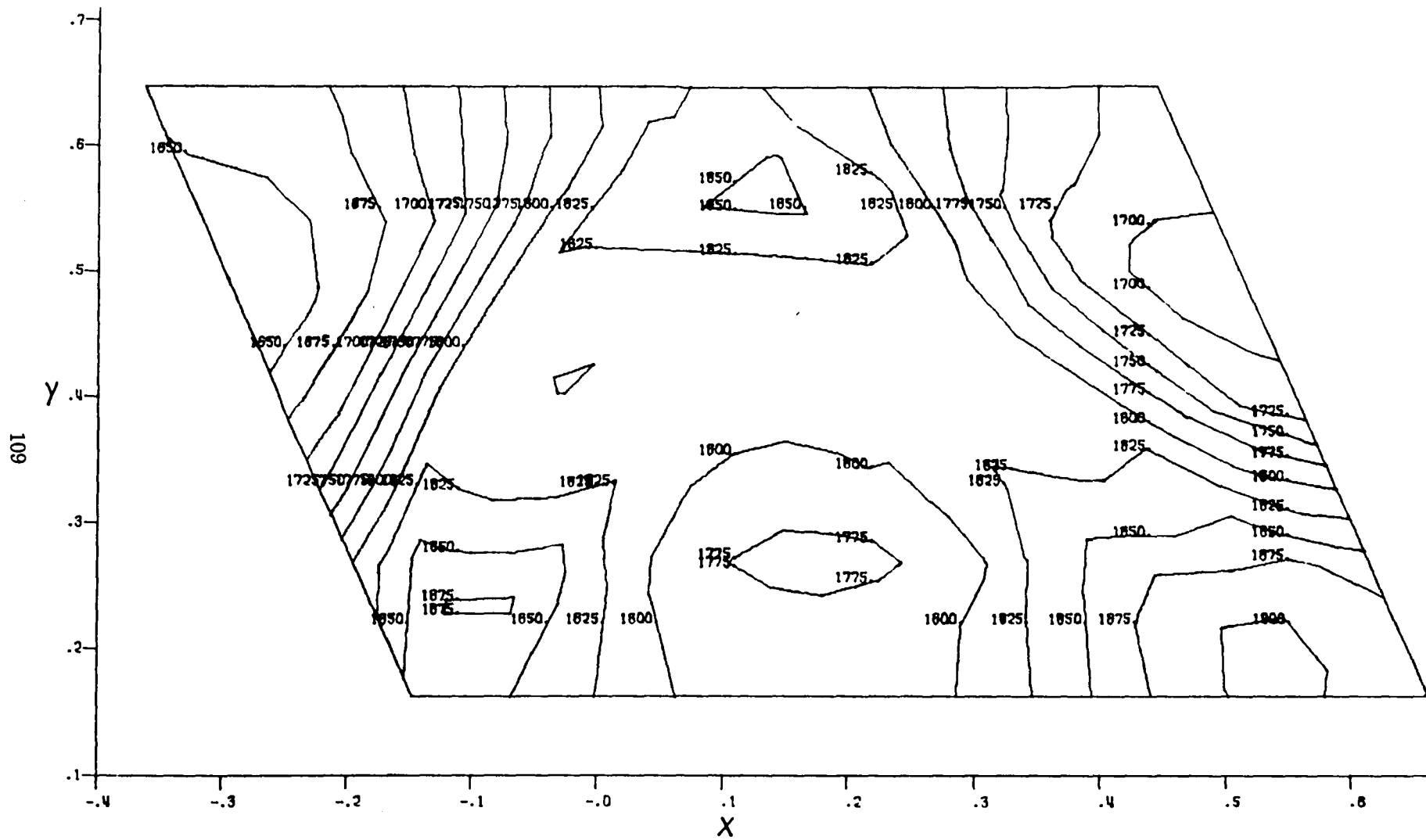
Figure B-11. Three-Dimensional Temperatures, Z = 0.2975 Plane
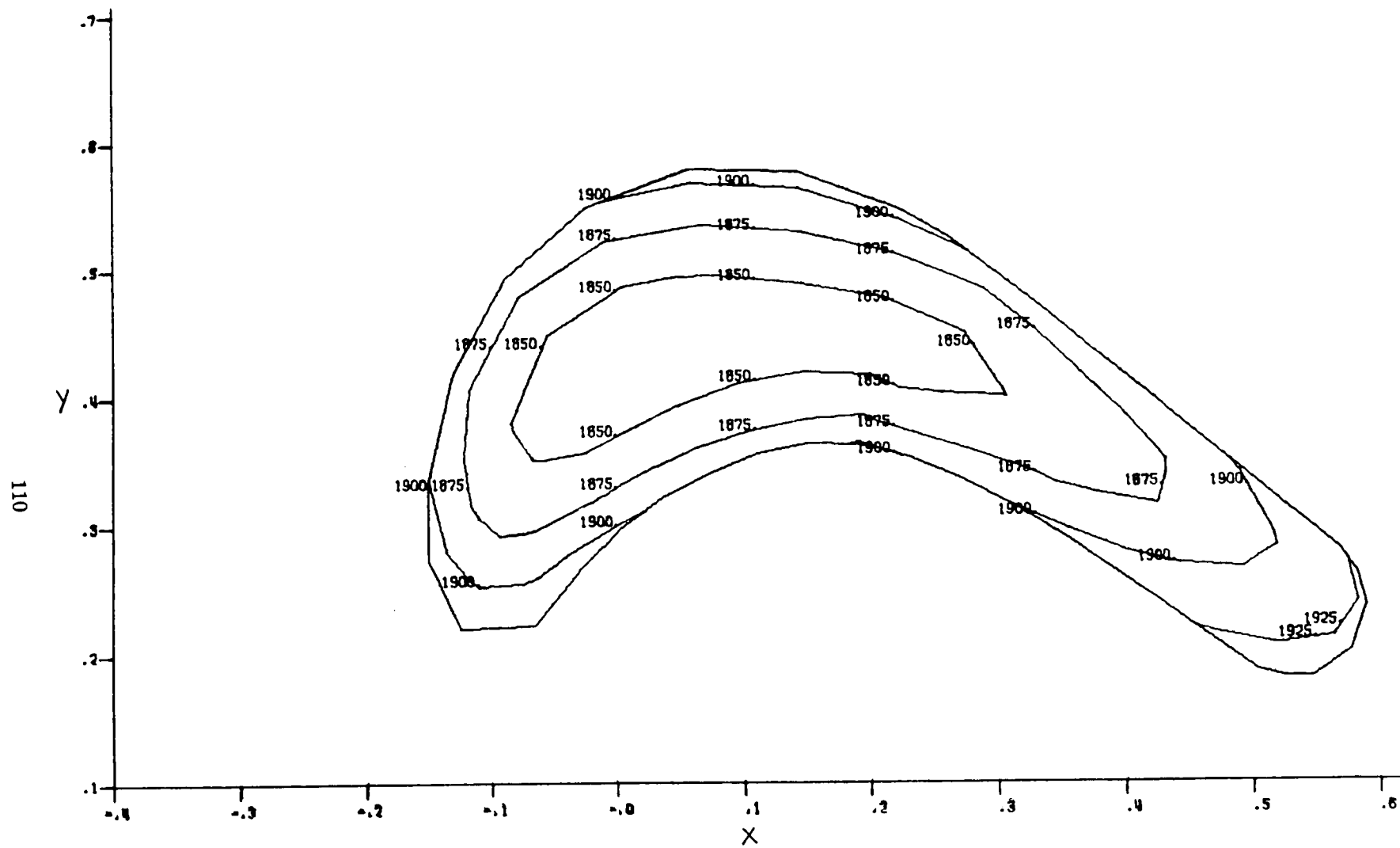
Figure B-12. Three-Dimensional Temperatures, Z = 0.3175 Plane
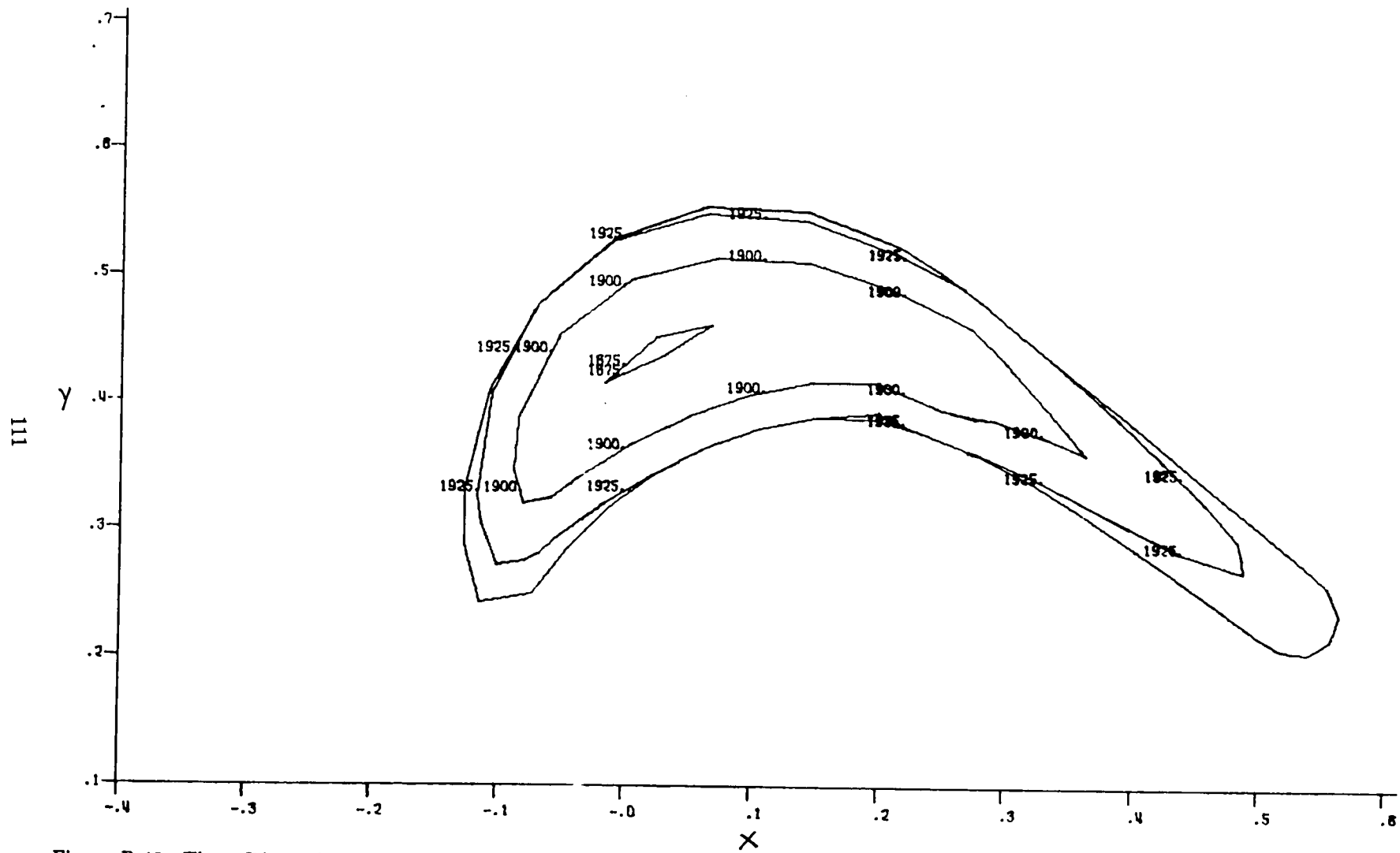
Figure B-13. Three-Dimensional Temperatures, Z = 0.3425 Plane
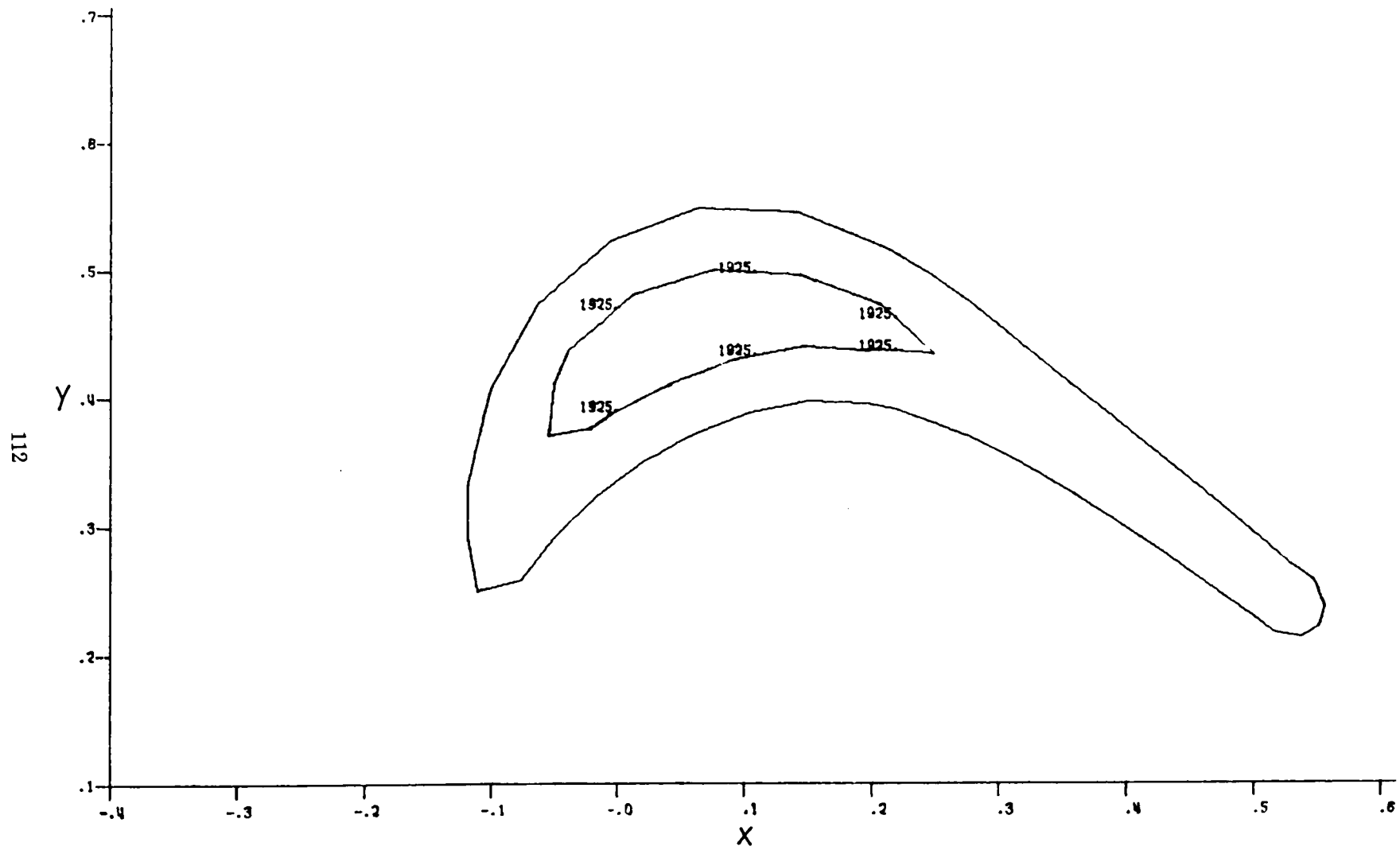
Figure B-14. Three-Dimensional Temperatures, Z = 0.3850 Plane

APPENDIX C

Results of Three-Dimensional Analysis;
Stress Distributions at 100% Design rpm

Stresses shown as ksi only
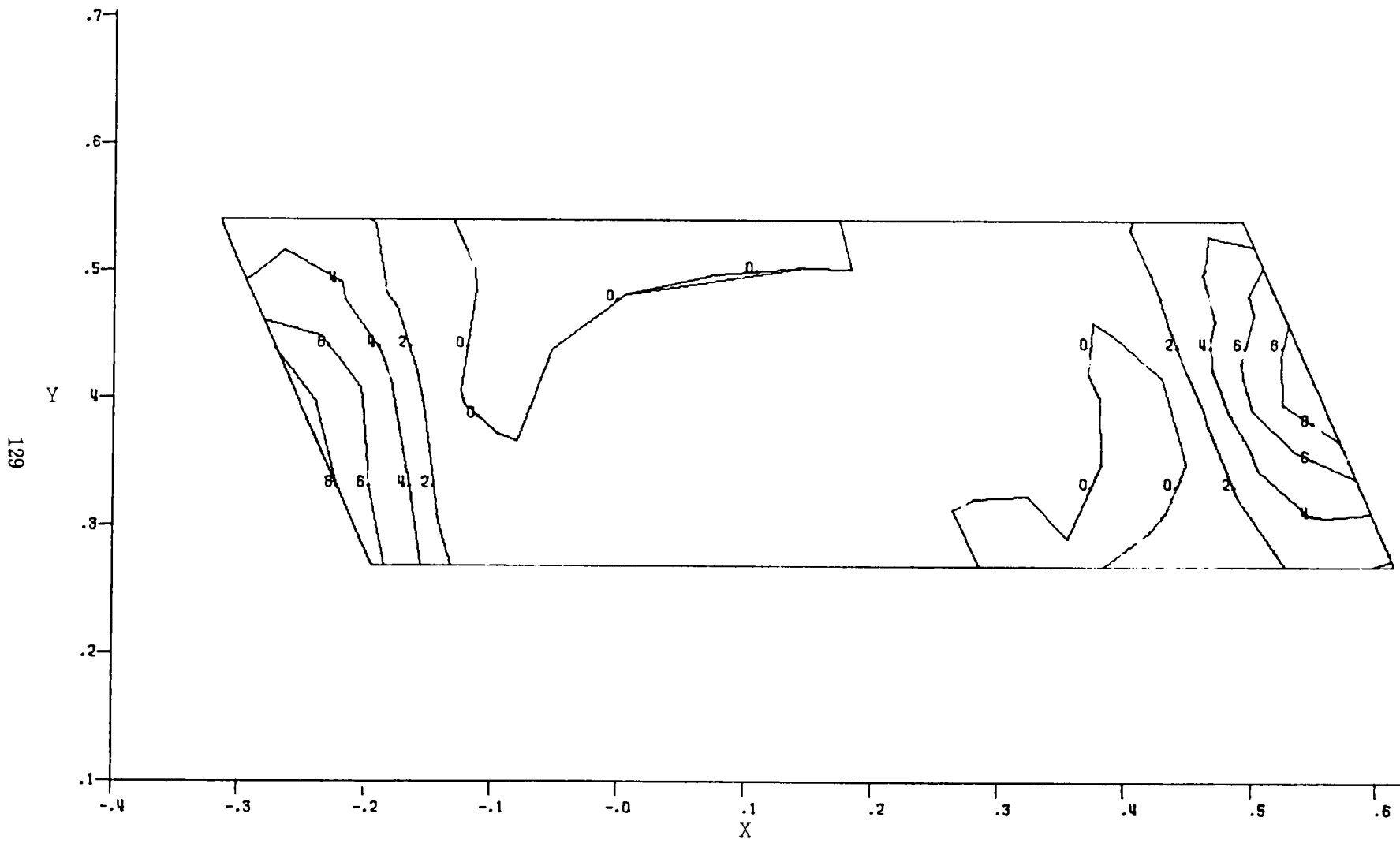### See Figure 55 for Z plane locations
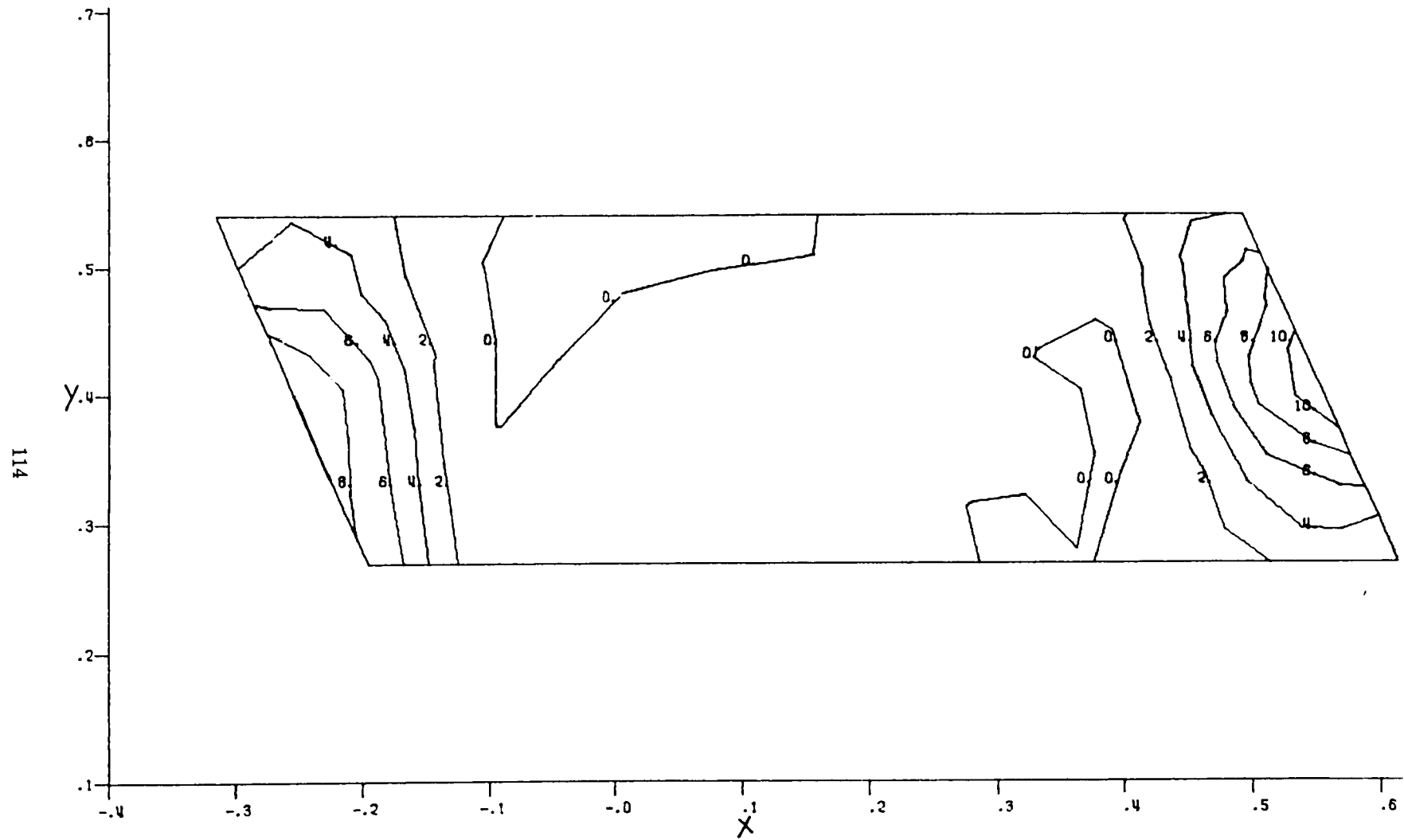
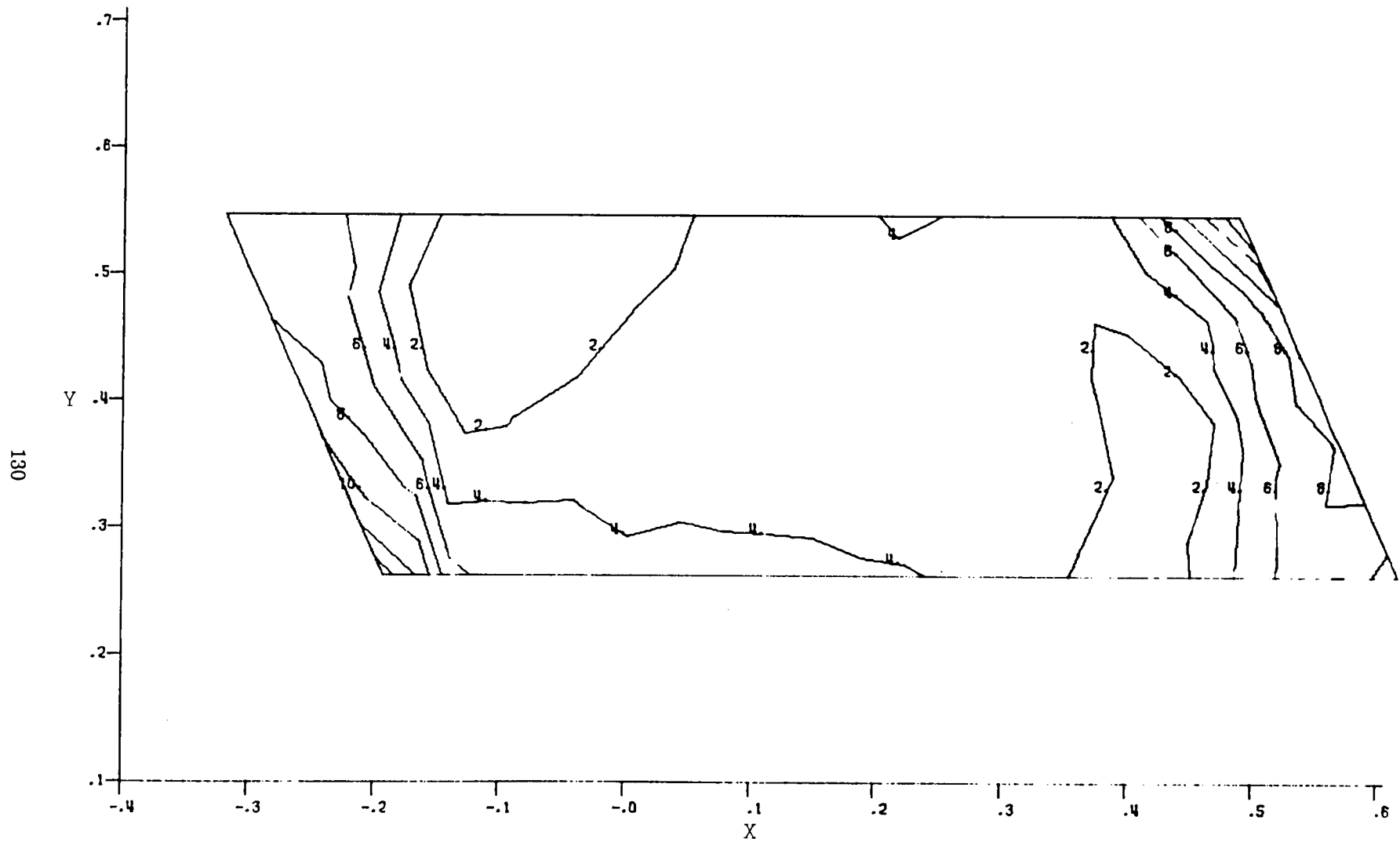Figure C-1. Three-Dimensional Tensile Principal Stresses, Z = 0.0250, rpm = 100%
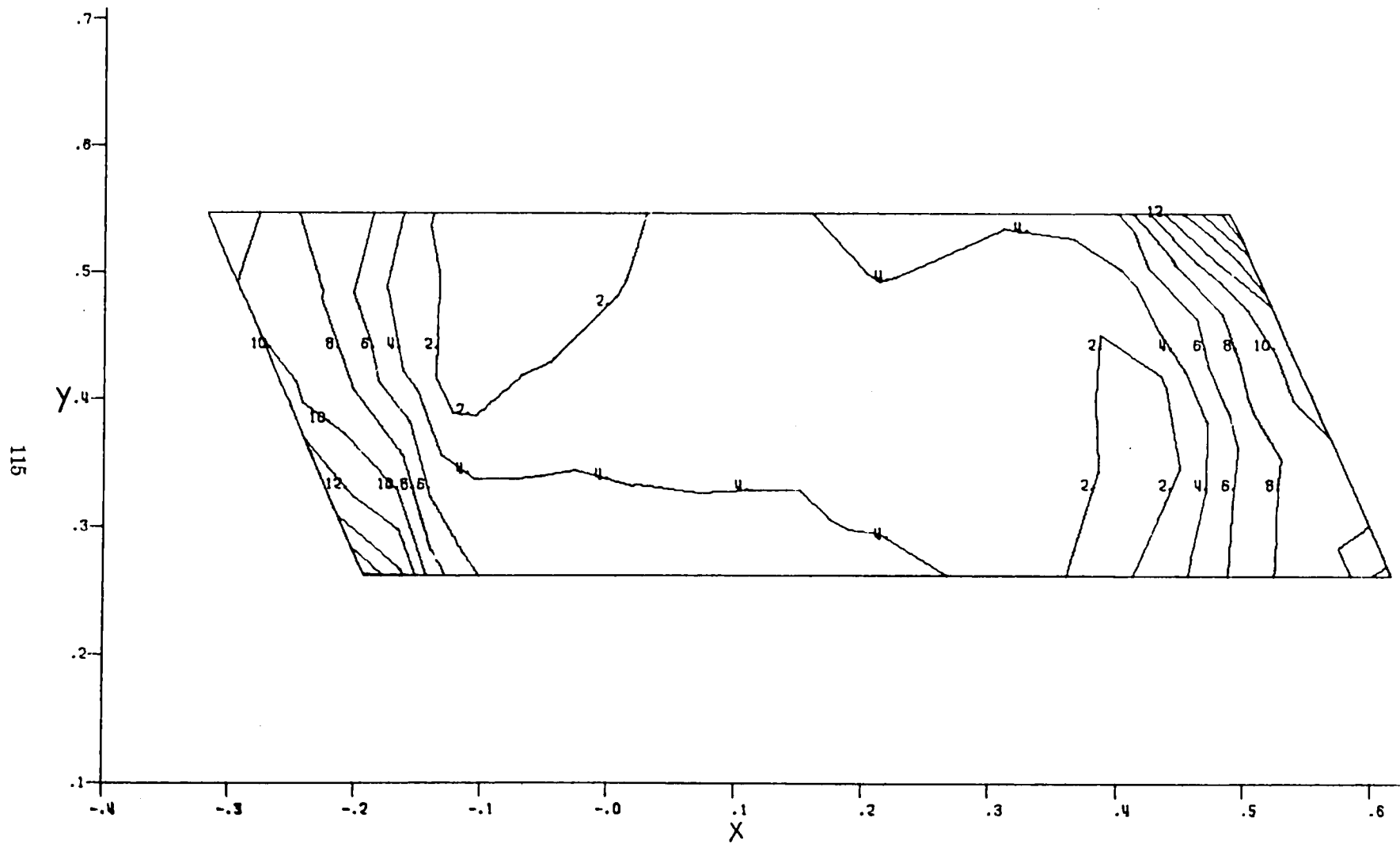
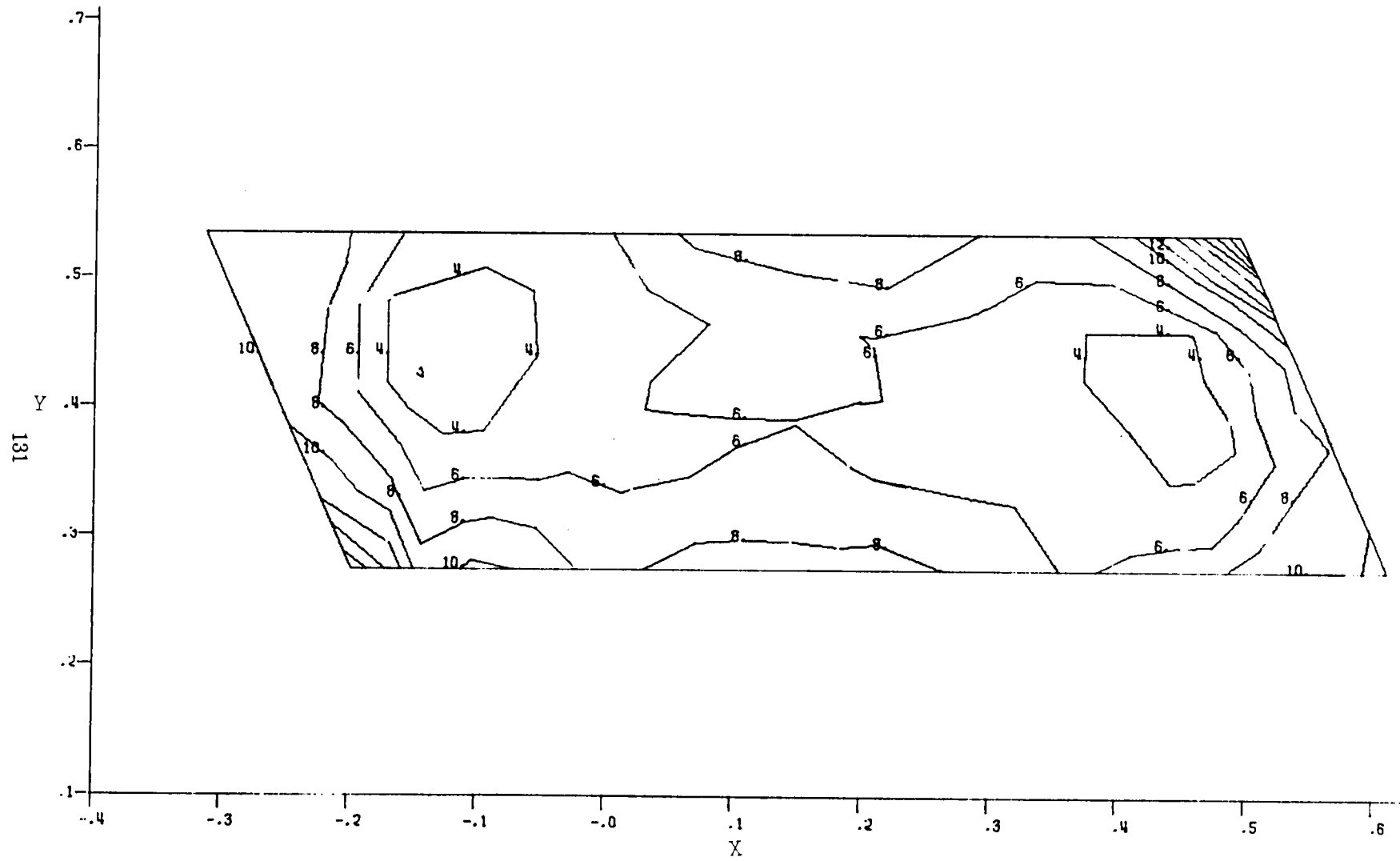*Figure C-2. Three-Dimensional Tensile Principal Stresses, Z = 0.0625, rpm = 100%*
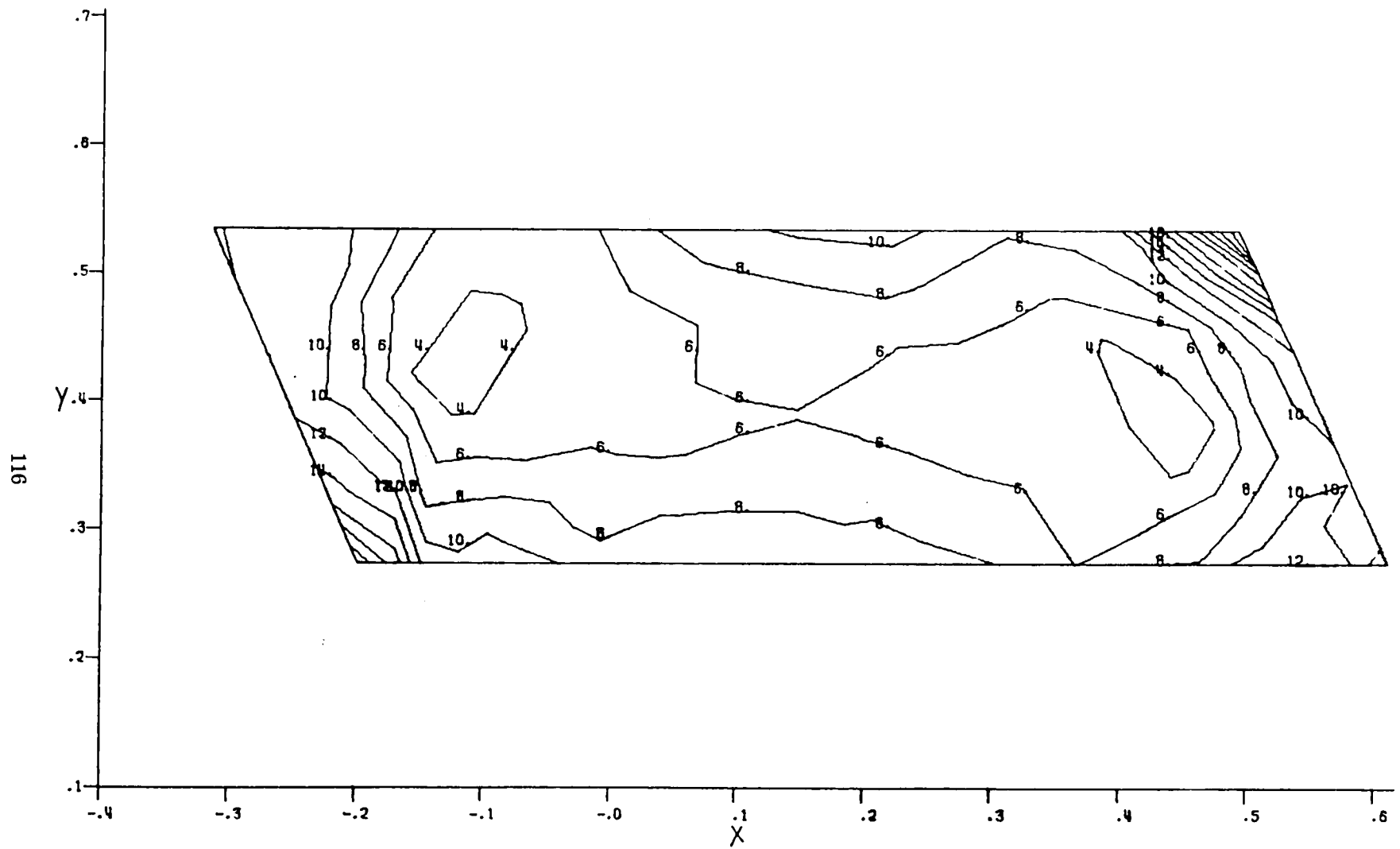
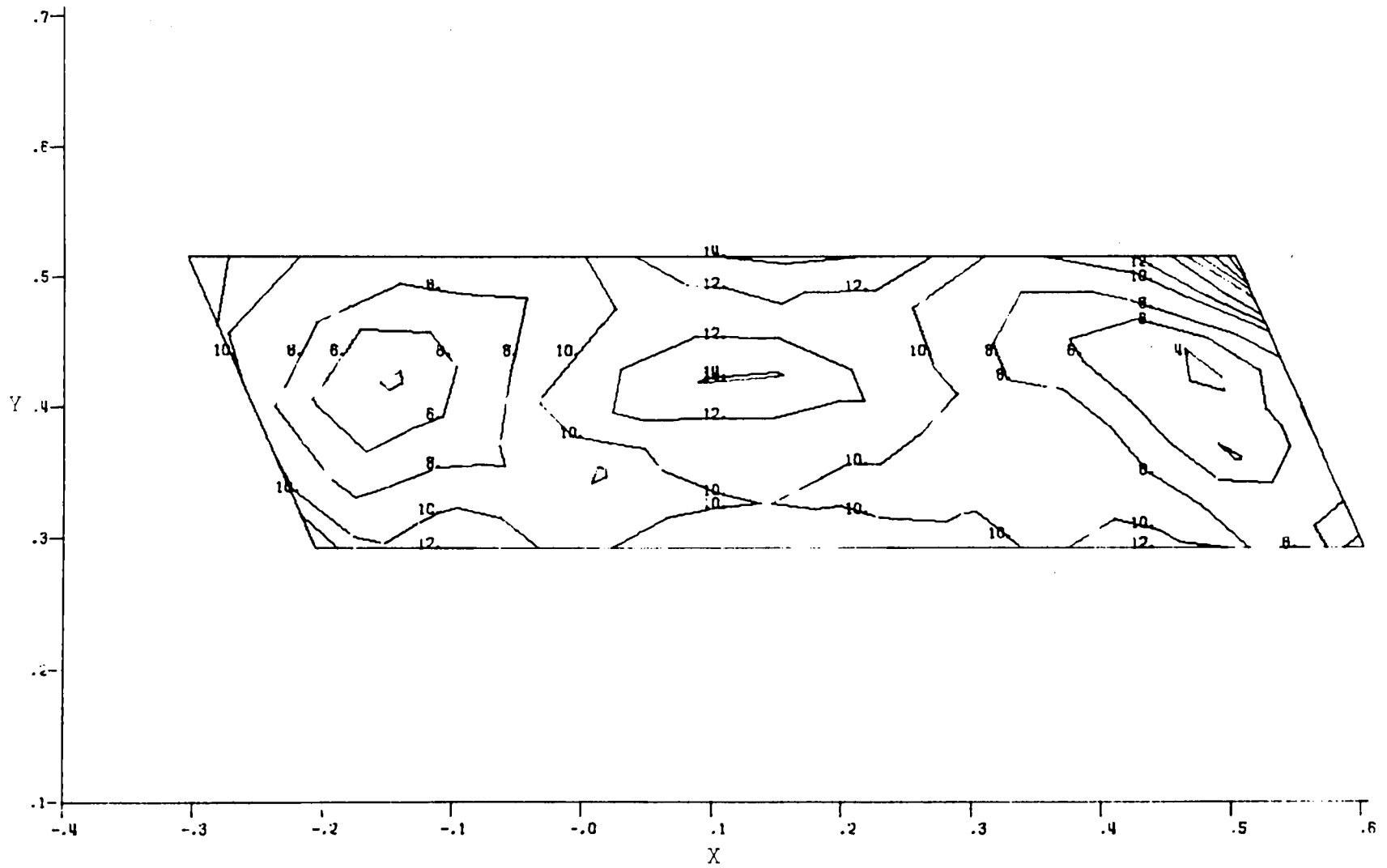*Figure C-3. Three-Dimensional Tensile Principal Stresses, Z = 0.0900, rpm = 100%*
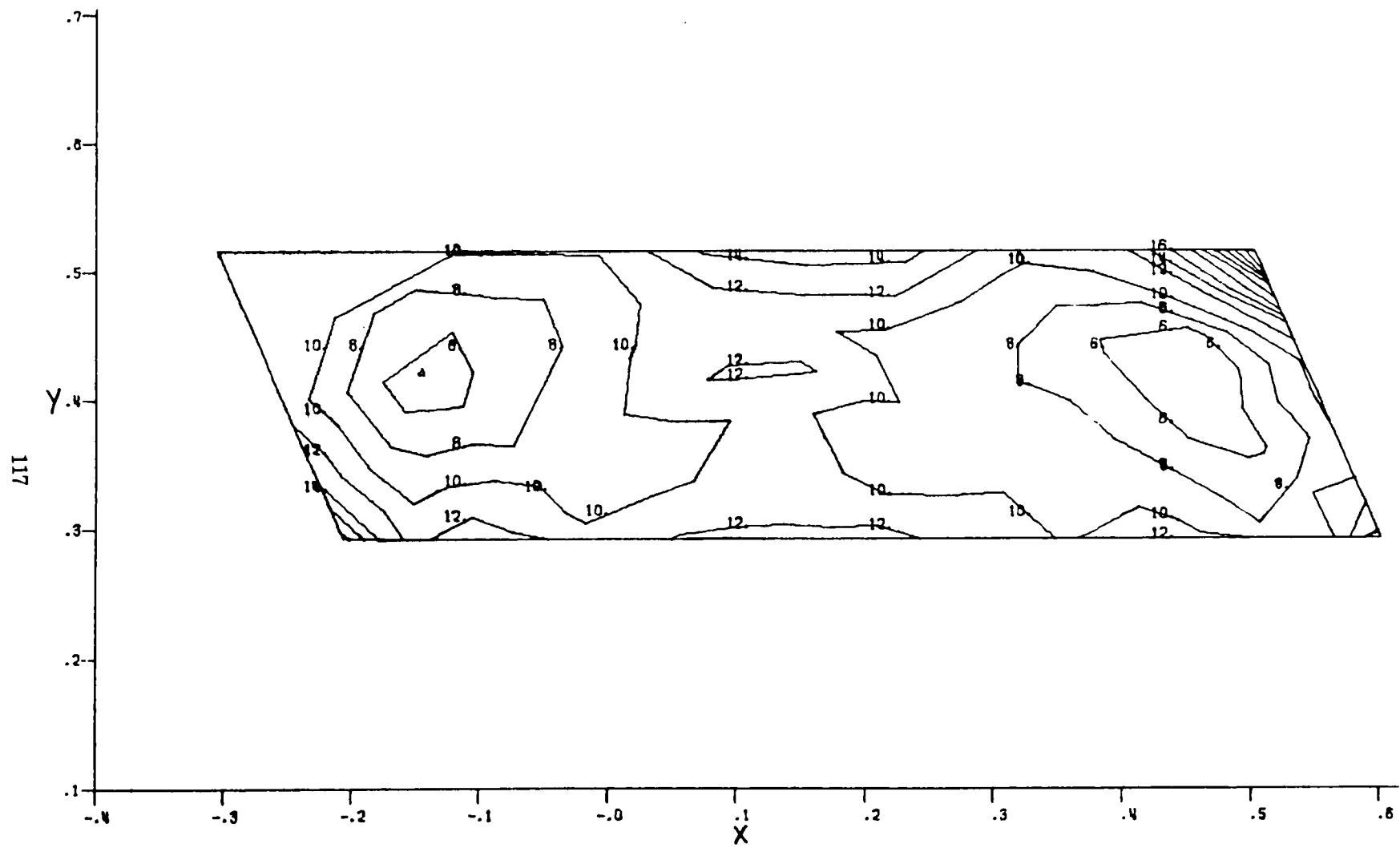
Figure C-4. Three-Dimensional Tensile Principal Stresses, Z = 0.1225, rpm = 100%
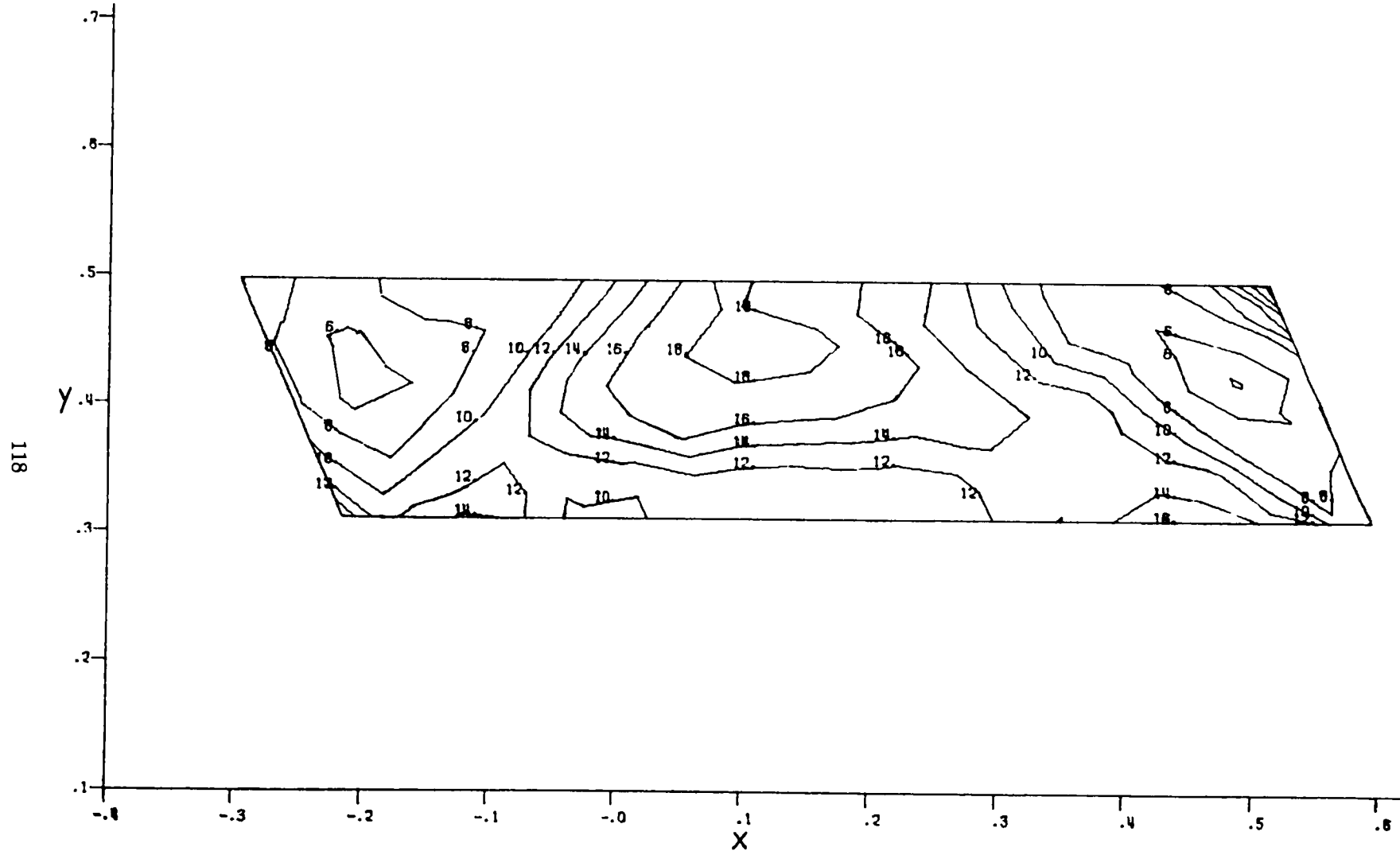
Figure C-5. Three-Dimensional Tensile Principal Stresses, Z = 0.1550, rpm = 100%

118
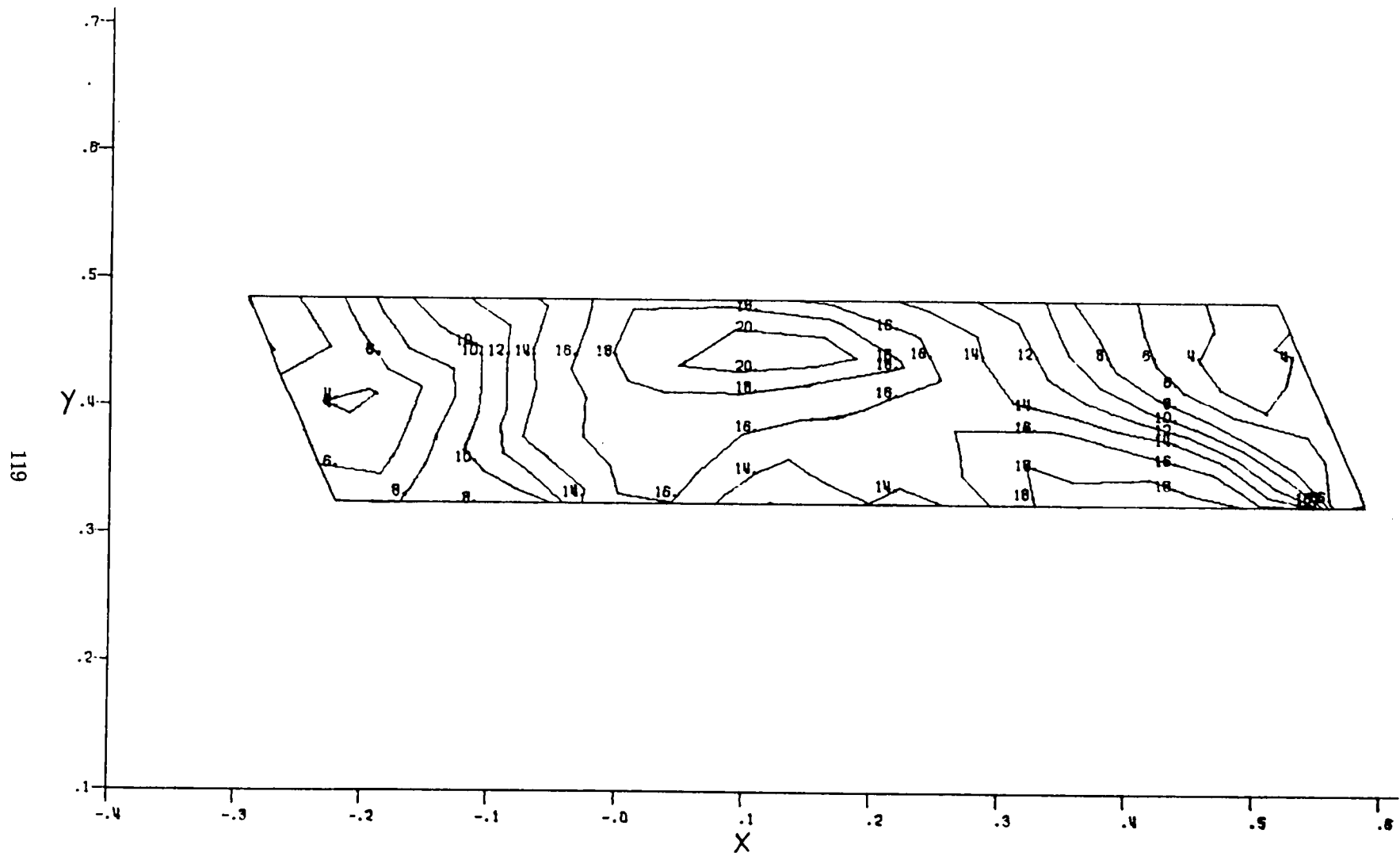
Figure C-6. Three-Dimensional Tensile Principal Stresses, Z = 0.1800, rpm = 100%
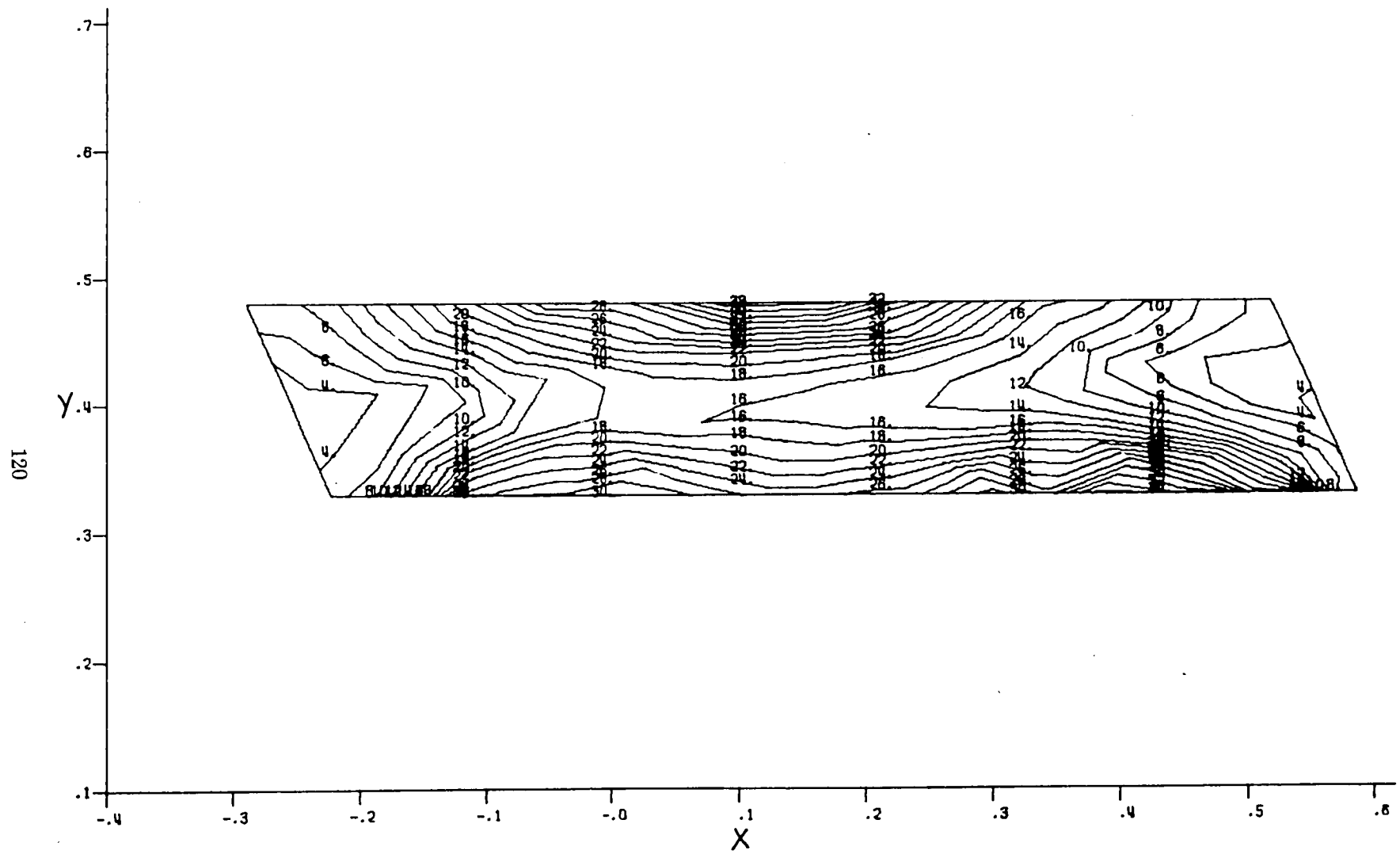
Figure C-7. Three-Dimensional Tensile Principal Stresses, Z = 0.2000, rpm = 100%
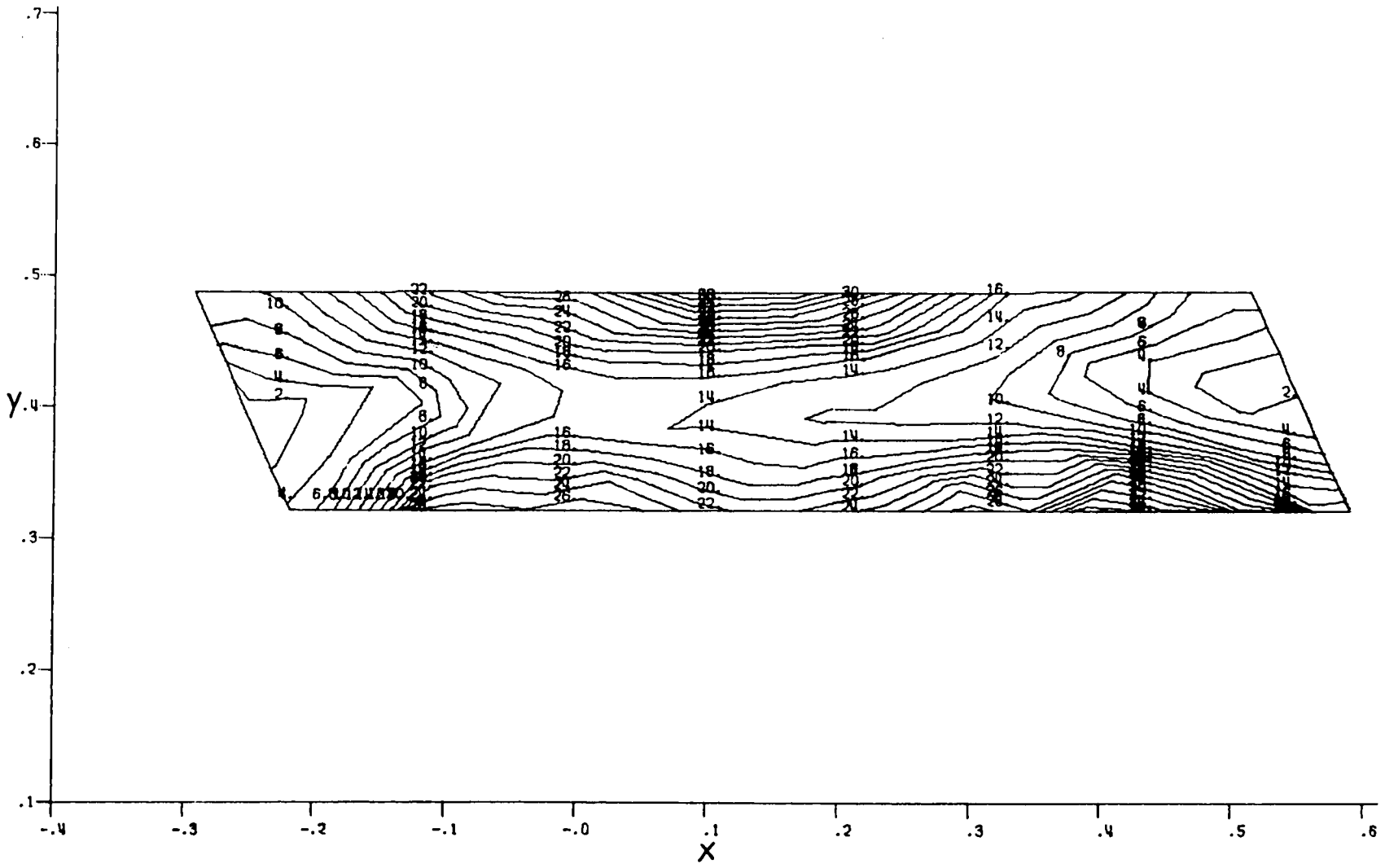
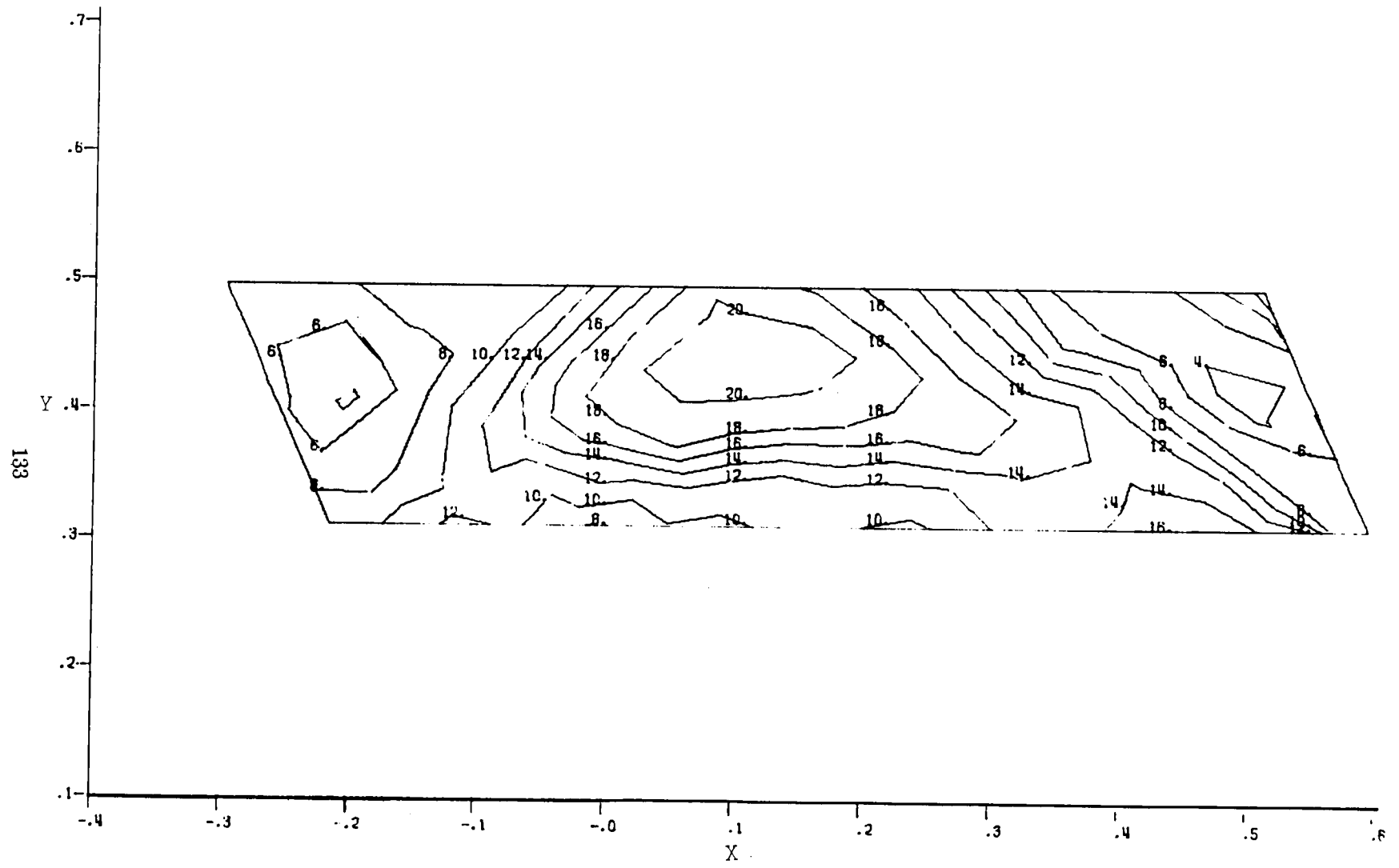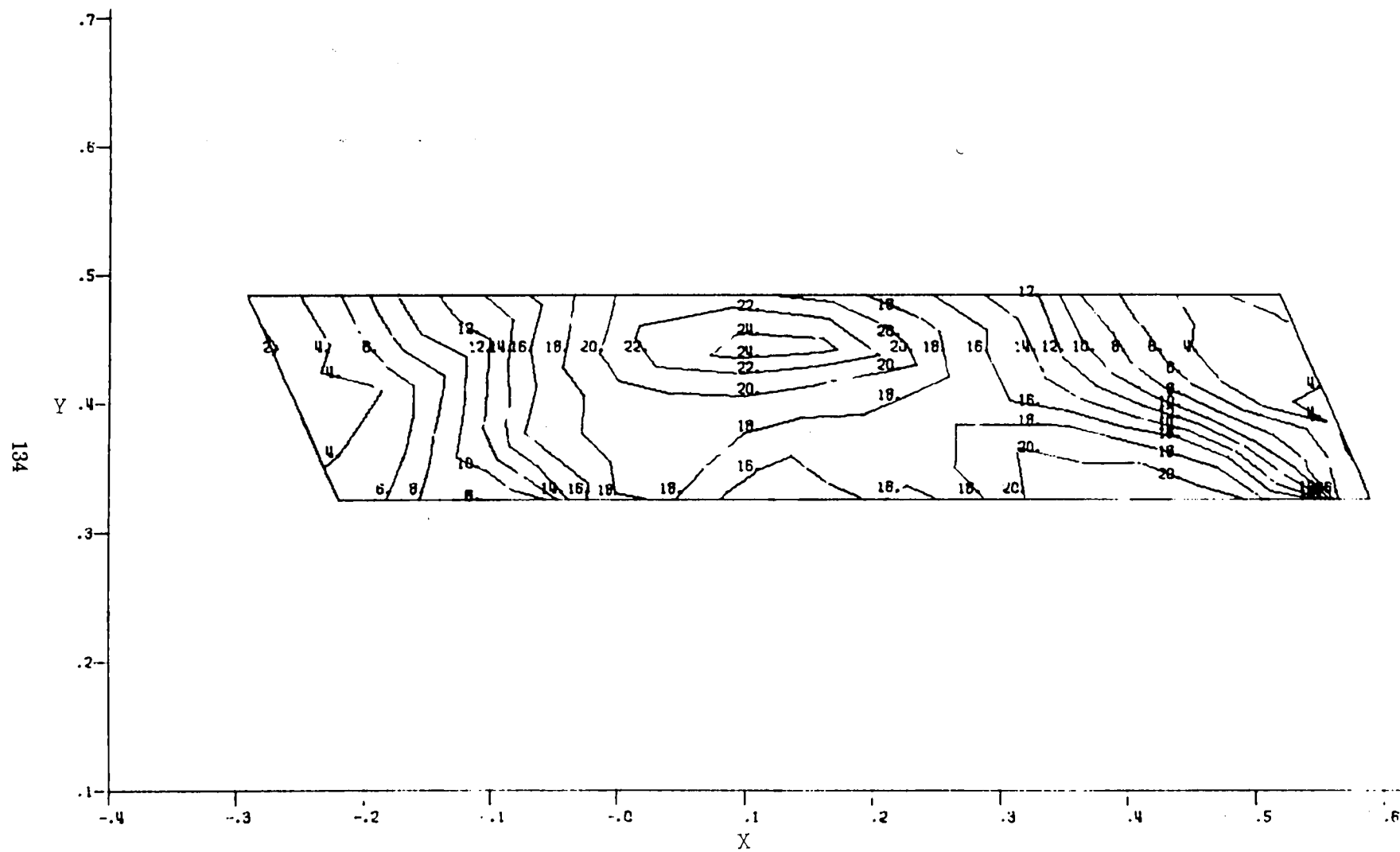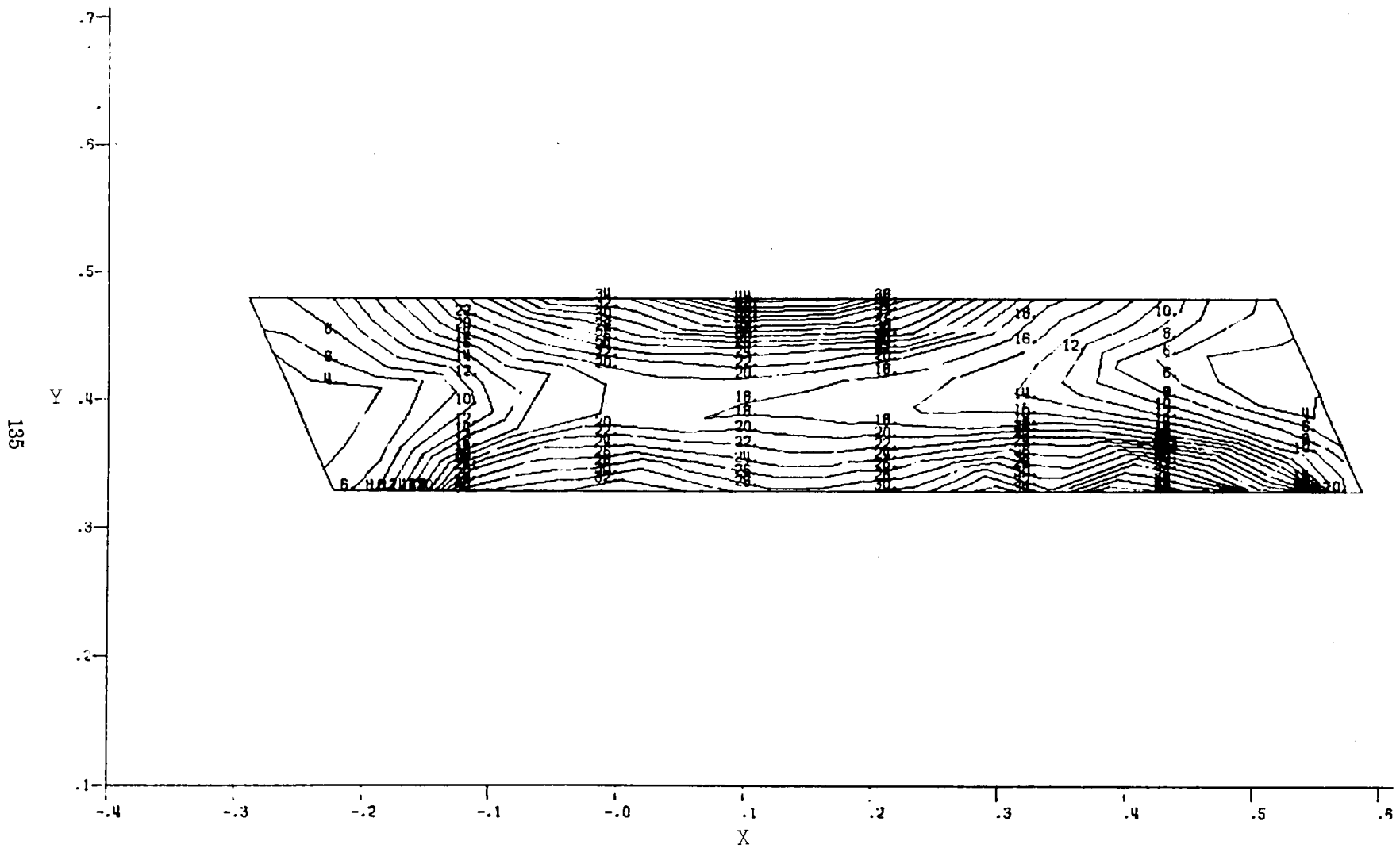*Figure C-8. Three-Dimensional Tensile Principal Stresses, Z = 0.2250, rpm = 100%*
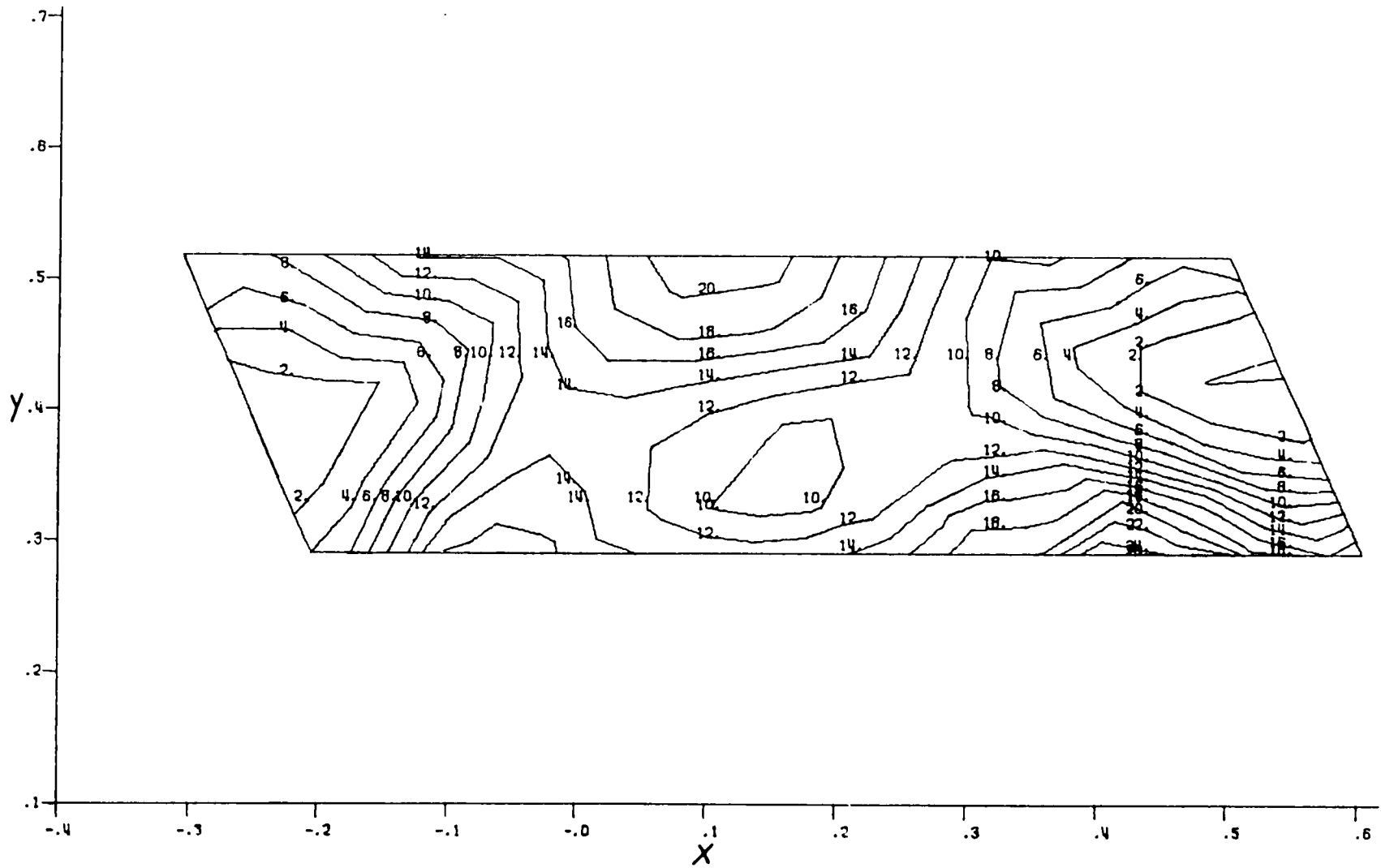
Figure C-9. Three-Dimensional Tensile Principal Stresses, Z = 0.2500, rpm = 100%
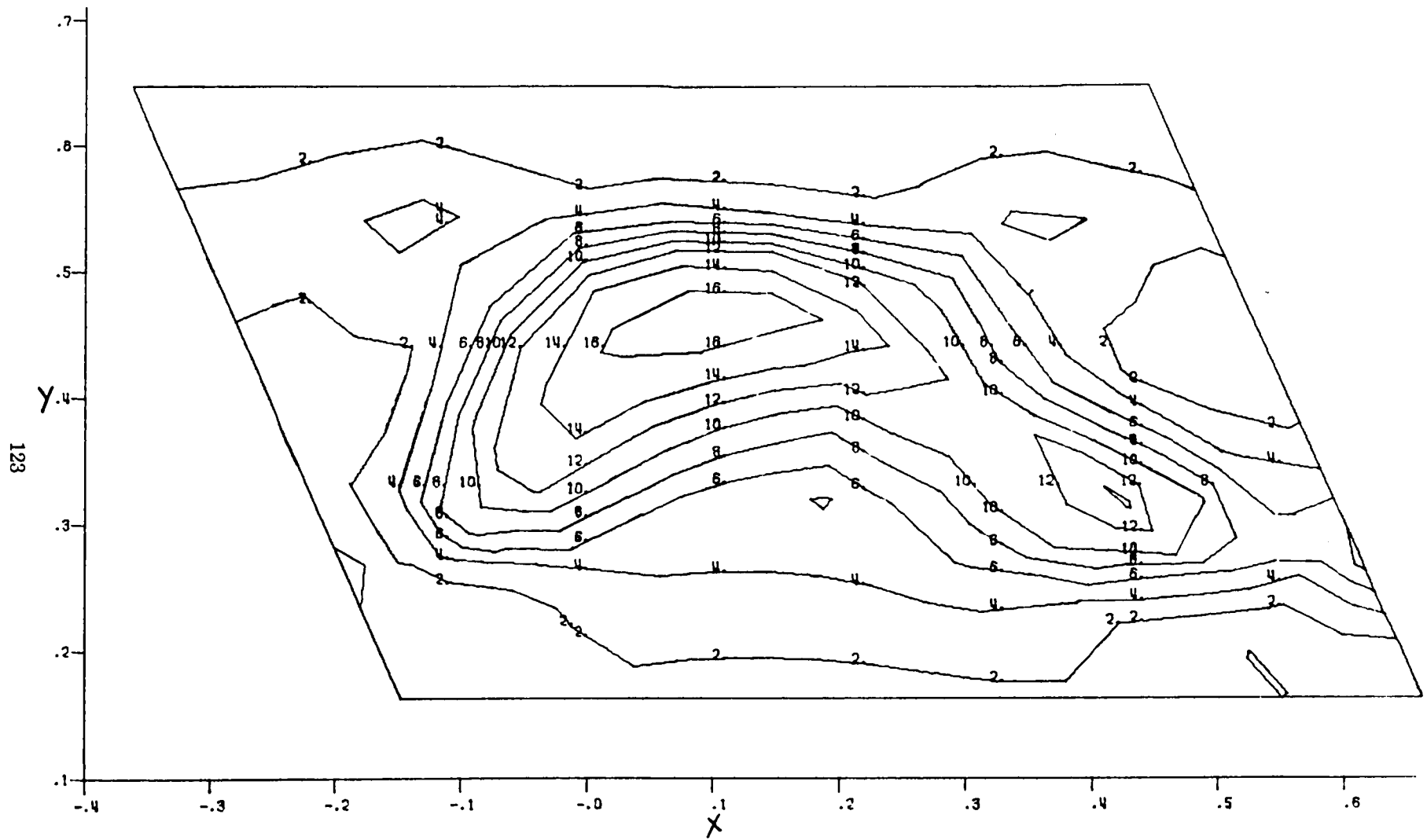
Figure C-10. Three-Dimensional Tensile Principal Stresses, Z = 0.2725, rpm = 100%
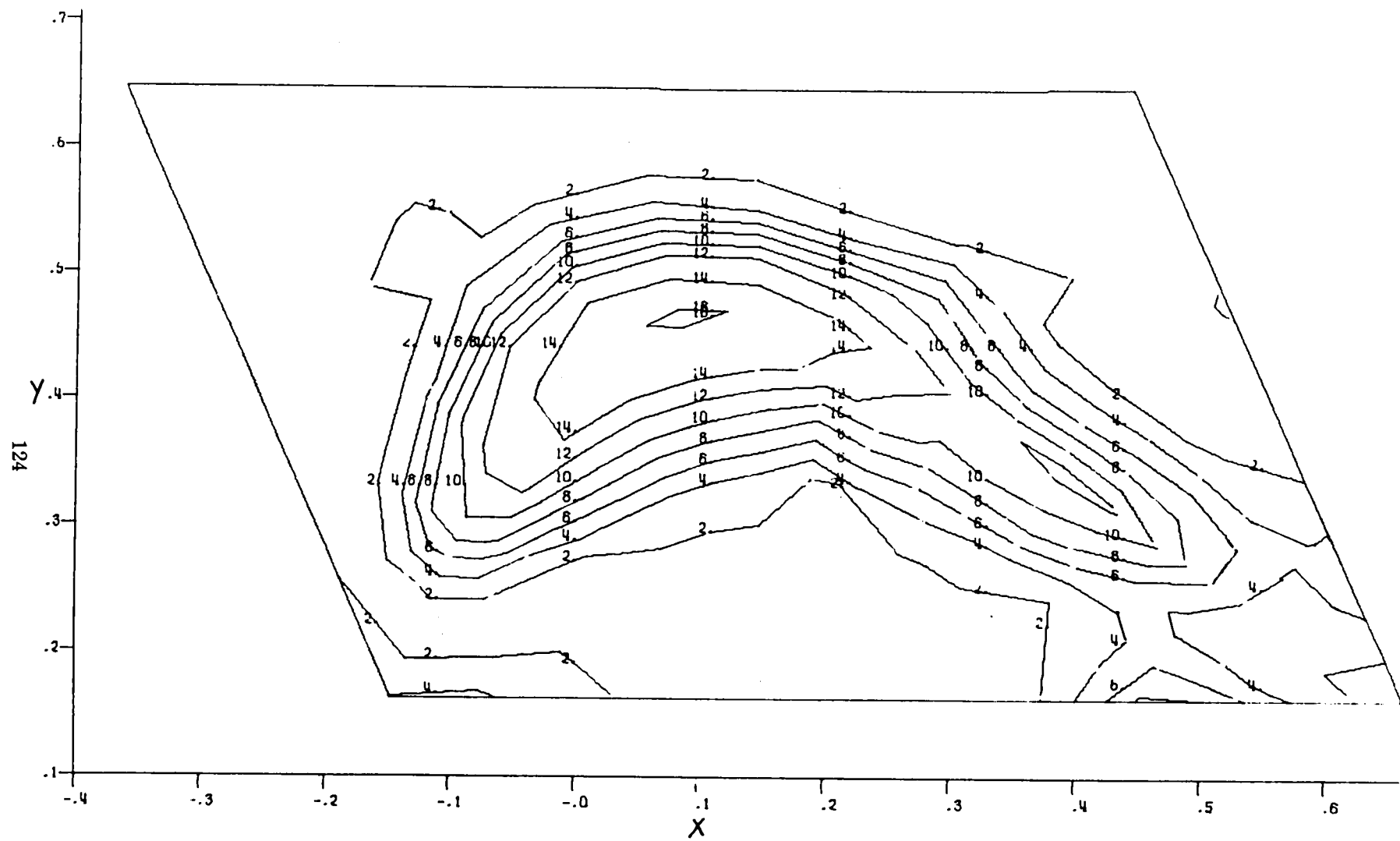
Figure C-11. Three-Dimensional Tensile Principal Stresses, Z = 0.2975, rpm = 100%

124
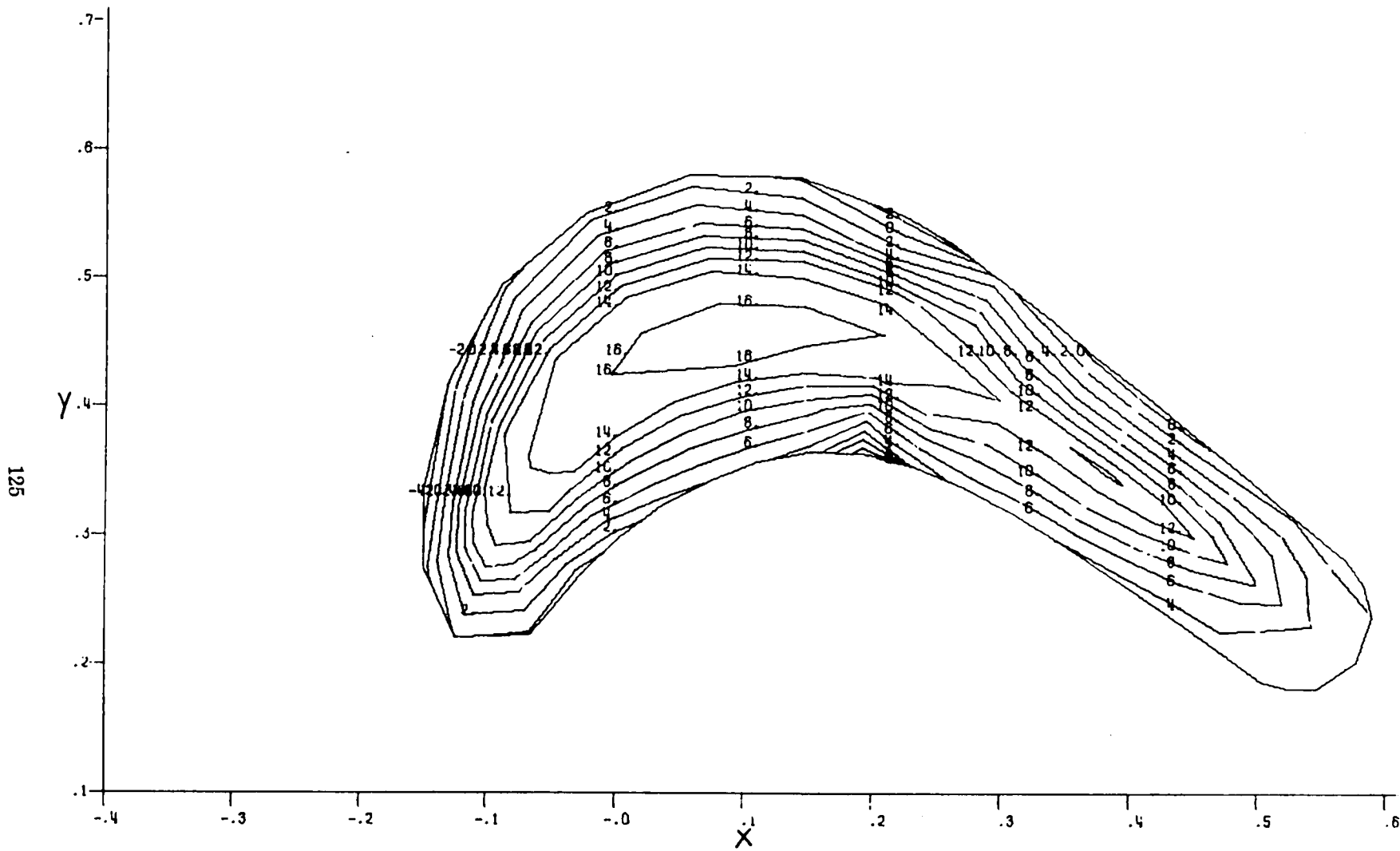
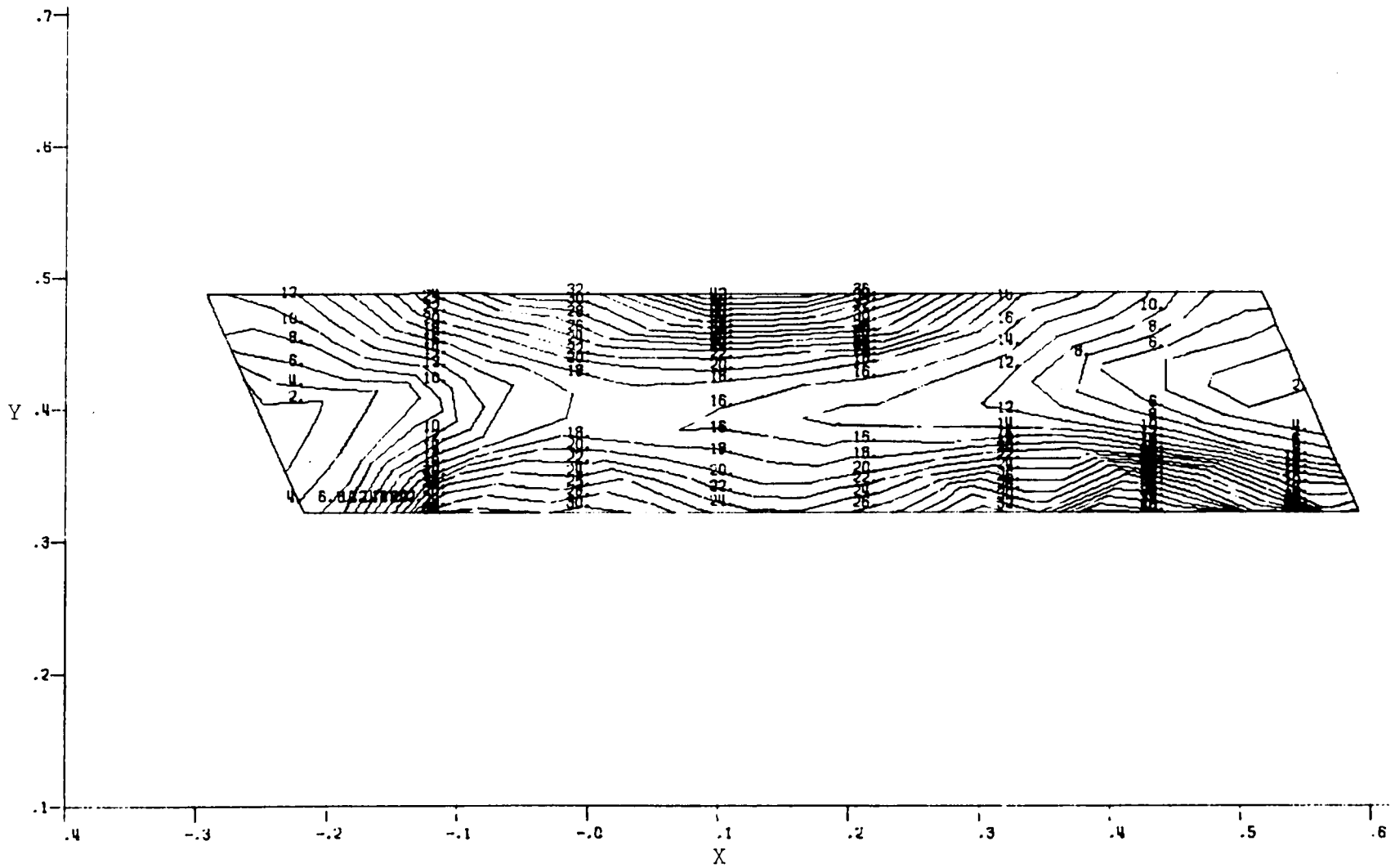*Figure C-12. Three-Dimensional Tensile Principal Stresses, Z = 0.3175, rpm = 100%*
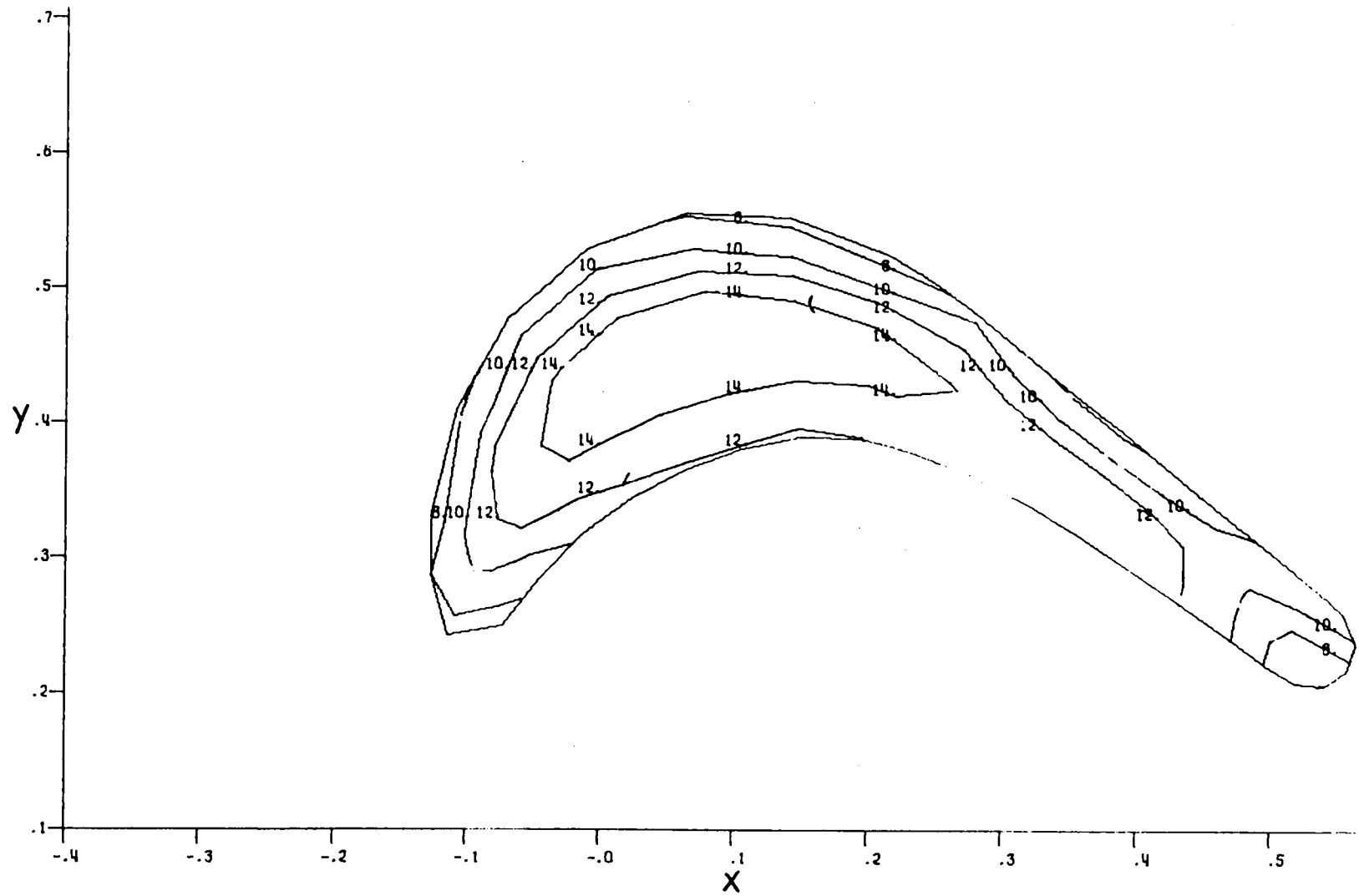
Figure C-13. Three-Dimensional Tensile Principal Stresses, Z = 0.3425, rpm = 100%
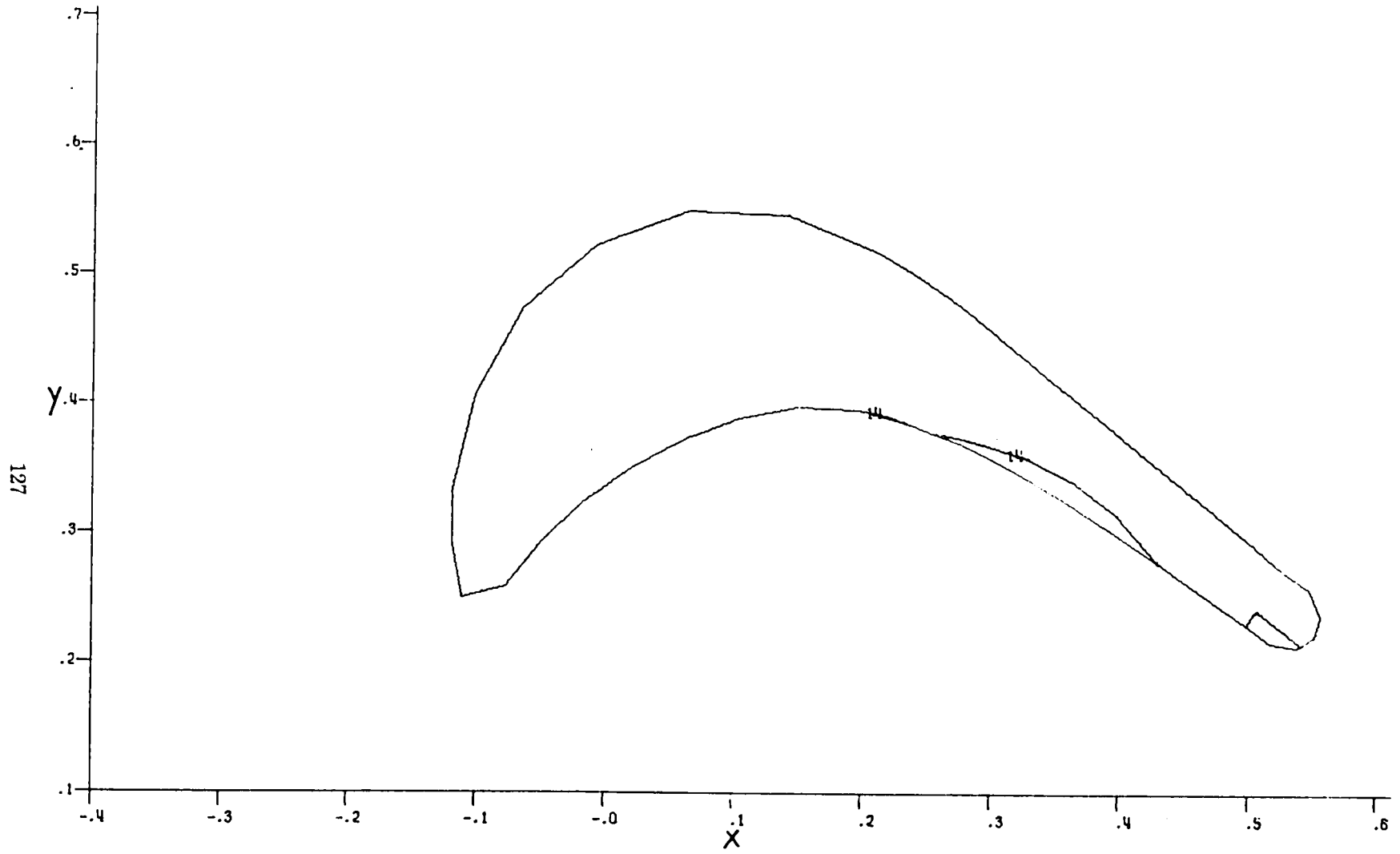
Figure C-14. Three-Dimensional Tensile Principal Stresses, Z = 0.3850, rpm = 100%

APPENDIX D

**Results of Three-Dimensional Analysis;
Stress Distributions at 110% Design rpm**

**Stresses shown as ksi only
See Figure 55 for Z plane locations**
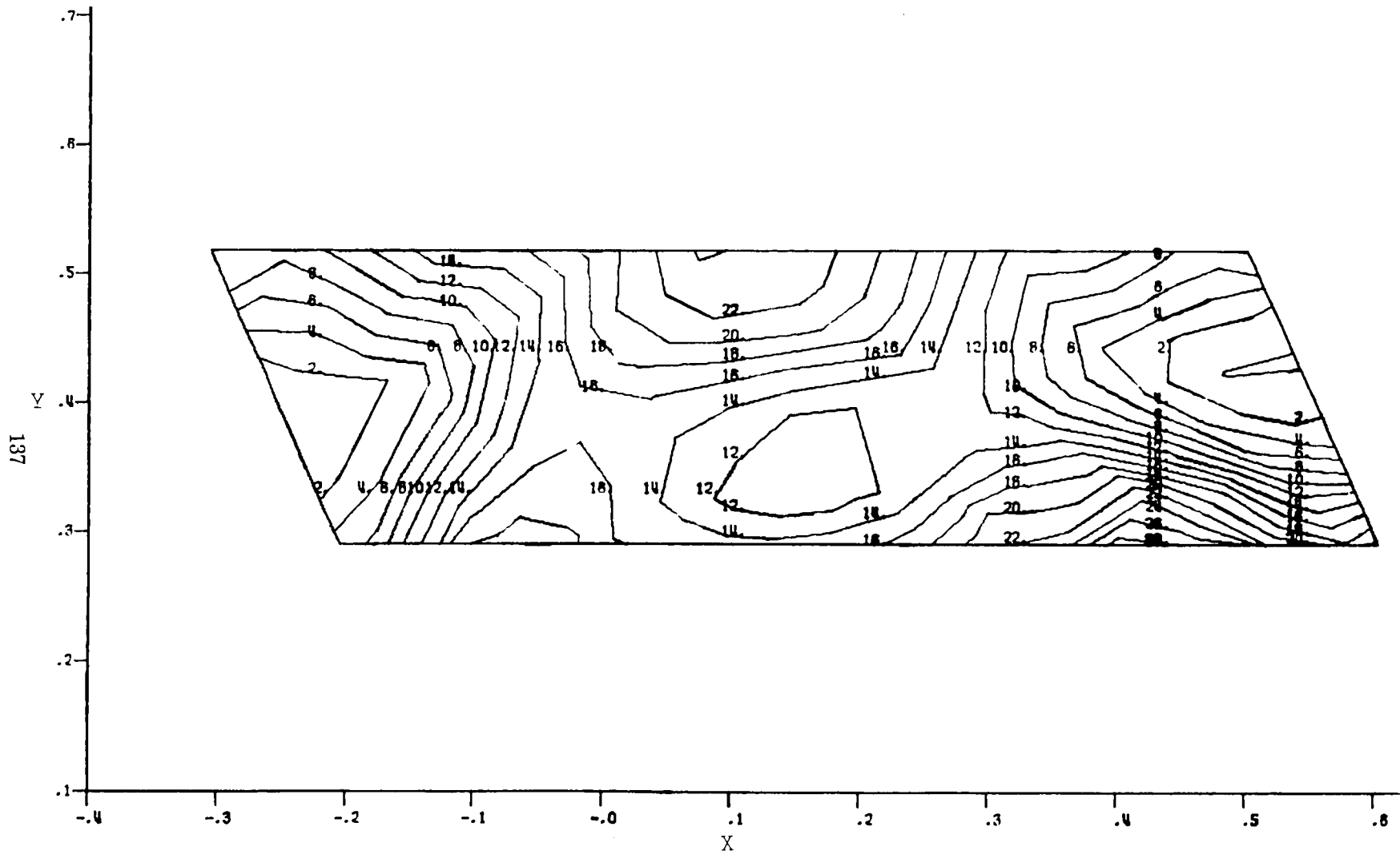
Figure D-1. Three-Dimensional Tensile Principal Stresses, Z = 0.0250, rpm = 110%

Figure D-2. Three-Dimensional Tensile Principal Stresses, Z = 0.0625, rpm = 110%

Figure D-3. Three-Dimensional Tensile Principal Stresses, Z = 0.0900, rpm = 110%

131

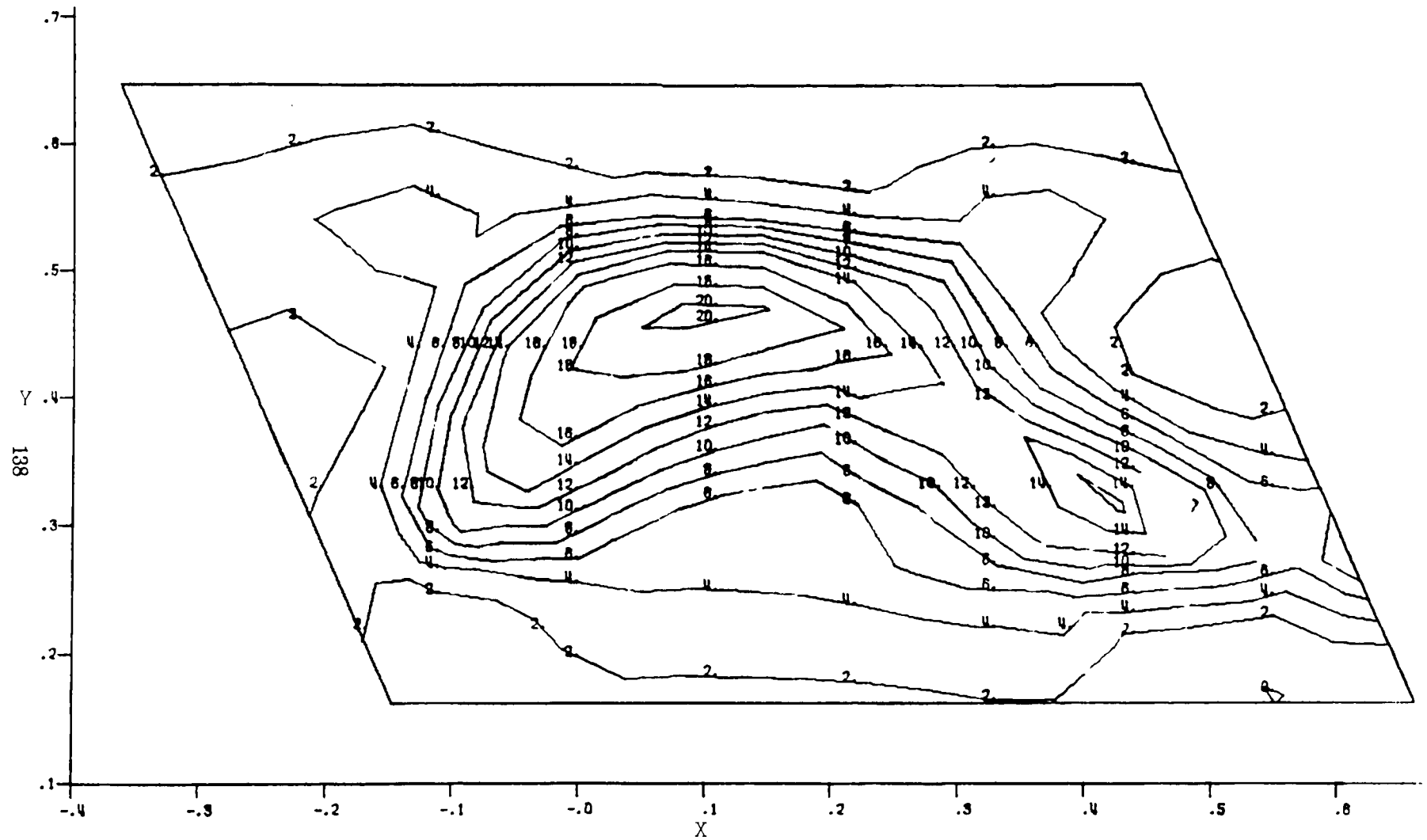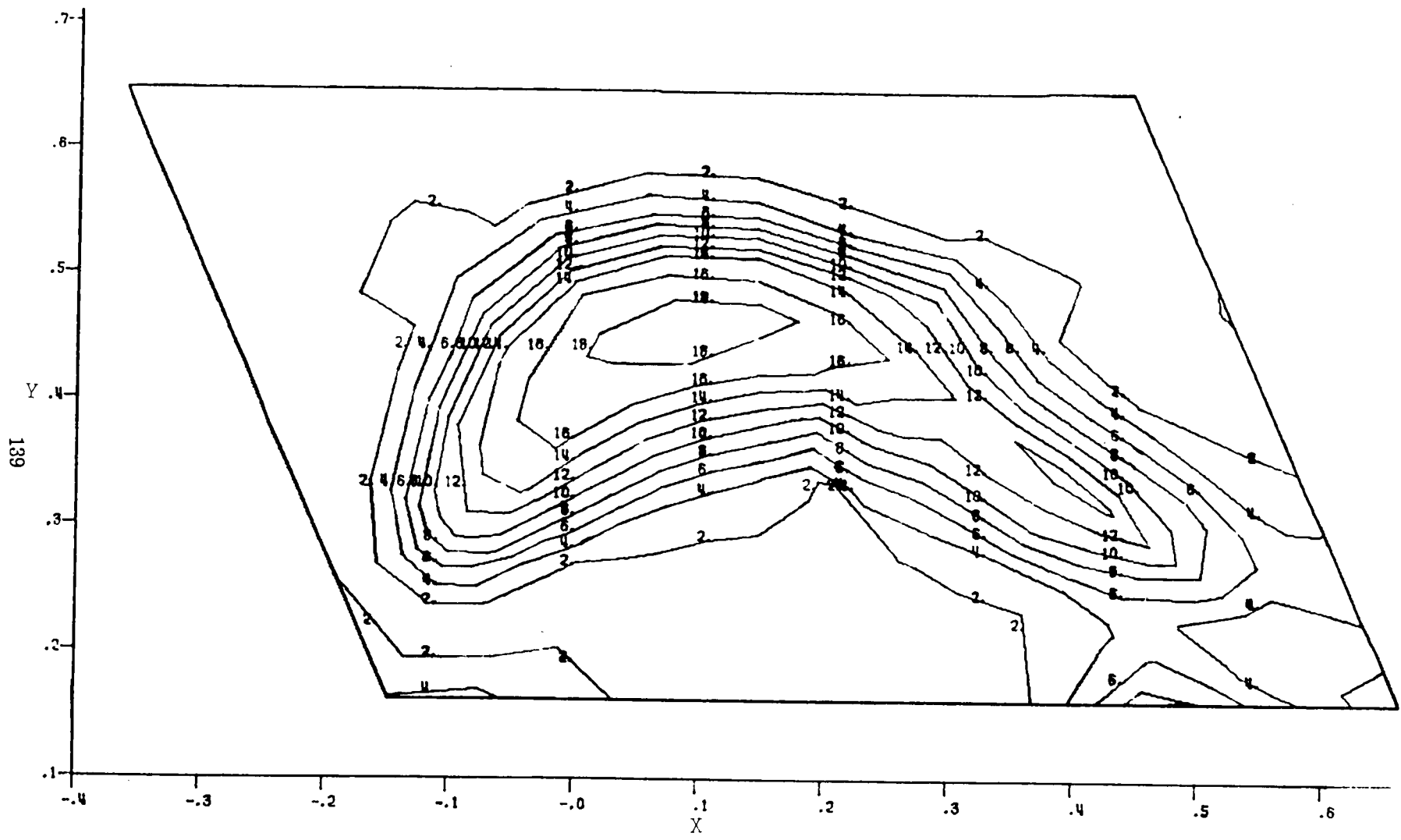*Figure D-4. Three-Dimensional Tensile Principal Stresses, Z = 0.1225, rpm = 110%*

Figure D-5. Three-Dimensional Tensile Principal Stresses, $Z = 0.1550$, rpm = 110%

Figure D-6. Three-Dimensional Tensile Principal Stresses, Z = 0.1800, rpm = 110%

Figure D-7. Three-Dimensional Tensile Principal Stresses, Z = 0.2000, rpm = 110%

Figure D-8. Three-Dimensional Tensile Principal Stresses, Z = 0.2250, rpm = 110%

Figure D-9. Three-Dimensional Tensile Principal Stresses, Z = 0.2500, rpm = 110%

Figure D-10. Three-Dimensional Tensile Principal Stresses, Z = 0.2725, rpm = 110%

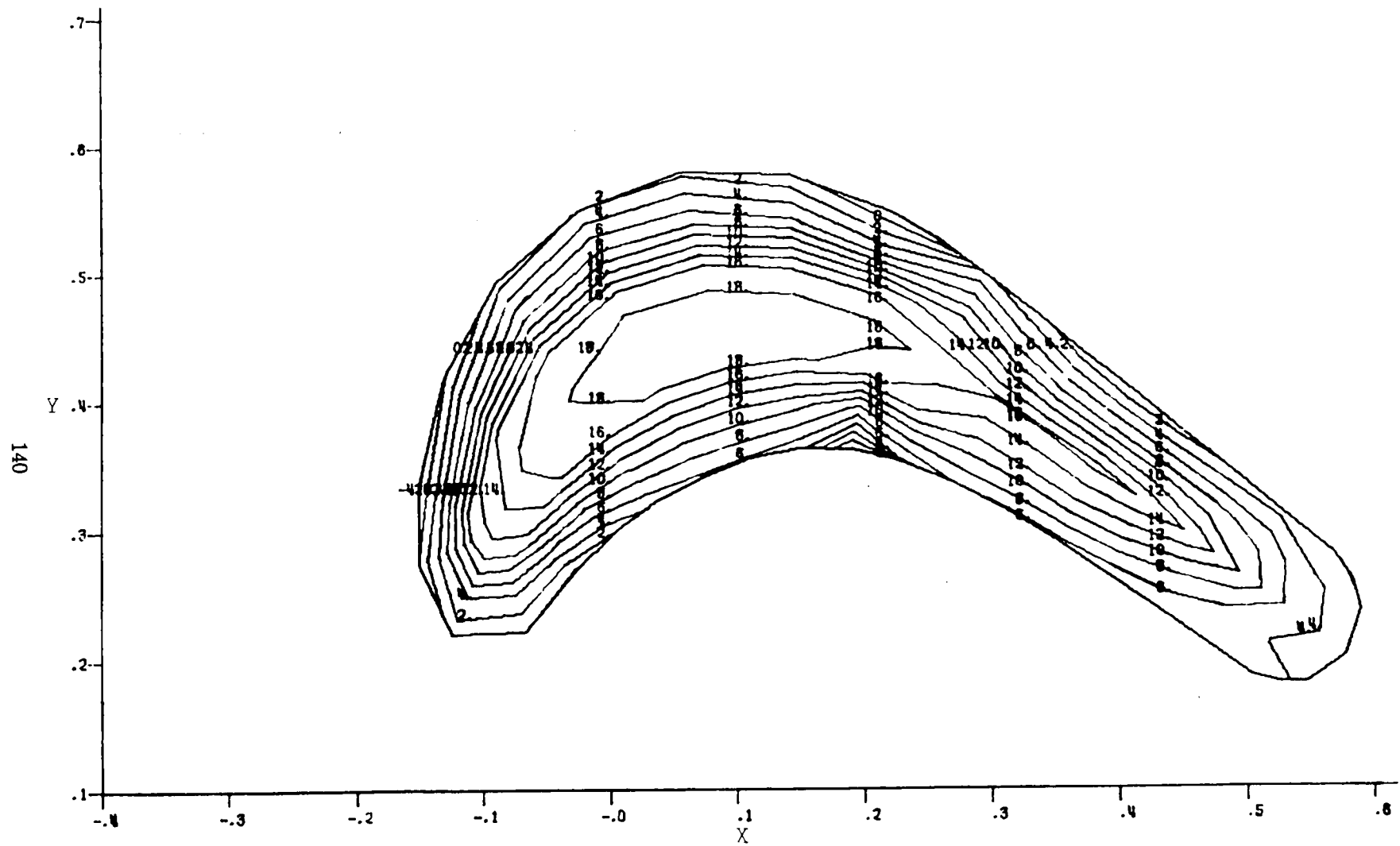*Figure D-11. Three-Dimensional Tensile Principal Stresses, Z = 0.2975, rpm = 110%*

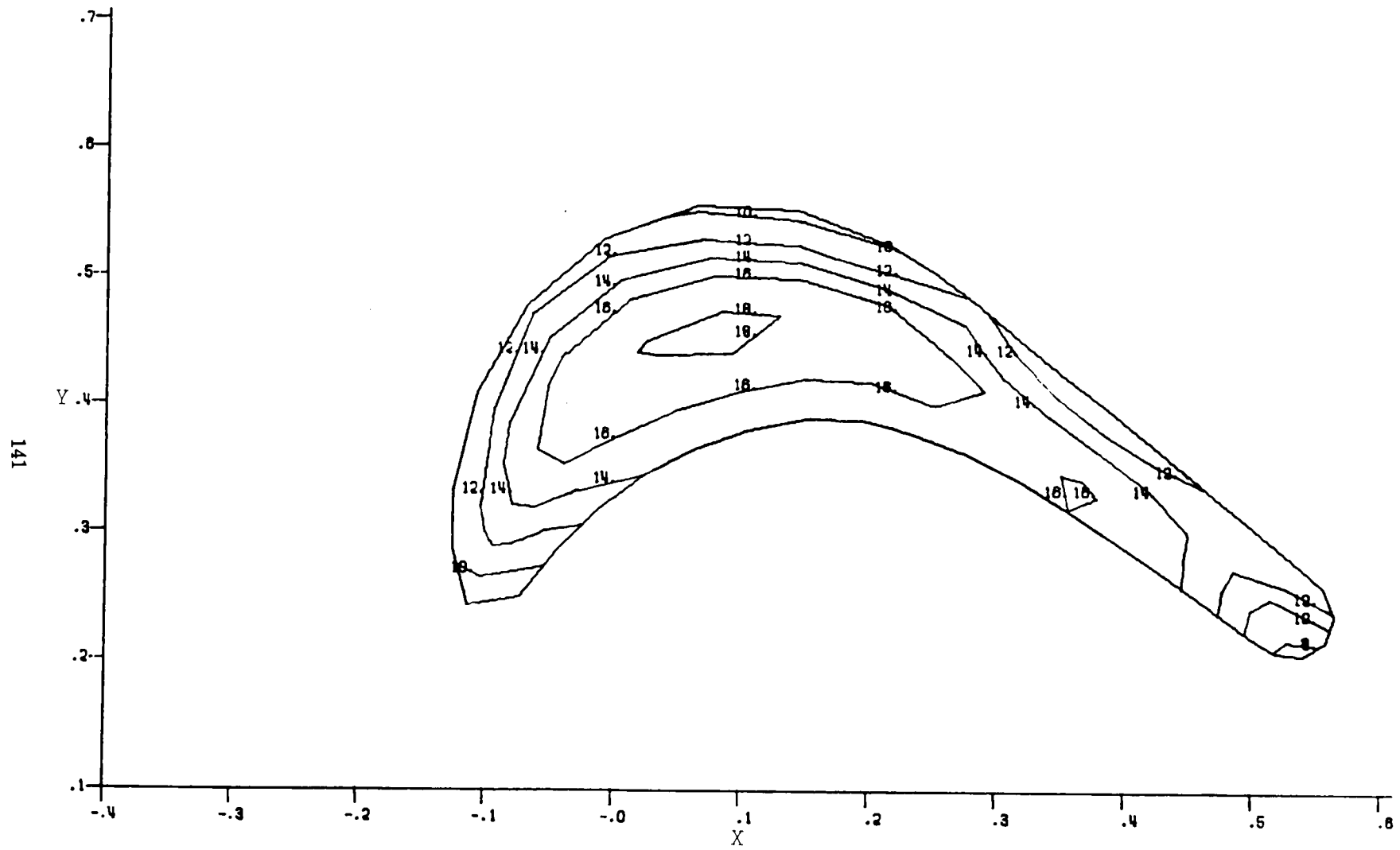Figure D-12. Three-Dimensional Tensile Principal Stresses, Z = 0.3175 rpm = 110%

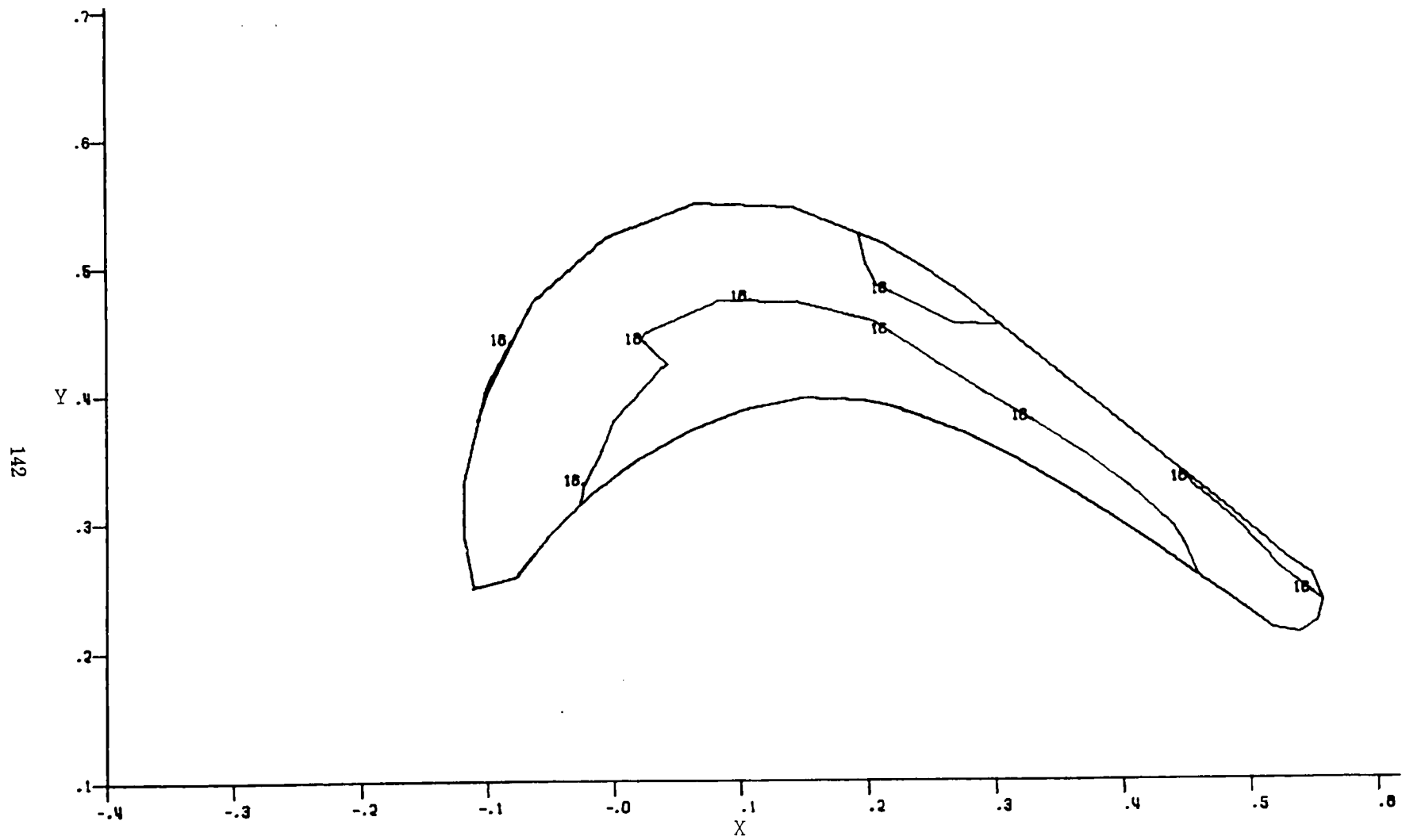Figure D-13. Three-Dimensional Tensile Principal Stresses, Z = 0.3425, rpm = 110%

Figure D-14. Three-Dimensional Tensile Principal Stresses, Z = 0.3850, rpm = 110%